Dissertation
submitted to the
Combined Faculty of Mathematics, Engineering and Natural Science
of the Ruperto Carola University Heidelberg, Germany
for the degree of
Doctor of Natural Sciences

Presented by
M.Sc. Yao Wu

born in: Henan, China
Oral examination: 09-07-2025

Advances in Fluid Inclusion Water Isotope Analysis and Late Quaternary Hydrological Environment Reconstruction in the Asian Monsoon Region

Referees: Prof. Dr. Norbert Frank
Prof. Dr. Oliver Friedrich

Abstract

This dissertation enhances the precision and stability of the Heidelberg fluid inclusion water stable isotope analytical setup through technical optimization, and identifies major sources of analytical uncertainty in fluid inclusion water isotope measurements through international interlaboratory comparisons. Building on these improved measurement techniques and using multi-proxy stalagmite reconstructions, it also investigates the coupling between natural and anthropogenic factors in hydrological and environmental changes in the Asian monsoon region during the mid- to late Holocene, and deepens the understanding of hydrological evolution mechanisms within this region since the last glacial period.

Methodologically, this dissertation evaluates isotopic deviation trends in low-volume water (<0.5 µl) sample measurements using the Heidelberg fluid inclusion measurement line and develops correction protocols. Optimizations in measurement procedures, data processing, and glass tube encapsulation techniques significantly reduce isotopic fractionation during heating, improving both measurement efficiency and accuracy. In cold-water coral applications, dissertation quantifies δ^{18}O and δ^{2}H fractionation under varying heating conditions, identifying exchangeable water reservoirs in coral skeletons that complicate the interpretation of original isotopic signatures. An international interlaboratory comparison involving 13 laboratories was conducted to evaluate the accuracy and limitations of fluid inclusion water stable isotope measurements.The results indicate that the accuracy and reproducibility of isotopic measurements are significantly better at larger water volumes (1 µl and 0.5 µl), while measurements at volumes below 0.5 µl exhibit increased uncertainty, underscoring the ongoing technical challenges in low water volume isotopic analysis.

For paleoclimate reconstruction, this dissertation establishes about 120 ka BP (ka = thousand years; BP = before present, where "present" is defined as 1950 CE) hydrological history for southwest China using speleothem δ^{18}O, δ^{13}C trace elements, and fluid inclusions δ^{18}O and δ^{2}H records. The δ^{18}O and δ^{2}H records from speleothem fluid inclusions during the mid- to late Holocene reveal that regional hydroclimate was influenced by a combination of natural (El Niño–Southern Oscillation) and anthropogenic activities, including agricultural development and population movements. During the last glacial period, Northern Hemisphere summer insolation intensity was identified as the primary control on phase variations in the regional hydrological environment and monsoonal precipitation, with global ice volume modulating the amplitude of hydrological responses to insolation changes.

Zusammenfassung

Diese Dissertation verbessert die Präzision und Stabilität der Heidelberger analytischen Plattform zur stabilen Wasserstoff- und Sauerstoff-Isotopenmessung von Fluideinschlüssen durch technische Optimierung und identifiziert sowie quantifiziert wesentliche Quellen analytischer Unsicherheiten bei den Messungen von Wasserisotopen in Fluideinschlüssen mittels internationaler ringversuche. Aufbauend auf diesen verbesserten Messtechniken und unter Verwendung von mehrdimensionalen Stalagmit-Rekonstruktionen untersucht sie außerdem die Kopplung zwischen natürlichen und anthropogenen Faktoren in hydrologischen und umweltbezogenen Veränderungen in der asiatischen Monsunregion während des mittleren bis späten Holozäns und vertieft das Verständnis der Mechanismen der hydrologischen Entwicklung in dieser Region seit dem Letzten Glazial.

Methodisch bewertet diese Arbeit Isotopenabweichungen bei Messungen von Wasserproben mit geringem Volumen (<0,5 µl) unter Verwendung der Heidelberger Messlinie für Flüssigkeitseinschlüsse und entwickelt entsprechende Korrekturverfahren. Optimierungen in den Messprotokollen, der Datenverarbeitung sowie der Verkapselungstechnik von Glaskapillaren verringern signifikant die Isotopenfraktionierung während der Erhitzung und verbessern sowohl die Effizienz als auch die Genauigkeit der Messungen. Bei der Anwendung auf Kaltwasserkorallen quantifiziert die Arbeit die δ^{18}O und δ^{2}H Fraktionierung unter verschiedenen Erhitzungsbedingungen und identifiziert austauschbare Wasserreservoire in den Korallenskeletten, die die Interpretation ursprünglicher Isotopensignaturen erschweren. Ein internationaler Ringversuch mit 13 Laboratorien wurde durchgeführt, um die Genauigkeit und Grenzen der Isotopenmessung in Flüssigkeitseinschlüssen zu bewerten. Die Ergebnisse zeigen, dass Genauigkeit und Reproduzierbarkeit bei größeren Wasservolumina (1 µl und 0,5 µl) deutlich besser sind, während Messungen mit weniger als 0,5 µl erhöhte Unsicherheiten aufweisen – ein Hinweis auf die anhaltenden technischen Herausforderungen in der Isotopenanalyse von Kleinstwassermengen.

Für die Paläoklimarekonstruktion stellt diese Dissertation eine etwa 120 ka BP (ka = Tausend Jahre; BP = vor heute, wobei „heute“ als 1950 n. u. Z. definiert ist) umfassende hydrologische Geschichte für Südwestchina anhand von Speleothem-δ^{18}O, δ^{13}C, Spurenelementen sowie Flüssiginklusionen-δ^{18}O und δ^{2}H-Aufzeichnungen auf. Die δ^{18}O- und δ^{2}H-Aufzeichnungen aus Speleothem-Flüssiginklusionen während des mittleren bis späten Holozäns zeigen, dass das regionale Hydroklima von einer Kombination natürlicher Faktoren wie der El Niño–Südlichen Oszillation und anthropogenen Aktivitäten beeinflusst wurde, zu denen landwirtschaftliche Entwicklung und Bevölkerungsbewegungen gehören. Während der letzten Vereisungsperiode wurde die Sommerinsolation der Nordhalbkugel als primärer Steuerfaktor für Phasenverschiebungen in der regionalen hydrologischen Umwelt und den Monsunniederschlägen identifiziert, wobei das globale Eisvolumen die Amplitude der hydrologischen Reaktionen auf Insolationsänderungen modulierte.

Contents

Introduction

Monsoons are climate phenomena governed by seasonally alternating atmospheric circulation, characterized by significant shifts in wind direction and precipitation between summer and winter. In the Asian monsoon region, seasonal circulation changes drive large-scale moisture transport and precipitation processes, profoundly influencing regional water resource distribution and ecosystem patterns. As the most intense and structurally complex monsoon system globally, the Asian summer monsoon (ASM) controls the seasonal variation of precipitation from South Asia to East Asia, playing a critical role in water supply, agricultural productivity, and ecological dynamics for billions of people. Land–sea thermal contrasts primarily drive the ASM. Its seasonal wind reversal and moisture transport exhibit pronounced spatiotemporal variability on interannual to orbital timescales, regulated by a combination of internal and external climate forcings (e.g., Cheng et al. (2022a); Ding et al. (2018); Niu et al. (2025) and their references). As global warming intensifies, the climatic and environmental challenges associated with changes in ASM strength are becoming increasingly complex (e.g., Lu et al. (2025); Zhao et al. (2025)). A comprehensive understanding of its variability, driving mechanisms, and potential socio-ecological impacts has emerged as one of the central issues in contemporary climate and environmental science. Therefore, reconstructing the evolution and spatial distribution of ASM intensity and precipitation across different timescales is crucial for elucidating the monsoon system's response mechanisms to climate change and its driving factors. Such reconstructions provide a scientific basis for assessing the impacts of monsoon variability on regional climate, agriculture, and water resources, and offer an essential foundation for addressing future climate challenges.

Among various paleoclimate archives, speleothems have emerged as a key archive for reconstructing ASM intensity and environmental evolution, owing to their precise chronological control and high-resolution deposition. Speleothem δ^{18}O a commonly used indicator, reflects variations in the δ^{18}O of precipitation and indirectly captures changes in ASM strength and large-scale circulation precipitation patterns (e.g., Cheng et al. (2019); Duan et al. (2016); Liu et al. (2020)). However, since multiple factors influence precipitation δ^{18}O it cannot be directly used to quantify rainfall amount, which limits its applicability in reconstructing regional hydroclimatic changes (Liu et al., 2020; Ruan et al., 2019; Tan, 2014). Recently, the emerging analysis of stable isotopes in speleothem fluid inclusions water (e.g., δ^2H and δ^{18}O) provides direct evidence of past precipitation isotope compositions, yielding valuable insights into atmospheric water cycling and vapour transport under monsoonal influences (e.g., Fleitmann et al. (2022); Sakai et al. (2024); Warken et al. (2022); Weissbach et al. (2023)). These isotopic signatures also offer the potential to reconstruct past temperatures, thereby enabling a more comprehensive understanding of paleoclimate conditions through simultaneous constraints on both the hydrological and thermal states of the environment (e.g., Affolter et al. (2019, 2025); Genty et al. (2002); Løland et al. (2022); Uemura et al. (2016); Wortham et al. (2022)). However, the small volume and instability of inclusion water render it susceptible to evaporation and isotopic fractionation during extraction, which impacts measurement precision. Variations in extraction methods and analytical procedures across laboratories can also result in systematic discrepancies in isotopic values (Affolter et al., 2025; de Graaf et al., 2020). These challenges highlight methodological limitations in the application of this proxy. Therefore, improving measurement accuracy and reproducibility, especially for small volume samples, and establishing standardised, intercomparable protocols are essential for advancing this field.

In light of these challenges, the first topic of this dissertation addresses the technical uncertainties in fluid inclusion water isotope analysis by evaluating improved measurement methods and inter-laboratory comparisons, thereby providing methodological support for the reliable application of this proxy. Furthermore, it integrates multi-proxy speleothem records, including carbonate stable isotopes, trace elements, and fluid inclusion water isotopes, since the last glacial period to investigate the variation of the ASM and its driving mechanisms on precipitation across different temporal and spatial scales.

The dissertation is structured around these two core issues and is organised as follows:

Chapter 1 introduces the dissertation's background, defines the central research questions, and provides an overview of the structure and methodologies employed.

Chapter 2 focuses on the systematic bias in stable isotope values observed in the Heidelberg fluid inclusion water measurement system under low water volume conditions (<0.5 µl). In response to this issue, this chapter presents a newly developed calibration protocol and optimised measurement and data processing procedures, thereby improving the accuracy and reliability of low-volume sample measurements and laying the technical foundation for subsequent analyses.

Chapter 3 investigates the evaporation of inclusion water and the associated isotopic fractionation during the pre-heating stage before measurement. Using cold water coral skeletons as case studies, this chapter quantitatively evaluates water loss and the resulting isotopic shifts induced by heating. A novel encapsulation technique employing glass tubes was developed to prevent evaporation and validate the improved approach's reliability. In addition, the chapter explores the potential for exchange between inclusion water and seawater in coral skeletons, as well as the associated uncertainties in interpreting isotopic signals. The results have been published to *Geochemistry, Geophysics, Geosystems*.

Chapter 4 presents an international inter-laboratory comparison involving 13 laboratories to systematically evaluate the accuracy and reproducibility of fluid inclusion isotope analyses. The effects of sample water volume, instrumental differences, and sample preparation procedures on the results are analysed, providing a basis for the standardisation and robust application of this emerging technique.

Chapter 5 focuses on multi-proxy reconstructions of ASM intensity and regional hydroclimate during the middle to late Holocene. Using the improved inclusion water isotope analysis protocol and a Rayleigh fractional model, the evolution of regional hydroclimate in southwestern China under the influence of the ASM is reconstructed. Combined with calcite stable isotope data, the chapter further explores centennial-scale variations in the ASM and their linkages to human activity and regional hydrological change.

Chapter 6 reconstructs orbital to millennial scale regional hydrological changes using carbon and oxygen stable isotopes and trace elements from a speleothem that grew during the last glacial period in southwestern China. This chapter examines the influence of Northern Hemisphere summer insolation and global ice volume on ASM intensity and regional precipitation patterns. It evaluates the applicability of speleothem δ^{18}O as an indicator of monsoon or hydrological intensity. Related findings have been published in *Geophysical Research Letters*.

Chapter 1

Background and Methods

Key Points:

- **Definition of the East Asian summer monsoon, its range of influence, and variations since the last glacial period.**
- **Various geochemical indicators in speleothems are widely used in paleoclimate and paleoenvironmental reconstruction.**
- **Key issues to be addressed in this dissertation and organisation of chapters.**

1.1 East Asian Summer Monsoon System

1.1.1 Basic Characteristics of the East Asian Summer Monsoon

As a part of the global monsoon system, the most significant feature of the Asian Summer Monsoon (ASM) is the seasonal reversal of atmospheric circulation, accompanied by alternating wet summers and dry winters (Ding and Chan, 2005; Ding et al., 2018; Wang et al., 2014, 2017). The ASM system predominantly affects regions in the tropical and subtropical zones and is composed of three subsystems: the South Asian Summer Monsoon (Indian Summer Monsoon, ISM), the Western North Pacific Summer Monsoon, and the East Asian Summer Monsoon (EASM) (Figure 1.1) (An et al., 2015; Wang et al., 2017). These subsystems are interconnected yet distinct, each responding differently to external and internal forcings (Ding and Chan, 2005; Ding et al., 2018; Wang et al., 2017). Every summer, the ASM prevails, continuously transporting water vapor from the ocean to the land (Figure 1.1), affecting the livelihoods of billions of people. The evolution of the ASM over different timescales also governs the hydrological environment and surface landscape, having a profound impact on the development of human societies and civilizations in Asia (Chen et al., 2021b; Liu et al., 2021; Meng et al., 2024). The EASM, a subtropical-temperate monsoon, influences eastern China, the Korean Peninsula, and southern Japan, covering a vast area between 20-45°N and 110-140°E (Ding et al., 2018; Wang et al., 2017).

The EASM is the primary driving force behind summer weather and climate changes in the monsoon region of China. It is also a key source of moisture for summer precipitation. The main driving factor of the EASM is the thermal contrast between land and sea, as well as between the hemispheres. During the boreal summer, temperatures in the Northern Hemisphere (NH), particularly over the Eurasian continent, rise, while temperatures in the Southern Hemisphere (SH) and over the oceans remain relatively lower (An et al., 2011; Cheng et al., 2021b; Huang et al., 2019). As a result, a high-pressure system forms over the southern Indian Ocean, such as the Mascarene High, while a low-pressure system develops over the Asian continent (Beck et al., 2018; Wang et al., 2017). Under the influence of the pressure gradient between the hemispheres, lower atmospheric air flows from the SH to the NH (Figure 1.1). Due to the Coriolis effect, southeasterly winds from the SH deflect into southwesterlies after crossing the equator over the western Indian Ocean, forming the Somali Jet (Cai et al., 2006; Caley et al., 2013; Wu et al., 2012). This westerly flow continues eastward across the Indian subcontinent and the Bay of Bengal (Figure 1.1). In the South China Sea, it converges with the cross-equatorial flow from Australia and the southerly winds on the western side of the Western Pacific Subtropical High (WPSH), turning northward (Ding and Chan, 2005; Ding et al., 2018; Wang et al., 2017). Together, these flows create a strong southwesterly monsoon originating from the tropics, which collectively influences the East

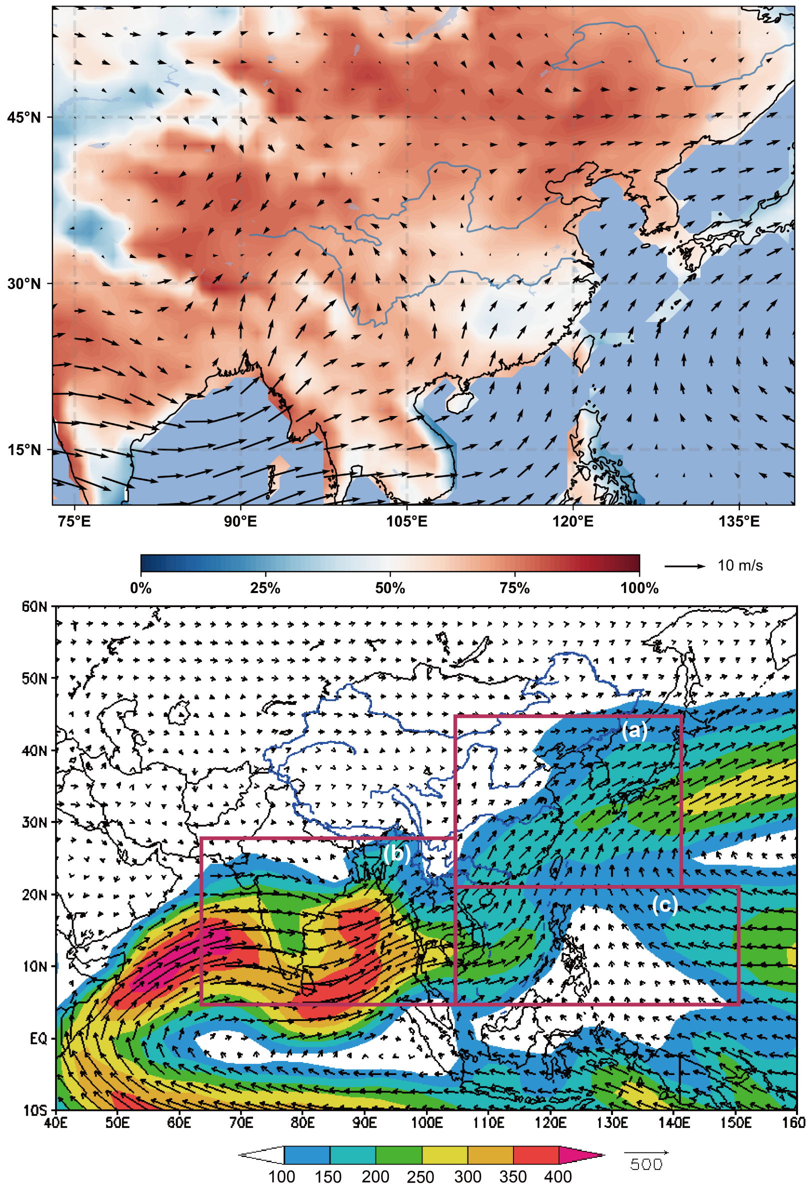

Figure 1.1. Precipitation and atmospheric circulation in the Asian summer monsoon region. The shaded areas in the left panel represent the proportion of monsoon precipitation (May–August) relative to the annual total during 1981–2010. The arrows indicate the vector wind fields at 850 hPa during May–August for the same period. The right panel depicts the vertically integrated water vapor flux (300–1000 hPa) in the Asian monsoon region during May–August of 1981–2010, with color changes indicating the magnitude of water vapor transport (unit: kg/s·m). The red boxes outline the primary influence regions of (a) the East Asian subtropical monsoon, (b) the Indian tropical monsoon, and (c) the western North Pacific tropical monsoon and the East Asian subtropical monsoon (Wang et al., 2017). Precipitation data are sourced from the Global Precipitation Climatology Centre Precipitation V2020 Combined Dataset (Schneider et al., 2020). Wind field data are from the NCEP-NCAR reanalysis datasets (Kalnay et al., 1996), and water vapor flux data and the base map are obtained from the National Climate Center of China (https://cmdp.ncc-cma.net/).

Asian region.

Accompanying the lower-level wind field is significant transport of water vapor from the ocean to the land. In the EASM region, summer precipitation can account for 40-50% or more of the annual total (Figure 1.1). The cross-equatorial transport of water vapor from Somalia and Australia, along with moisture from the western side of the WPSH, constitutes the main sources of water vapor for precipitation in the EASM region (Ding et al., 2018; Hu et al., 2022; Tan, 2014; Xue et al., 2023). The primary channel for water vapor transport is from the South Indian Ocean to the Arabian Sea, passing through the Bay of Bengal and the South China Sea (Ding et al., 2018). Therefore, from both the perspective of prevailing winds and water vapor transport, low-latitude oceans play a crucial role as sources of moisture and potential heat for the EASM region.

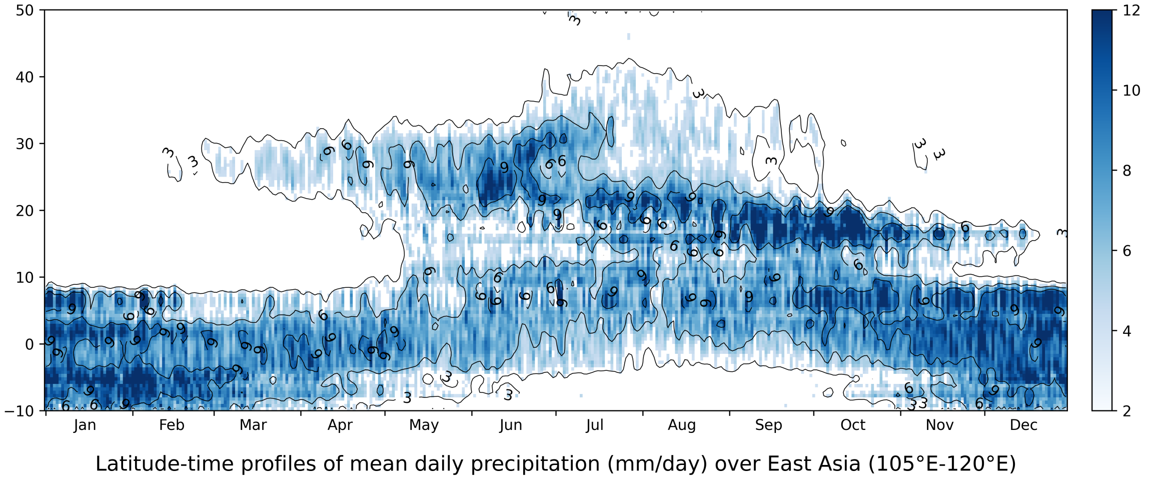

Figure 1.2. Hovmöller diagram of precipitation climatology in eastern China (1991–2020, mm/day). Precipitation data are sourced from the CPC global unified gauge-based analysis of daily precipitation dataset. The CPC dataset provided by the NOAA PSL, from their website at https://psl.noaa.gov.

On the seasonal scale, the EASM circulation exhibits distinct intraseasonal evolution characteristics, with two sharp northward shifts and three periods of stagnation (Chiang et al., 2017; Ding and Chan, 2005; Ding et al., 2020b, 2018). From early to mid-May each year, the EASM begins to form near the Indochina Peninsula, the South China Sea, and the Philippines. This process, known as the outburst of the South China Sea summer monsoon, marks the onset of the EASM and the rainy season (Ding and Chan, 2005). From early to mid-June, the EASM moves northward to the Yangtze River Basin and western and southern Japan (Ding et al., 2018). By mid-July, the EASM reaches its northernmost extent, shifting to North China and Northeast China. From August to September, the monsoon circulation rapidly shifts southward to South China, and by the end of September, the monsoon quickly withdraws from the South China Sea, signaling the end of the EASM season (Ding et al., 2020b). The movement of the monsoon rain belt corresponds with the north-south migration of the monsoon circulation (Figure 1.2). In May, sustained rainfall occurs in South China. By mid-June, the rain belt shifts to the Yangtze River Basin in central China, and in July, it further moves northward to Northeast China (Figure 1.2) (Ding et al., 2020a,b). On decadal or longer timescales, variations in the intensity of the EASM may lead to changes in the timing or spatial distribution of the rain belt (Chiang et al., 2015; Ding et al., 2020b; Zhang et al., 2020a).

1.1.2 Variation and Drivers in EASM Intensity During the Last Glacial Period and the Holocene

As a large-scale monsoon system, the EASM impacts hundreds of millions of people. Understanding its modern processes and reconstructing its historical variations are of great scientific and practical importance (Cheng et al., 2021b; Ding and Chan, 2005; Huang et al., 2019; Wang et al., 2017). The driving forces behind the evolution of the EASM are complex and multifaceted. Various internal and external factors interact, leading to changes in EASM circulation and its rain belt across different temporal and spatial scales (Cheng et al., 2021b; Herzschuh et al., 2019; Zhang et al., 2021b). The glacial-interglacial cycles are a major feature of Quaternary climate change. The last glacial period, as the most recent glacial period, experienced not only climate changes on orbital timescales but also a series of significant rapid climate events, such as Heinrich events (H events) and Dansgaard-Oeschger events (D/O events) (Barker et al., 2015; Bassis et al., 2017; Held et al., 2024; Martin et al., 2023; Roche et al., 2004). These millennial-scale events have widespread global impacts (Andrews and Voelker, 2018; Genty et al., 2003; Hemming, 2004; Wang et al., 2001; Zhou and McManus, 2024). The orbital-scale evolution of the EASM, as well as its response mechanisms to abrupt millennial events, has been a widely researched and focused scientific issue (Cheng et al., 2021b; Sun et al., 2022; Wang, 2021).

The Holocene, the warm interglacial period following the end of the last glacial period, also experienced a series of rapid climate events (Hu et al., 2008; McKay et al., 2024; Wanner et al., 2008; Zhang et al., 2023a, 2021g). The climate and environmental state could have undergone abrupt changes within decades or centuries (Duan et al., 2023a; Helama, 2024; McKay et al., 2024; Thomas et al., 2007). During the late Holocene, the gradual increase in human activities led to widespread and rapid warming of the global climate system (Ruddiman et al., 2016). In East Asia, the intensifying human activities during the late Holocene may have exceeded the influence of natural climate variability in regulating the regional environment (Chen et al., 2021b; Duan et al., 2023c; Jiang et al., 2014; Pei et al.,

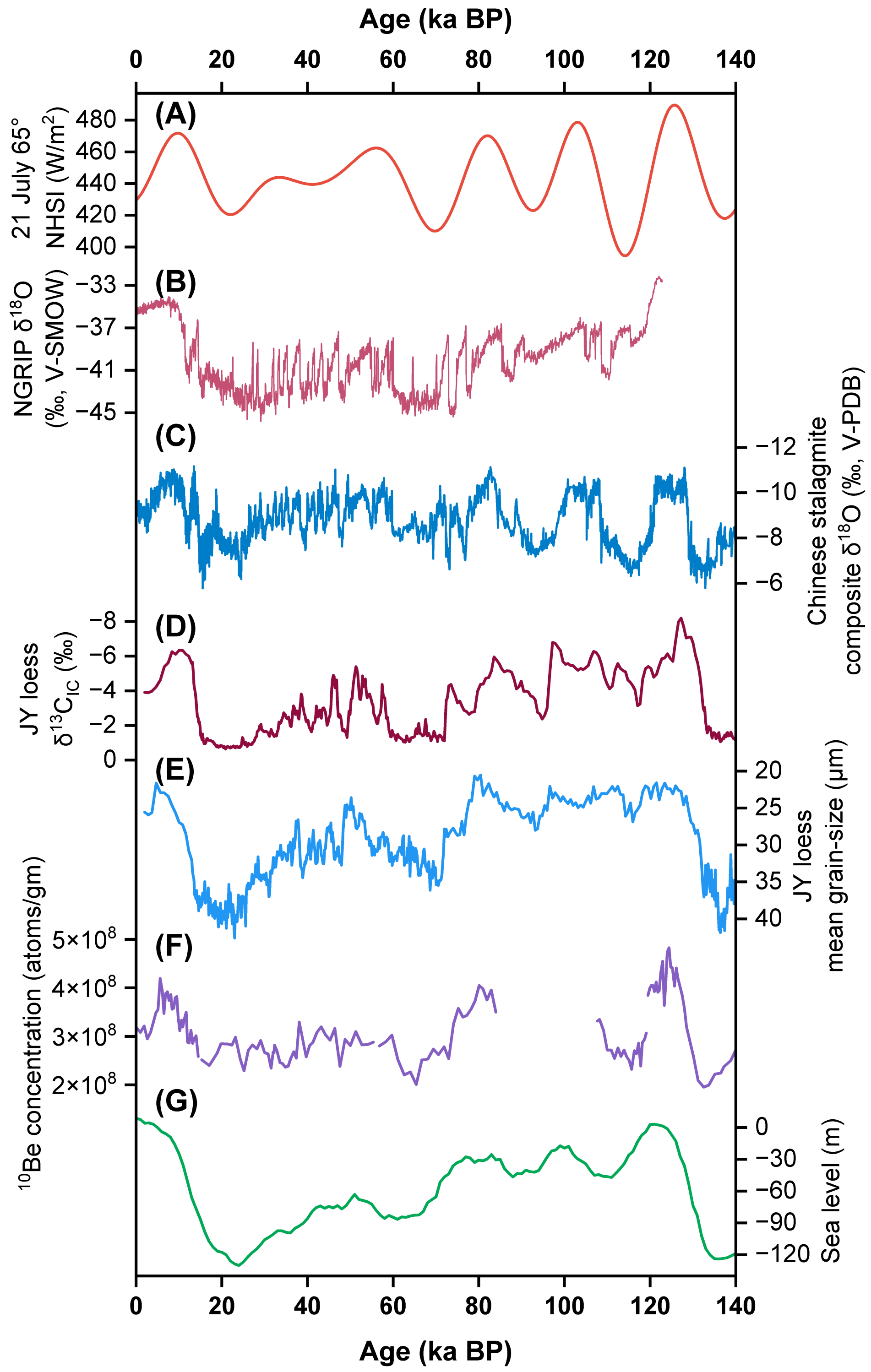

Figure 1.3. Comparison of representative Chinese paleoclimate records with Northern Hemisphere Summer Insolation and ice core δ^{18}O records. (A) 21 July insolation at 65°N (Laskar et al., 2004); (B) NGRIP ice core δ^{18}O record (NGRIP Members, 2004); (C) Chinese speleothem composite δ^{18}O record (Cheng et al., 2016a); (D) $\delta^{13}C_{IC}$ record from Jingyuan loess (Sun et al., 2019); (E) Mean magnetic susceptibility record from Jingyuan loess (Sun et al., 2021); (F) ^{10}Be record from the Chinese Loess Plateau (Beck et al., 2018); (G) Sea level change record (Spratt and Lisiecki, 2016).

2020; Song et al., 2022). This section will introduce variations in the EASM during the last glacial period and the Holocene, along with their potential driving mechanisms. Since the main area of influence of the EASM, as well as the focus of this dissertation, is mainland China, no substantial distinction will be made between the EASM region and the China monsoon region, unless otherwise stated.

Variations of EASM on Orbital Scales During the Last Glacial Period

The EASM circulation is essentially a large-scale ocean-land wind system driven by solar insolation, with variations in solar insolation being its most significant external forcing (Cheng et al., 2022a; Ding et al., 2018; Wang et al., 2017). The seasonal and latitudinal distribution of insolation on Earth's surface varies with orbital parameters, influencing the thermal contrast between ocean and land. As a result, the intensity of monsoon circulation and precipitation changes in response to fluctuations in insolation intensity (Cheng et al., 2022a; Wang et al., 2017). The Earth's orbital parameters primarily include precession, obliquity, and eccentricity, with main periods of approximately 23 ka, 41 ka, and 100 ka (Berger, 1988; Hays et al., 1976a; Milankovitch, 1941). Various geological records indicate that both the intensity of the EASM and precipitation records exhibit one or more of these periodicities (Figure 1.3) (Cheng et al., 2016b, 2019; Li et al., 2024; Sun et al., 2022). A key example is the high-resolution speleothem δ^{18}O (δ^{18}Os) records in the EASM region (Figure 1.3). The δ^{18}Os values show broad spatial coherence and closely align with changes in Northern Hemisphere summer insolation (NHSI), exhibiting a precessional cycle (Cheng et al., 2016b, 2019; Wang et al., 2008). When NHSI increases or decreases, δ^{18}Os values become negative or positive, indicating enhanced or weakened EASM circulation, respectively (Figure 1.3) (Cai et al., 2015; Cheng et al., 2016b, 2019; Wang et al., 2001). The widespread presence of precessional cycles in paleoclimate records of the EASM region supports the classical theory of monsoon driven by solar insolation. During periods of higher NHSI, the more pronounced thermal contrast between land and sea generates a stronger monsoon circulation (An et al., 2015; Wang, 2021; Wang et al., 2017). Consequently, the EASM can directly respond to changes in NHSI.

In the Chinese loess records, especially the magnetic susceptibility records indicating precipitation, the patterns are more consistent with global ice volume changes (Figure 1.3), while precessional cycles are not significantly evident (Beck et al., 2018; Cheng et al., 2021b; Sun et al., 2021). The differences in the dominant periods of EASM variations (100 ka or 23 ka) on orbital scales related to ice volume and precession, along with their underlying driving mechanisms, are referred to as the "100 ka problem" (Hays et al., 1976b). Recent research attempts to reconcile the two perspectives, suggesting that spatial heterogeneity in precipitation and wind fields may lead geological records from different regions to capture distinct aspects of EASM dynamics (Cheng et al., 2021b, 2019; Zhang et al., 2021b; Zhao et al., 2023b). During the low precession period (Pmin), the EASM strengthened, allowing monsoon circulation to penetrate further inland. Increased monsoon precipitation led to more pronounced Rayleigh fractionation of precipitation δ^{18}O (δ^{18}Op), resulting in generally more negative δ^{18}Op values across the EASM region (Cheng et al., 2021b, 2019; Liu et al., 2014; Maher and Thompson, 2012). The δ^{18}Os values across the East Asian monsoon region inherit the δ^{18}Op values (Chen and Li, 2018; Duan et al., 2016; Qiu et al., 2023). As a result, they may represent the circulation or intensity of precipitation across the entire EASM region, showing a precession-driven cycle (Figure 1.3). This perspective carries an important implication: δ^{18}Os can reflect large-scale monsoon circulation changes rather than necessarily indicating regional rainfall amounts. In contrast, other paleoclimate records, such as loess, may reflect changes in rainfall amounts (Beck et al., 2018; Li et al., 2024; Sun et al., 2021; Zheng et al., 2022). The inconsistencies between speleothem and loess records indicate that the relationship between EASM circulation and precipitation was spatially separated (Figure 1.3) (Cheng et al., 2021b, 2019; Zhang et al., 2021b; Zhao et al., 2023b).

Variations of EASM on Millennial Scales During the Last Glacial Period

The changes in the EASM during the last glacial period at orbital scales were also superimposed with a series of millennial-scale climate events. These events responded to the cold stadials and warm interstadials of the North Atlantic, as well as H events (EPICA Community Members, 2006; Hemming, 2004; NGRIP Members, 2004; Schulz et al., 1998). The EASM is teleconnected to climate change in the North Atlantic region through oceanic and atmospheric processes, experiencing rapid weakening or strengthening of intensity during stadial and interstadial periods (Figure 1.3) (Cheng et al., 2016a; Sun et al., 2021; Wang et al., 2008). However, the EASM does not directly follow the millennial events in the North Atlantic; rather, it exhibits a unique evolutionary process, evident in several aspects. (1) During abrupt climate change events, the EASM strengthens or weakens more gradually compared to the North Atlantic. For example, millennial events recorded by ice core δ^{18}O in Greenland tend to begin or terminate abruptly (NGRIP Members, 2004). However, the onset and termination of the EASM intensity response to abrupt change events are gradual, due to the slower response of low-latitude atmospheric and hydrological cycles to abrupt climate changes in the NH high latitudes (Cheng et al., 2021a; Liu et al., 2022a; Wu et al., 2023a; Zhang et al., 2021d). (2) EASM millennial events terminate earlier than those in the NH high latitudes, despite being initially triggered there. Increasing evidence suggests that millennial events first terminate in low-latitude regions before gradually propagating northward (Dong et al., 2022; Zhang et al., 2021e). (3) Variations in EASM intensity during millennial events exhibit distinct phases and instability. These events typically follow three phases: weakening, relative stabilization, and recovery, with decadal- to centennial-scale oscillations superimposed on each phase (Cheng et al., 2021a; Liu et al., 2022a; Wu et al., 2023a).

These features suggest that while the EASM responds rapidly to climate changes in NH high latitudes, it also bears a distinct imprint from low-latitude and SH influences (Dong et al., 2022; Zhang et al., 2021e). Key factors include shifts in the Intertropical Convergence Zone (ITCZ) (Zhang et al., 2020c), variations in the NH westerly jet (Chiang et al., 2015), the El Niño-Southern Oscillation (ENSO) (Zhang et al., 2021e), and greenhouse gas emissions influenced by the Southern Ocean (Liang et al., 2022). Recent studies also highlight the role of astronomical factors. During periods of high or low NHSI, the EASM's response to D/O events is either amplified or suppressed (Liu et al., 2022b).

Variation of EASM during the Holocene

During the Holocene, variations in the EASM can be categorized by timescales into orbital, millennial, centennial, and decadal scales. On the orbital scale, changes in solar insolation are the primary drivers of EASM intensity variations (Wang et al., 2008; Yuan et al., 2004; Zhang et al., 2021b). The NHSI reached its maximum during the early Holocene, resulting in a significant thermal contrast between land and sea, which led to the strongest monsoon circulation (Yang et al., 2019a; Zhang et al., 2021b). As the NHSI gradually decreased during the middle and late Holocene, the intensity of the EASM correspondingly weakened, a trend most evident in Holocene speleothem records from China (Hu et al., 2008; Yang et al., 2019a; Zhang et al., 2021b). On millennial scales, the long-term trend of EASM variation was interrupted by several millennial-scale events, including the prominent 8.2 ka and 4.2 ka events (Duan et al., 2023a; Pan et al., 2023; Zhang et al., 2023b). These events align with records from Greenland ice cores δ^{18}O records, suggesting a close linkage between low-latitude monsoons and high-latitude climate changes (Pan et al., 2023; Thomas et al., 2007; Wang et al., 2022b). However, recent studies indicate that events such as the 4.2 ka event were likely insufficient to induce significant climate and environmental changes on a global scale (McKay et al., 2024). On centennial to decadal scales, EASM variability is primarily influenced by factors such as solar activity, volcanic eruptions, and ENSO activities (Chen et al., 2021a; Shao et al., 2024; Zhao et al., 2015; Zhu et al., 2017).

Despite the increasing availability of high-resolution geological records with precise dating for studying the evolution of the EASM during the Holocene, significant discrepancies among these records highlight the complexity of Holocene EASM variations. Understanding the spatiotemporal patterns and driving mechanisms of EASM evolution during the Holocene remains a challenging and widely debated topic, particularly in the following aspects:

Firstly, there are discrepancies in the timing of the Holocene Climatic Optimum (HCO) across different regions of the EASM domain (Liu et al., 2015; Zhang et al., 2021g). The HCO is generally defined as the warmest and wettest period of the Holocene. While δ^{18}Os records indicate that the overall strength of the EASM was greatest during the early Holocene, gradually weakening throughout the mid to late Holocene (Fan et al., 2024; Yang et al., 2019a; Zhang et al., 2021b), it remains debated whether the HCO occurred synchronously across the EASM region (Liu et al., 2015). For example, An et al. (2000) suggest that the HCO first appeared in northern China during the early Holocene, whereas it emerged in central and southern China in the late Holocene. In contrast, Zhou et al. (2016) argue that the HCO began in the southern monsoon region of China during the early Holocene, with northern China experiencing it starting in the mid-Holocene. Some studies propose that the HCO was synchronous across the entire EASM region; however, the timing of its onset remains uncertain, with ongoing debate over whether it began in the early or mid-Holocene (Yang et al., 2019a; Zhang et al., 2021g; Zhao et al., 2009).

Despite these controversies, δ^{18}Os records from China consistently indicate that the EASM was strongest during the early Holocene, followed by a gradual weakening (Yang et al., 2019a; Zhang et al., 2021b). This discrepancy reflects a decoupling between the “wind” and “rain” components of the EASM: while the overall monsoon intensity was synchronous across the Chinese monsoon region, precipitation changes in different areas did not occur simultaneously (Cheng et al., 2019; Liu et al., 2020).

Secondly, Holocene EASM variations exhibit instability. Although the EASM was strong during the early Holocene, its variability was high, with frequent weak monsoon events, whereas the EASM was relatively stable during the mid-Holocene (Yang et al., 2019a; Zhang et al., 2021g). Another key aspect of EASM instability is the occurrence of significant climatic abrupt events. For instance, the EASM weakened considerably during the well-known 8.2 ka and 4.2 ka events; however, the timing, pattern, and driving mechanisms of these weakening phases remain debated (Duan et al., 2023a; Pan et al., 2023; Zhang et al., 2023b).

Thirdly, the complex interplay of multiple factors during the Holocene makes it difficult to identify the dominant controls on EASM intensity and precipitation (Lu et al., 2019a; Sun et al., 2024; Zhu et al., 2017). The factors influencing the EASM varied over time, with the relative importance of high-latitude influences such as AMOC and low-latitude processes like ENSO and the Western Pacific Warm Pool shifting throughout the period. Additionally, δ^{18}O records from China exhibit a pronounced negative anomaly after 2 ka BP, suggesting an intensification of monsoon activity over the past two millennia. This trend contrasts with the concurrent decline in NHSI during the same period (Cheng et al., 2016a, 2019).

Finally, the impact of mid- to late-Holocene human activities on climate and the regional hydrological environment remains a subject of debate. Changes in monsoon intensity and precipitation may have influenced the development of human civilization, while human activities have also significantly altered the surface environment. It is still contested whether climate change or human activities have been the primary driver of environmental transformations in China since the late Holocene (Chen et al., 2021a,b; Pei et al., 2020; Zhang et al., 2008).

The debate surrounding climate and environmental changes during the last glacial period and the Holocene in the EASM region partly stems from the inherent complexity of the driving factors behind the EASM and the evolution of precipitation distribution patterns (Cheng et al., 2021b; Herzschuh et al., 2019; Lu et al., 2019a; Zhang et al., 2021g). Disagreements often arise from differing interpretations of the climatic and environmental significance of various paleoclimate indicators (Cheng et al., 2019; Liu et al., 2020, 2014; Sun et al., 2022; Zhang et al., 2021b). A notable point of contention is the mismatch between Chinese δ^{18}Os records indicating monsoon intensity and other records of monsoon precipitation. This issue will be discussed in section 1.1.3.

1.1.3 Relationship between East Asian Summer Monsoon Precipitation and Monsoon Intensity

The rain belt of the EASM shifts with the north-south movement of the monsoon circulation (Figure 1.2), leading to significant spatial differences in summer precipitation (Chiang et al., 2020; Ding et al., 2020a). In years of strong EASM, the monsoon circulation shifts northward, bringing the rain belt to the north, affecting regions such as North China and Northeast China, while precipitation decreases in the Yangtze River basin, resulting in a rainfall distribution pattern of "floods in the south and droughts in the north" (Chiang et al., 2017; Ding and Chan, 2005; Ding et al., 2020a,b). Conversely, in years of weaker EASM, the weakened monsoon circulation causes the rain belt to shift southward, reinforcing the "floods in the south and droughts in the north" spatial pattern. Thus, with changes in the strength of the EASM circulation, the rain belt in the Chinese monsoon region exhibits periodic oscillations (Chiang et al., 2020; Ding et al., 2020b; Zhang et al., 2018). The interdecadal variability of modern precipitation in the Chinese monsoon region can be categorized into three main modes (Figure 1.4). The first mode is a "triple pattern", characterized by synchronous precipitation changes in South and North China, with an opposite trend in Central China (Figure 1.4). This is the primary mode of interdecadal precipitation variability in the eastern monsoon region of China. The second mode is a "dipole pattern", with roughly the Yangtze River as the dividing line, indicating higher precipitation in the south and lower in the north, or vice versa. The third mode exhibits an east-west dipole, often referred to as the "coast pattern", where precipitation in the southeastern region is out of phase with summer precipitation in the inland areas (Figure 1.4).

The three patterns have also been shown to be significant over longer timescales. For instance, paleoclimate reconstructions and simulations reveal a distinct "triple pattern" during the past four glacial and interglacial cycles on orbital timescales (Dai et al., 2022, 2021; Jiang et al., 2023). Similar characteristics are evident on millennial to centennial timescales. For example, during the weakened EASM of the Little Ice Age, southern China experienced wetter conditions, while northern China faced drought, contrasting with the opposite phase during the strong monsoon of the Medieval Warm Period (Jiang et al., 2021; Li et al., 2021b; Wanner et al., 2008; Yin et al., 2023a). Recent studies suggest that precipitation patterns in the southeastern coastal region over the past few thousand to ten thousand years have been out of phase with those in the eastern inland areas, highlighting the significance of the "coast pattern" (Cao et al., 2024). Despite the emphasis on the spatial heterogeneity of precipitation in the EASM region across different timescales, there is no consensus among these studies, and they may even present conflicting views.

What factors contribute to changes in the spatial pattern of precipitation in the EASM region over different timescales? Addressing this question relies heavily on reconstructions and modeling due to limited instrumental data. On orbital timescales, precipitation in northern China and the Yangtze River basin primarily following the 100 ka and 41 ka cycles, with the precession cycle being less significant (Dai et al., 2021; Sun et al., 2021, 2022; Zheng et al., 2022). However, some studies suggest that NHSI is the dominant factor controlling precipitation distribution. During periods of high (low) NHSI, the EASM strengthens (weakens), leading to increased (decreased) precipitation in northern and southern China, while central China receives less (more) rainfall (Cai et al., 2023, 2015; Cheng et al., 2021b; Weber and Tuenter, 2011). Other studies propose that north of 25°N in the Chinese monsoon region, changes in summer precipitation are primarily driven by the precession cycle. In contrast, south of 25°N, the 100 ka cycle of summer precipitation is more stronger (Lyu et al., 2021). The shift and duration of the rain belt are also linked to the meridional movement of the westerly jet relative to the Tibetan Plateau (the jet transition hypothesis) (Chiang and Bitz, 2005; Chiang et al., 2020). Additionally, the position of the ITCZ and ancient ENSO activity are also important factors (Chiang et al., 2015, 2017; Jiang et al., 2021; Wu et al., 2023a).

In summary, both reconstructions and simulations show uncertainty in characterizing the spatiotemporal evolution of precipitation in the EASM region, with underlying driving factors varying across studies.

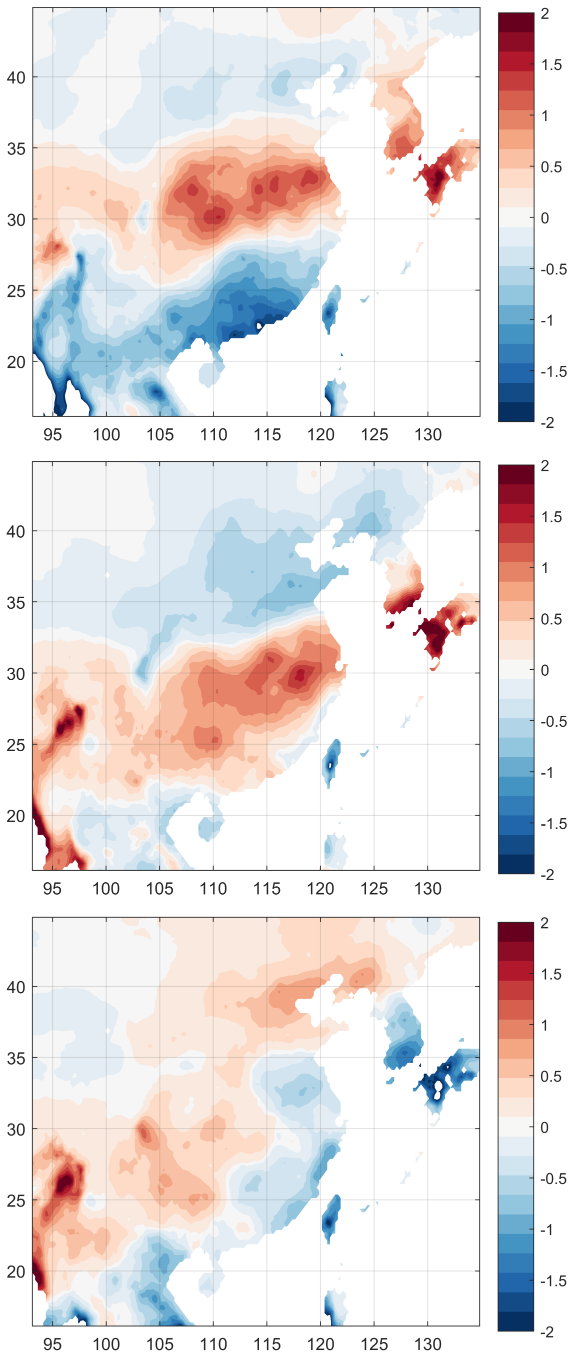

Figure 1.4. Modern spatial distribution patterns of precipitation in China. The empirical orthogonal function (EOF) analysis for May–August (JJA) precipitation during 1980–2007 C.E. is based on the Asian Precipitation-Highly-Resolved Observational Data Integration Towards Evaluation (APHRODITE) gridded rainfall dataset (Yatagai et al., 2012). EOF1, EOF2, and EOF3 explain 17%, 11%, and 8% of the total variance, respectively. EOF1 represents the triple pattern of monsoonal precipitation in China, EOF2 represents the dipole pattern, and EOF3 represents the coast pattern. Although EOF1–EOF3 represent key spatial modes, together they account for only 36% of the total variance. This suggests that precipitation variability may also arise from more localized, non-stationary, or higher-order processes not captured by the leading EOFs.

1.2 Paleoclimate and Paleoenvironmental Reconstruction using Speleothems Archive

1.2.1 Geochemical Indicators in Speleothems

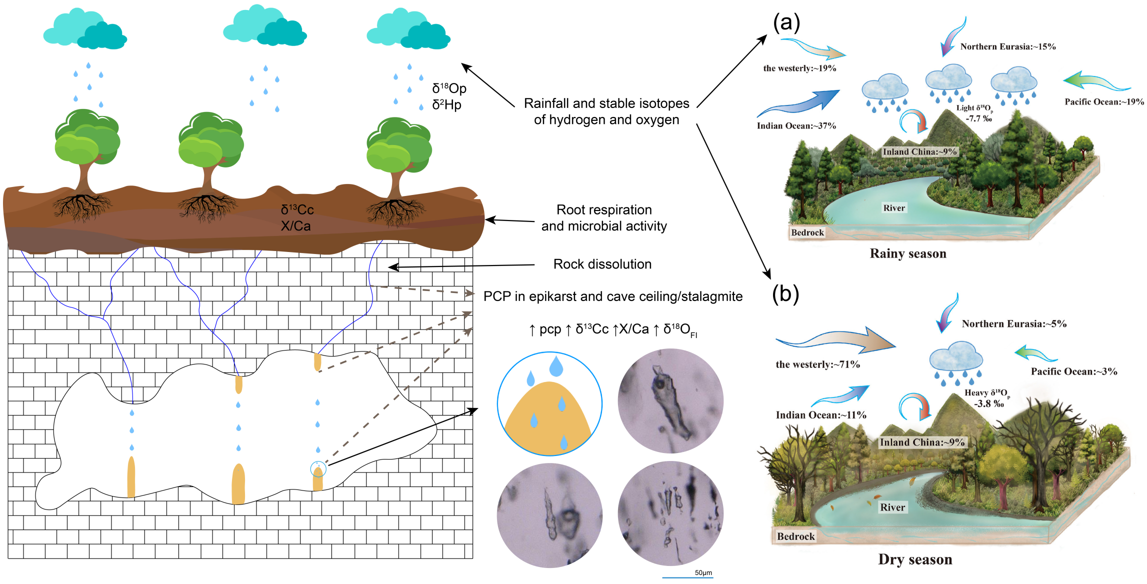

Figure 1.5. Schematic diagram of climate and environmental signal transmission within the cave system. The left panel illustrates the transmission process from rainfall to drip water, and eventually to speleothem formation. During this process, isotopic signals (δ^{18}O and δ^{2}H) from atmospheric precipitation and environmental signals (e.g., δ^{13}C, trace elements) from the epikarst are transferred from the surface to the speleothem and preserved. In addition to climatic and environmental factors, this process is influenced by the PCP effect. The circular diagram at the bottom center depicts the capture of cave drip water into inclusions, showing some forms of inclusions. The right panel (a) and (b), using southern China as an example, demonstrates how seasonal changes in atmospheric circulation influence variations in the oxygen isotopes of precipitation. These climatic isotopic signals are transferred via drip water to the cave and inherited by calcite and fluid inclusions within the speleothem. (a) and (b) are adapted from Xue et al. (2023).

Speleothems, including calcium carbonate deposits such as stalagmites and stalactites, are closely associated with the water cycle, surface biogeochemical processes, karst hydrological processes, and the growth mechanisms of carbonate minerals (Figure 1.5) (Baker and Genty, 1998; Baker et al., 2019; Fairchild et al., 2001, 2006; Hendy, 1971; Spötl and Mattey, 2006). Stalagmites, in particular, have the potential to effectively preserve signals of climatic and hydrological changes both within and beyond cave systems during their formation. When supported by long-term monitoring of cave environments and careful evaluation of site-specific conditions, they can serve as valuable archives of continental climate and environmental variability (Figure 1.5) (Cheng et al., 2019; Dreybrodt and Scholz, 2011; Fairchild and Treble, 2009; Fohlmeister et al., 2020; McDermott, 2004; Schwarcz et al., 1976; Spötl and Mattey, 2006).

Stalagmites, as products of cave carbonate deposition, form through a process intricately linked to water. In the surface environment, the decomposition of organic matter from plant roots and microbial activity leads to soil CO_2 concentrations, which are elevated compared to the atmosphere. When rainfall passes through the soil, it reacts with the CO_2, forming carbonic acid (H_2CO_3). As pH increases, carbonic acid dissociates into bicarbonate ions (HCO_3^-) and carbonate ions (CO_3^{2-}). This acidic solution then percolates into the karst zone, dissolving the surrounding carbonate rock. Due to the larger space within caves and better ventilation, the partial pressure of CO_2 (P_{CO2}) in caves is much lower than in the epikarst zone. As a result, the dissolved CO_2 in dripping water begins to degas, and evaporation of the water leads to the precipitation of calcium carbonate. Over time, this calcium carbonate slowly accumulates at the drip points, forming a large variety of cave carbonates, including stalagmites. Stalagmite growth may pause due to a halt in dripping, a change in CO_2 saturation, a dripping rate that is too rapid, or elevated cave CO_2 concentrations. Consequently, stalagmite growth is mostly discontinuous. Stalagmite growth depends on the transport of atmospheric precipitation from the surface to the cave, which is influenced by factors such as surface precipitation, P_{CO2} in the soil (which is related to biomass), dripping rate, cave temperature, and ventilation (Baker et al., 2019; Fairchild et al., 2006; Fairchild and Treble, 2009). These parameters are closely related to climate and environmental conditions both at the surface and within the cave (Figure 1.5) (McDermott, 2004). Therefore, stalagmites that accumulate over time can record climatic and other environmental information from different periods, including changes in land use, volcanic activity, and other external influences.

Stalagmites offer unique advantages in global paleoclimate research. First, they are widely distributed, forming in nearly all regions with developed karst landscapes, and are relatively unaffected by external secondary changes after their formation. Second, they have chronological advantages. Stalagmites can be dated using U-series dating methods, or by combining with annual growth layers, allowing for the construction of high-precision age models (Burns et al., 1998; Cheng et al., 2013; Scholz and Hoffmann, 2011). Third, stalagmites provide excellent continuity in paleoclimate records. A single stalagmite can span tens of thousands to hundreds of thousands of years, and by combining multiple stalagmites, one can obtain even longer continuous records (e.g., Wang et al. (2001, 2008)). Comparing different stalagmites records allows for an assessment of their reliability (replication test) (Dorale and Liu, 2009). Finally, stalagmites contain a wealth of climate and environmental indicators, including, but not limited to, the oxygen and carbon stable isotopes of calcium carbonate (Fairchild et al., 2006; McDermott, 2004), trace elements (Fairchild and Treble, 2009), magnetic minerals (Zhu et al., 2017), biological indicators (Blyth et al., 2008), growth rates and layer thickness (Baker et al., 2008; Tan et al., 2006), fluorescence intensity (Baker et al., 2008; Blyth et al., 2008), and fluid inclusions (Dennis et al., 2001; Kluge et al., 2008; Schwarcz et al., 1976). The following sections will focus on stable oxygen and carbon isotopes, trace elements, and fluid inclusions.

1.2.2 Oxygen Isotope Composition

When using stalagmites for paleoclimate reconstruction, the study of oxygen isotopes in calcium carbonate is of primary importance. Oxygen exists in three stable isotopes and can be found in gaseous, liquid, and solid forms. It is widely used as a tracer in geochemistry. In stalagmites, δ^{18}O is typically employed as an indicator of the provenance and strength of precipitation and temperature conditions.s (Fairchild et al., 2006; McDermott, 2004). The δ notation refers to the difference in the ratio of two stable isotopes of an element in a sample relative to a standard, expressed in per mil (‰). It is defined as:

$$\delta = \frac{(R_s - R_{\text{std}})}{R_{\text{std}}} \times 1000 \quad \text{or} \quad \delta = \left(\frac{R_s}{R_{\text{std}}} - 1\right) \times 1000 \tag{1.1}$$

for δ^{18}O :

$$\delta^{18}\text{O} = \left(\frac{\left(\frac{^{16}\text{O}}{^{18}\text{O}}\right)_s}{\left(\frac{^{16}\text{O}}{^{18}\text{O}}\right)_{\text{std}}} - 1\right) \times 1000 \tag{1.2}$$

where:

R_s : Ratio of the heavy to light isotope in the sample.
R_{std} : Ratio of the heavy to light isotope in the standard.
δ : The isotope delta value.
δ^{18}O : The oxygen isotope delta value.
s : Denotes the sample.
std : Abbreviation for standard.
If $\delta > 0$: Indicates enrichment in the heavier isotope compared to the standard.
If $\delta < 0$: Indicates enrichment in the lighter isotope compared to the standard.

The δ^{18}Os values are primarily controlled by changes in the δ^{18}O values of cave drip water (precipitation) and cave temperature (Baker et al., 2019; Fairchild et al., 2006; Mc-

Dermott, 2004). The fractionation coefficient between water and calcite, influenced by cave temperature, is relatively small (O'Neil et al., 1969). However, variations in the δ^{18}Os values can be for more substantial over different timescales, reaching several per mille. In the monsoon region of China, δ^{18}Os variation is usually attributed to fluctuations in the δ^{18}Op values (Chen and Li, 2018; Duan et al., 2016; Qiu et al., 2021). Specifically, the δ^{18}Op value is influenced by a variety of factors from the source area to downstream, including variations in moisture sources, moisture transport pathways, recycling of surface water, and evaporation below clouds (Figure 1.5) (Jian et al., 2022; Liang et al., 2024; Lin et al., 2024; Tan, 2014). For most caves, the mixing of cave drips during migration through the epikarst zone has smoothed out the seasonal characteristics of δ^{18}Os, effectively representing an annual weighted average of local δ^{18}Op (Chen and Li, 2018; Duan et al., 2016).

In the EASM region, the primary factors controlling precipitation and stalagmite δ^{18}O variations may vary across different timescales, complicating the interpretation of the climatic and environmental significance of δ^{18}Op and δ^{18}Os records. (Cheng et al., 2019; Liu et al., 2020). Early studies suggested that the δ^{18}Op values in China might reflect changes in the ratio of summer to winter precipitation, providing insights into variations in monsoon intensity (Wang et al., 2001). Subsequent research emphasized that δ^{18}O values are more significantly influenced by the "upstream loss mechanism". Variations in δ^{18}O values are controlled by the proportion of water lost from moisture sources to cave sites, which allows for the reconstruction of precipitation changes in different regions (Hu et al., 2008; Pausata et al., 2011; Ruan et al., 2019; Yuan et al., 2004). Although some studies have directly interpreted δ^{18}Os values as changes in rainfall amount in the tropics of the EASM region, the applicability of this interpretation throughout the EASM region remains highly debated (Cai et al., 2015; Tan et al., 2017). For example, modeling studies have shown that δ^{18}Os values and δ^{18}Op are primarily driven by changes in the δ^{18}O of water vapor sources or variations in the strength of atmospheric hydrological processes and circulation, rather than specific rainfall amounts (Chiang et al., 2020; Lin et al., 2024; Liu et al., 2014; Pausata et al., 2011; Ruan et al., 2019). The influence of the "circulation effect" has also generated considerable attention (Maher and Thompson, 2012; Tan, 2014). The ISM and EASM are the main sources of moisture and precipitation in the Chinese monsoon region, each leaving a distinct δ^{18}O imprint on the moisture (Figure 1.5). Generally, moisture from the ISM has more negative δ^{18}O values, while moisture from the EASM has more positive δ^{18}O values (Maher and Thompson, 2012; Tan, 2014; Yang et al., 2016). This difference arises because moisture from the Indian Ocean travels a longer distance and undergoes more extensive Rayleigh distillation during transport (Figure 1.5) (Eq. 1.3-1.4), leading to more depleted δ^{18}O signatures compared to the relatively proximal Pacific-sourced moisture. The "circulation effect" influences δ^{18}Op values in downstream areas by regulating the proportion of moisture from these two sources. For example, Figure 1.5 illustrates that the Indian Ocean and the Pacific Ocean serve as the primary moisture sources, contributing 37% and 19% of the total moisture during the monsoon season, respectively. These sources are characterized by distinct δ^{18}O signatures, and interannual variations in their relative contributions modulate the δ^{18}O values of precipitation in downstream regions.

The Rayleigh distillation process can be described by the following equation for the change in isotope ratio:

$$R = R_0 \cdot f^{(\alpha-1)} \tag{1.3}$$

Where:

- R: Current isotope ratio in the vapor (e.g., $^{18}\mathrm{O}/^{16}\mathrm{O}$)
- R_0: Initial isotope ratio in the vapor
- f: Fraction of vapor remaining
- α: Equilibrium fractionation factor between liquid and vapor

In terms of delta notation, the Rayleigh equation can be written as:

$$\delta = \left[(\delta_0 + 1000) \cdot f^{(\alpha-1)}\right] - 1000 \tag{1.4}$$

Where:

- δ: Current δ value (in ‰) of the vapor
- δ_0: Initial δ value (in ‰)
- f and α: same as above

Although interpretations and debates regarding δ^{18}Os values and δ^{18}Op persist, it is widely accepted that variations in δ^{18}Op, whether viewed through precipitation isotopes or large-scale circulation patterns, are associated with changes in the intensity and position of the EASM circulation (Cheng et al., 2016a, 2021b, 2019; Liu et al., 2020). This inference is consistent with modern instrumental data, as well as theoretical and empirical studies spanning from orbital to millennial timescales (Chen and Li, 2018; Cheng et al., 2016a; Duan et al., 2016; Zhang and Li, 2019). On monthly, seasonal, and interannual timescales, δ^{18}Op generally does not directly reflect local rainfall amounts. Instead, it is influenced by atmospheric convection in moisture source regions and isotopic fractionation resulting from the “rainout effect” during transport (Cai et al., 2018; Ruan et al., 2019; Wang et al., 2020; Yang et al., 2016; Zhang et al., 2020a; Zhou et al., 2019). Long-term cave monitoring studies in China further indicate that seasonal to interannual variations in cave drip water and stalagmite δ^{18}O values primarily reflect changes in δ^{18}Op driven by large-scale atmospheric circulation, such as the ENSO (Chen and Li, 2018; Duan et al., 2016; Qiu et al., 2021). Lower δ^{18}Op values may result from increased upstream rainfall or enhanced monsoon circulation or intensity, though local precipitation may not necessarily increase (Cheng et al., 2019; Liu et al., 2020; Ruan et al., 2019; Tan, 2014; Zhang et al., 2021b). Therefore, the spatial consistency observed in numerous δ^{18}Os records across the Chinese monsoon region suggests their potential as indicators of large-scale monsoon intensity, which does not contradict the heterogeneous spatial distribution of precipitation amounts.

1.2.3 Carbon Isotope Composition and Trace Elements

Stalagmite δ^{13}C (δ^{13}Cs), and trace element concentrations or ratios (e.g., Ca, Mg, Ba, Sr) typically reflect changes in surface vegetation, soil biological activity, and cave ventilation, all influenced by regional hydrological conditions (Figure 1.5) (Day and Henderson, 2013; Fairchild and Treble, 2009; Fohlmeister et al., 2020; Jochum et al., 2012; Tremaine and Froelich, 2013). The primary factors include biological processes related to changes in temperature and precipitation, alongside inorganic processes such as degassing of drip water and cave ventilation (Fairchild et al., 2006; Fairchild and Treble, 2009).

Due to the complex and multifaceted influencing factors, attributing the variations in δ^{13}Cs to a single process is inherently challenging (Figure 1.5). Research based on modern cave monitoring has demonstrated that the δ^{13}C signal in cave drip water is strongly influenced by soil CO_2 derived from biological processes (Fairchild et al., 2006; Fohlmeister et al., 2020; Li and Li, 2018; Spötl et al., 2005). This δ^{13}C signal is transmitted through cave drip water and speleothems, recording fluctuations in soil CO_2 and capturing changes in climate and environmental factors, such as surface vegetation, temperature, and precipitation. The primary influencing factors can be summarized as follows: (1) Changes in surface vegetation types. Humid climates generally favor the growth of C3 plants (δ^{13}C values from −20‰ to −34‰), while arid conditions are more conducive to C4 plants (δ^{13}C values from −9‰ to −16‰) (Cerling, 1984; Dorale et al., 1998; Genty et al., 2001). Shifts in vegetation types, driven by climate change, can be recorded in the variations of δ^{13}Cs. (2) Surface vegetation density, soil CO_2 production rate, and microbial activity (Cosford et al., 2009; Fohlmeister et al., 2020; Li et al., 2018). This factor is also closely linked to climatic conditions, as warm and humid climates promote vegetation growth and elevate CO_2 production rates. (3) Atmospheric CO_2 concentration changes (Genty et al., 2001; Spötl et al., 2005).

In addition to climatic and environmental factors, δ^{13}Cs is also influenced by non-climatic factors originating from the epikarst and cave interior, such as the state of the karst system (open/closed) and kinetic fractionation during carbonate deposition (Fairchild et al., 2006; Hendy, 1971). The relative importance of climatic versus non-climatic factors often depends on the specific characteristics of the karst system and the regional climate. In the Chinese monsoon region, δ^{13}Cs is commonly interpreted as reflecting shifts in vegetation types, as well as regional temperature and humidity, over millennial to orbital timescales (Li et al., 2018, 2020; Wang et al., 2022d; Wu et al., 2023a, 2020). In low-latitude regions, such as southern China, although temperature and vegetation cover decreased during the Last Glacial Maximum (LGM), no substantial change in vegetation types occurred (Wang et al., 2012; Xue et al., 2015). Nevertheless, the regional hydrological environment, influenced by temperature and precipitation, has had a profound effect on surface vegetation, soil microbial activity, and soil CO_2 production. Current research links variations in δ^{13}Cs with local hydrological conditions, often interpreting these variations in conjunction with climate fluctuations revealed by δ^{18}Os.

The concentrations and trace element ratios (X/Ca) in stalagmites are influenced by both climatic and non-climatic factors across different timescales (Figure 1.5) (Fairchild and Treble, 2009). The distribution coefficients of trace elements in calcite are strongly influenced by factors such as temperature, growth rate, precipitation, and water-rock interactions (WRI) (Duan et al., 2024; Fairchild and Treble, 2009; Stoll et al., 2023; Tremaine and Froelich, 2013; Wassenburg et al., 2024). For instance, a 2–3 °C temperature change can lead to an approximate 15% variation in Mg concentration (Huang and Fairchild, 2001). Stalagmite growth rate can also affect the distribution coefficients of Mg and Sr (Gabitov et al., 2014). Interpretations should consider sample-specific conditions and the broader context of temperature variations.

In paleoenvironmental reconstructions, the X/Ca in stalagmites is commonly used as quantitative indicator of regional wet-dry variations (Figure 1.5) (Fairchild and Treble, 2009; Stoll et al., 2023; Wassenburg et al., 2020). The distribution coefficients of trace elements are typically less than 1 and substantially lower than that of calcium, so prior calcite precipitation (PCP) indirectly reflects climatic and environmental changes by controlling the X/Ca ratio in both drip water and stalagmites (Fairchild and Treble, 2009). Under dry environments, characterized by reduced precipitation and enhanced evaporation-transpiration, water residence time in the surface karst zone increases. This results in lower drip rates and extended CO_2 degassing durations. Consequently, calcium ions are preferentially removed, leading to an increase in the X/Ca ratio in cave drip water and speleothems, with a higher concentration of trace elements such as Mg and Sr (Figure 1.5) (Fairchild et al., 2006; Tremaine and Froelich, 2013). Conversely, wet environments lead to a reduction in the X/Ca ratio. The residence time of drip water in the epikarst influences the duration of WRI (Fairchild and Treble, 2009; Huang and Fairchild, 2001; Wassenburg et al., 2020).

Longer WRI times allow for greater dissolution of trace elements from the bedrock into the drip water, thereby increasing the X/Ca ratio. Since PCP and WRI both influence trace element ratios in the same direction, wet-dry changes in the regional environment generally govern the X/Ca fluctuations in stalagmites through these processes.

In recent years, significant advances have been made in the study of trace elements and carbon isotopes in speleothems, revealing broad prospects for their application. On the one hand, the combination of trace element ratios such as Mg/Ca and Sr/Ca with calcium isotopes (δ^{44}Ca) enables semi-quantitative to quantitative reconstructions of past precipitation (de Wet et al., 2024; Stoll et al., 2023; Warken et al., 2024). A recent study proposed a method for estimating $\delta^{13}C_{init}$—the initial carbon isotope composition of drip water prior to significant CO_2 degassing and PCP, as a more robust proxy for interpreting vegetation, soil, and epikarst processes (Stoll et al., 2023). Compared to conventional δ^{13}C values, $\delta^{13}C_{init}$ has been shown to be more sensitive to environmental variables such as temperature and moisture. On the other hand, anomalous variations in the concentrations or ratios of specific trace elements during intervals can serve as indicators of abrupt climate events—such as rapid shifts in temperature or hydroclimate—thus providing crucial evidence for identifying the timing and environmental context of such changes (Warken et al., 2025). The ongoing development of these approaches marks an important direction in high-resolution paleoclimate research, emphasizing multi-proxy and quantitative reconstructions based on speleothem archives.

In the monsoon region of China, changes in δ^{13}Cs and X/Ca are primarily influenced by monsoon precipitation, which impacts effective soil moisture (Chen et al., 2021a,b; Wu et al., 2023a). Decreased monsoon precipitation and deteriorating hydrological conditions lead to reduced vegetation cover, lower soil microbial activity, decreased soil CO_2 productivity, diminished effective moisture, and increased PCP/WRI. These changes result in elevated δ^{13}Cs values and X/Ca ratios in cave drip water and stalagmites (Chen and Li, 2018; Cheng et al., 2022b; Wu et al., 2023a). The combined use of δ^{13}Cs and X/Ca, in conjunction with δ^{18}Os, not only enhances the understanding of the climatic significance of δ^{18}Os but also enables a more precise investigation of the relationship between EASM intensity and regional precipitation.

1.2.4 Fluid Inclusions

Fluid inclusions are formed by the entrapment and retention of small amounts of drip water or gas within the pore spaces during the deposition of speleothems (Figure 1.5). Thus, fluid inclusions represent unique remnants of ancient cave drip water that have been preserved for a certain period of time (Affolter et al., 2015, 2025; Dennis et al., 2001; Genty et al., 2002; Kendall and Broughton, 1978; Millo et al., 2017; Schwarcz et al., 1976). The size of speleothem fluid inclusions typically ranges from a few micrometers (μm) to tens of micrometers in diameter, with some, consisting of interconnected pore spaces, reaching lengths of over 1 cm. Based on their origin, fluid inclusions are classified into primary and secondary types (Figure 1.5) (Lopez-Elorza et al., 2021). Primary fluid inclusions contain water incorporated into the stalagmite during crystal growth and can exist as either intercrystalline or intracrystalline inclusions. In contrast, secondary fluid inclusions form after crystal growth has concluded and are unsuitable for paleoclimatic reconstruction (Lopez-Elorza et al., 2021). Careful examination of the petrographic characteristics of the inclusions is essential prior to analysis to confirm their primary nature.

Modern cave monitoring shows that the stable isotopic composition (δ^{18}O, δ^{2}H) of cave drip water generally approximates the weighted average of the local annual precipitation isotopic composition (Baker et al., 2019; Duan et al., 2016). If the fluid inclusion water does not exchange isotopes with the surrounding calcite after its formation, it can be used directly to measure the average isotopic composition of ancient rainwater (Affolter et al., 2019, 2015; Millo et al., 2017; Uemura et al., 2020; Warken et al., 2022). Laboratory experiments and cave monitoring studies demonstrate that the oxygen isotope fractionation between calcite and water depends on temperature changes under equilibrium fractionation conditions between calcite and water (Daëron et al., 2019; Johnston et al., 2013; Kim and O'neil, 1997; O'Neil et al., 1969; Tremaine et al., 2011). Based on the measurement of δ^{18}O and δ^{2}H of fluid inclusions ($\delta^{18}\mathrm{O}_{\mathrm{FI}}$ and $\delta^{2}\mathrm{H}_{\mathrm{FI}}$), combined with the corresponding calcite δ^{18}O, the paleotemperature during calcite precipitation can be calculated (Affolter et al., 2019; Genty et al., 2002; Schwarcz et al., 1976). The δ^{18}O values of the speleothem fluid inclusions and the surrounding stalagmite calcite δ^{18}O are combined to calculate the water-calcite oxygen isotope fractionation factor ($\alpha_{\text{calcite–water}}$), i.e., Eq. 1.5-1.11, which can reconstruct the paleotemperature of the cave or evaluate the isotope non-equilibrium fractionation effects during stalagmite formation (Figure 1.6) (Fernandez et al., 2023; Griffiths et al., 2010; Meckler et al., 2015; Millo et al., 2017; Rowe et al., 2012).

$$1000 \ln \alpha_{\text{calcite–water}} = 2.68 \times 10^{6} T^{-2} - 2.89 \quad \text{(O'Neil et al., 1969)} \tag{1.5}$$

$$1000 \ln \alpha_{\text{calcite–water}} = 18.03 \times 10^{3} T^{-1} - 32.42 \quad \text{(Kim and O'neil, 1997)} \tag{1.6}$$

$$1000 \ln \alpha_{\text{calcite–water}} = 16.1 \times 10^{3} T^{-1} - 24.6 \quad \text{(Tremaine et al., 2011)} \tag{1.7}$$

$$1000 \ln \alpha_{\text{calcite–water}} = 17.66 \times 10^{3} T^{-1} - 30.16 \quad \text{(Johnston et al., 2013)} \tag{1.8}$$

$$1000 \ln \alpha_{\text{calcite–water}} = 17.57 \times 10^{3} T^{-1} - 29.13 \quad \text{(Daëron et al., 2019)} \tag{1.9}$$

$$1000 \ln \alpha_{\text{aragonite–water}} = 18.56 \times 10^{3} T^{-1} - 33.49 \quad \text{(Patterson et al., 1993)} \tag{1.10}$$

$$1000 \ln \alpha_{\text{aragonite–water}} = 17.88 \times 10^{3} T^{-1} - 31.14 \quad \text{(Kim et al., 2007)} \tag{1.11}$$

$$\alpha_{\text{calcite/aragonite–water}} = \frac{1000 + \delta^{18}\mathrm{O}_{\text{calcite/aragonite}}}{1000 + \delta^{18}\mathrm{O}_{\text{water}}}, \quad T = \text{Kelvin}. \tag{1.12}$$

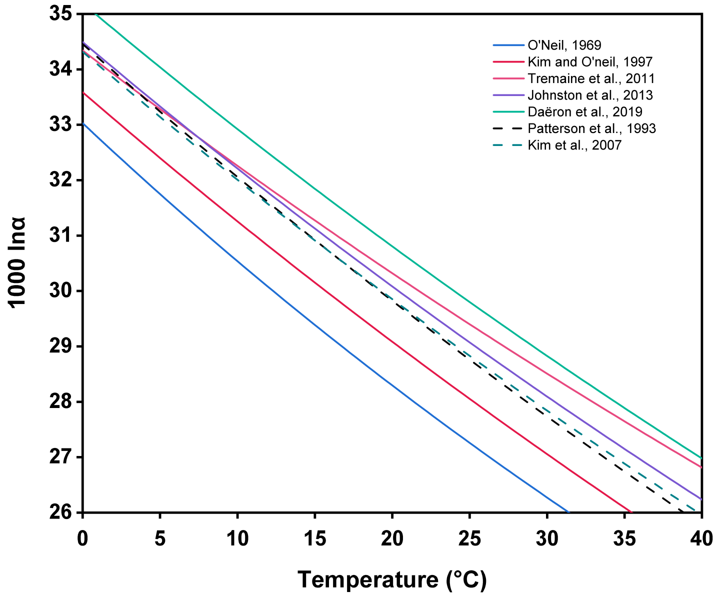

Figure 1.6. Equilibrium δ^{18}O fractionation between water and $CaCO_3$ (1000lnα) as a function of temperature. Solid lines and dotted lines represent calcite and aragonite respectively. Solid lines indicate calcite, dashed lines indicate aragonite.

Early studies on the stable isotopes of speleothem fluid inclusions primarily focused on δ^2H. The oxygen isotope in the water may exchange with the surrounding $CaCO_3$ after the formation of fluid inclusions (Schwarcz et al., 1976; Uemura et al., 2016), meaning the $\delta^{18}O_{FI}$ value of the inclusion water may not be reliable. During the deposition of calcite, δ^2H_{FI} is not affected by isotope fractionation, and once water is preserved in fluid inclusions, δ^2H_{FI} will remain unchanged because there is no hydrogen source in calcite (Affolter et al., 2019; Schwarcz et al., 1976). Therefore, in some studies, $\delta^{18}O_{FI}$ is calculated from the global meteoric water line (GMWL) or the local meteoric water line (LMWL) based on δ^2H_{FI} (Affolter et al., 2019; Genty et al., 2002; McGarry et al., 2004). Besides paleotemperature reconstruction, recent studies have highlighted that speleothem fluid inclusions can also be used to analyze changes in cave evaporation, moisture sources, and water vapor migration trajectories, showing great potential for future applications (Affolter et al., 2015, 2025; Fleitmann et al., 2022, 2003; Warken et al., 2022). However, the extraction of inclusion water and the precise measurement of isotopes present significant challenges, which will be explained in detail in the following sections.

1.3 Key Scientific Questions to be Addressed

1.3.1 The Hydro-climatological Significance of δ^{18}Os in Chinese Monsoon Region

As mentioned in Sections 1.1.3 and 1.2.2, the interpretation of δ^{18}Os values in the Chinese monsoon region as an indicator of local precipitation amounts remains controversial. The relationship between δ^{18}O-proxied EASM intensity and regional hydrological environments across different timescales continues to be an issue that requires clarification. The X/Ca ratio, $\delta^{18}O_{FI}$, and $\delta^{2}H_{FI}$ can provide insights into changes in regional hydrological environments from multiple perspectives. Comparing these measurements with δ^{18}Os values within the same chronological framework will improve the assessment of the meteorological and hydrological significance of δ^{18}Os, particularly in evaluating the relationship between regional hydrological conditions and EASM intensity.

1.3.2 Variations in The Precipitation and Regional Hydro-environment of the EASM Region During the Last Glacial Period and Holocene

Accurately describing the spatial heterogeneity of precipitation in the EASM region during the last glacial period and Holocene remains a challenge. The combined influence of astronomical, ice volume, and CO_2 forcings on the evolutionary processes and spatial variability of the EASM is complex. There is no consensus among these viewpoints, and they may even conflict with one another. Currently, research on the temporal and spatial patterns of precipitation evolution on orbital timescales heavily relies on model simulations, (e.g., Dai et al. (2022); Liu et al. (2022c); Lyu et al. (2021); Zhao et al. (2023a)) with very limited long paleoclimatic records available for reference. Furthermore, during the late Holocene, human activities and natural climate variability have intertwined, leading to ongoing debates about which factor has predominantly influenced the evolution of surface ecological environments. Clarifying this issue is crucial for assessing the evolution of regional hydrological environments and their impact on human-environment relationships in the context of future global changes.

1.3.3 Challenges and Improvements in Techniques for Analysing Stalagmite Fluid Inclusions Water Stable Isotope

Although fluid inclusion water isotopic analysis has made significant contributions to understanding stalagmite paleoclimate records, the original isotopic signal of precipitation may be altered. This is typically observed as a pronounced positive shift in $\delta^{18}O_{FI}$ and $\delta^{2}H_{FI}$ values, with data points enriched in δ^2H_{FI} and $\delta^{18}O_{FI}$ compared to the global or local meteoric water line and a fitted slope considerably lower than that of the water line. Several factors contribute to this phenomenon. For instance, precipitation evaporation may occur within the epikarst zone or cave environments, and isotopic exchange between inclusion water and the surrounding calcite may alter the original $\delta^{18}O_{FI}$ signal after the inclusion has formed.

There may also have been a significant impact from measurement techniques. Recent studies have highlighted that heating the sample during measurements produces significant isotopic artifacts (de Graaf et al., 2022; Fernandez et al., 2023). Evaporative water loss due to heating before the extraction/release of inclusion water for measurement can significantly increase the $\delta^{18}O_{FI}$ and δ^2H_{FI} values. Currently, this is a common issue in the isotopic analysis of stalagmite fluid inclusion water, especially in practical applications, where it is often difficult to determine whether abnormally high values are due to natural factors or analytical artifacts. Therefore, careful screening and evaluation of results are essential to exclude or correct anomalous data, or to obtain more reliable results by improving measurement techniques.

In addition to the factors mentioned above, it is important to note that different laboratories employ varying techniques for measuring fluid inclusion water isotopes, and even the same technique may involve differing measurement processes and parameters across laboratories. These differences can lead to potentially discrepancies in the isotope results obtained. For example, current research suggests that systematic biases may exist between Isotope Ratio Mass Spectrometry (IRMS) and Cavity Ring-Down Spectroscopy (CRDS) techniques when measuring $\delta^{18}O_{FI}$ and δ^2H_{FI} values biogenic carbonates (de Graaf et al., 2020). The optimal water volume range for measurement also varies between techniques, particularly for small-volume samples, which can result in reduced analytical reproducibility or systematic shifts in isotope values. It remains unclear whether significant biases exist between measurement results from different laboratory instruments, whether amount effects occur, or how these effects manifest. Further research is needed to address these potential issues and improve the reliability of analytical results, particularly in studies involving small-volume samples.

1.4 Dissertation Structure and Key Research Topics

Focusing on the three main issues mentioned above, this dissertation first examines the technical aspects of $\delta^{18}O_{FI}$ and δ^2H_{FI} measurements in fluid inclusion water. It then proceeds with reconstructions of EASM intensity and environmental changes during the Last Glacial and Holocene, using multiple indicators derived from stalagmites.

In Chapter 2, this dissertation quantitatively examines the systematic deviations observed in $\delta^{18}O_{FI}$ and $\delta^{2}H_{FI}$ values measured using the Heidelberg fluid inclusion line (HD line) under low water volume conditions, based on a substantial number of standard water injections. To address these deviations, a new calibration procedure was developed, which significantly enhances the reliability of measurements for samples with low water content (less than 0.2 µl). Additionally, the chapter highlights recent advancements in the HD line's measurement techniques and data analysis protocols, which have notably reduced measurement and heating times while ensuring high precision and accuracy.

In Chapter 3, this dissertation provides a quantitative evaluation of the phenomenon of fluid inclusion water vaporization caused by pre-heating before sample crushing, along with the resulting artifacts in isotope measurements. This analysis is based on measurements of biological carbonate archives, specifically cold-water corals from Iceland and Angola. To mitigate this issue, a novel measurement technique was developed, wherein samples are encapsulated in glass tubes to prevent evaporation. The chapter demonstrates the reliability of this method through an analysis of isotope results obtained with the new technique. This chapter highlights the methodological challenges and uncertainties in interpreting the $\delta^{18}O$ and $\delta^{2}H$ values of coral skeleton inclusion water, emphasizing the need for a better understanding of coral calcification and potential seawater exchange processes.

In Chapter 4, the dissertation focuses on the inter-laboratory comparison of fluid inclusion water isotope measurements. A comparison experiment was designed, involving 13 laboratories, in which standard water samples with varying volumes and isotope values were distributed to assess and compare the measurement results across different laboratories. This chapter identifies key factors that influence the accuracy of fluid inclusion water isotope analysis. The primary objectives include evaluating measurement precision both within and between laboratories, investigating the effect of water volume on isotope values, comparing results across laboratories, and examining the adsorption effects of freshly crushed calcite. The aim of this research is to optimize the use of fluid inclusion isotope techniques in paleoclimate studies and support their broader application.

In Chapter 5, the dissertation presents isotopic analyses of inclusion water from Chinese stalagmites from the middle to late Holocene. Time series of $\delta^{18}O_{FI}$ and $\delta^{2}H_{FI}$ for this period in southwestern China are established by employing the Rayleigh fractionation model and an improved measurement procedure, which eliminates anomalous isotopic results caused by the measurement process. By combining $\delta^{18}Os$ and $\delta^{13}Cs$ records, this chapter evaluates the relationship between EASM intensity, human activities, and regional hydrological conditions in southwestern China. It also explores the applicability of $\delta^{18}O$ as an indicator of EASM intensity or regional hydrological conditions.

Finally, in Chapter 6, the dissertation evaluates the climatic significance of $\delta^{18}O$ on the orbital scale in the EASM region by analyzing trace elements from a stalagmite that grew continuously during the last glacial period in southwestern China, alongside δ^{13}C records. The chapter examines the influence of NHSI and global ice volume on the phase and amplitude variations of the regional hydrological environment during the last glacial period. Furthermore, it explores the spatial distribution patterns and driving mechanisms of monsoonal precipitation in China on both orbital and millennium timescales.

1.5 Materials and Methods

Due to the use of various standard waters, cold-water coral, and speleothem samples from different environments and climate zones across the globe in different chapters, the preparation and measurement of these samples, as well as the sample pre-treatment and data analysis, vary significantly. To ensure the coherence of the dissertation, this section provides only general information about the measurement equipment primarily used in this study. Detailed information regarding the research areas of the sampling sites, sample pre-treatment, measurement procedures, and calibration processes will be provided in the respective chapters.

1.5.1 Fluid Inclusion Stable Isotope

Weissbach et al. (2023) developed a stable isotope measurement system for carbonate inclusion water based on CRDS at the Institute of Environmental Physics, Heidelberg University, which includes a data analysis protocol (Figure 1.7). All measurements and improvements to the stable isotope analysis of inclusion water in this dissertation were conducted using this system.

The measurement principle of the system involves artificially creating a stable background of water vapor with a known isotopic composition. After the sample is heated and crushed, the inclusion water is rapidly evaporated at high temperatures (120°C) (Figure 1.7). The resulting mixed signal from the water vapor background and the sample vapor is then simultaneously transmitted to the CRDS (Picarro L2130-i) for measurement. By subtracting the background signal from the mixed signal, the amount of water released from the sample and its isotopic values can be determined.

The measurement line consists of several components. First, a peristaltic pump mixes standard water with a known isotopic composition into a nitrogen gas flow, creating a stable water vapor background. The nitrogen flow rate is controlled at 320 mL per minute, maintaining a stable water vapor concentration of 6000–8000 ppmv (Figure 1.7). The samples are loaded into copper tubes with an inner diameter of 8 mm, which are sealed at both ends and connected to the line. A hydraulic crusher then crushes the copper tube and sample. Finally, the line is connected to the CRDS for online measurement. The mixing cavity, crushing unit, and connecting line are all placed in an oven set to 120°C. Sections of the line exposed outside the oven are heated to 120°C using heating tapes (Figure 1.7). The two mixing cavities are used to stabilize the signals from the water vapor and isotope backgrounds, as well as to mix the background and water vapor from the inclusion water.

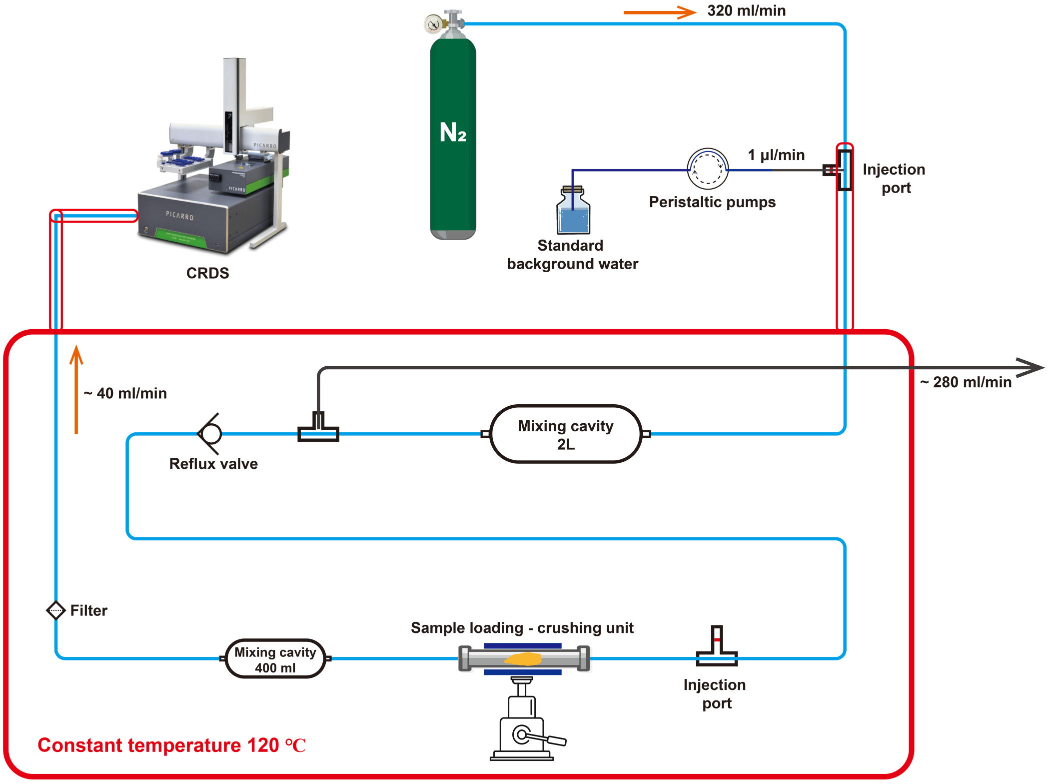

Figure 1.7. Schematic diagram of Heidelberg fluid inclusion measurement line. The red box indicates a 120 °C heated environment.

The measurement process and data evaluation protocol follows the method outlined by Weissbach et al. (2023). The general process involves determining the start and end points of the sample signal peak based on the slope. The measurement process is as follows: the sample is loaded into a copper tube, and once the water vapor and isotope background have stabilized, the copper tube is crushed using a hydraulic press to release water form sample. The entrapped water in the sample is then instantaneously evaporated at 120°C. The resulting sample water vapor is mixed with the background water vapor in the mixing cavity and subsequently transferred to the CRDS analyzer for online measurement.

The general data analysis process involves determining the start and end points of the sample signal peak based on the slope. The isotopic values and water volume of the sample are calculated by subtracting the background signal from the mixed gas measurement signal. The resulting data are then calibrated for isotopic values and water volume. For isotopic calibration, six different of standard waters are employed, with isotopic values measured using a separate CRDS system in the laboratory. These standards are cross-calibrated to the

International Atomic Energy Agency international standards. The calibration equation is derived by calculating the linear relationship between the measured stabilized water vapor background isotopic values and the true standard water isotope values. Water volume calibration is performed by measuring capillaries with known water volumes, establishing a linear relationship between the time-integrated water volume signal (ppmv·s) measured by CRDS and the known water volumes. A detailed description of the isotopic and water volume calibration processes is provided in Weissbach et al. (2023). The analytical precision of the measurement system is δ^2H ≤ ±1.5‰ and δ^{18}O ≤ ±0.5‰. Memory, adsorption, and amount effects in fluid inclusion isotope analysis are negligible for samples with ≥ 1 µl/g calcite. Isotopic interference is also negligible for sample isotope ratios within 10‰ (δ^{18}O) and 50‰ (δ^2H) of the water vapor background.

1.5.2 Trace Elements

The analysis of trace elements in stalagmites is performed at the Institute of Environmental Physics, Heidelberg University, using laser ablation inductively coupled plasma mass spectrometry (LA-ICP-MS). This technique offers low detection limits and high spatial resolution, enabling the simultaneous acquisition of multiple trace elements while minimizing physical damage to the samples (Figure 1.8). The Institute of Environmental Physics, the LA-ICP-MS setup couples a 193 nm ArF excimer laser (New Wave Research NWR193 UC) with an inductively coupled plasma quadrupole mass spectrometer (Thermo Fisher iCAP-Q). Line scans are conducted along the sample's long axis at a speed of 20 µm/s, with a rectangular spot size of 15 × 150 µm (the longer edge perpendicular to the scanning path). To minimize potential surface contamination, the scanning path is pre-ablated at a speed of 80 µm/s. The laser pulse repetition rate is set to 20 Hz, and each isotope is measured every 100 milliseconds on the mass spectrometer. Background counts are measured with the laser turned off and subtracted from the raw data.

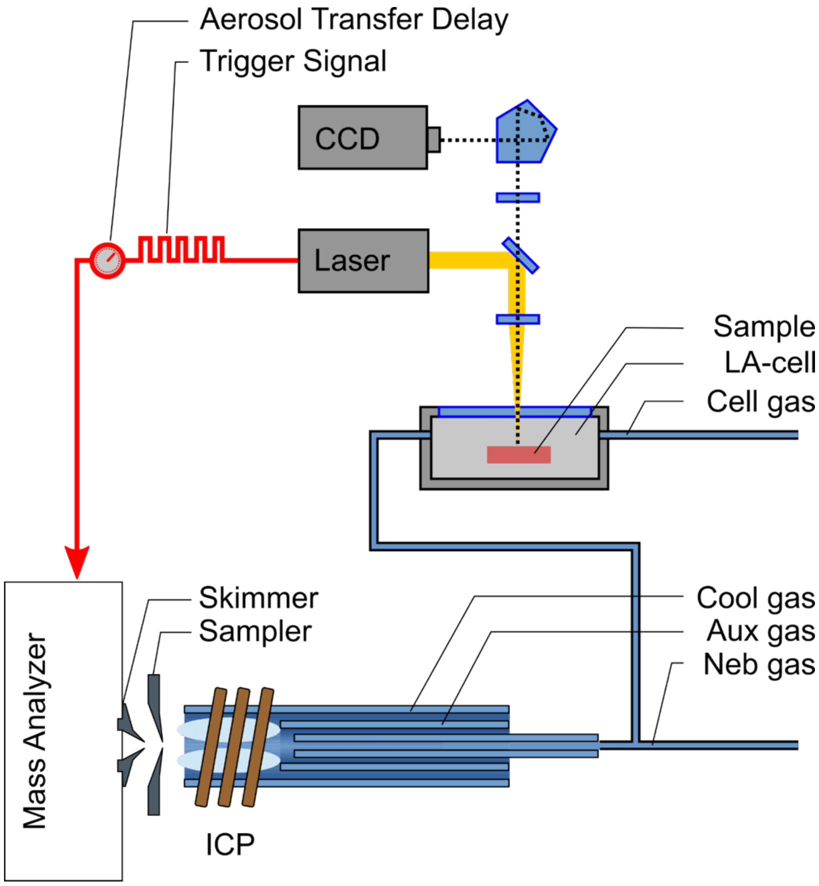

Figure 1.8. Schematic diagram of the laser ablation inductively coupled plasma mass spectrometry system. A laser beam (yellow optical path) is emitted by the Laser System and focused onto the sample surface in the Sample Chamber through a series of mirrors and lenses, inducing laser ablation and generating fine aerosol particles. These particles are carried by the Carrier Gas Flow and transported into the Plasma Torch. The Charge-Coupled Device (CCD) records optical signals generated during laser ablation to assist with data analysis.The image is cited from https://www.tofwerk.com/zh-hans/laser-ablation-icp-ms-imaging/.

Chapter 2

Technical Improvements of Heidelberg Fluid Inclusion Measurement Line

Key Points:

- **With decreasing water volume (less than 0.5 µl), the δ^{18}O and δ^{2}H values measured by the Heidelberg fluid inclusion line exhibit systematic deviations from expected values.**
- **The isotope value increases logarithmically with decreasing water volume, which can be corrected using an appropriate calibration procedure.**
- **The latest improvements to the measurement line and data analysis protocols have shortened the measurement and heating times for individual samples while maintaining the original accuracy and precision.**

This chapter builds upon the work of Dr. Therese Weissbach and her colleagues (Weissbach et al., 2023), who established the fluid inclusion measurement line at Heidelberg (HD) University based on the CRDS system as part of her doctoral research. Their setup enabled isotopic analysis of fluid inclusions extracted under stable and controlled water vapor background conditions. Long-term stable calibration of both isotope ratios and water volume for the CRDS system was achieved. To evaluate the performance of fluid extraction and measurement, they used syringe injections and borosilicate capillaries filled with reference water. Their experiments demonstrated that the setup does not introduce isotopic shifts for small water volumes, and that memory effects can be minimized if the isotopic composition of the background vapor closely matches that of the sample (within 10‰ for δ^{18}O and 50‰ for δ^{2}H).

Building on previous work, the Heidelberg fluid inclusion measurement line was further optimized during the course of the my doctoral research, through extensive repeated measurements of standard waters, along with comprehensive data quality assessment and analysis. The HD measurement line shows high reproducibility and accuracy for large water volumes, but when measuring small volumes (below 0.5 µl), accuracy and reproducibility degrades, affecting result reliability. Although previous studies reported no significant isotopic shifts in small-volume samples, the limited number of repeated measurements leaves some effects insufficiently constrained. This chapter quantifies isotopic shifts in small-volume measurements and provides a revised calibration approach. It also addresses measurement efficiency and the impact of prolonged heating, which may cause water evaporation and isotopic fractionation. The HD measurement line is further optimized to reduce measurement and heating times, improving efficiency while maintaining accuracy. In addition, this chapter provides an evaluation of the long-term performance of the HD line from 2021 to 2025, demonstrating its stability and accuracy in the measurement of fluid inclusion stable isotopes over extended periods.

2.1 Introduction

Since the 1970s, isotopic analysis techniques for fluid inclusions water in speleothems have undergone significant development (Harmon et al., 1978; Schwarcz et al., 1976), evolving from offline IRMS to continuous-flow IRMS (CF-IRMS) (Dublyansky and Spötl, 2009; Schwarcz et al., 1976; Vonhof et al., 2006), and more recently to laser spectroscopy methods such as CRDS (Affolter et al., 2014; Arienzo et al., 2013). Early studies employed offline crushing extraction methods (e.g., Schwarcz et al. (1976)), which required 1 to 4 g of sample per measurement and could only determine δ^{2}H. In 2006, Vonhof et al. (2006) integrated online crushing techniques with CF-IRMS, enabling simultaneous determination of δ^{2}H and

δ^{18}O with analytical precisions of ±1.5‰ for δ^2H and ±0.5‰ for δ^{18}O while reducing the required water volume to about 0.25 μl. Since 2013, laser spectroscopy methods such as Picarro CRDS have gradually become the mainstream approach (e.g., Affolter et al. (2014); Arienzo et al. (2013); Uemura et al. (2020); Weissbach et al. (2023)). These methods allow simultaneous measurement of δ^2H, δ^{18}O and δ^{17}O, with improved precisions of ±0.2‰ for δ^{18}O and ±1.0‰ for δ^2H and require as little as 0.05 μl of water (Affolter et al. (2025) and their references). Concurrently, water extraction techniques have diversified, primarily including mechanical crushing and high-temperature thermal decrepitation (Schwarcz et al., 1976). Mechanical crushing, which effectively avoids isotopic fractionation caused by high temperatures, has emerged as the dominant technique in current research.

These technological advancements have significantly improved the analytical precision of stable isotopes in fluid inclusion water and expanding the range of measurable samples to those with low water content (<0.5 μl) (e.g., Affolter et al. (2014); Vonhof et al. (2006)). However, current research has largely focused on optimizing technical aspects, such as refining water extraction methods, while paying relatively little attention to the "volume dependent effect" in isotopic measurements under low water volume conditions (<0.5 μl). A limited number of studies have indicated that as water volume decreases, systematic positive or negative shifts in isotopic values may occur, accompanied by substantial declines in measurement precision and reproducibility (de Graaf et al., 2020). This issue is particularly pronounced in measurements conducted using CRDS-based systems (de Graaf et al., 2020). The accuracy, stability, and volume dependence of isotopic measurements from fluid inclusions with <0.5 μl water remain poorly understood, and standardized correction protocols are lacking.

In addition, different measurement systems vary significantly in sample measurement efficiency, with the number of samples that can be measured each day ranging from a few to a dozen or even dozens (e.g., Affolter et al. (2014); de Graaf et al. (2020); Uemura et al. (2020)). Improving measurement efficiency not only enables the acquisition of more sample data within a limited timeframe but, more importantly, substantially reduces the heating and waiting time of samples within the system. This, in turn, minimizes potential water loss and associated isotopic fractionation effects (Fernandez et al., 2023). Therefore, optimizing measurement efficiency is not only a critical means of enhancing measurement productivity but also a key factor in ensuring the accuracy of isotopic measurements under low water volume conditions.

Building upon this, the chapter focuses on isotope measurement and data analysis of water samples with volumes less than 0.5 μl using the Heidelberg measurement platform. The research aims to: (1) quantify assess the measurement precision and stability of CRDS-based fluid inclusion isotopic analysis under extremely low water volume conditions; (2) to enhance measurement efficiency by reducing both the heating and analysis time per sample, without compromising the current levels of precision and accuracy; and (3) propose a fractionation correction model suitable for low-water conditions.

To achieve these objectives, this chapter using the fluid inclusion measurement platform developed by the Institute of Environmental Physics at Heidelberg University, conducting a systematic evaluation of isotopic measurement performance under conditions of water volume less than 0.5 µl. This platform, based on a CRDS system, has already demonstrated excellent measurement accuracy and repeatability under high-water sample conditions (>1 µl) (δ^2H ≤ ±1.5‰, δ^{18}O ≤ ±0.5‰) (Weissbach et al., 2023). However, under low water volume conditions (<0.5 µl), there remains a lack of systematic research and quantitative evaluation on the stability of isotopic measurements and the sources of potential bias.

Firstly, the measurement reproducibility deteriorates as the water volume decreases. For water volumes greater than 1 µl, the reproducibility of injected standard water ranges from 0.1 to 0.3 ‰ for δ^{18}O and 0.2 to 0.7‰ for δ^2H. However, for water volumes between 0.1 and 0.5 µl, the reproducibility significantly decreases to 0.4–0.5‰ for δ^{18}O and 1.1–1.9 ‰ for δ^2H. It is noteworthy that the reproducibility for these low water volumes was derived from a very limited number of replicate measurements (six measurements per 0.1 µl gradient) (Weissbach et al., 2023).

Secondly, the effect of water volume on measured isotopic values is a key issue. Taking the quantitative injection measurement of standard water as an example, as the water volume decreases, the measured δ^{18}O and δ^2H values gradually deviate from the standard water isotopic values. Although Weissbach et al. (2023) claimed that “for smaller water volumes, our device does not cause isotopic value drift”, this effect may be overlooked or obscured due to the limited number of replicate measurements. Given that numerous fluid inclusions in speleothems release less than 0.5 µl of water per measurement, and although increasing sample mass can improve precision, it also entails consuming more material and reducing resolution, making it crucial to understand and correct the volume dependency of isotopic measurement accuracy and reproducibility at low water volumes.

Finally, measurement efficiency and sample heating time are critical concerns. In the current HD line design and measurement procedure, a full measurement cycle—including sample loading, system stabilization, crushing, and measurement—takes 90 to 120 minutes. With the system’s initial morning stabilization, only 3 to 4 samples can be processed in a working day, and this number decreases further when standard water measurements are included. This efficiency is insufficient for analyzing large numbers of samples.In contrast, other analytical platforms developed based on the CRDS platform can process a dozen or even several dozen samples in a single day (e.g., Affolter et al. (2014); de Graaf et al. (2020); Tian et al. (2020); Uemura et al. (2020)), highlighting the urgent need to improve and optimize the HD line.

After loading a sample, a 30- to 40-minute wait is required for system stabilization following background disturbance from opening the system. During this time, samples awaiting crushing remain heated at 120 °C. Given the relatively porous and unique crystalline and depositional structures of speleothems and corals, prolonged heating can lead to water evaporation from fluid inclusions and isotopic fractionation (for detailed evaluation, see Chapter 3).

Optimizing the HD line to shorten individual measurement times while maintaining accuracy and precision would significantly improve efficiency. Reducing heating duration would also help minimize water evaporation and isotopic fractionation in some samples.

By measuring numerous laboratory standard water samples with known hydrogen-oxygen isotopic compositions and varying volumes, the effect of water amount on isotopic values can be investigated and calibrated. This process enhances measurement accuracy and facilitates error assessment. This section systematically evaluates the reproducibility, accuracy, and volume effects in isotopic measurements, specifically targeting fluid inclusion water samples with sub-0.5 µl. Based on 147 replicate measurements of different volumes of three standard waters, new calibration scripts were developed to account for the water amount dependence of isotopic measurements. Additionally, improvements to the HD line and the existing analytical protocol reduced both measurement and heating times, enhancing efficiency while maintaining accuracy and precision. These enhancements also minimized water evaporation and isotopic fractionation caused by heating.

2.2 Methods

Six internal laboratory standards were used as reference waters in the system. VE50% was prepared by evaporating 1L of VE standard water to 50% of its original volume (Table 2.1). The δ^{18}O range of these standards is -30.68‰- 3.91‰, and the δ^{2}H range is -243.97‰-21.67‰. The isotopic values of these reference waters were measured using another CRDS (Picarro) system in the laboratory, and the calibration was performed using international standards from the IAEA. To examine the water amount dependency of δ^{18}O and δ^{2}H values, VE50%, VE, and CC were selected for injection experiments. VE water was used as the water vapor background for all measurements.

In the isotope value amount dependency experiments, the injection volumes of each standard water ranged from 0.03 to 0.80 µl. The injection measurements were carried out under stable line conditions (i.e., within 20 minutes prior to injection, the standard deviation of water vapor concentration changes was less than 20 ppmv, and the standard deviations of δ^{18}O and δ^{2}H changes were less than 0.25‰ and 1.00‰, respectively). Each measurement

Standard	δ^{18}O **(‰, V-SMW)**	**SD (1σ)**	δ^{2}H **(‰, V-SMW)**	**SD (1σ)**
VE	-8.50	0.00	-60.34	0.02
VE70%	-1.82	0.07	-39.80	0.49
VE60%	0.92	0.05	-31.27	0.56
VE50%	3.91	0.20	-21.67	1.09
CC	-15.15	0.14	-110.88	0.39
IIIa (NG a)	-30.68	0.02	-243.97	0.12

Table 2.1. Standard water used in the Heidelberg fluid inclusion measurement line. The isotopic values of the standard water are measured by another CRDS in the laboratory.

lasted 30 to 60 minutes. The different volumes three standard waters were measured 51 (VE50%), 58 (VE), and 38 (CC) times, respectively, between February 2022 and February 2023.

The calibration of raw data for CRDS analysis follows the protocol outlined by Weissbach et al. (2023). The isotope results are then calibrated using the linear regression equation derived from line measurements and the true values of the lab internal standard water. Water volume calibration is performed using the linear regression equation between the time-integrated measurement volume signal (in ppmv) and the water volume of the glass capillary (in µl). The above analysis process is implemented using the Python Jupyter script provided by Weissbach et al. (2023). For further details on the analytical protocol and specific linear equations, please refer to Weissbach et al. (2023), as they are not reiterated here.

2.3 Results

The overall measurement results for the three standard waters are shown in Figure 2.1 and Table S2.1 in Supplementary Information B.1. The standard deviations of isotope measurements for the three standard waters are similar. For δ^{18}O, the standard deviations are 0.34‰ (VE5), 0.50‰ (VE50%), and 0.47‰ (CC). For δ^{2}H, the standard deviations are 0.85‰ (VE), 1.18‰ (VE50%), and 0.95‰ (CC) (Figure 2.1). This consistency with Weissbach et al. (2023)'s findings primarily reflects fundamental variations in the isotopic dataset. To better assess the accuracy and reproducibility of isotope measurements at different water volumes, the data were arranged according to water volume and analyzed using a moving standard deviation approach.

The 7-point standard deviations of δ^{18}O and δ^{2}H for the three standard waters clearly demonstrate a dependence of isotope values on water volume (Figure 2.2). For δ^{18}O, reproducibility is better than 0.2‰ for water volumes greater than 0.5 µl. For volumes between

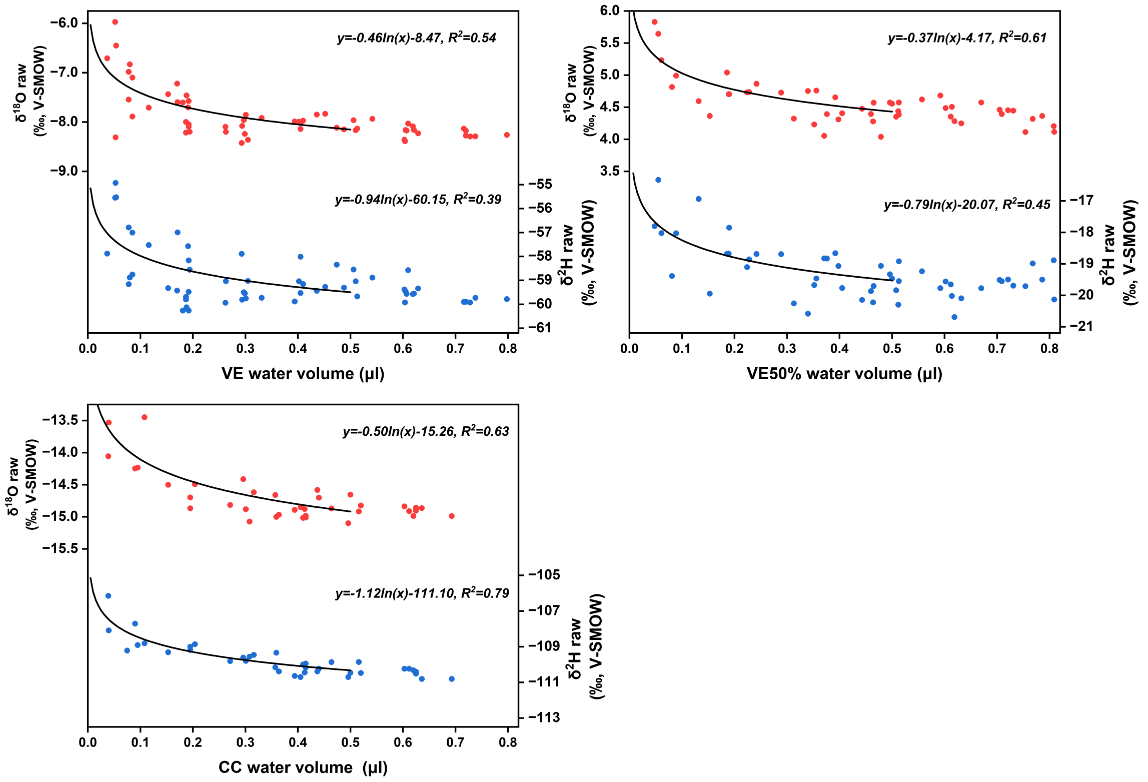

Figure 2.1. Quantitative injection results for three standard waters. Red and blue colors indicate δ^{18}O and δ^{2}H respectively. The black lines indicate the fitted curves for the respective data sets, which show a decrease in the volume of injected water and a logarithmic trend of increasing isotopic values. The background water used during the measurement was VE water. As shown in the figure, when the volume exceeds 0.5 µl, the isotopic values remain relatively stable; however, when the volume is less than 0.5 µl, significant deviations in isotopic values are observed.

0.2 µl and 0.5 µl, reproducibility ranges from 0.2‰to 0.5‰. For volumes below 0.2 µl, reproducibility deteriorates significantly, ranging from 0.4‰ to 0.8‰. A similar volume dependence is observed for δ^{2}H measurements (Figure 2.2). When the water volume exceeds 0.5 µl, reproducibility is approximately 0.5‰. For volumes between 0.2 µl and 0.5 µl, reproducibility remains below 1.0‰. For volumes smaller than 0.2 µl, reproducibility deteriorates further, with two standards showing values between 1.0‰ and 1.5‰, while one standard ranges from 1.2‰ to 2.0‰. These results indicate that isotope measurement reproducibility is strongly dependent on water volume, with higher reproducibility achieved at larger volumes.

Water volume also affects the absolute values of isotope measurements. As water volume decreases, the δ^{18}O and δ^{2}H values for the three standard waters exhibit a positive shift, with deviations from the standard water isotopic values increasing as the water volume de-

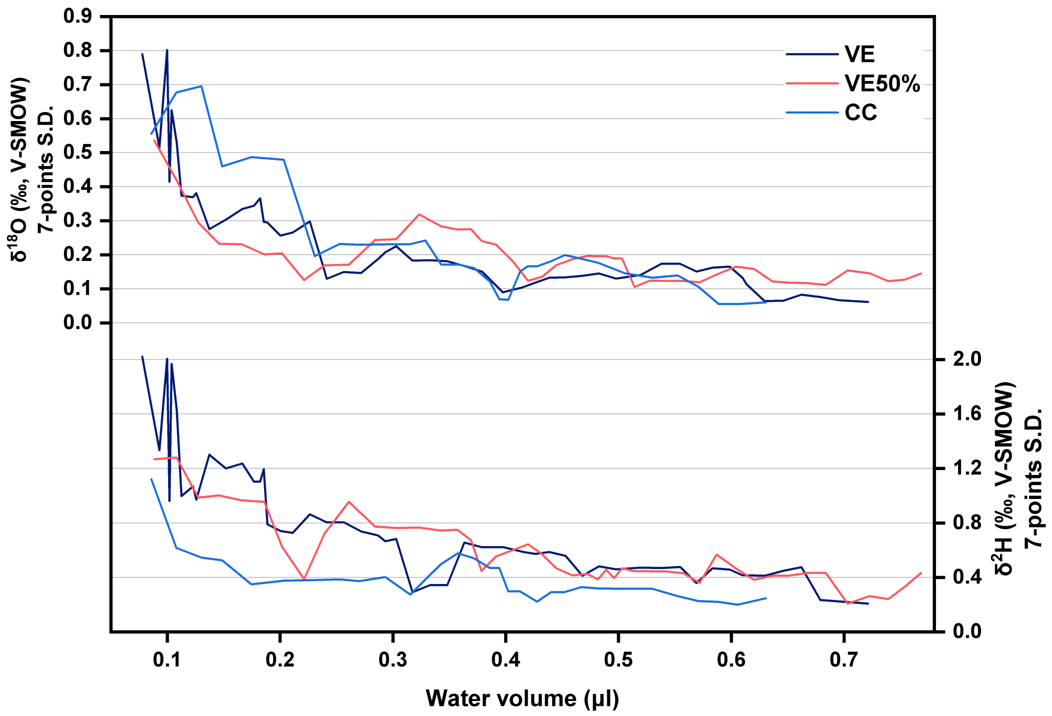

Figure 2.2. The 7-point standard deviation of the three standard water isotope results.

creases (Figure 2.1). Specifically, the positive shift for δ^{18}O values ranges between 1.0‰ and 2.0‰, while for δ^{2}H values, the shift ranges between 2.0‰ and 4.0‰ (Figure 2.1). Curve fitting results indicate that isotope values generally follow a logarithmic increase as water volume go to zero. No correlation was observed between measurement accuracy and precision and the isotope values of different standard waters; instead, accuracy and precision were dependent on water volume. Note that the differences observed at small volumes are also independent of the isotopic differences between the standards and the water vapor background.

2.4 Discussion

2.4.1 Water Amount Effects of Isotope Values

Compared to the fewer injection measurements reported by Weissbach et al. (2023), this dissertation offers a more comprehensive characterization of the isotopic accuracy and precision of the HD line across different water volumes through extensive repeated injections (n=147) (Figure 2.1). As water volume decreases, the measured δ^{18}O and δ^{2}H values show significant deviations from standard water isotopic values, and reproducibility decreases as expected from the decrease in integration area (Figure 2.1 and Figure 2.2). Specifically, measurements remain stable for water volumes of 0.5 µl or greater (reproducibility of 0.2‰ for δ^{18}O and 0.5‰ for δ^{2}H). For water volumes between 0.2 and 0.5 µl, isotopic accuracy and precision show a slight decline but systematic. When volumes are less than 0.2 µl, precision and accuracy markedly decrease (Figure 2.1 and Figure 2.2). Similar effects of water volume on isotope values have been observed in fluid inclusion measurements in some laboratories. For example, in the study by de Graaf et al. (2020), the water volume effect resulted in shifts of approximately 0.5–1‰ for δ^{18}O and 1–2‰ for δ^{2}H.

The lowered accuracy and precision of isotope values for water volume less than 0.5 µl may be related to several factors. First, the influence of background is a likely contributor. After injection or sample crushing, the evaporated water vapor mixes with the background vapor within the mixing cavity, resulting in the measured δ^{18}O and δ^{2}H values being a weighted mixture of the sample and the background. During measurement, if an amount of water more than 0.5 µl is released, the sample-derived vapor dominates the mixed vapor signal. For example, with an injection volume of 1 µl, the change in water vapor concentration is 3500 ppmv, which is substantial when compared to the baseline level of 6000 to 8000 ppmv (i.e., 30–50%). In contrast, an injection volume of just 0.1 µl leads to a change of only 350 ppmv in water vapor concentration, representing approximately 0.5% of the baseline value. As the released water volume decreases, the proportion of sample-derived vapor in the mixing process is reduced, leading to a greater influence from the background and, consequently, a deviation in the final isotope values.

It is worth noting that both δ^{18}O and δ^{2}H values tend to exhibit a systematic shift toward more positive values as the injected water volume approaches zero. This positive deviation appears to be independent of the isotopic composition of the background standard water. For example, even when the injected standard water VE50% has higher δ^{18}O and δ^{2}H values than the background, the measured isotopic values still increase as the water volume decreases (Figure 2.1). The underlying reason for this consistent positive trend—rather than a shift toward the isotopic composition of the background water—remains unclear. Further experiments under background conditions with varying isotopic characteristics are needed to determine whether the direction of this deviation is influenced by the isotopic composition of the background water.

Despite the unknown mechanisms described above, it is important to note that the same background standard water (VE) was used consistently in this experiment as well as during routine line operation and calibration. Moreover, the three standard waters used in the injection experiments span a broad range of isotopic compositions—δ^{18}O from +3.91‰ to –15.15‰ and δ^{2}H from –21.67‰ to –110.88‰—which covers the typical isotopic range observed in fluid inclusions from speleothems and corals samples. Therefore, empirical correction formulas can still be effectively applied to account for the observed isotopic deviations.

Temperature fluctuations from opening the heating box, which is turned off for 1-2 minutes during sample crushing, may also affect measurements. The mixing cavity, sample-holding copper tube, and connecting lines are housed within the heating box. At high water volumes, strong vapor signals from the sample overshadow temperature-induced background fluctuations. However, at low volumes, the limited vapor release makes background variations more pronounced, leading to reduced measurement reproducibility.

Based on the above findings, the measurement performance of the HD line can be improved in at least two ways. First, as water volume decreases, the measured isotope values deviate in a predictable manner, aligning well with the fitted curve. This deviation can be corrected through an additional isotope-water correction process. Second, the impact of vapor mixing and background fluctuations can be mitigated by adjusting the size of the mixing cavity. A smaller cavity shortens the mixing time between sample and background vapor, reducing background influence and significantly shortening the measurement time. These improvements will be discussed in Sections 2.4.2 and 2.4.3.

2.4.2 Calibration of Isotope Values for Water Volume Effects

Quantifying and correcting for the volume effect on isotope values could further enhance the accuracy of fluid inclusion measurements, especially under low water volume scenarios. Similar trends have been observed in the CRDS-based system developed by de Graaf et al. (2020) in Mainz, which features a design comparable to ours and has successfully implemented calibration. However, it remains uncertain whether the same calibration process can be applied to the HD line. To address this, the correction process used by de Graaf et al. (2020) was adapted to fit the HD measurement line, based on the isotope results of our three standard waters.

The fitting results indicate that the δ^{18}O and δ^{2}H values increase logarithmically as the water volume decreases, a trend that can be expressed by the Eq. 2.1. For the three standard waters, the fitted results are described by the equation Eq. 2.2-2.7.

$$y = A \cdot \ln(x) - B \tag{2.1}$$

where:

A : Coefficient dependent on the sample isotopic values.
B : Another coefficient dependent on the sample isotopic values.
$ln(x)$: Natural logarithm function of x.

$$y = 0.37 \cdot \ln(x) - 4.17 \quad (r^2 = 0.61,\ \text{VE50\%},\ \delta^{18}\text{O}) \tag{2.2}$$

$$y = 0.46 \cdot \ln(x) - 8.47 \quad (\text{r}^2 = 0.54, \text{VE},\ \delta^{18}\text{O}) \tag{2.3}$$

$$y = 0.50 \cdot \ln(x) - 15.26 \quad (\mathrm{r}^2 = 0.63, \mathrm{CC}, \delta^{18}\mathrm{O}) \tag{2.4}$$

$$y = 0.79 \cdot \ln(x) - 20.07 \quad (\mathrm{r}^2 = 0.45, \mathrm{VE50\%}, \delta^{2}\mathrm{H}) \tag{2.5}$$

$$y = 0.94 \cdot \ln(x) - 60.15 \quad (\mathrm{r}^2 = 0.45, \mathrm{VE}, \delta^{2}\mathrm{H}) \tag{2.6}$$

$$y = 1.12 \cdot \ln(x) - 110.10 \quad (\mathrm{r}^2 = 0.79, \mathrm{CC}, \delta^{2}\mathrm{H}) \tag{2.7}$$

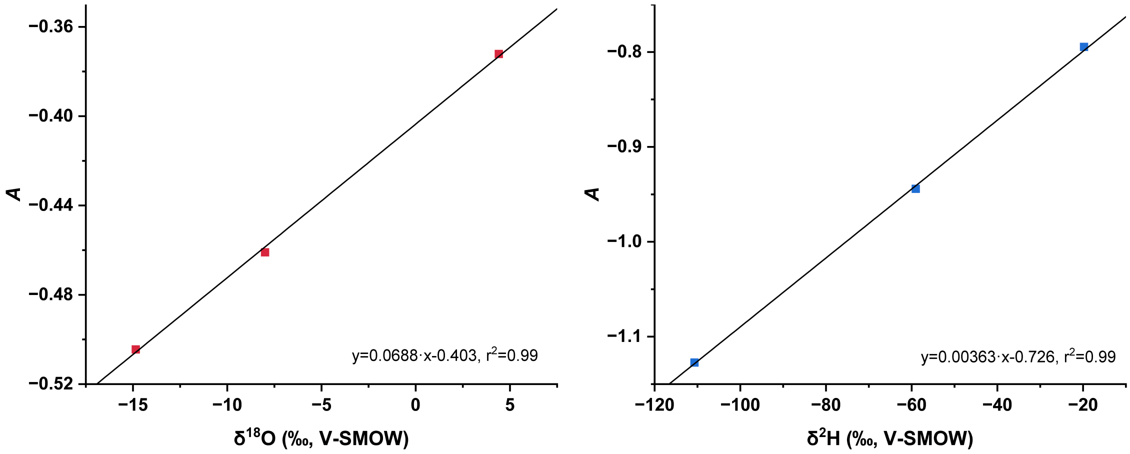

Figure 2.3. Correlation of the coefficient A of the logarithmic trend with isotopic values measurements at 0.4 µl. The results show a positive correlation between the coefficient A and the isotopic values.

Given that the volume effect on isotopic values becomes particularly pronounced for water volumes below 0.4 µl (Figure 2.1 and Figure 2.2), it may be ideal to correct water volumes smaller than 0.4 µl to 0.4 µl. To this end, the coefficient A of the logarithmic functions from different standards was fitted using the isotopic measurements at 0.4 µl. The results show a linear relationship between coefficient A and the standard water isotopic values at 0.4 µl, which can be expressed by the Eq. 2.8-2.9 (Figure 2.3). Based on Eq. 2.2-2.7 and Eq. 2.8-2.9, it is concluded that the volume effect on isotopic values in the system is systematic, with the isotopic values exhibiting a logarithmic increase as the water volume decreases, and that the coefficient A of the logarithmic trend is dependent on the isotopic values (Figure 2.3).

$$y = 0.00688 \cdot x - 0.403 \quad (\mathrm{r}^2 = 0.99, \delta^{18}\mathrm{O}) \tag{2.8}$$

$$y = 0.00363 \cdot x - 0.726 \quad (\mathrm{r}^2 = 0.99, \delta^{2}\mathrm{H}) \tag{2.9}$$

where:

x : Standard water isotopic values at 0.4 µl.
y : Coefficient A of fitted logarithmic functions.

The above results are very similar to the phenomena observed by de Graaf et al. (2020). Due to variations in system design and heating temperatures, our fitting results and coefficients, however, differ from theirs. Given that the deviations in isotopic values are systematic and follow a predictable pattern, isotopic values volume corrections can be implemented using this calibration approach.

The whole idea of the calibration is to add to the original isotope values a variable n :

$$n = \frac{a \cdot \delta_{\text{raw}} + b}{(\log(0.4) - \log(\mu))^{-1} - a} \tag{2.10}$$

where:

a : Slope of the fit between the isotope ratios measured at 0.4 µl.
b : Intercept of the fit between the isotope ratios measured at 0.4 µl.
$log(\mu)$: logarithm function of water volume.

Substituting the parameters in Eq. 2.8-2.9 for:

$$n = \frac{0.00688 \cdot \delta_{\text{raw}} + 0.403}{(\log(0.4) - \log(\mu))^{-1} - 0.00688} \quad (\delta^{18}\text{O}) \tag{2.11}$$

$$n = \frac{0.00363 \cdot \delta_{\text{raw}} + 0.726}{(\log(0.4) - \log(\mu))^{-1} - 0.00363} \quad (\delta^{2}\text{H}) \tag{2.12}$$

The final correction equation can be expressed as C_d in Eq. 2.13

$$C_d = R_d + n \tag{2.13}$$

where

C_d : The corrected isotope value
R_d : Raw isotope value.
n : The corrected variable calculated by Eq. 2.11-2.12.

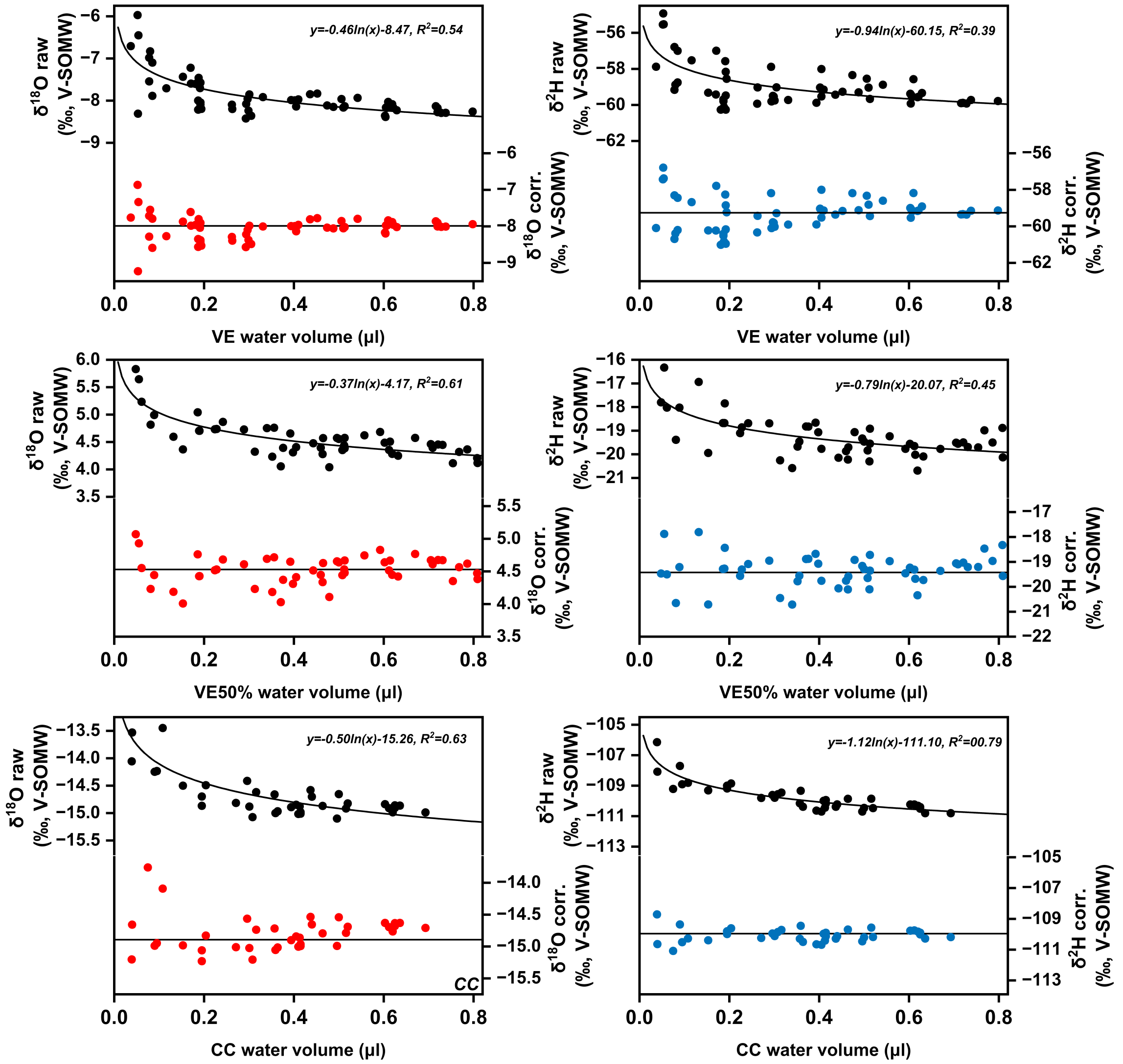

Figure 2.4. Result of the volume effect correction for isotopic values. The black dots indicate raw isotopic values and red and blue dots indicate corrected δ^{18}O and δ^{2}H values. The results show that the logarithmic trend of the isotopic values is removed.

This correction process can be implemented in Python using the Jupter script for adjusting the drift of isotope values (Supplementary Jupyter script in Supplementary Information B.1). The calibration results indicate that the deviation trends of δ^{18}O and δ^{2}H values for the three standards have been significantly corrected, bringing them closer to the expected values (Figure 2.4).

Overall, through extensive standard water injection measurements, the water volume dependence of isotopic results below 0.5 µl water volume (Eq. 2.2-2.7) and the deviation is related to the isotopic values of the samples (Eq. 2.8-2.9). The newly developed calibration process can effectively eliminate the deviation trends in isotopic values under low water volumes, particularly for volumes smaller than 0.4 µl, thereby improving the accuracy of isotopic measurements, and improving the measurement range from 0.5 - 2 µl to 0.1 to 2 µl. This performance is comparable to other measurement platforms developed using IRMS and CRDS under vacuum or wet background conditions (Affolter et al. (2025) and their references), with notably improved precision for low water volume samples, particularly those below 0.3 µl.

2.4.3 Long-term Stability

Over the past three to four years, the regression equations relating CRDS isotope measurements to reference values have been updated biannually. The linear regression relationship has remained nearly constant across different periods, highlighting the long-term stability of the system (Figure 2.5). Regarding water volume, measurements over the past three years have consistently reflected the volume of water in the capillaries (Table 2.2). These findings demonstrate that the HD line maintains exceptional stability, enabling precise measurement of both water volume and isotope values without the need for calibration for several months or even years.

Dates	Filled water volume (µl)	Measured water volume (µl)
08/02/2022	2.67	2.69
29/06/2022	1.84	1.90
01/09/2022	0.76	0.79
02/06/2023	1.43	1.48
20/11/2023	1.62	1.69
07/03/2024	1.25	1.30
09/07/2024	1.99	2.00
09/08/2024	1.46	1.47

Table 2.2. Results of glass tube filled water volume and measured water volume at different times for HD line.

According to the original analysis protocol, three speleothem samples can be analyzed in a standard working day (Weissbach et al., 2023), accounting for both the instrument startup time in the morning and the time required for sample changes. However, the daily measurement efficiency at Heidelberg is relatively low compared to other CRDS-based systems, primarily due to two factors.

The first is the size of the mixing cavity used to mix the sample and background water vapour. The mixing cavity offers two primary advantages. First, it extends the measurement time of the sample, enhancing stability. Currently, the 400 ml mixing cavity extends

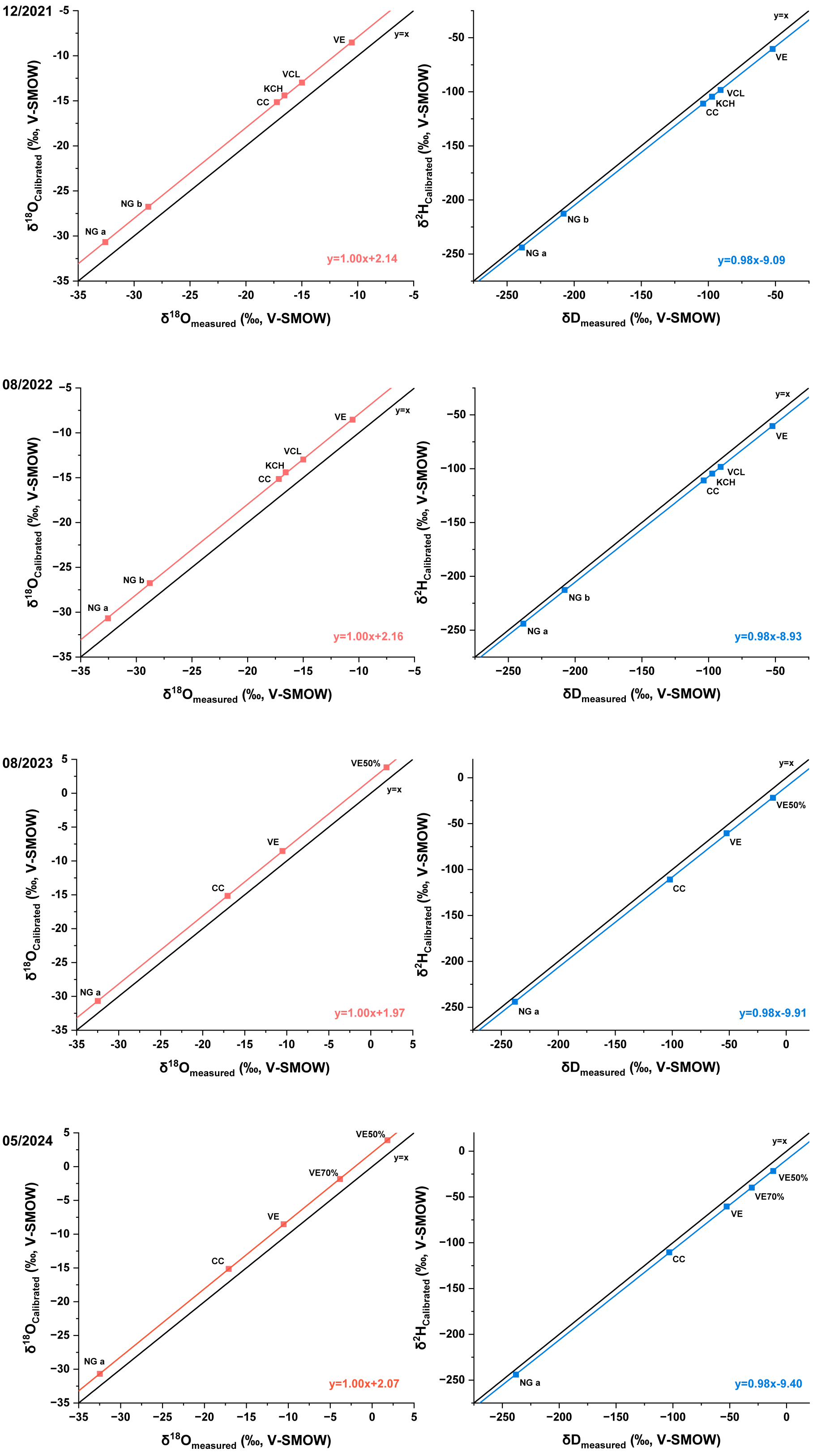

Figure 2.5. Results of a linear fit between $\delta^{18}O$ (left) and $\delta^{2}H$ (right) measurements and calibration values for HD line at different periods ($r^2 = 0.99$). The results show that the linear relationship between the isotopic measurements and the calibration values of the HD line remains stable over time.

the measurement time to between 30 minutes and 1 hour, depending on the amount of water released. Second, it improves measurement accuracy. During sample evaporation, lighter isotopes reach the CRDS quickly via airflow, in less time than the 0.8-second interval between CRDS recording points. A smaller mixing cavity may result in the loss of some isotopic signals. However, large mixing cavities also have drawbacks. A larger cavity increases the background disturbance time caused by loading the sample, leading to longer waiting times before crushing. For example, with a 400 ml mixing cavity, the waiting time is approximately 30–60 minutes. Prolonged heating can cause inclusion water to leak and undergo isotopic fractionation due to evaporation (see Chapter 3). The dynamics of isotopic exchange during mixing can also affect the final measurement results, a phenomenon known as the background effect. Larger mixing cavities result in longer mixing times between sample vapor and background vapor, which may amplify the influence of background isotope values, particularly when there is a significant difference between the sample and background isotopic values or when the sample volume is very small. Therefore, selecting an appropriately sized mixing cavity is crucial for ensuring accurate sample measurements while minimizing heating and background effects.

The second consideration is the current analysis protocol. According to the established protocol, it is crucial to maintain stable water vapor background with a standard deviation no greater than 20 ppmv before crushing or injection. After completing the sample measurement, a new sample cannot be immediately replaced within the following 20 minutes. This is because the average water vapor and isotope background values during the 20-minute intervals before and after the sample measurement are used to generate a regression curve, which calculates the integral area of the sample signal. The 20-minute interval ensures the optimal probability and stability for the best fit. However, when accounting for the stable background periods before and after, in addition to the sample measurement time, the total measurement time per sample exceeds one hour.

To improve the efficiency of single-sample measurements, shortening the stable background period before and after measurement may be a feasible approach. For example, reducing this period from 20 minutes to 10 minutes while simultaneously decreasing the allowable standard deviation of water vapor background fluctuations from 20 ppmv to 10 ppmv could enhance stability within a shorter timeframe. This adjustment may preserve the original measurement accuracy and precision while minimizing heating duration and overall measurement time per sample, thereby improving daily measurement efficiency.

Building on the two aforementioned considerations, the measurement line and analysis protocol were optimized. First, the mixing cavity volume, responsible for blending sample and background vapour, was reduced from 400 ml to 100 ml. Secondly, the background stabilization time before and after measurement was reduced from 20 to 10 minutes, alongside a decrease in the allowable standard deviation of water vapor background fluctuations from 20 ppmv to 10 ppmv. These modifications ensure sufficient sample-background mixing and stable background conditions while simultaneously minimizing sample heating and background isotope influence. Comparisons between the new mixing cavity and measurement protocol with previous results confirmed that isotope value accuracy and precision remained consistent.

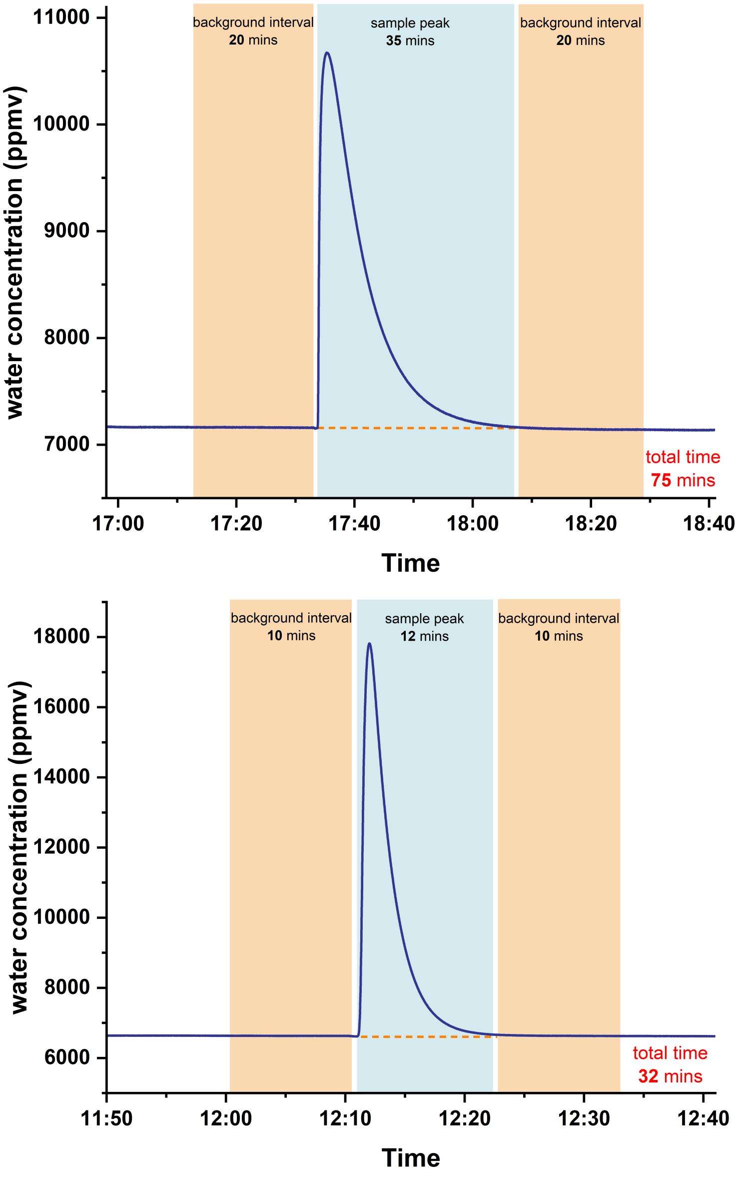

Figure 2.6. Comparison of measurement times of the improved mixing cavity and analysis protocol for a single sample (1 µl). On the top is the total measurement time (75 minutes) for a single sample (1 µl) with a large mixing cavity (400 ml) and a 20-minute background stabilization time. On the bottom is the total measurement time (32 minutes) for a single sample (1 µl) with a small mixing cavity (100 ml) and a 10-minute background stabilization time.

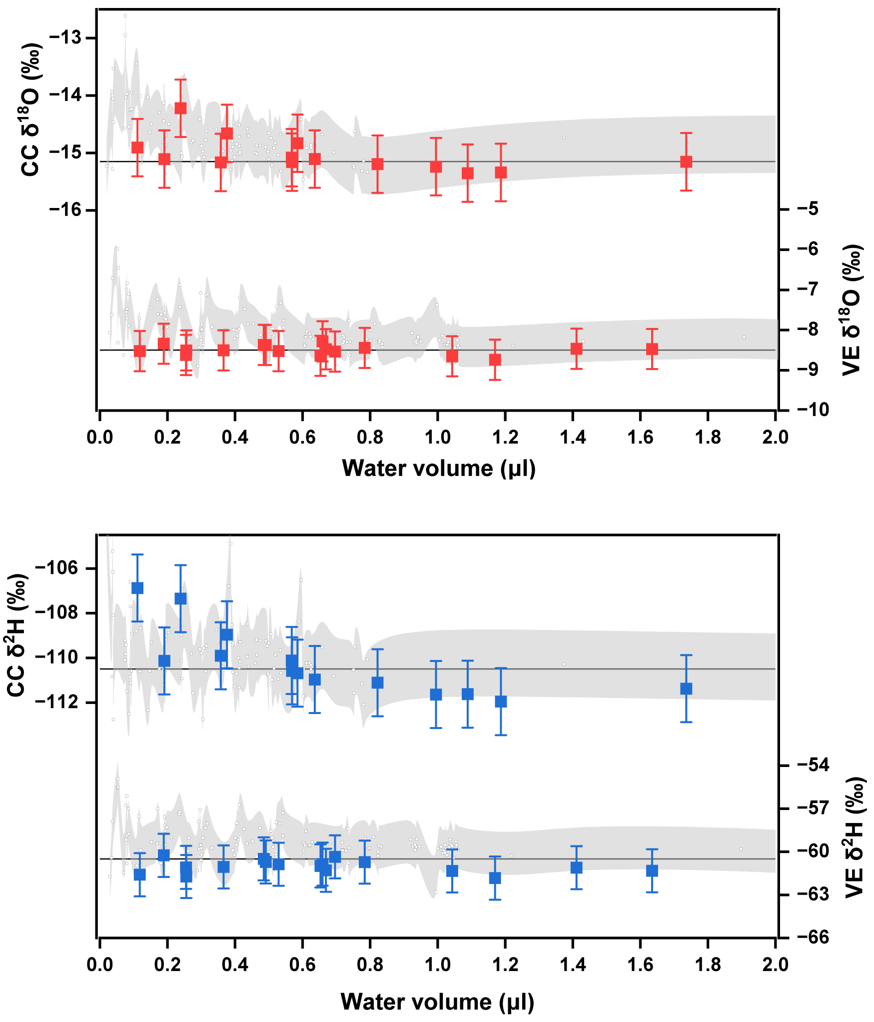

Figure 2.7. Results of isotope measurements of two standard waters, CC and VE, using a 400 ml (left) and 100 ml (right) cavity. The white square dots and grey bars indicate isotope values and their errors measured using the 400 ml cavity. The red and blue data points indicate the isotope values and their errors measured using the 100 ml cavity.

The first aspect considered is the measurement duration per sample and the overall daily analysis efficiency. The results indicate that using a 1 µl sample volume with a 100 ml mixing cavity and a 10-minute background stabilization period significantly reduced the total measurement time per sample (Figure 2.6). Specifically, compared to the previous setup with a 400 ml mixing cavity and a 20-minute background stabilization period, the total measurement time decreased from 70–80 minutes to 30–40 minutes (Figure 2.6). In addition, the required sample heating duration was reduced from 30–60 minutes to 20–30 minutes, which mitigated the evaporation of water from the inclusions in the sample and isotope fractionation. Overall, the number of samples that can be analyzed per day has more than doubled—from three in the previous setup to six or more under the optimized conditions, considering the waiting time required for background stabilization after opening the system.

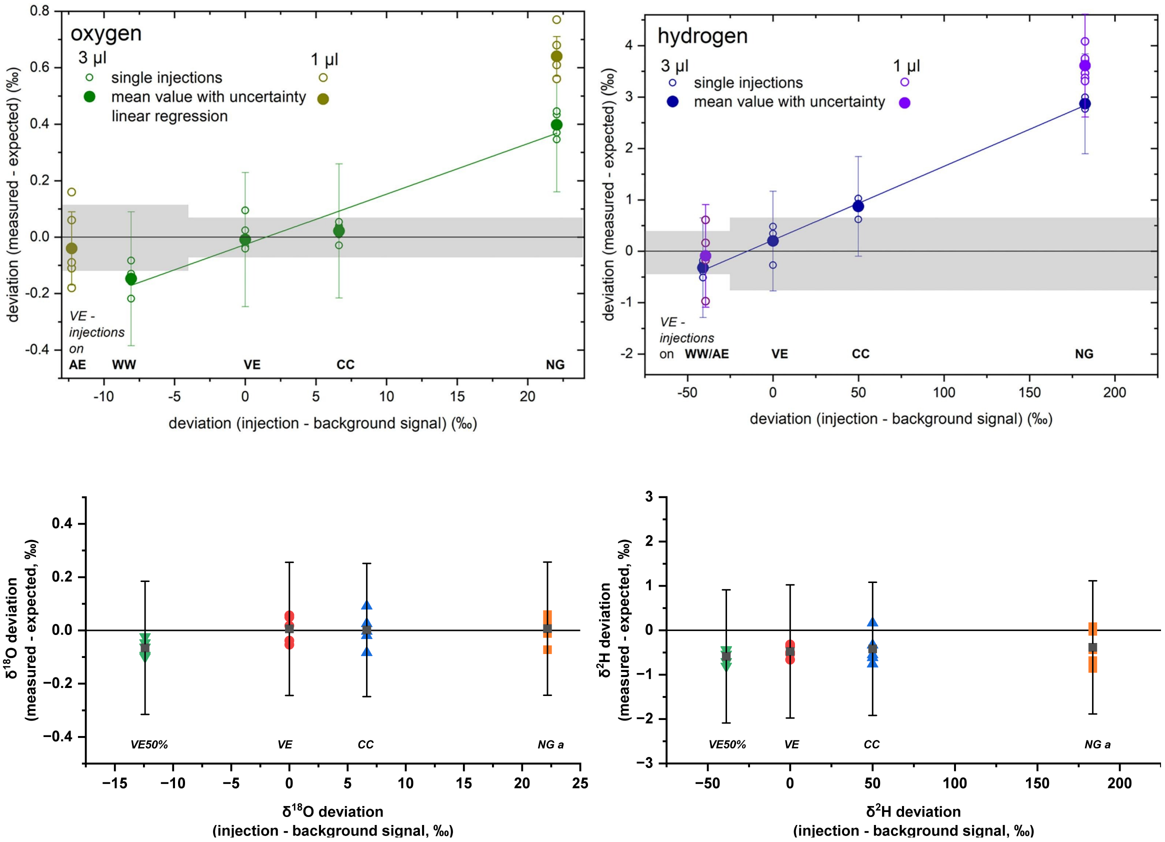

Figure 2.8. Deviation of measured injection isotope values relative to expected values. The top plot represents measurements for a 400 ml mixing cavity (Weissbach et al., 2023) and the bottom for 100 ml. The different shapes and colors of the points indicate the results of single injection (1 µl) measurements of VE standard water in different water backgrounds. The black dots and error bars indicate the mean value and its uncertainties. The results show that the measurements with the 100 ml mixing cavity do not show significant isotopic background effects.

Secondly, regarding the accuracy of isotope value measurements, the 100 ml mixing cavity and the revised analysis protocol yielded isotope values for the two standard waters (VE and CC) that were consistent with previous results within the margin of error (Figure 2.7) (Table S2.2 in Supplementary Information B.1). The repeatability of isotope measurements also showed no significant difference from the previous setup and even improved under the new conditions, particularly for low water volumes (Figure 2.7).

Finally, regarding background interference, prior research by Weissbach et al. (2023) indicated that significant discrepancies between the isotope values of sample water and background vapor could lead to measurement deviations due to isotopic kinetic effects (Figure 2.8). As the difference between the injected and background isotope values increases, the deviation between the measured and expected isotope values also grows (Figure 2.8) (Table S2.3 in Supplementary Information B.1). It was recommended that the differences in δ^{18}O and δ^{2}H values between the sample and background should not exceed 10‰ and 50‰, respectively. However, such background effects are less pronounced in a smaller mixing cavity, even when there is a considerable isotopic difference between the sample and background (Figure 2.8). This reduction in interference is likely due to the shorter mixing time between sample water vapor and background vapor in a smaller cavity, which significantly mitigates the background effect.

In summary, the implemented improvements have enhanced analytical efficiency while preserving the original measurement accuracy and precision. The use of a smaller mixing cavity (100 ml) and a shorter background stabilization time (10 mins) has reduced both measurement and heating durations for individual samples, helping to prevent water evaporation and isotopic fractionation during the preheating of fluid inclusions. Additionally, these modifications improve the accuracy and repeatability of isotope measurements in low-water conditions and mitigate background interference.

2.5 Conclusions and Significance

Measurements by Weissbach et al. (2023) demonstrated the stability of the newly developed fluid inclusion HD line at water volumes exceeding 0.5 µl. However, their assessment of isotope value deviations at lower water volumes remained inconclusive. Based on the analysis and improvements in this section, the following conclusions can be drawn:

(1) The isotope values measured by the HD line systematically deviate from expected values following a logarithmic trend as water volume decreases, with a concurrent decline in measurement repeatability.

(2) The observed trend in isotope value deviation can be corrected through a calibration process, thereby optimizing analytical performance at low water volumes.

(3) The HD line exhibits excellent long-term stability within uncertainty of calibration. By refining the analytical protocol and optimizing the sample mixing cavity, measurement efficiency has been increased while maintaining high accuracy and precision. These improvements also reduce sample heating time and minimize the influence of background water vapor.

Chapter 3

Environmental and Calcification Impacts On the Oxygen and Hydrogen Isotope Composition of Cold-Water Coral Skeleton Fluid Inclusions

Key Points:

- **High-temperature heating during coral skeleton inclusion analysis produces significant kinetic isotope fractionation.**
- **Enclosing a coral sample in glass tubes prevents continuous water loss during measurement and significantly reduces isotopic variance.**
- **Extracted water has a strong hydrogen isotope fractionation signature, but the origin of the water remains uncertain.**

Coral skeletons serve as valuable archives for reconstructing past marine environments, offering precise chronologies and high resolution. The hydrogen and oxygen isotopic compositions of skeleton inclusion water provide insights into paleo climate and paleo oceanographic changes. However, analyzing these isotopes is challenging due to the influence of analytical methods and evaporation temperature on the measurements. This chapter introduces an improved method, where coral fragments are encapsulated in glass tubes prior to crushing, yielding more reliable results with reduced isotope fractionation. No significant differences in δ^{18}O or δ^{2}H values are observed between Holocene and Last Glacial period samples. Compared to surrounding seawater, cold-water corals exhibit δ^{2}H values that are approximately 50‰ lower, while δ^{18}O values remain relatively unchanged. Additionally, immersion experiments suggest some water in coral skeletons may exchange with external water.

Part of the dataset used in this chapter is derived from the bachelor theses of Dana Hölkermann and Amrei Grund, which I co-supervised. They measured a portion of the samples and provided an initial description and discussion of the dataset in their theses. In this study, I reanalyzed the data and evaluated the reliability of the glass tube encapsulation method, as well as the isotopic fractionation behavior of the samples. The results confirm that the proposed method significantly improves the reliability of the measurements. These contributions are central to this chapter. Based on this work, I have written a manuscript, which has been accepted for publication in *Geochemistry, Geophysics, Geosystems* (https://doi.org/10.1029/2024GC011981). The co-authors include Dana Hölkermann, Amrei Grund, Dr. Sophie Warken, and Prof. Dr. Norbert Frank. Dr. Sophie Warken reviewed the manuscript, Prof. Dr. Norbert Frank conceptualized and supervised the research. This chapter represents the published content, with the supplementary material placed as Section B.2 Supplementary Information for Chapter 3. Additionally, to ensure a smooth flow in the main text, the tables from the original manuscript have been included as supplementary tables in the supplementary material.

3.1 Introduction

Biogenic carbonate skeletons contain water at levels up to 2.5% of the total weight of the skeleton (Cuif et al., 2004; Gaffey, 1988). Water in coral skeletons can exist in various forms, including the hydration water associated with organics, free water trapped in fluid inclusions, water absorbed on the surface, and water potentially derived from metabolic processes (Cuif et al., 2004). Heating experiments have revealed that major water loss at 275° - 330 °C is linked to the dehydration of skeleton organic materials (Cuif et al., 2004). Extractable amounts of skeleton water (about 0.1% weight), here identified as extractable skeleton inclusion water or inclusion water, may evaporate at temperatures much lower than 100 °C (Cuif et al., 2004; de Graaf et al., 2022; Krief et al., 2010; Nooitgedacht et al., 2021). The hydrogen and oxygen isotopic compositions of such skeleton inclusion water can provide information on the fluid trapping process, calcification, or paleoenvironment (de Graaf et al., 2022). However, assessing the isotopic composition of the initial coral skeletal water remains very difficult. One aspect of this challenge stems from extracting coral skeletal inclusion water and accurately analyzing its hydrogen and oxygen isotopic compositions without fractionation (Cuif et al., 2004; de Graaf et al., 2022; Nooitgedacht et al., 2021; Pederson et al., 2019). Second, our understanding of how coral physiology affects the isotopic composition of skeletal inclusion water remains unclear. Corals precipitate their skeletons from a semi-isolated extracellular calcifying fluid (ECF), also known as the calcifying medium or subcalicoblastic space (Tambutté et al., 2011; Venn et al., 2011). This thin fluid layer, located between the skeleton and calicoblastic epithelium, is spatially separated from seawater and actively regulated in pH and ion concentrations (Allemand et al., 2011; Tambutté et al., 2011). Elevated pH and carbonate ion levels within the ECF promote aragonite precipitation and enable calcification even under suboptimal external conditions (Allemand et al., 2011; Tambutté et al., 2011). Understanding ECF chemistry is essential for interpreting skeletal geochemical proxies and coral responses to environmental change (Sevilgen et al., 2019). Corals use a calcifying fluid to synthesize their skeletons. This fluid contains various dissolved ions and chemical components, primarily calcium and carbonate ions. Coral physiology thus impacts the composition of the calcifying fluid from which the skeleton is precipitated (Cohen and Gaetani, 2006; Cohen et al., 2006; Cuif and Dauphin, 2005; Dever et al., 1982; Rollion-Bard et al., 2010; Wefer and Berger, 1991)

Early studies, such as Lécuyer and O'Neil (1994), measured the hydrogen and oxygen isotopic compositions of skeletal inclusion water in 11 marine and freshwater biogenic skeletal carbonates by thermal decrepitation, and the results differed considerably from those of the seawater in the surrounding environment. Over the past decade, measurement setups based on CRDS and IRMS have been widely used to effectively determine the water volume and hydrogen and oxygen isotopic compositions of fluid inclusion water from stalagmites (Affolter et al., 2014, 2019; de Graaf et al., 2020; Uemura et al., 2016; Vonhof et al., 2006; Warken et al., 2022; Weissbach et al., 2023). Recently, de Graaf et al. (2022) measured the hydrogen and oxygen isotopic compositions of inclusion water in coral skeletons using three analytical methods developed on the basis of CRDS and IRMS. The findings of de Graaf et al. (2022) indicate difficulties in obtaining accurate, reproducible, and unfractionated hydrogen and oxygen isotope results of the initial fluid of coral skeletons using these measurement setups and methods. First, water loss due to the heating of coral fragments prior to crushing results in significant isotopic fractionation de Graaf et al. (2022).

Second, coral skeletons are permeable, and internal water may be overprinted by external water. It remains unclear whether there are multiple pools of internal water, some of which are easily exchangeable and others are not. For example, when coral skeletons are submerged for several days (72 hours), the initial water is almost entirely replaced, and the final isotopic results reflect the isotopic composition of the water they were immersed in de Graaf et al. (2022). Therefore, the initial water may not be adequately preserved. Even if there is no significant loss of water, under prolonged heating conditions at high temperatures (175 °C for 90 min), there is a possible exchange of oxygen isotopes between biogenic aragonite carbonates and inclusion water, which results in an increase in the isotopic value of the inclusion water (about 4-6‰) (Nooitgedacht et al., 2021). These observations call into question the feasibility of extracting information on the isotope ratios of initial inclusion water from coral skeletons.

Water loss and isotope fractionation strongly depend on different measurement systems and heating techniques. Isotope fractionation through continuous water loss may be reduced or avoided by improved methods, or data may be artifact-corrected on the basis of reliable skeleton inclusion water isotope reconstructions. This dissertation aims to advance the understanding of coral skeleton inclusion water using techniques well established for speleothem fluid inclusion isotope studies (Warken et al., 2022; Weissbach et al., 2023). The origin of artifacts in coral skeleton inclusion measurements was explored, along with methods to avoid these artifacts in cold-water coral measurements. Furthermore, the potential for linking hydrogen and oxygen isotope results from coral skeleton inclusion water, produced by current measurement methods, to environmental changes and coral calcification processes was assessed.

3.2 Material and Methods

3.2.1 Study Area and Sample

This study examined cold-water coral samples collected from two distinct locations: Iceland and Angola (Figure 3.1). All the corals collected belong to the species Desmophyllum pertusum, which is a cosmopolitan deep-sea species found in the modern ocean. The analysis utilized only one sample from Iceland (ICEFI), which grew in modern times. This sample was obtained during the ICECTD cruise on June 25th, 2012, from Reykjanes Ridge at a depth of 685 m. The local conditions at the sampling time included a temperature of 5.84 °C, a salinity of 35.06 psu, and an oxygen content of 6.94 ml/l in the seawater. In Angola, samples were retrieved from the Valentine Mound at 338 to 457 m water depth during the M122 ANNA cruise in January 2016. The detailed ^{230}Th/U dating results for each coral sample are shown in Table S3.1 in Supplementary Information B.2. These fossil corals are from either the Holocene or the last glacial period. The sampling area in Angola presented temperatures ranging from 7.8 °C to 8.5 °C, with significantly lower oxygen levels ranging from 0.8 to 1.1 ml/l, which was attributed to the high productivity and hypoxic conditions in the upwelling region of Angola (Figure 3.1). The collected corals were stored dry for preservation. The corals were well preserved, with occasional minor surface coverage of sediment and tissue. Prior to measurement, the corals were mechanically cleaned using a handheld Dremel tool to remove any noncarbonate coating or other substances. The cleaned coral samples were then cut into small pieces for measurement. The weight of the coral fragments used for each measurement ranged from 0.5–1.0 g (Table S3.2 and S3.3 in Supplementary Information B.2). Because coral aragonite is suspected to be highly permeable, internal water may be exchanged with outside water (see Section immersion experiment), so the samples were kept dry throughout cleaning and cutting.

3.2.2 Measurement Method

Measuring Devices and Processes

Hydrogen and oxygen isotope ratio measurements were carried out on a CRDS-based instrument using a Picarro L2130-i analyzer at the Institute of Environmental Physics, Heidelberg University (Weissbach et al., 2023). The line is equipped with a device that mechanically crushes the coral samples to analyze the released water in the spectrometer. A constant background water vapor flow was maintained throughout the line at 120 °C. Standard water of known isotopic composition was mixed with dry carrier gas (nitrogen) and pumped into the line. This makes the system less susceptible to disturbances such as memory effects (Affolter et al., 2014). Water volume calibration was performed by measuring capillaries with known water volumes and establishing a linear relationship between the CRDS-measured time-integrated water vapor signal (ppmv·s) and the water volume (Weissbach et al., 2023). The accuracy of measurements using water injections and water-filled glass capillaries crushed in the system has been demonstrated to be better than 0.08‰ for δ^{18}O values and 0.3‰ for δ^{2}H values. In terms of precision, the measurements exhibit values of $\delta^{2}\mathrm{H} \leq \pm 1.5‰$ and $\delta^{18}\mathrm{O} \leq \pm 0.5‰$ (Weissbach et al., 2023).

For the measurement procedure, pieces of the coral skeleton were placed inside a copper tube and fixed with glass wool. The copper tube was then connected to a part of the measurement line located in an oven, which was heated to 120 °C. Since this step required opening the oven door, ambient air and water could enter the system and disturb the background equilibrium. When the system reached stable conditions again, which was determined from the standard deviation of the measured isotope values of the water vapor background, the

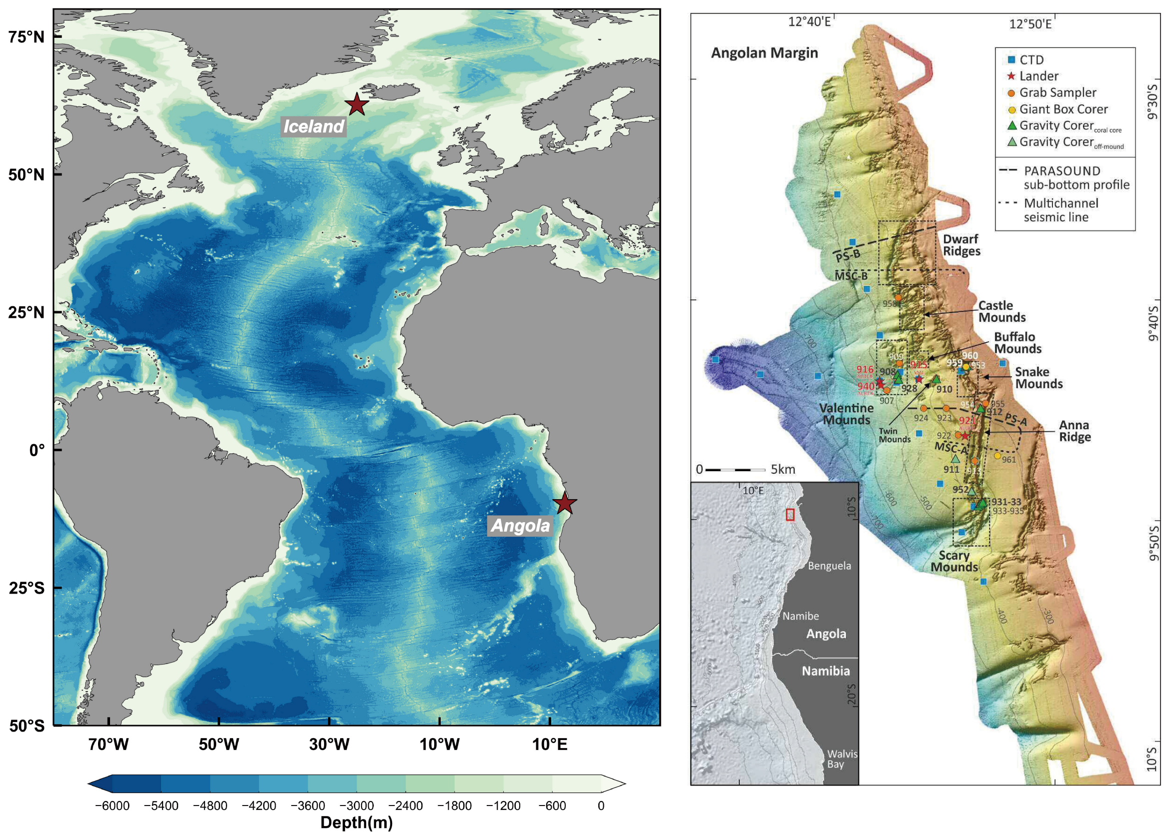

Figure 3.1. Location of the study area. Location of the study area. In the figure on the left, the dark red stars indicate the research sites for this study. Bathymetric data from the ETOPO 2022 60 Arc-Second Global Relief Model (NOAA National Centers for Environmental Information. (https://doi.org/10.25921/fd45-gt74)). The figure on the right shows a map overview of the Angola cold-water coral mound area; the sampling positions are indicated (GeoB20xxx), and the measured samples originate from Scary Mounds (Hebbeln et al., 2017).

copper tube and, thus, the sample were crushed using a hydraulic hand pump. Under normal conditions, perturbations in the water and isotope backgrounds due to the line being open to load the sample normalized within 20–30 minutes (the standard deviation of the water vapor concentration over 20 minutes was less than 20 ppmv) (Figure S3.1 in Supplementary Information B.2). However, additional perturbations in the water and isotope backgrounds result if the sample continues to release water due to heating (Figure S3.1 in Supplementary Information B.2). Therefore, inspection of the water and isotopic background variations after a sample is loaded can help detect if there is significant water leakage from the sample. The standard heating time for samples was 40–60 minutes, but the heating time was in some cases longer in order to wait for the background to stabilize owing to the background perturbations introduced by samples not measured in glass tubes. The number of Angora corals measured using the above method is n=11. The remaining samples were measured in glass tubes using the method described in Section “Measurements in glass tubes”.

Fractionation Experiment

Previous studies have reported variations in coral skeleton inclusion water isotope ratios depending on the preheating time of the samples in the oven prior to crushing and subsequent measurement (de Graaf et al., 2022; Nooitgedacht et al., 2021). The first experiment on the modern sample ICEFI was designed to understand the effect of preheating time on water release from the skeleton. In this experiment, 10 subsamples were selected from this branching coral (Figure S2 in Supplementary Information B.2). Seven of the samples were loaded into the line and heated in the oven for 30 to 150 minutes prior to the δ^{18}O and δ^{2}H isotope measurements. The measurement procedure for these samples was the same as that described in Section “Measuring devices and processes”, except for the use of different heating times. The remaining three samples were enclosed in glass tubes for measurement for comparison (see Section “Measurements in glass tubes”).

Measurements in Glass Tubes

To prevent preheating water loss into the system, a new sample hosting technique was developed. Instead of placing the samples in open copper tubes, they were inserted into glass tubes and tightly sealed by melting the glass tube’s open ends, as shown in Figure S3 in Supplementary Information B.2. One end of the glass Pasteur pipette was first melted using a flame, and the pipette was then preheated in the flame to prevent any potential water vapor adsorption on the surface of the glass walls. The coral fragments were then quickly inserted into the pipette, and the other end was sealed by melting it with the flame. The flame was always kept at least 1 cm away from the sample to prevent heating of the sample. After the sealing process, the glass tube was visually inspected for any cracks or unsealed sections at both ends. In this way, any water vapor that might evaporate during exposure to heat in the oven would be captured and accumulate in the glass tube and released only when crushed together with the remaining inclusion water in the crushed sample. Except for sealing the coral fragments in glass tubes, the remaining measurement steps and parameters are consistent with those described in Section “Measuring devices and processes”. The numbers of Angola corals and Icelandic corals measured using the glass tubes are n=30 and n=3, respectively.

Adsorption of atmospheric water on the sample surface may occur before the sample is loaded into the line. In the absence of a glass tube, the adsorbed water evaporates at high temperatures and thus has no influence on the measurement results after crushing. The sample measured in the glass tube, however, may not be able to release water adsorbed on the surface of the sample efficiently because of the enclosed space, or the air trapped in the glass tube may also influence the measurement results. Therefore, an additional blank experiment was designed to rule out the potential impact of atmospheric water vapor trapping. Glass tubes were loaded with waterless Iceland spar and a capillary filled with laboratory internal standard water ($\delta^{18}O$ = -8.53‰, $\delta^{2}H$ = -60.41‰), which was prepared from deionized tap water, to simulate real sample measurements. The surface properties of Iceland spar are recognized to be different from those of cold-water coral skeletons, potentially introducing bias into the blank experiment. This compromise was chosen because it is not feasible to assume that there is no water present in the coral skeleton. For example, water associated with the hydration of organics is dispersed in the coral skeleton and is difficult to remove by heating at approximately 100 °C. Even though drying at very high temperatures may remove inclusion water from the coral skeleton, it will alter the aragonite structure of the coral and its water absorption capacity. Thus, in the absence of a water-free coral, dry Iceland spar seems to be a reasonable alternative for quantifying whether or not external water can be adsorbed in the process.

Immersion Experiment on Coral Skeleton Inclusions

To assess whether inclusion water in coral skeletons can be entirely replaced by surrounding seawater or pore water after formation, an immersion experiment was performed. This approach also allowed for the investigation of whether the water in the exchangeable water pool of the coral skeleton evaporates and is removed after being separated from the seawater. A total of three coral skeleton samples were used in the experiment. Each sample was specifically taken from a single branch to ensure consistency in subsampling. The first and second samples were modern corals from Angola, labeled A and B, respectively. Each of these samples was divided into two subsamples: the first subsample was measured without immersion and was not subjected to additional drying (labeled NimA and NimB), whereas the second subsample was immersed and dried before measurement (labeled imA and imB). The third sample was a fossil coral skeleton from Angola, labeled C. This sample was divided into three subsamples: the first subsample was measured without immersion (NimC), and the second and third subsamples were measured after immersion and drying (imC1 and imC2). The experiment consisted of two parts. In the first part, imA, imB and imC1, each weighing approximately 2 grams, were immersed in seawater collected from the Angola coral sampling site. The $\delta^{18}O$ and $\delta^{2}H$ values of this seawater were -0.08‰ and -0.49‰, respectively. The immersion time was 5 days. After immersion, the coral samples were retrieved, mechanically cleaned to remove surface impurities, and then dried at 60 °C for 24 hours before being measured. In the second part of the experiment, imC2 was subjected to a longer immersion treatment, with an immersion time of 34 days. This sample was then heated at 60 °C for 7 days before measurement. All the samples were analyzed according to the methods described in Section "Measurements in glass tubes". Detailed information on the immersion times, drying temperatures and times of the coral samples can be found in Table S3.4 in Supplementary Information B.2.

3.3 Results

3.3.1 Fractionation Experiment

The heating time experiment using seven aliquots of the ICEFI coral (without using glass tubes) yielded water contents between 1.3 and 2.0 µl/g. Significant correlations are found between the heating time of the samples and the measured δ^{18}O and δ^{2}H values at $r = 0.71$ and 0.72 ($p<0.05$), respectively. Longer heating times, such as 150 and 120 minutes, tended to produce heavier isotopic values (Figure 3.2). The δ^{18}O and δ^{2}H values of the released skeleton inclusion water varied from -6.00‰ to 18.50‰ and from -58.07‰ to -32.90‰, respectively (Figure 3.2) (Table S3.2 in Supplementary Information B.2). The results of the blank experiments revealed that the isotope values from crushing the Iceland spar along with the standard water capillary were consistent with the expected values within the errors (Figure S4 in Supplementary Information B.2). Fluctuations in the water vapor and isotopic background of the measurement line were detected when measuring coral fragments that were not in the glass tube. After sample loading, the water concentration background initially increased steadily, forming a small, smooth peak before slowly declining (Figure S1 in Supplementary Information B.2). Even after 120 min of heating, the water background was greater than that before loading. Like the water concentration background, a significant negative isotopic peak occurred after the sample was loaded into the line, after which the isotopic background gradually returned to normal as water release decreased. These phenomena suggest that coral skeletons undergo continued water evaporation and isotopic fractionation during heating at 120 °C, whereas samples measured enclosed in glass tubes do not show these patterns.

The isotopic values of the three ICEFI samples measured in glass tubes exhibited significantly less variance and systematic shifts than those measured without glass tubes and at variable heating times, with δ^{18}O values 10‰-20‰ lower (-6.00-3.60‰) and δ^{2}H values 20‰-30‰ lower (-72.51-55.50‰). In the case of lower heating times (30 minutes), the isotope values measured both with and without the glass tube are significantly lower but can still differ (Table S3.2 in Supplementary Information B.2).

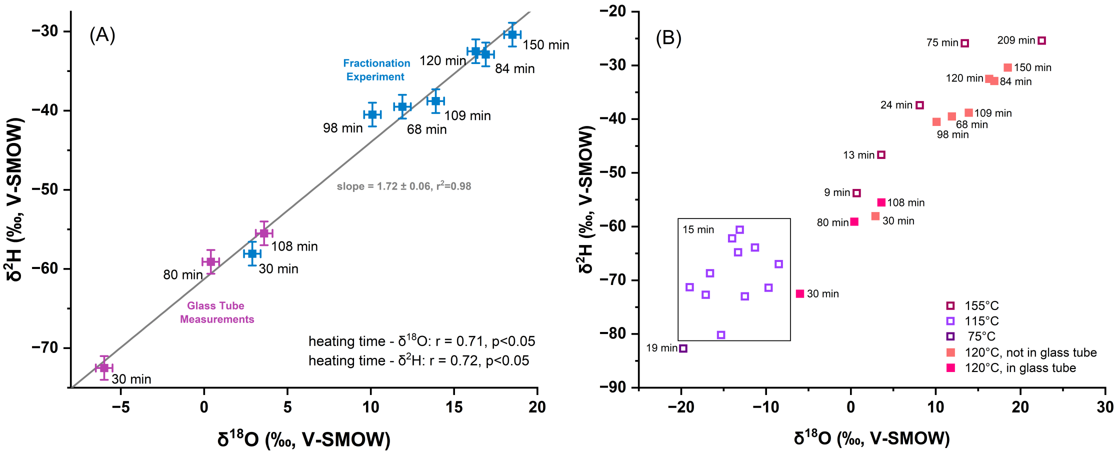

Figure 3.2. Stable isotope fractionation of coral skeleton inclusion water due to heating. (A) The blue dots indicate coral fragments not measured in the glass tube. The red dots indicate coral fragments measured in glass tubes. The gray line indicates a linear fit to all the data (slope = 1.72±0.06, r^2 = 0.98). The black numerical label indicates the heating time (120 °C). The correlations between heating time and δ^{18}O and δ^{2}H values are 0.71 and 0.72, respectively ($p<0.05$). The error bars indicate measurement errors. The errors for the δ^{18}O and δ^{2}H values are 0.5‰ and 1.5‰, respectively. (B) Comparison of the results of the Heidelberg heating experiment with the results from the de Graaf et al. (2022) heating experiment. The open square points indicate data from de Graaf et al. (2022). The square points indicate data from the Heidelberg heating experiment. The numerical labels indicate the heating time of the samples. The different colors indicate the temperature at which the coral fragments were heated.

3.3.2 Comparison of Measurements of Angola Corals With and Without Glass Tubes

Comparative measurements of Angola corals with and without glass tubes were performed to visually assess the influence of isotopic fractionation from heating on the δ^{18}O and δ^{2}H values of the coral skeletal inclusion water. All measurements are shown in Figure 3.3 and Table S3.3 in Supplementary Information B.2. The overall dataset can be divided into two subgroups. The first group consists of samples of Angola corals not measured in glass tubes. These data are characterized by high δ^{18}O and δ^{2}H values and very systematic variability, with variations of 21.71‰ (21.12‰ - 42.83‰) and 39.28‰ (-18.43‰ - 20.85‰), respectively (Figure 3.3). The second group includes Angola corals measured in glass tubes, with δ^{18}O values ranging from -3.92‰ to 8.07‰ and δ^{2}H values ranging from -80.30‰ to -57.92‰ (Figure 3.3). The δ^{18}O and δ^{2}H values for these samples are approximately 30‰

and 80‰ lower, respectively, than those of measurements conducted without the use of glass tubes.

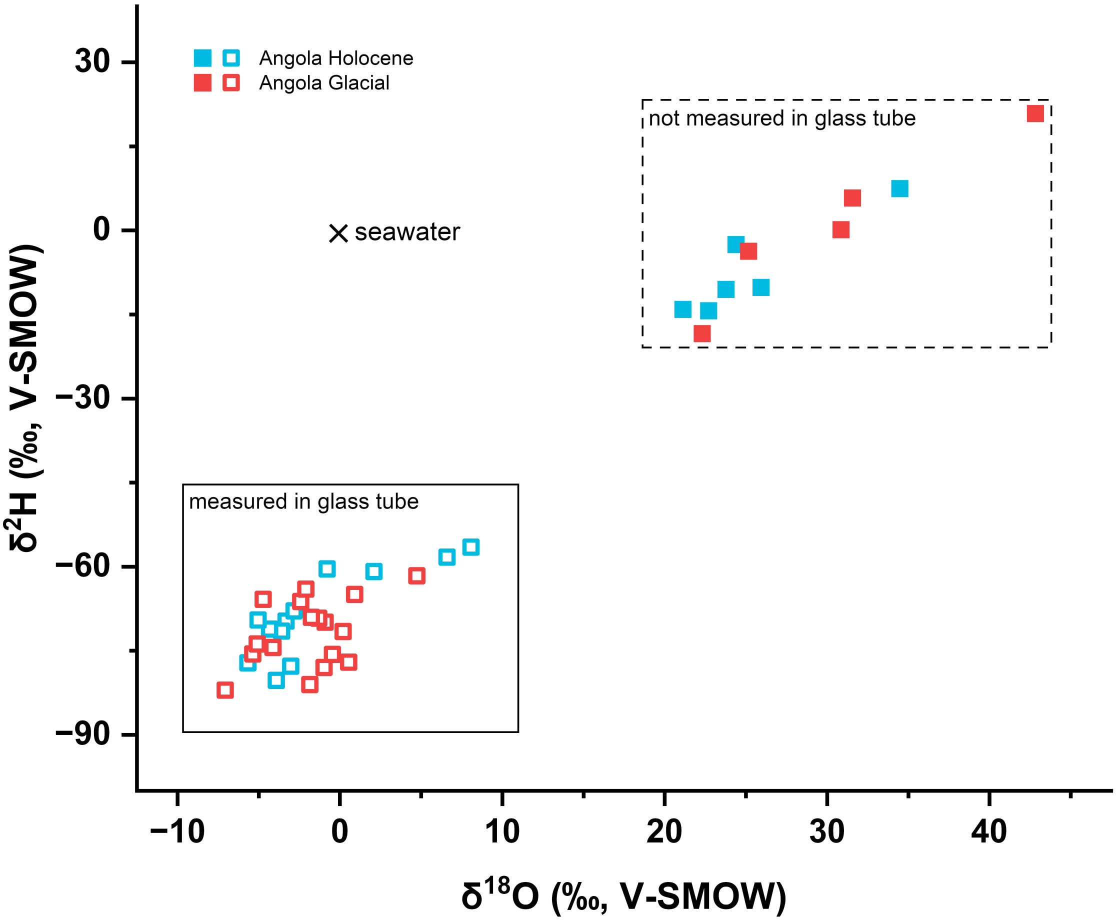

Figure 3.3. Measurements of coral samples from Angola over different time periods. The open square points indicate samples measured in glass tubes. The square points indicate samples not measured in glass tubes. The black X symbol indicates the isotopic values of seawater from the Angola coral fossil sampling sites (the values of δ^{18}O and δ^{2}H are -0.08‰ and -0.49‰, respectively). Cyan and red colors indicate coral samples from the Holocene and last glacial period, respectively. The heating times for each sample are presented in Table S3.2 and S3.3 in Supplementary Information B.2.

When exclusively considering samples measured in glass tubes, the temporal disparity in δ^{18}O and δ^{2}H values between the last glacial period and Holocene periods appears insignificant (Figure 3.4). The mean δ^{18}O values for the last glacial period and the Holocene are 0.15‰ and -0.15‰, respectively, and the mean δ^{2}H values are -66.90‰ and -71.53‰, respectively. The δ^{18}O values range from -5.67‰ to 8.07‰ (a total range of 13.74‰) for the Holocene samples, and from -2.40‰ to 4.73‰ (a total range of 7.14‰) for the last glacial period samples. The δ^2H values are 22.38 (-80.30‰ to -57.92‰) during the Holocene and 19.39‰ (-81.04‰ to -61.64‰) during the last glacial period (Figure 3.4). The magnitude of variation in δ^2H values shows no significant difference between the Holocene and last glacial periods (22.38‰ and 19.39‰). In contrast, the magnitude of variation in the δ^{18}O values during the Holocene seems greater than that during the last glacial period (13.74‰ and 7.14‰). The large range of Holocene δ^{18}O values is influenced primarily by a few high-value outliers, with most data points falling below the average of both the Holocene and last glacial period. In contrast, the glacial values are distributed closely around the mean of 0.15‰ (Figure 3.4).

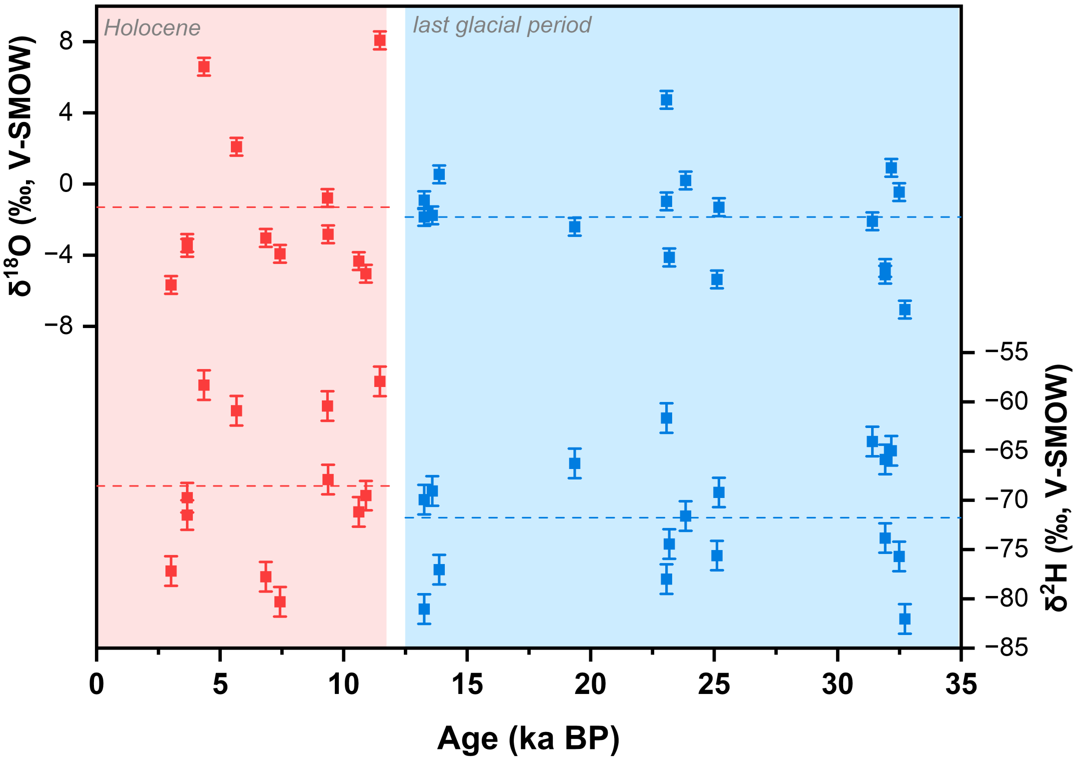

Figure 3.4. Holocene (red) and last glacial period (blue) inclusion water δ^{18}O and δ^2H results from Angola coral skeletons measured in glass tubes. The different colored dashed lines indicate the mean δ^{18}O and δ^2H values for the Holocene and glacial periods. The error bars indicate measurement errors. The δ^{18}O and δ^2H error values are 0.5‰ and 1.5‰, respectively.

In terms of water content, coral fragments measured without glass tubes present a relatively low water content and higher isotopic variance. For example, when the δ^{18}O and δ^2H values exceed 20‰ and -20‰, respectively, the water content is almost always less than 1 µl/g (Figure S5 in Supplementaryorting Information B.2). In contrast, the water content distribution in coral samples measured using glass tubes across ages during both the Holocene and last glacial period was dispersed with no systematic trends or significant differences.

3.3.3 Isotope Values of Inclusions in Coral Skeletons in the Immersion Experiment

In the immersion experiment, the four subsamples were immersed in seawater from the sampling site and then dried at 60 °C before measurement. The results show that the δ^{18}O and δ^{2}H isotope values of the coral skeleton inclusion water measured after immersion and drying were significantly higher than those of the not-immersed coral skeletons (Figure 3.5). However, the isotope values of the inclusion water in the coral skeleton after immersion and drying did not fully reflect or approach the isotope values of the immersion liquid (seawater) but instead exhibited a stable distribution along the fitted slope. Even for the samples with longer immersion times (such as imC2) (Figure 3.5), the higher isotope values observed after extended drying still followed the fitted slope.

3.4 Discussion

3.4.1 Fractionation of Coral Inclusions During Measurements

Previous studies have shown that coral skeleton water release processes are closely linked to temperature (Cuif et al., 2004). As the temperature increases, absorbed water evaporates (60–75 °C), followed by the free water in aragonite (100–150 °C) and, finally, a major release of organic hydrated water and decomposition of the organic matrix occur at higher temperatures (Cuif et al., 2004). de Graaf et al. (2022) conducted a heating experiment on coral samples using a CRDS-based fluid inclusion measurement setup to examine the effects of heating-induced diffusion and evaporation on the measured δ^{18}O and δ^{2}H values. These results suggest that the remaining water yields higher δ^{18}O and δ^{2}H values when coral samples have longer heating times. Owing to the use of a similar measurement setup, the results of our heating experiments are highly consistent with those of de Graaf et al. (2022). The longer heating and higher temperatures produced very high isotopic values and systematic variations (Figure 3.2). The anomalous fluctuations in water vapor and δ^{18}O and δ^{2}H backgrounds before the measurements attest to the persistence of this water evaporation and its resulting isotopic fractionation (Figure S1 in Supplementary Information B.2). Since our heating experiments kept the temperature stable (120 °C), a clear heating time dependence of the isotopic values is presented (Figure 3.2). Overall, the changes in the δ^{18}O and δ^{2}H values resulting from our heating experiments reached 24‰ and 42‰, respectively. In the

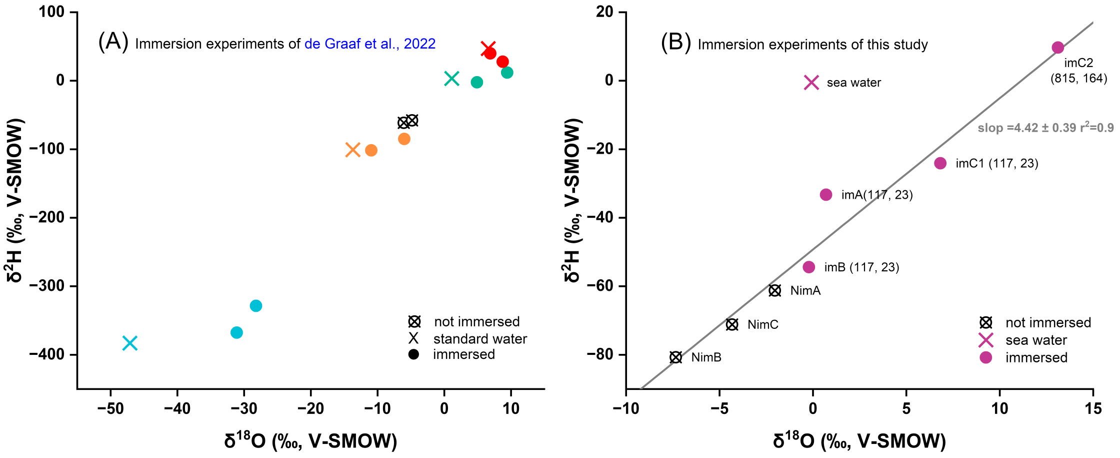

Figure 3.5. Isotopic results of the coral skeleton fluid inclusion immersion experiment. (A) Results from de Graaf et al. (2022). The gray circles and X-marked symbols represent the isotopic values of nonimmersed coral skeleton fluid inclusions. The colored X-mark indicates the isotopic values of the standard waters used for immersion. The colored circles show the isotopic measurements of the coral skeletons after immersion. More details are available in de Graaf et al. (2022). (B) Results from this study. The black circles and X-marked symbols represent the isotopic values of nonimmersed coral skeleton fluid inclusions (Nim). The purple circles show measurements after immersion and drying (im), with parentheses specifying immersion and heating durations (hr). The purple X symbols indicate the isotopic values of seawater from the sampling sites. The gray line represents the linear fit between the immersed and nonimmersed isotopic values.

CRDS-based setup in Mainz, the range of isotope value changes is even more pronounced (42‰ and 57‰ for δ^{18}O and δ^2H), with a more dispersed data distribution, as they employed a broader range of temperatures and heating times (Figure 3.2).

The coral dataset was evaluated using a Rayleigh fractionation model recently proposed by Fernandez et al. (2023) to further investigate the evaporation of coral skeleton inclusion water and its isotopic fractionation behavior. It is assumed that the fractionation process occurs in a “free atmosphere” of fixed humidity and isotopic composition. The equilibrium fractionation factor at 120 °C is calculated on the basis of the relationship proposed by Horita and Wesolowski (1994). The relative humidity, h, depends on the range of variation in the water vapor background in the line (h=0.42–0.49% for 6000–7000 ppmv, T=120 °C). The isotopic composition of the water vapor in air was set to laboratory standards (δ^{18}O for 3.91‰, δ^2H for -21.67‰). The Craig–Gordon evaporation model is used, with the diffusion fractionation factor taken from Mickler et al. (2004), and the exponent of turbulence set to 0.8-1, corresponding to evaporation scenarios from porous materials such as soil or leaf water (Gonfiantini et al., 2018; Horita and Wesolowski, 1994).

This Rayleigh fractionation model predicts slopes of 1.31-1.42 (mean 1.36±0.06, 1σ) for evaporation within the measurement line. The slope of the dataset (1.72±0.06) is slightly larger than our predicted range when uncertainties are considered (Figure 3.2). The reason may be that not all skeletal inclusion water experienced significant leakage or that the water released during coral fragment crushing was a mixture of non-leaked and partially evaporated water, thus deviating from the slope of a fully fractionated distribution. In addition, other factors, such as the surface and porosity of the coral skeleton and the water content, may influence the fractionation process during heating and the final isotopic results. Across the entire dataset (Figure 3.2 and Figure 3.3), high-temperature preheating before crushing clearly resulted in significant alterations in the isotopic values. The artifacts introduced during the analysis process are sufficient to obscure any climate and environmental information contained within the original isotopic values of the coral skeletal inclusion water.

3.4.2 Methodological Influences

In addition to heating parameters, different analysis setups, such as CRDS- and IRMS-based measurement setups, produce different isotope fractionation processes and analytical artifacts. Isotopic findings are incorporated into the dataset proposed by de Graaf et al. (2022), which includes data from three analytical setups for a comprehensive evaluation (Figure 3.6). In a parallel analytical setup (CRDS), the evaporation of coral skeletal inclusion water and the resulting δ^{18}O and δ^{2}H fractionation behaviors exhibit apparent similarities (such as the fitted slope), which are influenced mainly by temperature and heating time (Figure 3.2). However, owing to variations in the employed heating temperature and time, there are discrepancies in the absolute isotopic values measured by the two parallel setups (Figure 3.2 and Figure 3.6). For example, the CRDS dataset from Mainz, which employed lower heating temperatures and shorter heating times, exhibits markedly lower isotopic values than our dataset does. The isotopic results produced by the IRMS-based measuring setup also differ markedly from those produced by the CRDS (Figure 3.6). Overall, the absolute values of the δ^{18}O and δ^{2}H results are not comparable, either on the basis of different setups or parallel setups using different temperature parameters. Each device produces a dataset with very high internal variability. In contrast, the samples in glass tubes had much more reproducible data (Figure 3.2 and Figure 3.6). For example, the isotopic values of inclusion water from Angola coral skeletons measured in glass tubes exhibit standard deviations of 3.51‰ (δ^{18}O) and 7.15‰ (δ^{2}H) (n = 30), whereas those not enclosed in glass tubes have standard deviations of 6.58‰ (δ^{18}O) and 11.66‰ (δ^{2}H), respectively (n = 11). This method offers a potential avenue for exploring the climatic and environmental significance of isotope results.

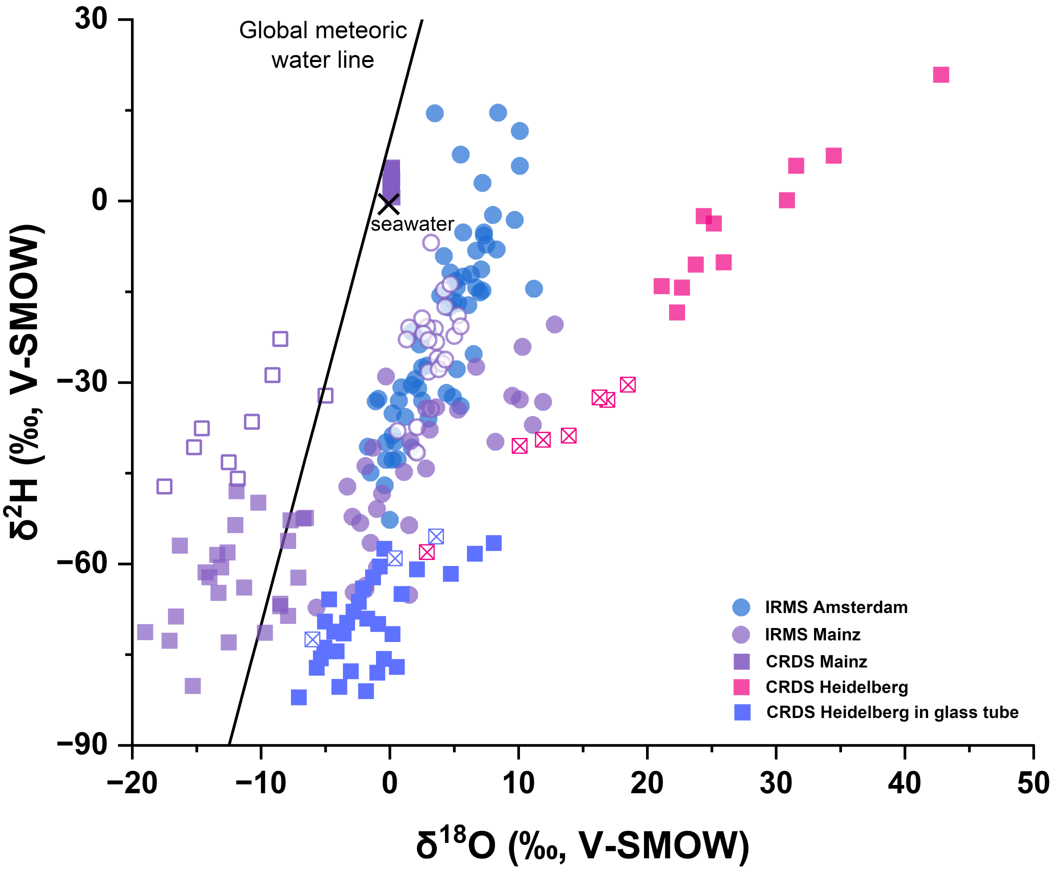

Figure 3.6. Interlaboratory comparison of isotope data from water trapped inside coral skeletons. The circles and squares indicate isotopic results from different experimental setups at different laboratories or by different methods. Open and closed data points indicate tropical and cold-water corals, respectively. The black X symbol indicates the isotopic values of seawater from the Angola coral fossil sampling sites. Data form de Graaf et al. (2022). In the Heidelberg measurements, Iceland and Angola coral samples are distinguished by crossed squares and plain squares, respectively. Notably, in our measurements, the samples measured using glass tubes exhibit higher consistency in mean values and show lower variability. In contrast, the Heidelberg coral samples measured without glass tubes, as shown in the figure, display greater dispersion. The inclusion water isotope mean values of the Iceland and Angola samples under non-glass tube conditions differ significantly and include outlier (Figure 3.2 and Figure 3.3), which is likely the main reason why this data set appears more scattered visually. Especially when comparing samples from the same location separately—whether Iceland (Figure 3.2) or Angola (Figure 3.3)—the standard deviations of measurements with and without glass tubes do not show a clear difference. Therefore, the visual high dispersion of non-glass tube data in the figure does not affect our interpretation of the results.

In addition to the influences from measurements, another source of uncertainty arises from the coral samples themselves. Repeated measurements of Holocene and last glacial period coral samples from Angola reveal significant deviations in the isotopic values of three out of the five replicates of samples. These deviations exceed the measurement uncertainty despite the samples being subjected to identical heating times and temperature conditions (Figure S6 in Supplementary Information B.2). Note that two of the replicates have a very close age at 35 ka BP.

This discrepancy suggests that not only does the measurement process introduce uncertainty but also that there may be substantial variances in the δ^{18}O and δ^{2}H values of inclusion water across different parts of the coral skeleton. First, there may be differences in the degree of isotopic fractionation of the calcifying fluid in different parts of the coral during growth. Second, during heating, only a portion of the unstable inclusions may experience significant changes in water isotopes due to leakage, whereas some inclusions remain well preserved. Owing to the uneven distribution of these two types of inclusions in the sample, the final measurement results are a mix of both, leading to a decrease in the reproducibility of the results.

The possibility that volatile organic compounds might be released from coral samples during crushing and heating, potentially affecting the spectral performance of the CRDS analyzer, was considered in this dissertation. However, the specific impact of volatile organic compounds in the water vapor on the measurement results is difficult to quantify. Nevertheless, the experimental results obtained via the glass tube method demonstrate that this approach effectively avoids significant fractionation, producing a more consistent dataset with lower variability, which further supports the feasibility of the method. Additionally, the glass tube method has potential for application with measurement devices that are less sensitive to organic compounds, such as IRMS, which not only can generate more reliable datasets but also offers a new avenue for further investigating the impact of organic compounds on CRDS analysis. Therefore, this method may offer the potential for more precise results in future research.

3.4.3 Insights from Immersion Experiments

The internal water pool within the coral skeleton may undergo varying degrees of internal–external water exchange. These complex factors present challenges for quantitative assessment and lead to reduced reproducibility of isotope measurements. De Graaf et al. (2022) immersed corals for 72 hours in four standard waters with a range of δ^{18}O values of 60‰ and δ^{2}H values varying by approximately 400‰ and then dried the corals in laboratory air for one day before measurement. The results revealed that the isotope values of the water within the coral skeleton gradually approached the isotope values of the immersion water (Figure 3.5). Consequently, they concluded that the internal water pool in the coral skeleton is unlikely to preserve original fluids, as the internal water pool was almost completely replaced by external water after only a few days of immersion de Graaf et al. (2022).

Compared with the experiment by de Graaf et al. (2022), this study introduced two major adaptations: first, in our immersion experiments, in situ seawater from the coral sampling site was used to simulate natural environmental conditions more closely; second, after the immersion treatment, the coral samples were dried at 60 °C to accelerate the evaporation process. These adjusted experimental methods offer insights into whether coral skeletons can partially retain the isotopic signature of the original fluids under seawater immersion conditions and whether the partially replaced water can be removed through evaporation after the corals are removed from the immersion environment. The results revealed that the isotope values of the coral skeleton inclusion water after immersion and drying were higher than those of the not immersed samples (Figure 3.5). However, unlike the findings of de Graaf et al. (2022), the isotope values of the dried samples after immersion did not fully resemble the isotope values of the seawater used for immersion but instead followed a fixed slope (Figure 3.5). This distribution pattern suggests that the isotope fractionation behavior induced by heating during the drying process may be stable, and this fractionation phenomenon seems to be more influenced by the drying time than by the immersion duration. In addition, the δ^2H values of the inclusion water in the immersed coral skeletons remained significantly lower than those of the seawater (Figure 3.5). This suggests that while skeleton fluid water isotope exchange occurred, complete replacement is rather unlikely. If the internal water pool in the coral skeleton had been completely replaced by immersion water, the isotope fractionation induced by heating and evaporation should have started from the isotope values of the seawater.

A possible explanation for this phenomenon is that prolonged immersion may lead to more thorough exchange between the internal water and the immersion water. However, longer heating times could completely remove the water from the easily exchangeable water pool. Additionally, some of the water that is less easily exchanged with the external environment may also have evaporated at high temperatures. As a result, under fixed heating temperatures and identical measurement methods, the isotope values of inclusion water in coral skeletons show a nearly constant slope across different heating times.

Our immersion experiments further support the idea that the water reservoirs within the coral skeleton might be divided into at least two components. One component readily exchanges with external water but gradually evaporates after being removed from the aqueous environment, as shown by the immersion experiment (Figure 3.5). The other components may remain relatively stable and not easily exchange with external water. The relative size and isotopic endmember composition of both reservoirs remain unknown, and the origin of the water in the calcifying fluid remains poorly constrained. Over months or years of drying, the water in the exchangeable reservoir may eventually evaporate, leaving behind a fluid of unknown but primary origin within the coral skeleton. If the original calcifying fluid at the time of coral skeleton formation was entirely replaced by seawater, the δ^{18}O and δ^{2}H values of both immersed and long-term dried corals would closely match those of modern seawater. Based on the immersion experiment with seawater, it cannot be concluded that the δ^{18}O values are close to the seawater composition. In the absence of an alternative explanation, it is assumed that some of the inclusion water in the coral skeleton underwent exchange with external water, while some inclusion water was likely well preserved. Therefore, from a methodological perspective, during the pretreatment of coral samples before the isotopes of fluid inclusions in coral skeletons are measured, contact with any liquids should be avoided.

In previous experiments by de Graaf and colleagues, with widely varying immersion water isotopic compositions but without actively drying coral fragments afterward, the δ^{18}O and δ^{2}H values were roughly equally impacted by isotope exchange. Compared with heating, the evaporation of easily exchangeable water in corals may occur more slowly, with only a small amount of immersion water being removed, leading to the immersion water's isotope signal dominating during measurement. In addition, previous works did not use capillary-sealed coral skeleton samples in their measurements, which may have led to more significant isotope fractionation during the measurement process. Therefore, the isotopic results for immersed corals were always slightly more positive than those for immersion water (Figure 3.5).

3.4.4 Potential Sources of Hydrogen and Oxygen Isotope Signals in Coral Skeleton Fluid Inclusions

Oxygen Isotope Composition Stability and Seawater Influence

Since the initial isotopic values of samples measured without glass tubes were significantly altered, measurements with less variability in glass tubes are used to assess whether they may contain information about their origin. The means and range of δ^{2}H and δ^{18}O do not significantly differ over time (Figure 3.4). The mean δ^{18}O values for Angola corals from the last glacial period and the Holocene are 0.15‰ and -0.15‰, respectively, which are identical to the modern seawater values observed in the seawater bathing the corals (-0.08‰, see immersion experiment). Compared with those of the Holocene, the δ^{18}O values of deep-sea water during the last glacial maximum were shifted positively by approximately 1.05±0.20‰ Duplessy et al. (2002). The glacial–interglacial variations in seawater δ^{18}O values in the deep Atlantic may be even smaller, between 0.7 and 0.8‰ (Schrag et al., 2002). Given the indistinguishability of the δ^{18}O values measured during the last glacial period and the Holocene, it is not possible to accurately determine the expected magnitude of difference between the two periods' samples. The variance of individual measurements and replicates does, of course, not allow us to observe such a small isotope shift.

The reason that the δ^{18}O values are very close to those of seawater may be that the effect of the calcification process on δ^{18}O values is much smaller than its effect on δ^{2}H values, leading to δ^{18}O values that are closer to those of seawater when the inclusions formed. In addition, some of the coral skeleton inclusion water may have been exchanged with modern seawater, which could have obscured the small differences in δ^{18}O values between the primary calcified inclusion water from the glacial and Holocene periods. Compared with that of hydrogen, the isotope exchange of oxygen is faster, which aligns the final δ^{18}O values with those of modern seawater, whereas deuterium still represents some of the original stable water pool. This possibility requires further investigation into isotope exchange rates, but on the basis of the equally strong response of corals to immersion water with strongly differing δ^{18}O and δ^{2}H values reported by (de Graaf et al., 2022), this process does not seem very likely.

Potential Causes of Hydrogen Isotope Composition Depletion in Coral Fluid Inclusions

The most striking feature of the stable isotopes in coral skeleton inclusion water is their markedly low δ^{2}H values, approximately 50‰ lower than that of modern seawater (0.49‰) used in the immersion experiment (Figure 3.4 and Figure 3.6). A question arises regarding the origin of the strong deuterium fractionation observed in the corals. Neither the treatment nor the storage of the corals can explain this isotopic composition. Even when partial seawater replacement occurs in primary coral skeleton inclusion water, the δ^{2}H values do not fully align with those of seawater, and the observed deviation (about 50‰) exceeds the δ^{2}H variations between the glacial and Holocene periods, which are expected to be less than 10‰. The low δ^{2}H values observed in coral skeletal inclusion water are not unique (Lécuyer and O'Neil, 1994). Prior investigations have documented δ^{2}H values for inclusion water in calcite and aragonite biocalcified materials across various environments, ranging from -38‰ to -69‰, which is significantly lower in comparison to seawater (Figure 3.6) (de Graaf et al., 2022).

The strong fractionation observed in δ^{2}H values but not in δ^{18}O values suggests a possible biological influence, potentially from a fractionation process unique to coral organisms. The exact mechanism by which corals incorporate water into their skeletons and its impact on isotope fractionation remains unclear (D'Olivo and McCulloch, 2017; Mass et al., 2017; McCulloch et al., 2012; Nash et al., 2019; Rollion-Bard et al., 2010; Saenger et al., 2012). Additionally, the quantity and origin of the initially preserved water cannot be quantified. A potential explanation for fractionation involves the biological processes of coral calcification, where mixing between calcifying fluid with a lower δ^2H value and seawater could result in intermediate δ^2H values, or part of the δ^2H signature of the calcifying fluid may be inherited from the coral's diet. However, assuming a universal metabolic fractionation or organic influence on δ^2H values may oversimplify complex biological and environmental interactions. Future research could involve controlled laboratory experiments and the culturing of corals under varying environmental conditions with isotopically constrained seawater and distinct food sources. The improved analytical methods developed in this study could help determine whether metabolic processes create unique isotopic signatures and if biological fractionation selectively affects δ^2H values while leaving δ^{18}O values largely unchanged.

3.5 Conclusions

A new constant vapor stream analytical methodology is used in this dissertation to measure skeleton inclusion water in corals. It is confirmed that evaporation due to heating (temperature and time) of the coral before crushing induces strong instrumental isotopic fractionation. The δ^{18}O and δ^2H results obtained from various analytical setups and parallel setups with different temperature parameters are not comparable because of the inability to reproduce measurements accurately. However, the isotopic fractionation of samples encapsulated in glass tubes is minimal, demonstrating better reproducibility. This method offers a potential avenue for elucidating the climatic and environmental significance of isotopic results. The δ^{18}O and δ^2H values of Angola coral skeletal inclusions did not significantly differ between the Holocene and the last glacial period. In contrast to the δ^{18}O values, the δ^2H values are significantly lower than those of seawater, possibly because of the biological processes involved in coral calcification or the mixing of the calcifying fluid with seawater. The immersion experiments demonstrate the existence of an easily exchangeable water pool that needs to be considered in future preparations and during the interpretation of the isotope results. Detailed studies of water release at different temperatures are required to test whether an inert water pool exists that provides information on the fluid water composition or the isotopic composition of the environment. Investigating the isotopic composition of coral skeletal inclusion water and its interactions with seawater under controlled conditions will provide critical insights into the mechanisms of isotopic fractionation in cold-water corals.

Chapter 4

Fluid Inclusion Lines Interlaboratory Comparison Experiment Data Summary

Key Points:

- **The isotopic results from 13 laboratories show differences. At higher (1.0 µl) and moderate (0.5 µl) water volumes, most results are closer to the standard values with smaller standard deviations. At lower volumes (≤0.2 µl), accuracy and reproducibility decrease noticeably.**
- **In 13 out of 14 reports, δ^{18}O and δ^{2}H values change systematically with decreasing water volume. The shift usually ranges from 2 to 5‰.**
- **In experiments where capillaries were crushed with Iceland spar, the mean isotope values show no systematic deviation from the standard. There is also no clear difference compared to experiments without Iceland spar.**

Recent advances in δ^{18}O and δ^{2}H isotope measurement techniques for speleothem fluid inclusions have significantly enhanced their potential as reliable hydroclimate proxies. To evaluate the consistency of isotopic analyses, we conducted an interlaboratory comparison study was conducted using a set of artificial samples. Capillaries filled with standard waters of varying δ^{18}O and δ^{2}H values were prepared across a range of water volumes and analyzed by 13 laboratories. Under higher (1.0 µl) and moderate (0.5 µl) water volume conditions, the average isotope values in most reports are close to the standard, with small standard deviations. However, under lower water volume conditions (0.2 µl), some reports showed small deviations, and the results were generally less favorable compared to those at higher and moderate volumes. Additionally, some reports exhibited larger deviations from the standard isotope values at this water volume. This study emphasizes the value of using glass tubes filled with standard water for calibration and offers valuable insights into the sources of measurement errors, contributing to greater consistency across different experimental setups.

This project was carried out in collaboration with 12 laboratories (a full list is provided in this chapter). The participating laboratories were responsible for the isotope measurements of the standard water samples. I prepared and distributed all capillaries filled with standard waters, conducted the complete data analysis and summary, and authored the content of this chapter. Throughout the process, members of the "comparison project core group" — Jenny Maccali, Alvaro Fernandez Bremer, Sam Nicholson, Stéphane Affolter, Timon Kipfer, Anna Nele Meckler, and Hubert Vonhof — provided input on the experimental design and feedback on the chapter content.

4.1 Introduction

The water in speleothem fluid inclusions represents a unique archive for paleoclimate reconstructions, serving as a natural reservoir of cave drip water. The hydrogen and oxygen isotopic composition of inclusion water directly reflects the isotopic signature of past precipitation (Affolter et al., 2015, 2025; Fleitmann et al., 2003; Schwarcz et al., 1976; Uemura et al., 2020; Weissbach et al., 2023). When combined with the stable isotopes of calcite, it can be used for paleotemperature reconstructions or to provide insights into moisture sources and cave evaporation processes in relation to past climatic and environmental conditions (Affolter et al., 2019; Azharuddin et al., 2025; Fleitmann et al., 2022; Maccali et al., 2023; Meckler et al., 2015; Schwarcz et al., 1976; Warken et al., 2022; Wilcox et al., 2020).

Although stable isotopes in fluid inclusions have been widely applied in paleoclimate reconstructions, their analysis remains challenging (Affolter et al., 2025). The size of fluid inclusions in speleothems typically ranges from a few to several hundred µm, necessitating the extraction of inclusion water from these small cavities before analyzing its hydrogen and oxygen isotopic composition (Affolter et al., 2025; Fairchild and Baker, 2012; Kendall and Broughton, 1978; Lopez-Elorza et al., 2021; Treble et al., 2005). Over the past decades, two primary techniques have been used for water extraction from speleothem fluid inclusions: the crushing method and the thermal decrepitation method. In the former, inclusions are physically crushed, followed by either direct online measurement or offline analysis after cryogenic trapping of the released water (Affolter et al., 2014; de Graaf et al., 2020; Dennis et al., 2001; Dublyansky and Spötl, 2009; Schwarcz et al., 1976; Vonhof et al., 2006). The latter involves heating carbonate samples under vacuum conditions at high temperatures (400–900°C), leading to their decomposition into CaO and CO, during which inclusion water is released and cryogenically trapped (Goede et al., 1986; Matthews et al., 2000). Compared to the crushing method, this technique yields a greater amount of water; however, it may induce isotopic fractionation effects, requiring additional correction procedures to adjust the isotopic results (Matthews et al., 2000; McGarry et al., 2004; Verheyden et al., 2008). Alternatively, improved reproducibility and accuracy can be achieved by optimizing heating temperatures and refining the water extraction process.

In terms of analytical techniques, isotope analysis combined with IRMS allows for reliable determination of the oxygen and hydrogen isotope ratios in sub-microliter quantities of fluid inclusion water (de Graaf et al., 2020; Dublyansky and Spötl, 2009; Vonhof et al., 2006). Over the past decade, laser spectroscopy has undergone rapid development, with CRDS emerging as a precise and reliable method for isotopic analysis of water samples (Brand et al., 2009; Gupta et al., 2009). CRDS-based fluid inclusion analysis employs crushing devices similar to those used in IRMS setups and can operate under dry nitrogen, a wet carrier gas with a constant background of standard water, or vacuum conditions, enabling simultaneous measurement of hydrogen and oxygen isotopic compositions in speleothem inclusion water in a single run (Affolter et al., 2014; Arienzo et al., 2013; de Graaf et al., 2020; Maccali et al., 2023; Uemura et al., 2016; Weissbach et al., 2023). The introduction of this technique has significantly simplified and enhanced the feasibility and reliability of isotopic analysis of fluid inclusion water in speleothems. It allows for the simultaneous measurement of δ^2H_{FI}, $\delta^{18}O_{FI}$, and $\delta^{17}O$ with relatively straightforward operation (Affolter et al., 2015; Affolter and Leuenberger, 2021) and has gradually become the mainstream method for analyzing the isotopic composition of speleothem fluid inclusion water.

The development and application of these techniques have significantly improved the accuracy of isotopic measurements of speleothem fluid inclusions (Affolter et al., 2025). However, special attention should be given to differences in measurement procedures and parameters between different techniques or even among laboratories using the same technique. To date, only a limited number of studies have compared isotopic results obtained from different measurement setups and analyzed potential analytical biases. For instance, a comparison of two IRMS techniques revealed a systematic offset of approximately 1‰ in $\delta^{18}O_{FI}$ values between the two methods (Wainer et al., 2011). Comparisons between different techniques have shown that $\delta^{18}O_{FI}$ values measured by IRMS for fluid inclusion water in speleothem samples tend to be lower than those obtained using CRDS, while $\delta^{2}H_{FI}$ values exhibit better reproducibility between the two techniques (Meckler et al., 2015). Another study found systematic differences in both $\delta^{18}O_{FI}$ and $\delta^{2}H_{FI}$ values, with CRDS yielding $\delta^{18}O_{FI}$ values approximately 0.7‰ lower and $\delta^{2}H_{FI}$ values about 2.5‰ lower than those measured by IRMS (Arienzo et al., 2013). Notably, a recent study reported that isotopic results from IRMS- and CRDS-based setups were highly consistent, providing evidence that different techniques can yield highly consistent isotopic results (de Graaf et al., 2020).

Furthermore, the range of water volumes that can be analyzed varies across different techniques and instruments, spanning from sub-microliter to several microliters. Particularly, there are substantial differences among techniques in terms of the minimum measurable water volume. Some setups also exhibit a pronounced isotope-volume effect, which manifests in two key aspects: (1) the reproducibility of measurements may decline significantly as the sample volume decreases, and (2) isotopic values may show systematic positive or negative shifts with decreasing water volume. However, whether and to what extent different setups exhibit volume effects remains unclear. Further research is required to verify these potential influences and enhance the reliability of analytical results, especially in studies involving small-volume samples.

Given the differences in measurement setups, laboratory protocols, and the impact of sample volume on isotopic results in fluid inclusion analysis, there is an urgent need for more systematic inter-laboratory comparison studies to apply fluid inclusion isotopic analysis techniques more effectively. Additionally, some studies have reported that during the sample crushing process, water adsorption on the freshly fractured calcite surface may lead to significant isotopic shifts in $\delta^{2}H_{FI}$ and $\delta^{18}O_{FI}$ values (Dennis et al., 2001). It remains unclear whether adsorption effects are widespread across different techniques and laboratories and whether these effects significantly influence isotopic results. Therefore, this study conducted an inter-laboratory comparison experiment aimed at optimizing the application of fluid inclusion isotopic analysis techniques in paleoclimate research. Specifically, the objectives of this study are as follows: First, to evaluate the accuracy and precision of isotopic measurements within and across laboratories through repeated analyses of standard water samples. Second, to examine the effect of water volume on isotopic values by measuring standard water across different volume gradients and identifying potential systematic shifts in isotopic values. Finally, to investigate potential adsorption effects in freshly crushed calcite and assess their influence on isotopic values.

4.2 Expected Objectives

Inter-lab versus Intra-lab Reproducibility

The reproducibility of the water amount and isotope results is checked by performing repeatable measurements on the same volume of standard water. Therefore, triplicates of each sample will be provided. All measurements will be used for inter-laboratory comparison of different aspects.

Dependence on Water Amount

To detect whether the measured hydrogen and oxygen isotope values are systematically shifted with increasing/decreasing water amounts, a 7-step standard water volume gradient from 0.1 µl to 2 µl was designed. The feasible range of water volumes to be measured varies considerably between labs. The volume of water in each capillary is marked and it is up to the laboratory to decide if they can analyse the respective amounts or not.

Adsorption and/or Desorption on the Calcite Surface

Adsorption on a calcite surface and on freshly crushed carbonate with a large surface to volume ratio provides the possibility to alter the isotope values of the fluid inclusion water. In order to simulate speleothem fluid inclusion analysis, a procedure was designed in which inclusion-free Iceland spar was co-crushed with capillaries. The crushing of the compact Iceland spar pieces provided fresh and fine-grained calcite for interaction and adsorption testing. Glass capillaries filled with standard water are crushed with inclusions-free Iceland spar to mimic speleothem fluid inclusion analyses.

4.3 Design of Capillary Experiments

The capillary tubes are approximately 15-20 mm in length and are processed from Pasteur pipettes. The standard water is injected into pipettes that contain glass wool using 1 µl syringes made by TRAJAN (accuracy and reproducibility ± 2%) and closed with a torch. There are 39 capillaries in each group. The volume of the standard water filled in each capillary tube has been labelled (Table 4.1 and Table 4.2).

To assess the reliability of the capillaries, isotope and water volume measurements were conducted on capillaries filled with various standard waters and volumes. These capillaries, randomly selected from those prepared under the same standard procedure, were tested using identical preparation and measurement methods applied throughout the production process. As an initial step, capillaries containing 1.0 µl of water from three different standards were

Standard water	δ^{18}O (‰, V-SMOW)	δ^{2}H (‰, V-SMOW)
1	-1.82	-39.80
2	-15.15	-110.88
2	-30.68	-243.97

Table 4.1. The volume and hydrogen and oxygen isotope composition of the standard water used.

Volumes	2 µl	1 µl	0.8 µl	0.5 µl	0.3 µl	0.2 µl	0.1 µl	Total
Standard 1	3	3	3	3	3	3	3	21
Standard 2		3		3		3		9
Standard 3		3		3		3		9
Total	3	9	3	9	3	9	3	39

Table 4.2. Number of samples provided for each laboratory.

analyzed, and the outcomes were evaluated against those obtained through syringe injection. The analysis showed no significant differences in δ^{18}O and δ^{2}H values between the capillaries and syringe injections. Additionally, the measured water volumes from the capillaries were consistent with the expected values (Figure 4.1).

Secondly, to assess the reproducibility of capillaries filled with varying water volumes for isotopic measurements, a series of capillaries filled with Standard Water 1—ranging from 2 µl to 0.1 µl—were analyzed, and the results were compared with those obtained via syringe injection (Figure 4.2). The results indicated that the standard deviation (1σ) of water volumes measured from the capillaries ranged from 0.0005 to 0.0228 µl, while the standard deviation for δ^{18}O ranged from 0.04 to 0.11‰, and for δ^{2}H, it ranged from 0.03 to 1.81‰ (Table 4.3). Measurements of water δ^{18}O and δ^{2}H values in capillaries of different standards and volumes were also not significantly different compared to injection. The capillary was prepared under a uniform standard. After the standard water was injected into the capillary, it was immediately sealed with a flame while maintaining a specific distance between the flame and the water to minimize evaporation and isotope fractionation. These measures were verified through repeated testing, demonstrating that the capillaries are reliable and suitable for inter-laboratory comparisons.

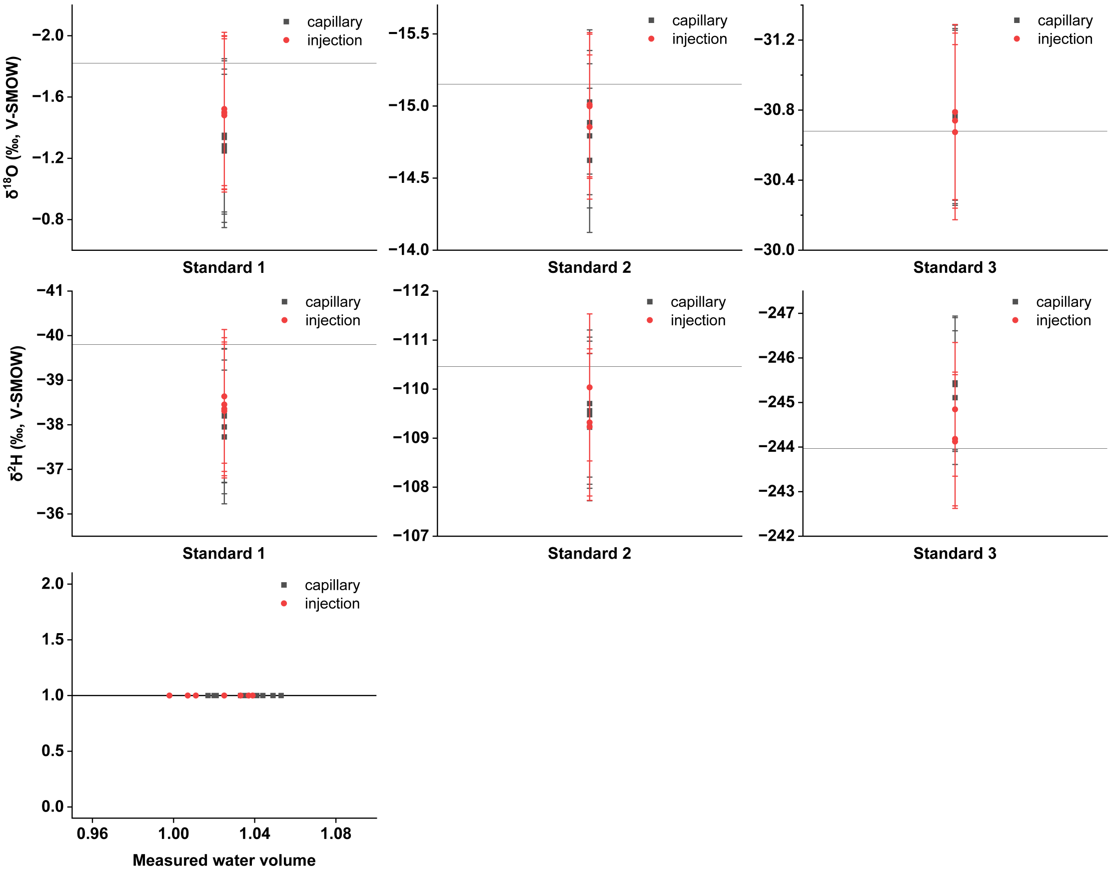

Figure 4.1. Comparison of the water volume and isotope values measured by capillary and injection. The measurement results of isotopes and water volume from capillaries filled with 1 µl of standard water 1 are shown in gray. The red data represent measurements obtained from direct injection of 1 µl of standard water 1 using a syringe. There is no significant difference between the two in terms of isotope and water volume measurements.The error bars for δ^{18}O and δ^{2}H are 0.5‰ and 1.5‰, respectively.

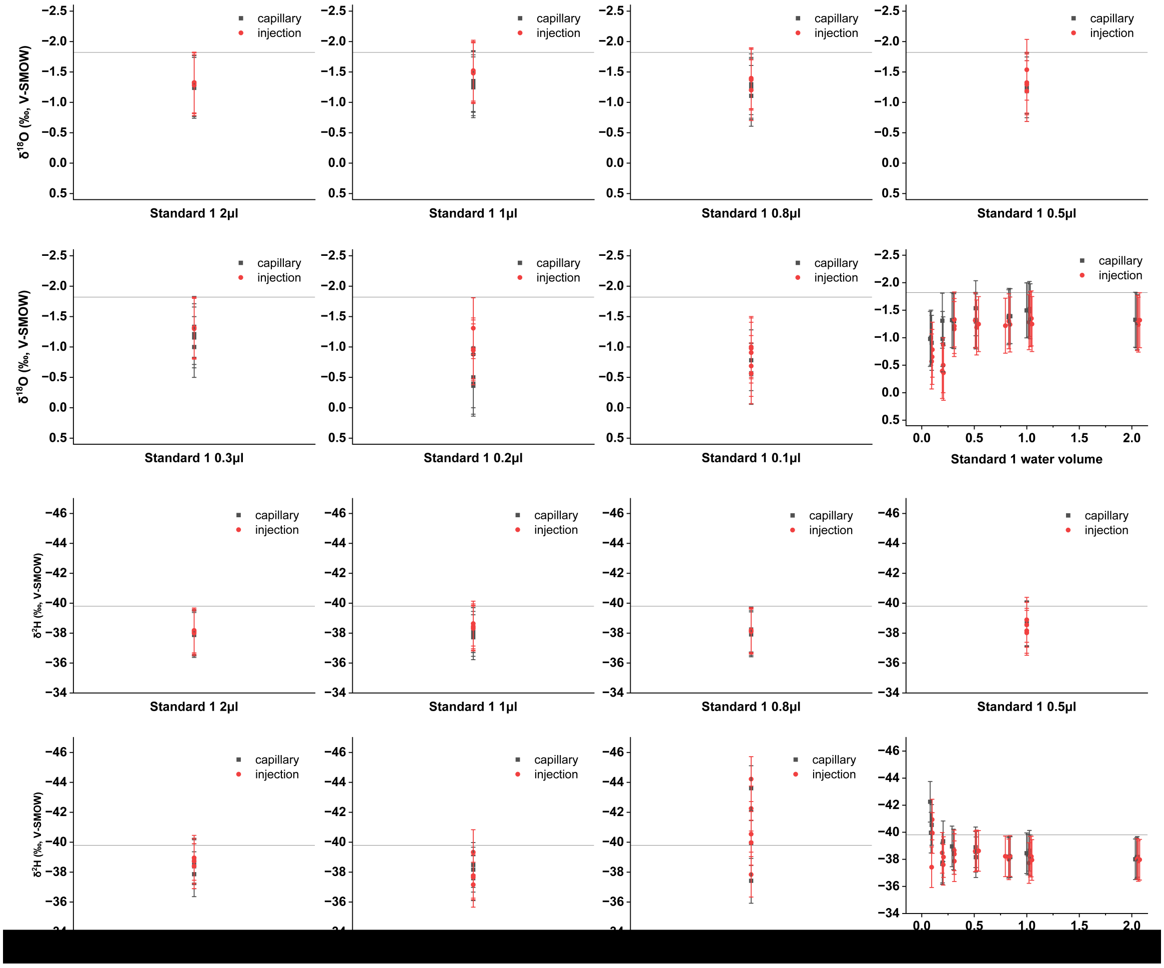

[redacted]

Figure 4.2. Comparison of the water volume and isotope values measured by capillary and injection. The measurement results of isotopes and water volume from capillaries filled with 2, 1, 0.8, 0.5, 0.3, 0.2, and 0.1 µl of standard water 1 are shown in gray. The red data represents measurements obtained from direct injection of varying volumes of standard water 1 using a syringe. There is no significant difference between the two in terms of isotope and water volume measurements.The error bars for δ^{18}O and δ^{2}H are 0.5‰ and 1.5‰, respectively.

Water vol. (µl)	Injection vol. (µl)	δ^{18}O, ‰ VSMOW	δ^{2}H, ‰ VSMOW	Capillary vol. (µl)	δ^{18}O, ‰ VSMOW	δ^{2}H, ‰ VSMOW
2	0.01	0.02	0.09	0.01	0.04	0.08
1	0.01	0.01	0.14	0.01	0.06	0.15
0.8	0.01	0.01	0.04	0.02	0.04	0.13
0.5	0.00	0.13	0.37	0.02	0.06	0.03
0.3	0.01	0.01	0.28	0.00	0.09	0.41
0.2	0.00	0.23	0.94	0.01	0.07	0.45
0.1	0.01	0.05	1.19	0.01	0.11	1.81

Table 4.3. Standard deviations (1σ) of isotope measurements for various volumes of standard water 1 capillaries compared to syringe injection measurements. Each volume was injected/capillary measured 3 times.

4.4 Description of the Dataset

4.4.1 Number of Capillary Measurements

A total of 13 labs participated in the comparison and submitted 14 reports (Figure 4.3). One of the labs provided capillary results for two inclusions measurement lines. In the 14 reports provided, a total of 426 measurements of capillaries were recorded (Table 4.4). Among them, 12 reports measured three standards each, one report measured two standards, and one report measured a single standard. Some laboratories removed or marked outliers when submitting their reports, or excluded data for other reasons, such as exceeding the measurable water volume range (either upper or lower limits) or data loss due to failed individual measurements. These outliers are not included in the analysis and should not be considered for further comparison. Regarding the measured water volumes, seven reports covered all seven types of water volumes from 0.1 to 2.0 µl, two reports measured six types, four reports measured five types, and one report measured four types. Ten reports conducted measurements by crushing both capillaries and Iceland spar together. Almost all the reports provided measured results for 0.8, 0.5, 0.3 and 0.2 µl capillary. The 2µl capillary may exceed the measurement capacity of some labs, with only 8 reports providing measurement results. There are 11 reports that provide measurements for low water volume capillaries (0.1 µl). No significant deviation from the expected values was observed for the measurement results obtained by crushing the capillary with Iceland spar, regardless of whether in high or low water volumes (Figure 4.4). Compared to reports without the crushing of Iceland spar, the measured water volumes also did not exhibit significant differences.

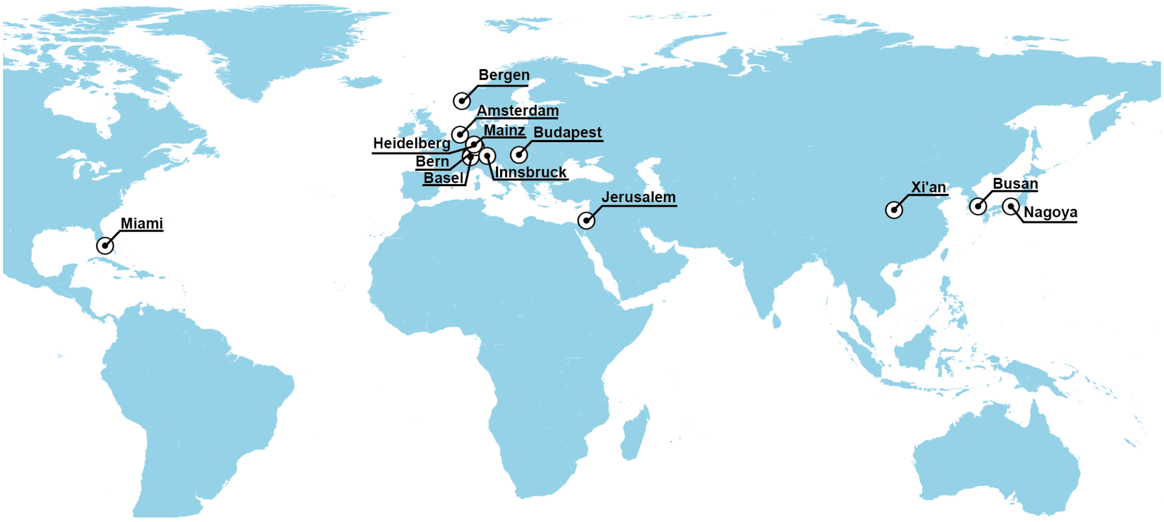

Figure 4.3. Distribution of laboratories participating in the comparison program.

Report number	Measured standards	Number of measured water volumes	Measured capillary water volume range (μl)	Total number of measure-ments	Note
1	3	7	2.0 - 0.1	26	CRDS, dry
2*	3	7	2.0 - 0.1	39	CRDS, wet
3*	3	7	2.0 - 0.1	29	CRDS, wet
4*	3	6	1.0 - 0.1	35	CRDS, wet
5*	3	5	0.8 - 0.1	27	CRDS, wet
6*	3	5	2.0 - 0.3	27	CRDS, wet
7*	2	5	1.0 - 0.2	24	CRDS, wet
8*	3	5	1.0 - 0.2	33	CRDS, wet
9*	3	6	1.0 - 0.1	35	CRDS, wet
10	1	7	2.0 - 0.1	20	CRDS, wet
11*	3	7	2.0 - 0.1	36	OA-ICOS
12	3	7	2.0 - 0.1	37	/
13*	3	4	0.5 - 0.1	23	CF-IRMS
14	3	7	2.0 - 0.1	35	CF-IRMS

Table 4.4. Number of capillaries measured in each report. Total of 426 measurements, including outliers. The * denotes reports where Iceland spar was crushed together with capillaries. The Note specifies the measurement setup used and indicates whether a dry or wet background was applied.

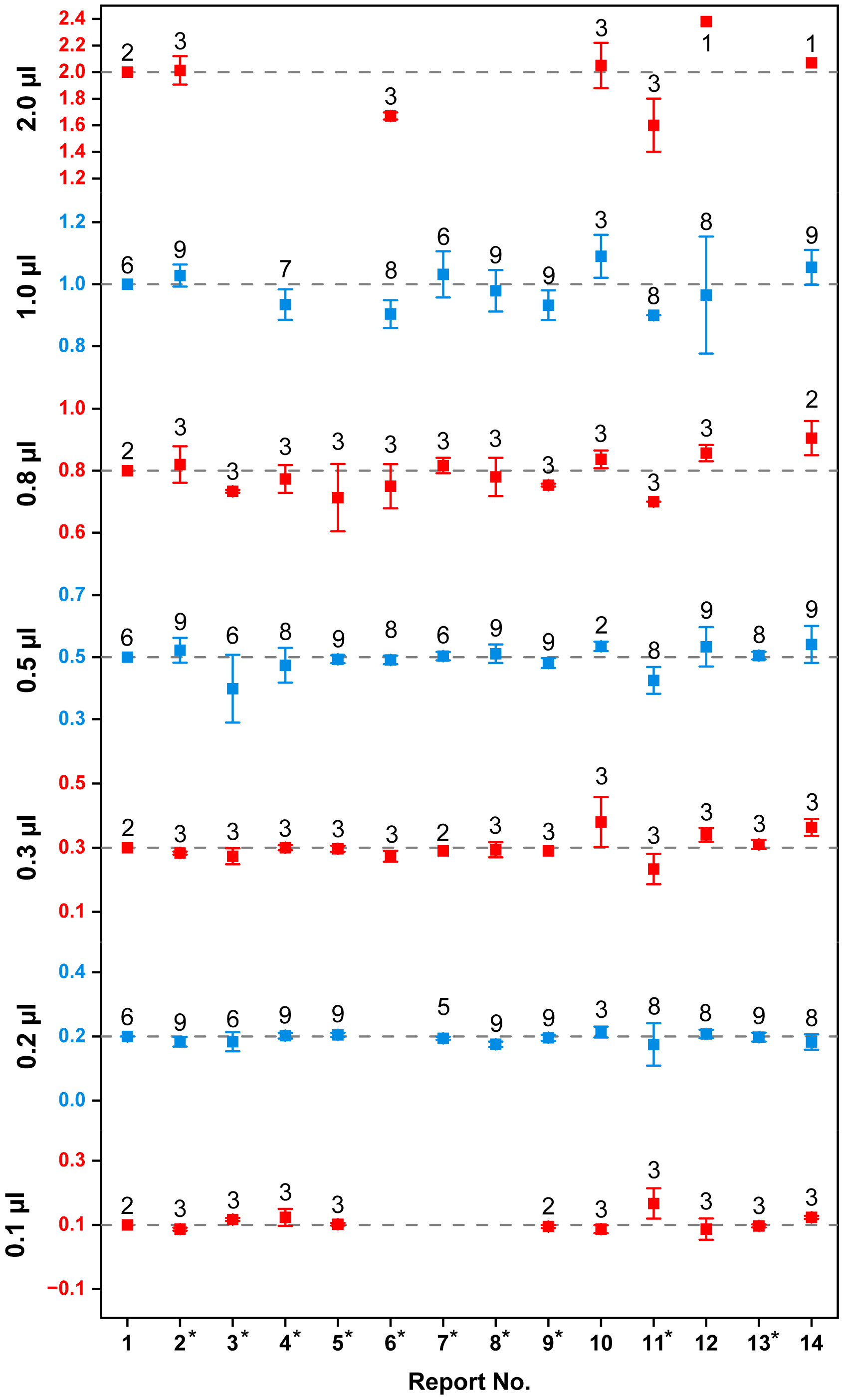

Figure 4.4. Measurements of water volume per report (mean and 1 SD (1σ)). The grey dashed lines indicate the volume of water filling the capillary. The * denotes reports where Iceland spar was crushed together with capillaries. The number indicates the number of capillaries measured. Outliers marked in each report are not included.

4.4.2 The Amount Effect of Isotope Values

In the measurement results for standard water 1, 13 out of 14 reports observed a systematic increase or decrease in isotope values as the water volume decreased (Figure 4.5) or decreased as the water volume decreased. For example, the δ^{18}O and δ^{2}H values in reports 2, 4, 5, 6, 7, 9, and 13 exhibited a positive shift with decreasing water volume, while reports 1 and 14 showed a negative shift in δ^{18}O and δ^{2}H values as the water volume decreased. There were also some reports where only δ^{18}O showed a deviation trend, such as reports 8, 10, and 11. The δ^{18}O values in reports 8 and 10 showed a positive shift, while in report 11, the δ^{18}O value exhibited a negative shift, with no trend observed in their δ^{2}H values. Report 12 was the only case where δ^{18}O and δ^{2}H showed opposite trends. Except for a few reports that show a large change in isotopic values with water volume (e.g., report 14), the range of δ^{18}O and δ^{2}H values in most reports varies with water volume between 2 and 5‰ (Figure 4.5).

Reports where the glass capillaries were crushed together with Iceland spar, such as reports 2, 4, 5, 6, 7, and 9, mostly showed a consistent positive shift in δ^{18}O and δ^{2}H values as the water volume decreased. In contrast, reports where the capillaries were not crushed with Iceland spar, such as reports 1, 10, 12, and 14, exhibited less consistent or no trends in δ^{18}O and δ^{2}H values. Considering the differences in measurement methods and calibration protocols across reports, further evidence is required to determine whether this isotopic shift is related to the presence of Iceland spar.

4.4.3 The Reproducibility of Isotope Values

Given that most reports exhibited a systematic shift in measured isotope values as water volume decreased, directly comparing the averaged isotope measurements of all capillary volumes across reports may not accurately reflect the true measurement conditions of specific laboratory. Therefore, the mean values and reproducibility of isotopic results for three standards under larger water volumes (1 µl) are first reported across different datasets (Figure 4.6 - Figure 4.8).

For δ^{18}O except for reports 1 and 14, at least one average δ^{18}O value of standard water in the other reports is distributed within ±1‰ of the standard water δ^{18}O values. The average δ^{18}O values of all measured standard waters in reports 2, 4, 7 (which did not measure standard water 3), 8, 9, 10 (which did not measure standard waters 2 and 3), 11, and 12 fall within ±1‰ of the standard water δ^{18}O values. For δ^{2}H except for reports 1, 12, and 14, at least one average δ^{2}H value of standard water in the other reports is distributed within ±2‰ of the standard water δ^{2}H values. Only the mean δ^{2}H values for all three standard waters in report 8 were distributed within ±2‰ of the standard water δ^{2}H values. The mean δ^{2}H

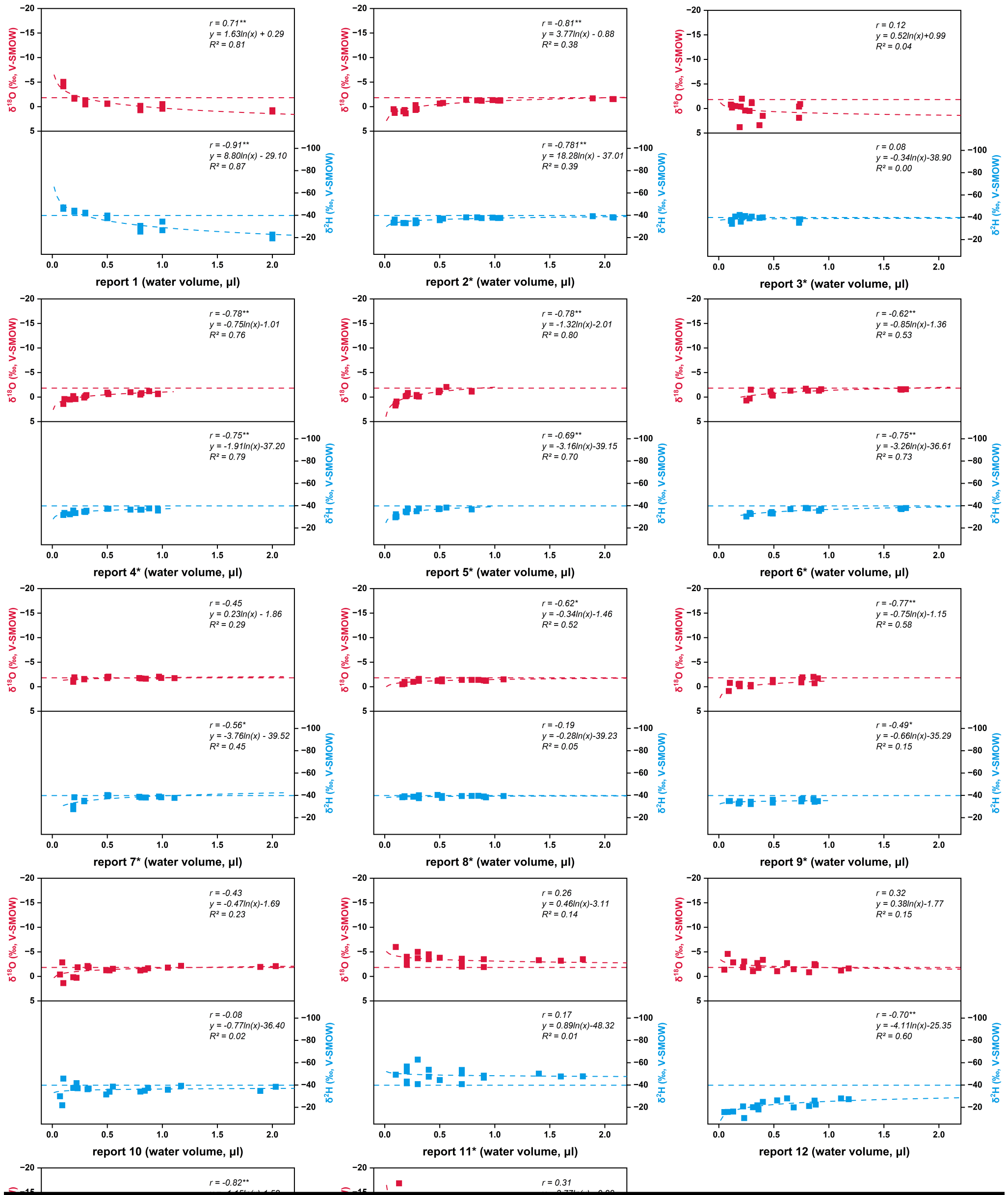

[redacted]

Figure 4.5. Isotope measurements of different volumes of standard water 1 in various reports. The red and blue dashed lines represent the isotope values of standard water 1. The red and blue dots show the δ^{18}O and δ^{2}H measurements for each report. The r value denotes the Pearson correlation between water volume and isotope values (* and ** indicate p<0.05 and 0.01 respectively), while the red and blue trend lines, along with the R^2 values, represent the result of the logarithmic fit. The * denotes reports where Iceland spar was crushed together with capillaries.

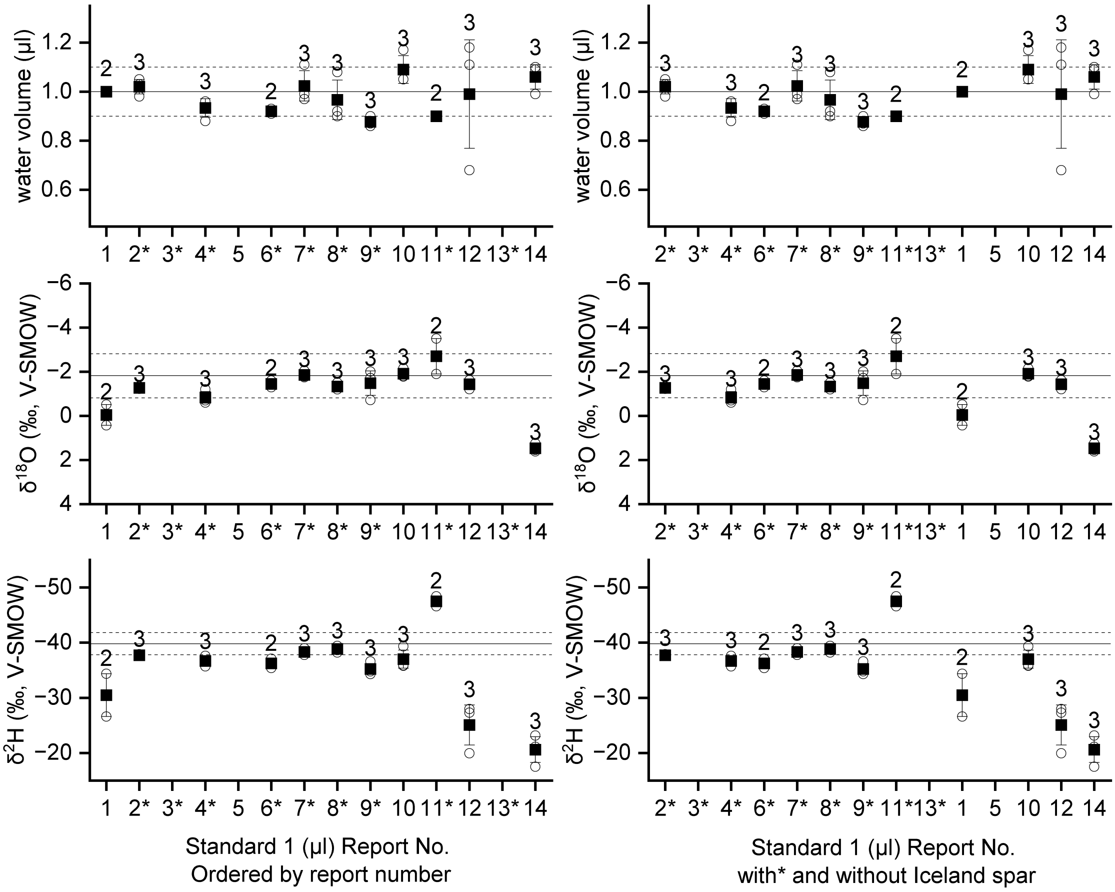

Figure 4.6. Mean values and SD (1σ) for water volume and isotope measurements of 1 µl standard water 1 from various reports. The left side is organized by report number, while the right side is arranged by whether the capillary tube is crushed together with the Iceland spar. The hollow dots indicate individual measurement data. The * denotes reports where Iceland spar was crushed together with capillaries. The dotted lines indicate ±0.1 µl of filled water volume, ±1‰ for δ^{18}O and ±2‰ for δ^{2}H respectively.

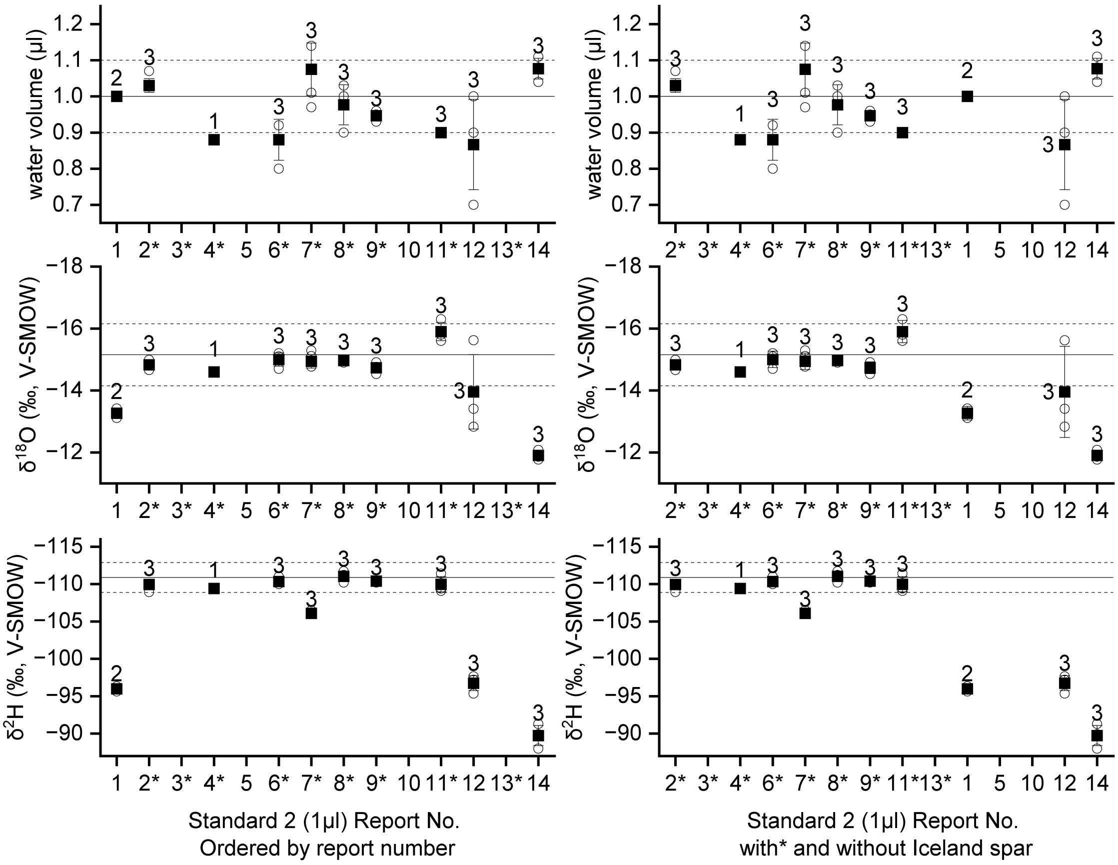

Figure 4.7. Mean values and SD (1σ) for water volume and isotope measurements of 1 µl standard water 2 from various reports. The left side is organized by report number, while the right side is arranged by whether the capillary tube is crushed together with the Iceland spar. The hollow dots indicate individual measurement data. The * denotes reports where Iceland spar was crushed together with capillaries. The dotted lines indicate ±0.1 µl of filled water volume, ±1‰ for δ^{18}O and ±2‰ for δ^{2}H respectively.

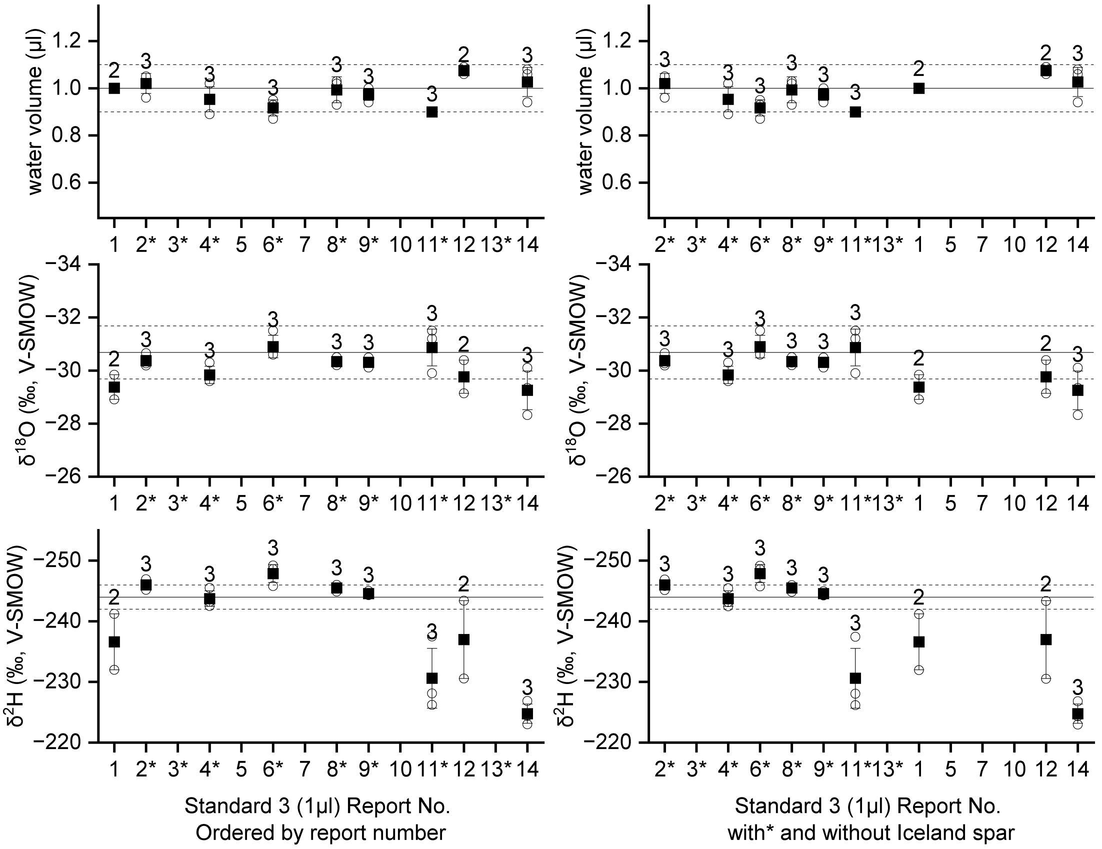

Figure 4.8. Mean values and SD (1σ) for water volume and isotope measurements of 1 μl standard water 3 from various reports. The left side is organized by report number, while the right side is arranged by whether the capillary tube is crushed together with the Iceland spar. The hollow dots indicate individual measurement data. The * denotes reports where Iceland spar was crushed together with capillaries. The dotted lines indicate ±0.1 μl of filled water volume, ±1‰ for δ^{18}O and ±2‰ for δ^{2}H respectively.

values for the two standard waters in reports 3 and 9, respectively, are distributed within ±2‰ of the standard water δ^2H values.

In the comparison between crushing the capillary tubes with Iceland spar and without, no systematic differences were observed in the isotopic values obtained under both scenarios. The isotopic values measured from the capillary tubes crushed with Iceland spar were not systematically higher or lower than the isotopic values of the filled standard water (Figure 4.6 - Figure 4.8). This phenomenon suggests that the adsorption effect caused by crushing the calcite samples may not be significant, or that using bulk Iceland spar during crushing may not effectively simulate the adsorption effect exhibited by the crushed calcite powder.

A comparison of isotopic values and water volumes measured with capillaries of 0.5 µl and 0.2 µl is also provided (Figure S4.4 - S4.9 in Supplementary Information B.3). Under both water volume conditions, the average isotopic values in different reports showed varying deviations relative to the isotopic values of the standard water, with characteristics similar to those observed at 1.0 µl. Specifically, some reports for small water volume capillaries still yielded isotopic measurements close to the isotopic values of the filled standard water, with smaller standard deviations (e.g., reports 2, 4, 5, 8, 9), indicating that these laboratories also exhibited high measurement stability and accuracy under smaller water volume conditions. However, some reports showed larger deviations from the isotopic values of the standard water under low water volume conditions (e.g., reports 11, 12, and 14). These observations suggest that the measurements from some laboratories under smaller water volume conditions are still influenced by various factors, including instrument sensitivity, operational procedures, and the potential impact of water volume on isotopic fractionation effects. Additionally, under the 0.5 µl and 0.2 µl water volumes, no significant systematic differences were observed in the isotopic values between reports where the capillary tubes were crushed with or without Iceland spar (Figure S4.4 - S4.9 in Supplementary Information B.3) .

The trend in the standard deviation of isotopic values was analyzed for each set of capillaries containing the same water volume from the same standard, as the water volume varied (Figure 4.9). For δ^{18}O the SD values ranged from 0.2‰ to 3.0‰, with an overall trend of increasing SD as the water volume decreased. At larger water volumes (≥1 µl), the SD values were generally smaller and more concentrated, ranging mainly from 0.2‰ to 1.0‰, indicating good reproducibility of δ^{18}O measurements under high water volumes. However, as the water volume decreased, the SD values increased significantly and displayed greater dispersion. When the water volume was between 0.1 and 0.5 µl, the SD values exhibited a wider distribution, and even without considering individual extreme values, the SD could reach 1.5‰ or higher. Additionally, the distribution of SD became more sparse and un-

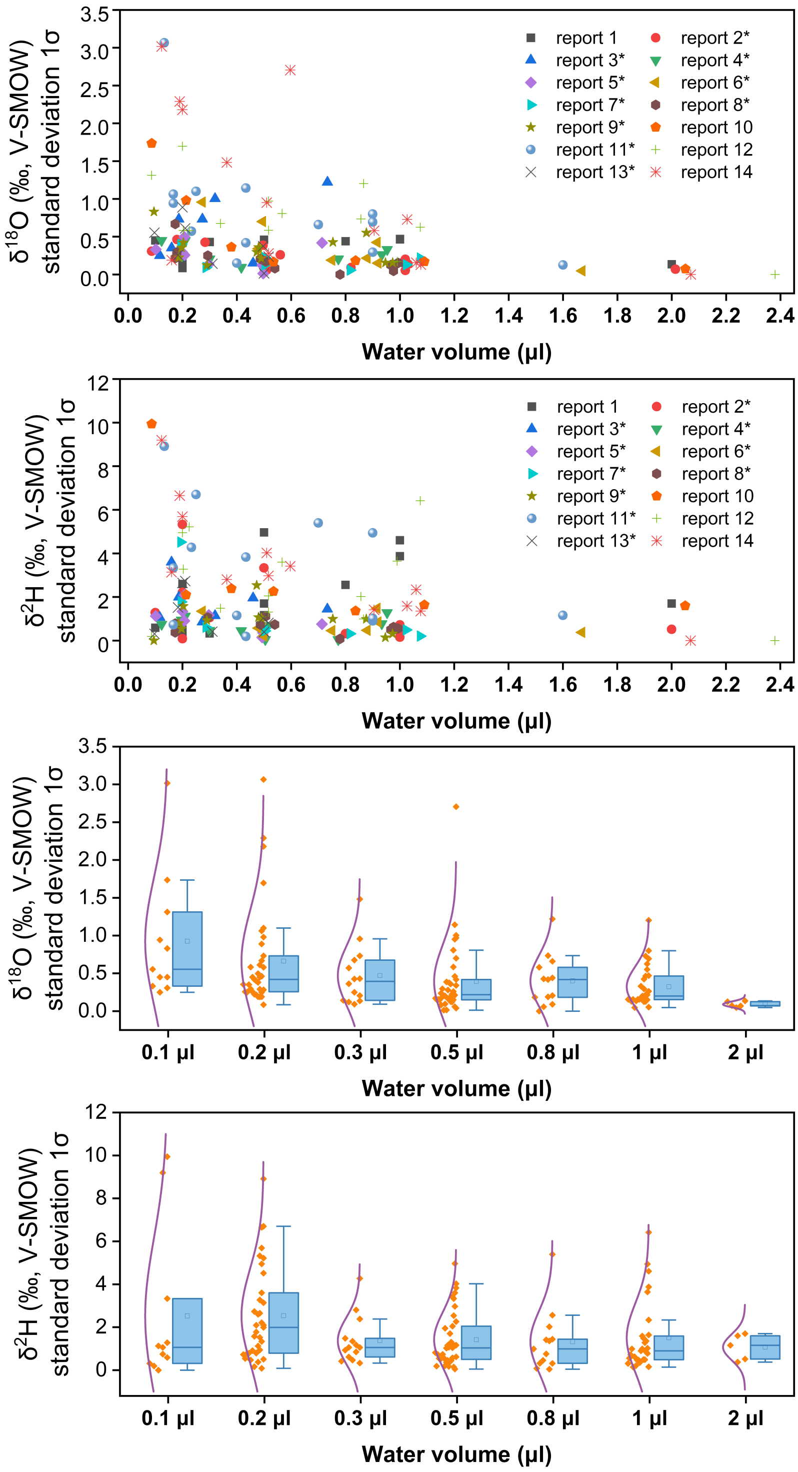

Figure 4.9. Relationship between the standard deviation (1σ) of δ^{18}O and δ^{2}H values and water volume. The upper panels show SD variations with water volume. Water volume and SD are calculated from a set of capillary measurements for each water volume of different standard water. The lower panels display box plots of SD for δ^{18}O and δ^{2}H where water volume refers to the filled volume in the capillaries. Box edges represent the first and third quartiles, the line inside indicates the median. The range of whiskers is outlier (coef=1.5). The curve next to it shows the normal distribution curve of the SD value.

even. At water volumes close to 0.1 and 0.2 µl, the SD values fluctuated most significantly, with some data exceeding 2‰, reflecting a substantial increase in the instability of δ^{18}O measurements under low water volume conditions.

For δ^{2}H the distribution range of SD values is broader, varying from 0.2‰ to 10‰, showing greater variability than δ^{18}O (Figure 4.9). Under larger water volumes (≥1 µl), the SD values are generally smaller and more stable, primarily ranging from 0.2‰ to 2‰, indicating higher measurement stability for δ^{2}H . However, as the water volume decreases, the SD values increase rapidly. Particularly when the water volume is between 0.1 and 0.5 µl, the SD values are highly dispersed and can reach 10‰ or more. At a water volume of 0.2 µl, the dispersion of SD values for both δ^{18}O and δ^{2}H is most pronounced. When the water volume approaches 0.1 µl, the SD values fluctuate the most, and the data points are more scattered. Since only one standard water capillary was used at 0.1 µl, the data volume is small, which results in less pronounced dispersion characteristics compared to the 0.2 µl volume. Overall, both δ^{18}O and δ^{2}H SD values show a significant increase as the water volume decreases. Under larger water volumes (>0.5 µl), both δ^{18}O and δ^{2}H exhibit better reproducibility, with more concentrated data distribution and higher measurement stability.

Cross-plotting of δ^{18}O and δ^{2}H measurements for each standard water across all reports was performed to identify systematic deviations from the standard water isotope values and potential fractionation effects (Figure S4.1 - S4.3 in Supplementary Information B.3). For Standard 1, the δ^{18}O and δ^{2}H values in report 11 and report 13 show an overall negative deviation relative to the isotope values of the standard, with report 14 being the most pronounced. The δ^{2}H values in report 12 are systematically lower than the standard by approximately 10-20‰, while the δ^{18}O deviation is not significant (Figure S4.1 in Supplementary Information B.3). For Standard 2, the distribution of isotope data points is more scattered compared to Standard 1 (Figure S4.2 in Supplementary Information B.3). Significant outliers, deviating from the standard isotope values, are observed in reports 3 and 11. In reports 1 and 14, both δ^{18}O and δ^{2}H are systematically higher than the standard values. The δ^{2}H values in report 12 are systematically higher than the standard by approximately 10-20‰, while the δ^{18}O deviation is not significant. The isotope values of Standard 3 are more dispersed (Figure S4.3 in Supplementary Information B.3) . For example, nearly all δ^{18}O and δ^{2}H values in reports 1 and 14 are significantly higher than the standard, with report 14 exhibiting the greatest degree of dispersion. The δ^{2}H values in report 11 are systematically higher than the standard by about 10‰, while the δ^{18}O values, although not showing a systematic shift, display greater variability compared to the δ^{2}H values. Additionally, the range of variation in δ^{18}O values provided in these reports, approximately 10-15‰, is significantly smaller than that of δ^{2}H which ranges from 40-50‰. Most of the isotope outliers occur for small water volumes (e.g. 0.1 and 0.2 µl), which is similar to the previous description of the change in standard deviation with water volume. The reproducibility of the isotope values deteriorates as the water volume decreases.

4.5 Summary

1. Under higher (1.0 µl) and moderate (0.5 µl) water volume conditions, the average isotope values in most reports are close to those of the standard water, with relatively small standard deviations. For δ^{18}O, the average measured values of the three standard waters typically deviate from the standard values by ±1‰ to ±2‰, with the standard deviation (SD) of repeated measurements generally under 0.5‰ (1σ). For δ^{2}H, the average measured values of the three standard waters typically deviate from the standard values by ±1‰ to ±3‰, with the SD of repeated measurements generally under 2‰.

2. Under lower water volume conditions (0.2 µl), some reports (e.g., 2, 3, 4, 5, 7, 8, 9, 13) still show small deviations, but the results are less favorable than those under higher and moderate water volumes. The deviations for average measured δ^{18}O and δ^{2}H values relative to the standard water range from ±1‰ to ±3‰ and ±2‰ to ±4‰, respectively. Some reports (e.g., 11, 12, and 14) show larger deviations from the standard water isotope values under this water volume.

3. Within laboratories, isotopic differences are mainly observed in relation to water volume. For larger volumes ($\geq$1 µl) in capillaries, the SD of δ^{18}O and δ^{2}H are relatively small, ranging from 0.2‰ to 1.0‰ and 0.2‰ to 2‰, respectively. For smaller volumes ($\leq$0.5 µl), especially at 0.1 and 0.2 µl, SD increases significantly. The SD of δ^{18}O can reach 1.5‰ or higher (with extreme values exceeding 3‰), while δ^{2}H exhibits even greater dispersion, with maximum values exceeding 10‰.

4. Most reports (13 out of 14) observed a systematic increase or decrease in δ^{18}O and δ^{2}H values as water amount decreased, with variations in direction and magnitude. The change in isotope values generally ranges from 2 to 5‰. Reports where glass capillaries were crushed together with Iceland spar predominantly exhibited a positive isotopic shift, while those without Iceland spar showed less consistent or no trends. However, further evidence is needed to confirm the role of Iceland spar in this shift.

5. The overall reproducibility of δ^{18}O (0.2–3.0‰) is better than that of δ^{2}H (0.2–10.0‰). The SD values of δ^{18}O and δ^{2}H show a significant increasing trend with decreasing water volume. The reproducibility of δ^{18}O and δ^{2}H measurements is better at larger water volumes (>0.5 µl).

6. In reports where the capillaries were crushed together with Iceland spar, the measured mean isotope values did not exhibit a systematic deviation from the standard water isotope values. There was also no significant difference in the mean isotope values compared to reports where the capillaries were not crushed with Iceland spar.

7. The most suitable water volume and isotope range for analysis may vary depending on the analytical setups and protocols. Most reports showed limited ability to handle high water volume (2 µl) samples. Overall, isotopic results from the 0.5–1 µl water volume range in all reports are closest to the expected values and exhibit good internal reproducibility.

Chapter 5

Variations in Regional Hydrological Environment and Human Activities Inferred From Oxygen and Hydrogen Isotope Composition of Stalagmite Fluid Inclusions in Southwest China

Key Points:

- **The variations in oxygen and hydrogen isotope composition values of fluid inclusion water primarily reflect environmental dry-wet changes and evaporation.**
- **In the mid-to late Holocene, four significant drought events in southwest China coincided with a weakening of Asian summer monsoon intensity.**
- **The oxygen isotope composition of inclusion water records regional environmental degradation events in southwest China caused by human activities during 950-1100 BP.**

The interpretation of carbonate δ^{18}O and δ^{13}C values from stalagmites in China is complex. Human activities during the mid-to-late Holocene have complicated the distinction between natural and anthropogenic influences on regional environmental changes. This chapter presents a record of $\delta^{18}O_{FI}$ and $\delta^{2}H_{FI}$ values from fluid inclusions in a stalagmite from southwestern China, covering 6290 to 690 years BP. By excluding measurement artefacts using Rayleigh fractionation models and improved methods, reliable results were obtained. The $\delta^{18}O_{FI}$ values were found to be sensitive to regional hydrological changes. High $\delta^{18}O_{FI}$ and $\delta^{2}H_{FI}$ values corresponded to periods of weak Asian summer monsoon. Notably, between 950 and 1150 BP, $\delta^{18}O_{FI}$ values showed a dramatic shift (7‰), reflecting environmental degradation due to cropland expansion from population migration.

This study builds upon the work of Duan et al. (2023b), who previously reported the chronology and stable isotope data of the stalagmite used in this chapter. I developed and implemented a research framework during my PhD to reconstruct past climate and environmental changes using the stable isotopes of fluid inclusions (δ^{18}O and δ^{2}H) in the stalagmite. To achieve this goal, I systematically carried out sample pretreatment and analytical procedures, completed the stable isotope measurements of fluid inclusion water, established a rigorous quality control protocol, and performed comprehensive data evaluation. By applying Rayleigh fractionation models in combination with improved analytical techniques, measurement artefacts and systematic errors were effectively minimized, ensuring the reliability of the dataset. Based on these robust data, I reconstructed regional hydrological and environmental variability, and identified significant climate signals associated with changes in the Asian summer monsoon and human activities.

5.1 Introduction

Southwest China is influenced by the ASM and exhibits high sensitivity to global climate change (Chen et al., 2021a,b; Duan et al., 2023b). In the past 38 years, the intensity and frequency of extreme precipitation events in southwestern China have shown an increasing trend (Shao et al., 2021). These extreme drought and flood events are primarily influenced by large-scale atmospheric circulation patterns (Shao et al., 2021; Wang et al., 2024; Yin et al., 2023b). With future global warming, climate aridification in this region is projected to intensify, leading to longer durations and higher frequencies of such events (Leng et al., 2015). Southwest China features extensive karst landscapes, characterized by a fragile ecological environment that is susceptible to environmental variations induced by monsoonal precipitation and human activities (Guo et al., 2023; Jiang et al., 2014). Consequently, southwest China hosts abundant speleothem archives spanning the Holocene. However, controversial interpretations of the climatic or environmental significance of speleothem proxies limit our ability to assess the relationship between ASM intensity and the regional hydrological environment more quantitatively. For instance, uncertainties persist regarding the sensitivity of speleothem calcite δ^{18}O (δ^{13}C) values to the thermodynamic and dynamic aspects of the ASM, including factors such as precipitation and monsoon intensity (e.g., Cheng et al. (2019); Liu et al. (2020); Wu et al. (2023b); Zhao et al. (2023b)). The interpretation of the climatic and environmental significance of stalagmite δ^{13}C (δ^{13}Cs) values and trace elements are also complicated by factors such as climate as well as local ecological and karst processes (Chen et al., 2021a,b; Fohlmeister et al., 2020; Li et al., 2018). This often results in poor reproducibility of δ^{13}Cs and trace elements records from different regions, thus precluding a comparison on a larger spatial scale. Comparing multiple indicators from speleothems, especially those sensitive to changes in the regional hydrological environment, across different regions helps overcome the limitations of relying on a single indicator for reconstructions (Chen et al., 2021a,b; Wu et al., 2023b; Yin et al., 2023b; Zhai et al., 2024).

Since the mid- to late Holocene, human activities have substantially disrupted the ecological environment's natural evolution process in southwest China, exacerbating environmental deterioration, notably manifested by the severe phenomenon of rocky desertification (Chen et al., 2021b; Duan et al., 2023b). The karst landscape in China covers an approximate area of 3.44 million km^2, with as much as 82% of the rocky desertification occurring predominantly in southwest China (Bai et al., 2013; Jiang et al., 2014; Li et al., 2009) (Figure 5.1). The ecological and hydrological environments in these areas are ongoing very fragile and subject to a serious ecological degradation crisis (Zhang et al., 2021f). The debate persists regarding whether rocky desertification in southwest China has been predominantly influenced by climate change or human activities across different periods (Chen et al., 2021b; Jiang et al., 2014). Using paleoclimate proxies directly linked to fluctuations in environmental dry-wet, such as effective moisture, and conducting regional comparisons could significantly contribute to elucidating this issue (Chen et al., 2021b; Duan et al., 2023b,c).

The hydrogen and oxygen isotope compositions of fluid inclusion water ($\delta^{18}O_{FI}$ and $\delta^{2}H_{FI}$) in stalagmites are increasingly used as proxies for paleo-precipitation δ^{18}O and δ^{2}H (δ^{18}Op and δ^{2}Hp) values to infer variations in hydrological environments such as terrestrial temperature (Affolter et al., 2019; Løland et al., 2022; Matthews et al., 2021), effective humidity (Wortham et al., 2022), and moisture sources (Fleitmann et al., 2022). The surface vegetation degradation and soil deterioration resulting from rocky desertification indirectly influence the soil's permeability and the precipitation infiltration process within the epikarst zone (Jiang et al., 2014), which in turn affects the cave drip rate and possibly also the evaporation experienced by inclusions water. Therefore, analyses of $\delta^{18}O_{FI}$ and $\delta^{2}H_{FI}$ also have the potential to reflect the evaporation processes occurring in the epikarst zone and cave.

Combined $\delta^{18}O_{FI}$, $\delta^{2}H_{FI}$, and δ^{18}Os values could enable a more robust discussion and

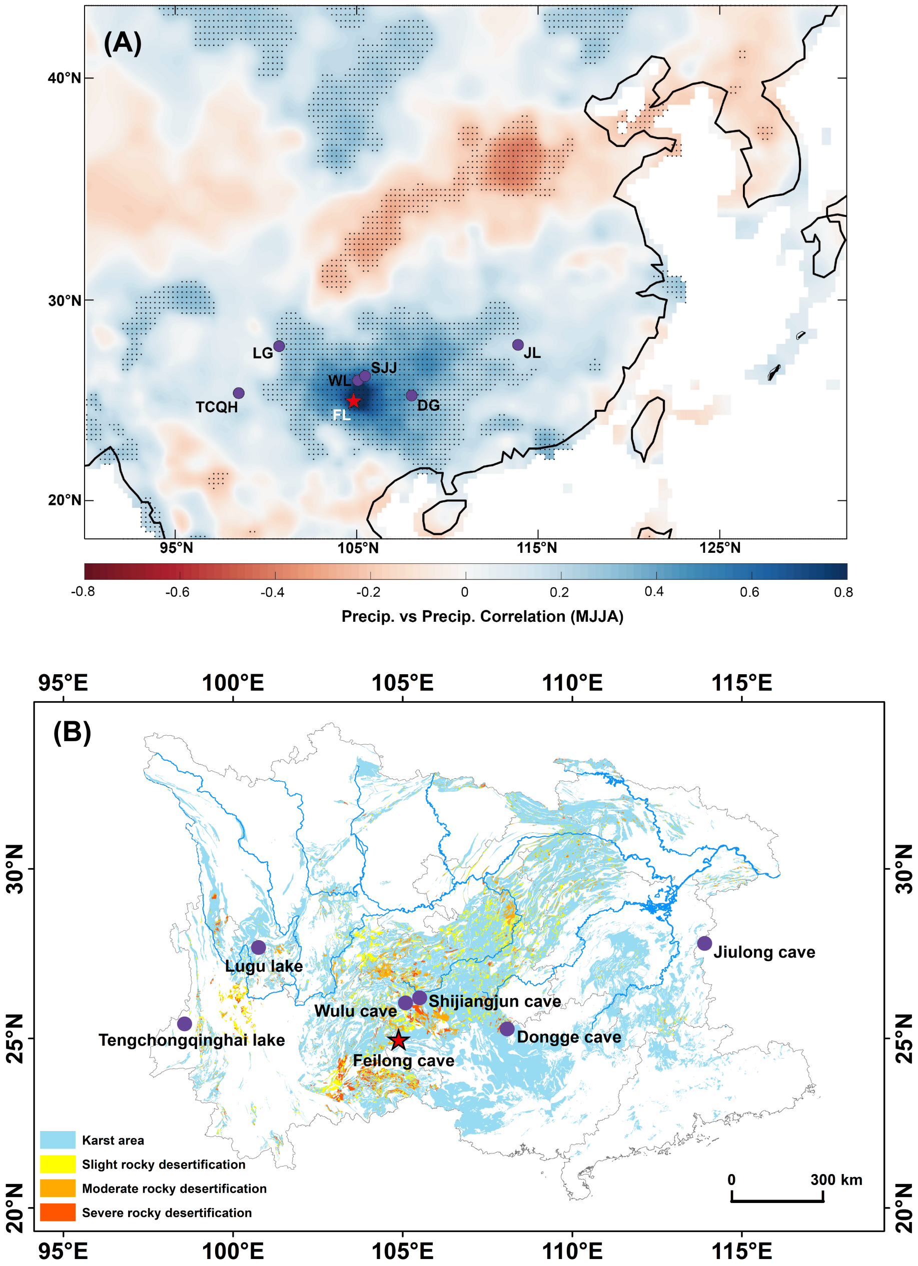

Figure 5.1. Location of study area. The correlation map of May - August precipitation between the study area and other regions from 1950 to 2019 C.E. The precipitation data are from the Global Precipitation Climatology Centre with a grid resolution of 0.25°×0.25° (Schneider et al., 2020). The red triangle indicates the locations of Feilong cave (this study). The red triangle indicates the locations Shijiangjun cave and Wulu cave (Chen et al., 2021a; Zhao et al., 2020), Dongge cave (Yang et al., 2017), Jiulong cave (Zhang et al., 2021a), Lugu lake (Zhao et al., 2021), and Tengchongqinghai lake (Xiao et al., 2023). (B) The karst areas of southwest China, and the distribution and extent of rocky desertification. Green colour indicates karst area. Yellow, orange, and red indicate slight, moderate, and severe rock desertification, respectively. Data from Bai et al. (2013); Li et al. (2009).

differentiation of thermodynamic and dynamic processes associated with the ASM, such as precipitation and atmospheric circulation. While isotopic analysis of fluid inclusions water significantly contributes to the comprehensive reconstruction of regional palaeohydrological changes, the preserved original signals of δ^{18}Op and δ^{2}Hp within inclusion might be modified, mainly in the form of large positive shifts relative to the local or global meteoric water line (LMWL/GMWL) (Fernandez et al., 2023; Matthews et al., 2021; Warken et al., 2022; Wortham et al., 2022). The reasons for this phenomenon are related to several assumptions. Firstly, evaporation of meteoric waters occurs within the epikarst zone or cave environments. Prolonged degassing of drip water and cave ventilation result in significant isotopic fractionation, leading to a significantly lower slope of $\delta^{2}H_{FI}/\delta^{18}O_{FI}$ compared to the MWLs (Warken et al., 2022; Wortham et al., 2022). However, there is also a potential impact from the measurement techniques. Recent studies have emphasized that heating of the sample during measurements produces significant isotopic artefacts (Fernandez et al., 2023). Evaporative water loss due to heating before the extraction/release of inclusion water for measurement could significantly increase the $\delta^{18}O_{FI}$ value (de Graaf et al., 2022; Fernandez et al., 2023). Therefore, the results must be carefully screened to exclude or correct anomalous data, or to produce more reliable results through improved measurement methods.

Here, this dissertation analyzed the hydrogen and oxygen composition of stalagmite fluid inclusion water from Feilong Cave in the monsoon region in southwest China, where research on the isotopic composition of stalagmite fluid inclusions is very scarce. By employing a Rayleigh fractionation model and improved measurement procedures, exclude artefacts in the isotopic signals and obtained reliable results. This dissertation have established a time series of δ^{18}O and δ^{2}H values of fluids entombed as inclusions during the mid-to late Holocene in this region. In combination with δ^{18}Os and δ^{13}Cs records, our approach thus provides a new pathway for evaluating the relationship between ASM intensity, anthropogenic activities, and the regional hydrological environment in southwest China.

5.2 Material and Methods

Feilong cave (24.97°N, 104.88°E, 1357 m above sea level) is located in Guizhou province, southwest China (Figure 5.1). The cave is about 1000m long, developed in Triassic dolomitic limestone, and the rock above the cave is about 60m thick (Liu et al., 2008b). The region has a subtropical humid monsoon climate that is affected by the ASM. Instrumental climate data from the nearest meteorological station (Xingyi station, 25 km northeast of Feilong cave) (http://www.cma.gov.cn/), reveal that the 1981-2010 averages of annual temperature and precipitation amount are 16.4°C and 1451 mm, respectively, while May-October precipitation accounts for 80% of the entire year (Duan et al., 2023b). The average temperature inside the cave is approximately 17.0°C and the humidity is close to 100% (Guo et al., 2006). The modern vegetation above Feilong cave primarily consists of subtropical shrubs. The FL2 stalagmite is about 430 mm long and grew between 6290 and 690 years before present (1950 CE). The chronology and calcite stable oxygen/carbon isotope results have been reported by Duan et al. (2023b).

The measurements of $\delta^{18}O_{FI}$ and $\delta^{2}H_{FI}$ values were performed at the Institute of Environmental Physics, Heidelberg University, using an analytical setup based on CRDS. Samples for analysis were cut using band saws near the FL2 stalagmite growth axis, with individual samples weighing between 0.30-1.00g. Stalagmite samples were loaded into copper tubes, either directly or enclosed in glass tubes, which were afterwards connected to the measuring line. Inclusion water hydrogen and oxygen isotope composition measurements were carried out on an artificial, stable, moist water vapour background of known $\delta^{18}O$ and $\delta^{2}H$ values. The stalagmite samples were crushed after heating at 120°C for 40-60 minutes, the released water was transported online to the CRDS system for analysis. The results of the analyses are presented relative to V-SMOW. For speleothem samples with water volumes greater than 0.2 µl, the reproducibility (1σ) is <0.5 ‰ for $\delta^{18}O$ values and <1.5 ‰ for $\delta^{2}H$ values (Weissbach et al., 2023).

5.3 Results

5.3.1 Petrographic Characterisation of Fluid Inclusions and Calcite Fabrics

The petrographic thin sections (25×40 mm) were prepared at 1 mm, 160 mm, 210 mm, 310 mm, and 350 mm from the top of the stalagmite. The petrographic characteristics of the stalagmite, including the typical shapes and distributions of fluid inclusions, were observed using a Keyence VHX-6000 digital microscope with transmitted light. The stalagmite is rich in fluid inclusions primarily arranged along growth surfaces (Figure S5.1 in Supplementary Information B.4). Layers with abundant inclusions alternate with layers with few or no inclusions, and many small inclusions are dispersed throughout the matrix. The sizes of these inclusions vary, ranging from a few µm to several tens of µm (Figure S5.1 in Supplementary Information B.4), and exhibit shapes such as pyriform, elongated, thorn-, or spindle-shaped. These inclusions are typically filled with water, but two-phase inclusions (water and air) are also present (Figure S5.1 in Supplementary Information B.4). The orientations of the inclusions are often parallel to the growth axis and are frequently concentrated within the same growth layer, likely captured within the same time interval. No evidence of dissolution or

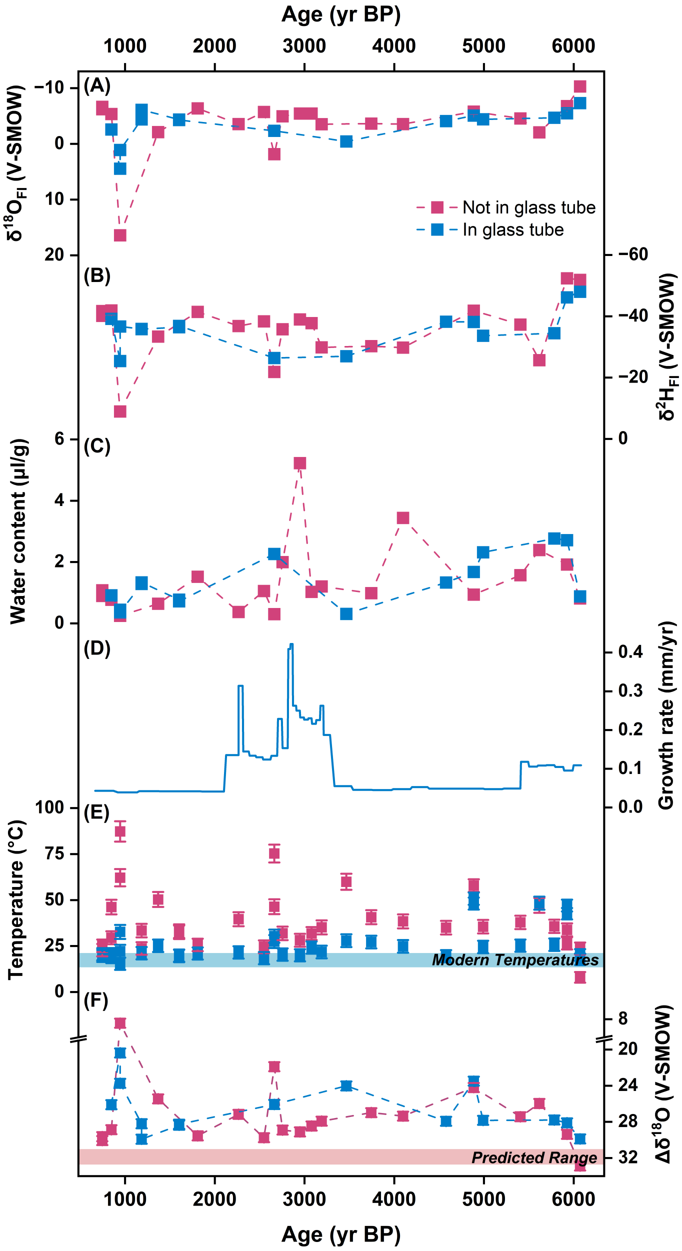

Figure 5.2. Results of fluid inclusion analysis of stalagmite FL2. (A) $\delta^{18}O_{FI}$. (B) $\delta^{2}H_{FI}$. The red and blue points indicate samples not in the glass tube and in the glass tube for Individual measurement. Measurement uncertainties (0.5‰ for $\delta^{18}O_{FI}$ and 1.5‰ for $\delta^{2}H_{FI}$) are not shown in (A) and (B) due to the large range of axes. (C) Water content of samples. (D) Calculated growth rates based on calcite stable isotope age model. (E) Calculation of palaeotemperatures based on the empirical equations of Tremaine et al. (2011), δ^{18}Os and $\delta^{2}H_{FI}$. The blue shading indicates the range of cumulative mean annual temperatures (13.3-21.1°C) at Xingyi station (25 km northeast of Feilong cave) from 1980 to 2010. (F) $\Delta\delta^{18}O$ values calculated using $\delta^{18}O_{FI}$ and δ^{18}Os values. The pink bars are the range of predicted $\Delta\delta^{18}O$ values determined using the mean δ^{18}Os, cumulative annual mean temperature, and empirical equations from Tremaine et al. (2011).

calcite crystal recrystallization was observed in the thin sections, indicating that these fluid inclusions are primary and contemporaneous with the host calcite. The two clear dark layers were found at about 13 mm (about 950 yr BP) of the stalagmite. These dark layers have distinct boundaries. Compared to the lighter layers, the darker layers have a loose sedimentary structure with more impurities and granular pores (Figure S5.2 in Supplementary Information B.4).

5.3.2 Comparison of Inclusion Water Isotopes Composition and Modern LMWL

A total of 34 measurements of fluid inclusions in speleothem samples were conducted at 25 different depths (Table S5.1 in Supplementary Information B.4). Of these, 19 samples were directly loaded into copper tubes for measurement, while the remaining 15 were enclosed in glass tubes. Comparative measurements in and out of glass tubes were performed on samples from five growth layers. Overall, the water content of all samples from different depths varied between 0.24 and 5.22 μl/g (Figure 5.2). The $\delta^{18}O_{FI}$ and $\delta^{2}H_{FI}$ values ranged from -6.76 to 16.40‰ and -52.36 to -8.95‰, respectively. The Pearson correlation analysis revealed a significant positive correlation between $\delta^{18}O_{FI}$ and $\delta^{2}H_{FI}$ values (r=0.83, p<0.01). The $\delta^{18}O_{FI}$ and $\delta^{2}H_{FI}$ results are compared with $\delta^{18}Op$ and $\delta^{2}Hp$ data from the Global Network of Isotopes in Precipitation (GNIP) station in Guiyang, located approximately 250 km northeast of the cave site, over a 4-year period (1988-1992). Compared to modern precipitation isotopes, most measurements are at the unweighted average of the rainy (May-October) and dry (November-April) season isotopic values distributions (Figure 5.3). Some values also showed significant positive deviations, with isotopic values exhibiting notable enrichment compared to modern precipitation. This is reflected in the fitted slope (1.45 ± 0.19, $r^2 = 0.63$), which is considerably lower than both the GMWL and the LMWL. Additionally, some outliers exhibited unreasonably high isotopic values.

5.3.3 Temporal Variation in the Inclusion Water Isotopes Composition and Calculated Paleo-temperatures

Between 6290 and 1600 yr BP, the variation of $\delta^{18}O_{FI}$ and $\delta^{2}H_{FI}$ ranges from +16.40 to -10.30‰ and -8.95 to -52.36‰, respectively (Figure 5.2). At about 5600, 3450, and 2260 yr BP, $\delta^{18}O_{FI}$ and $\delta^{2}H_{FI}$ exhibited millennial-scale positive fluctuations with average amplitudes of 2 to 6‰ and 4 to -14‰, respectively. The most significant fluctuations in $\delta^{18}O_{FI}$ and $\delta^{2}H_{FI}$ records occur about 1000 yr BP, with $\delta^{18}O_{FI}$ and $\delta^{2}H_{FI}$ values increasing rapidly by about 18‰ and about 40‰, reaching their most positive values around 950 yr BP and decreasing swiftly after that (Figure 5.2).

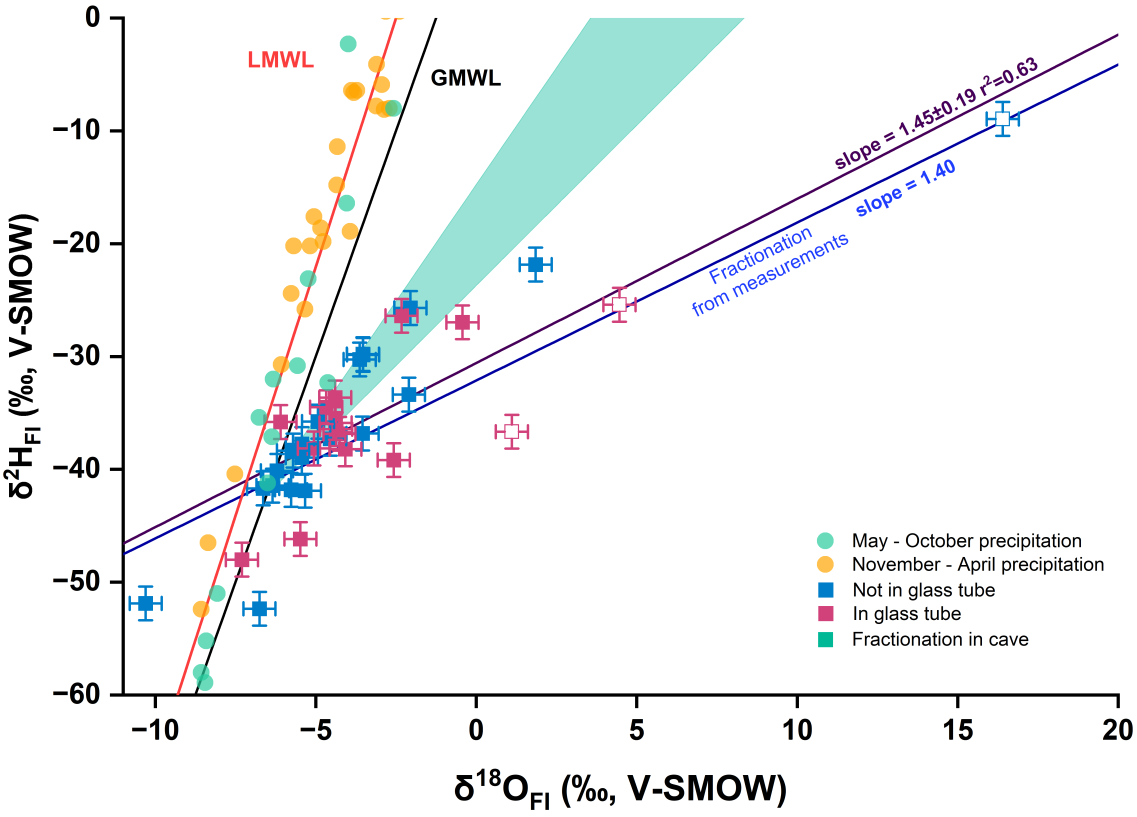

Figure 5.3. Results of δ^{18}O vs. δ^{2}H values of stalagmite FL2 The cyan and yellow points indicate precipitation isotope data from May - October and November - April, respectively (1988-1992). δ^{18}Op and δ^{2}Hp data are from the Global Network of Isotopes in Precipitation (GNIP) Guiyang site (about 250 km northeast of the cave site). The blue and red square points indicate inclusions samples measured not in and in glass tubes, respectively. The hollow points indicate samples of about 13 mm growth layer. The orange and black straight lines indicate LMWL ($\delta^{2}\mathrm{Hp} = 8.8 \times \delta^{18}\mathrm{Op}$ + 22‰ r^2=0.98) and GMWL. The purple line indicates the fitted line for all the $\delta^{18}\mathrm{O}_{\mathrm{FI}}$ and $\delta^{2}\mathrm{H}_{\mathrm{FI}}$ data ($\delta^{2}\mathrm{H}_{\mathrm{FI}} = 1.45 \times \delta^{18}\mathrm{O}_{\mathrm{FI}}$ - 32.15‰ r^2=0.63). The dark blue line indicates the predicted occurrence of isotopic Rayleigh fractionation processes in the measurement setup (slope=1.40). The cyan shading indicates the range of slopes predicted by the Rayleigh fractionation model for evaporation in cave (2.84-4.13).

In the absence of modern monitoring data, the widely accepted empirical formula from Tremaine et al. (2011) is used to calculate paleotemperatures based on δ^{18}Os and $\delta^{18}\mathrm{O}_{\mathrm{FI}}$ values. Additionally, paleotemperatures are also calculated using the more recent equation proposed by Daëron et al. (2019). The results show that the calculations of the two equations are very similar and almost indistinguishable within uncertainty range (Figure S5.3 in

Supplementary Information B.4). However, most of these estimates are unrealistically high compared to this region's modern cumulative annual mean temperatures (13.3-21.1°C) (Figure 5.2) (Figure S5.3 in Supplementary Information B.4). Based on the inversion of $\delta^{18}O_{FI}$ derived via the LMWL using $\delta^{2}H_{FI}$ values, our calculations still yield unreasonably high temperatures but considerably less deviant from modern temperatures (Figure 5.2) (Figure 2E and S3). Using the empirical formula from Tremaine et al. (2011) and δ^{18}Os, the difference between the δ^{18}O value of cave drips at calcite formation and $\delta^{18}O_{FI}$ ($\Delta\delta^{18}$O) was calculated. The range of variation in $\Delta\delta^{18}$O was predicted based on the mean value of δ^{18}Os and the cumulative annual mean temperature (13.3-21.1°C) (Figure 5.2). The results show that $\Delta\delta^{18}$O is consistent with the pattern of calculated temperature variations and moves away from the predicted range for most periods. Especially during about 5600, 3450, and 2260 yr BP, positive fluctuations occurred in inclusion temperatures, accompanied by corresponding decreases in $\Delta\delta^{18}$O with the most significant shifts in both occurring about 1000 yr BP (Figure 5.2). This phenomenon suggests that these samples potentially significant isotopic fractionation, with the original δ^{18}Op and δ^{2}Hp information undergoing varying degrees of modification. Preheating at 120°C prior to measurement may cause notable isotope fractionation. However, replicate samples from four growth layers measured both in and outside of glass tubes show no clear differences in isotope values (Figure S5.4 in Supplementary Information B.4). Only the isotope values of replicate samples from one growth layer show significant differences between measurements taken in and outside of glass tubes. Compared to measurements without glass tubes, $\delta^{18}O_{FI}$ and $\delta^{2}H_{FI}$ values measured within glass tubes are lower and closer to the GMWL (Figure S5.4 in Supplementary Information B.4).

5.4 Discussion

5.4.1 Influence of Evaporation from Natural and Artificial Sources on the Isotopic Fractionation of Inclusions

Evaporation and Isotopic Fractionation from Measurement

Given the pronounced enrichment characteristics of isotope values in some measurements, along with the two distinct isotope variation patterns observed in different growth layers with and without the use of glass tubes, it is necessary to carefully evaluate whether these isotope results are suitable for environmental reconstruction. For significantly enriched isotope values, which deviate from the GMWL and LMWL, one potential explanation could be evaporation within the cave during stalagmite deposition (Warken et al., 2022). Another possibility is that the heating process of about 40-60 min (120°C) before sample crushing may cause inclusions water leakage and evaporation (Fernandez et al., 2023). Two methods were employed to identify potential artifacts during the measurement process. First, a Rayleigh evaporation model, similar to that of Fernandez et al. (2023), was used to assess the fractionation generated during the measurements. Second, the samples were encapsulated in glass tubes during measurement, a method known to effectively reduce moisture loss and isotopic fractionation caused by preheating.

The Rayleigh fractionation model predicts evaporation slopes resulting from the measurement process from 1.35 to 1.46 (the mean of 1.40 ± 0.06, 1σ) (Supplementary text) (Figure 5.3). The very enriched outliers are distributed along the predicted evaporation slope (Figure 5.3), which implies that these samples experienced significant water loss and isotopic fractionation before being crushed. Alternative evidence of substantial isotope fractionation from preheating before measurements involves comparing samples closed within glass tubes and those subjected to direct measurements. In most cases (4 out of 5 growth layers), there is no significant difference between samples measured in and not in glass tube (Figure S5.4 in Supplementary Information B.4). The reason may be attributed to two potential factors. Firstly, most inclusions remain well preserved, precluding water leakage induced by heating. Secondly, the leaking inclusions will completely evaporate after prolonged exposure to high temperatures (120°C, 40-60min) and therefore will not affect the final isotopic results. Consequently, throughout the temporal series, the isotope value differences between samples inside and outside glass tubes are not very large (Figure 5.2).

The only possibly “leaked” sample occurred at about 13 mm from the stalagmite, coinciding with a pronounced alteration in the deposition morphology of the stalagmite (Figure S5.2 in Supplementary Information B.4). The $\delta^{18}O_{FI}$ and $\delta^{2}H_{FI}$ values measured in glass tubes are lower and closer to the GMWL in comparison to measurements not in the glass tube (Figure S5.4 in Supplementary Information B.4). Petrographic observations show that these samples from the about 13mm dark layer are structurally loose and full of pores (Figure S5.2 in Supplementary Information B.4). In 120°C heating, the pressure of the fluid will increase with the increase in temperature. Water in such inclusions may be lost by evaporation along crystal boundaries of loose calcite and pores in stalagmites, leading to significant isotopic fractionation. The altered depositional morphology of the stalagmite has resulted in unstable inclusions that are more susceptible to leakage under heat (Figure S5.2 in Supplementary Information B.4). The measurements were entirely distributed along the evaporation slope caused by the measurements, further Supplementary our suspicions (Figure 5.3). However, samples measured in glass tubes should be able to preserve potentially pre-evaporated water from the sample, thereby reducing isotopic fractionation induced by heating. As a result, these measurements are closer to the original isotopic values of the inclusion water. Based on petrographic examination and comparative measurements in glass tubes, it is suggested that the inclusions in the samples at approximately 13 mm may have undergone significant evaporation and isotopic fractionation during preheating prior to measurement. Consequently, the measurements at around 13 mm that were not taken in glass tubes have been rejected, and only the values obtained from two measurements within the glass tubes were used. In contrast, the depositional morphology of the rest of the stalagmite remained stable, with inclusions distributed in bright layers characterized by stable calcite depositional structures, in which water was well preserved (Figure S5.2 in Supplementary Information B.4). Repeated measurements of samples inside and outside the glass tube also revealed no significant differences (n=4). Thus, for samples from other depths of the stalagmite, no evidence of significant preheating-induced evaporation was observed, making them suitable for paleoclimate and environmental reconstruction. Finally, except for the measurements at approximately 13 mm, where those not taken in the glass tube were excluded, the average isotopic values from repeated measurements at the same depth were used. This resulted in a total of 25 isotopic values for inclusions at different depths in the stalagmite. The uncertainty of the mean value is calculated based on the error propagation principle, by summing the squares of the uncertainties of the two measurements, taking the square root, and then dividing by the number of measurements (Table S5.2 in Supplementary Information B.4).

It is suggested that thorough petrographic examination and repeated comparative measurements can yield more reliable $\delta^{18}O_{FI}$ and $\delta^{2}H_{FI}$ results. Even for samples prone to inclusion leakage, the use of glass tubes may still provide more reliable results that closely approximate the original isotopic composition of the inclusion water. Some outliers exhibit noticeable enrichment, but the petrology and the deviation of these values from the Rayleigh fractionation slope suggest that these samples are minimally affected by analytical artifacts (Figure 5.2). The anomalous isotope values may thus rather reflect the “true” composition of the fluid water, potentially influenced by processes such as cave evaporation.

Isotopic Fractionation of Fluid Inclusions Water Caused by Cave Evaporation

Climate-driven cave ventilation and drip rates significantly affect the evaporation of stalagmite surface water, which may modify the isotope signatures of inclusion water (Deininger et al., 2012; Lyu et al., 2024; Warken et al., 2022; Wortham et al., 2022). Considering the close correlation between cave evaporation processes and relative humidity (Lyu et al., 2024), the Craig-Gordon model was also used to simulate the potential isotopic fractionation occurring within the cave (Gonfiantini et al., 2018) (Text S5.1 in Supplementary Information B.4). This model explains the combined effects of equilibrium and kinetic isotope fractionation during the phase transition from liquid water to vapor and is widely used to simulate the isotope composition of natural water systems such as oceans, lakes, and atmospheric water.

The slope predicted by the evaporation model in the cave is 2.84-4.13 (Text S5.1 in Supplementary Information B.4). Considering the uncertainties, almost all the isotope-enriched data are distributed within this slope range (Figure 5.3), indicating that the isotopic anomalies could be explained by cave evaporation (Figure 5.2). It is common for cave evaporation to lead to isotopic enrichment of inclusions, and our evaporation slopes are comparable to previous reports (Warken et al., 2022; Wortham et al., 2022). There are also some outliers that are below the predicted fractionation line, but also show a clear trend towards enrichment. This may be attributed to changes in the initial hydrogen and oxygen isotope composition of the drip water preserved in these samples. In general, the δ^{18}O and δ^{2}H values of cave drips inherit the annual weighted isotopic values of local precipitation (Baker et al., 2019; Duan et al., 2016). This feature is also shown by most of our results, with data points clustered around the mean positions of isotopic distributions during the rainy (May to October) and dry (November to April) seasons (Figure 5.3). The observation that some values are slightly lower than the annual mean precipitation values suggest they may be biased towards the rainy season's δ^{18}Op and δ^{2}Hp information. This could be due to seasonal increase in monsoon precipitation during certain periods, resulting in lower annual weighted mean values of δ^{18}Op and δ^{2}Hp. As a result, the $\delta^{18}O_{FI}$ and $\delta^{2}H_{FI}$ values tend to be low overall, leading to a decrease in the intercept of the fractionation equation.

Positive shifts in δ^{18}O and δ^{2}H values of cave drip and inclusion water due to evaporation in soils, epikarst zones, and cave environments are widespread phenomena (Baker et al., 2019; Duan et al., 2016; Horita et al., 2008). The high correlation between the Intrinsic Mode Function (IMF) 1 of δ^{18}Os and δ^{13}Cs ($r=0.99$, $p<0.01$) that were isolated using EEMD demonstrates kinetic isotope effects during stalagmite deposition (Duan et al., 2023c; Wu and Huang, 2009) (Figure S5.5 in Supplementary Information B.4). The IMF1 extracted from δ^{18}Os and δ^{13}Cs primarily reflects changes on interannual to decadal time scales (periods less than 50 years). The significant positive covariation between δ^{18}Os and δ^{13}Cs is partly attributed to isotopic disequilibrium fractionation caused by prior calcite precipitation, which occurs due to rapid CO_2 degassing from dripping water on cave ceilings and stalactite/stalagmite surfaces (Duan et al., 2023c). Upon entering the cave, dripping water experiences a rapid drop in PCO_2 , triggering CO_2 degassing. The δ^{18}O value of the precipitated calcium carbonate mirrors the δ^{18}O value of HCO_3^-, which was in isotopic equilibrium with the water (Dreybrodt and Scholz, 2011). After the rapid precipitation of calcite, the residual water on the stalagmite surface is affected by evaporation. On one hand, the timescale for oxygen isotope exchange and equilibrium between water and HCO_3^- is significantly longer than that for calcite deposition (Liu and Ding, 1998). On the other hand, evaporation accelerates the depletion of HCO_3^- and Ca^{2+} ions. As most calcium ions precipitate during the initial stage of CO_2 degassing, the calcite formed later becomes negligible due to the exponential decline in calcium concentration (Deininger et al., 2012; Dreybrodt and Scholz, 2011; Scholz et al., 2009). Even if significant evaporation enriches the isotopic values in the residual dripping water, this enrichment affects only a small portion of the precipitated calcite (Deininger et al., 2012).

Furthermore, the continuous addition of new dripping water and ongoing calcite deposition further limit the impact of evaporation on the isotopic composition of calcite. Therefore, short-term evaporative fractionation has limited impact on δ^{18}Os variations over centennial to millennial scales driven by climate changes and human activities (Duan et al., 2023c; Warken et al., 2022), as supported by the broad similarity of δ^{18}Os and δ^{13}Cs to the stalagmite records from southern China (Chen et al., 2021a; Yang et al., 2017; Zhang et al., 2021a) (Figure 5.4). In contrast, evaporation significantly enriches the δ^{18}O and δ^{2}H values of dripping water, which are subsequently captured in fluid inclusions and result in isotopic compositions not in equilibrium with the surrounding calcite.

The evaporation of water on the surface of stalagmite is typically influenced by factors such as the relative humidity of cave air, cave ventilation, and drip rate (Deininger et al., 2012; Fairchild et al., 2006; Lyu et al., 2024). Especially in subtropical monsoon regions, seasonal temperature differences between cave air and outside atmosphere tend to regulate the strength of ventilation (Lyu et al., 2024; Vieten et al., 2016). However, on the centennial to millennial scale, our $\delta^{18}O_{FI}$ record does not exhibit similar variation patterns with reconstructions and simulations on the coldest month temperatures or interannual temperature anomalies in southwest China (Shi et al., 2021; Xiao et al., 2023) (Figure S5.6 in Supplementary Information B.4). However, the possibility that the variation in $\delta^{18}O_{FI}$ could be influenced by cave ventilation, resulting from seasonal and interannual temperature variations, cannot be excluded. On the other hand, the positive anomalies in $\delta^{18}O_{FI}$ values may be associated with a more arid environment and reduced precipitation.

A comparably arid environment increases the extent of oxygen and hydrogen isotope evaporative fractionation of precipitation in soil, surface karst, or cave environments. The reduced supply of cave drip water also results in slower drip rates and longer degassing times. The inclusion water experienced significant evaporation before being confined, resulting in higher $\delta^{18}O_{FI}$ and $\delta^{2}H_{FI}$ values relative to wetter environments. On the millennial scale, the frequent fluctuations of $\delta^{18}O_{FI}$ can thus be interpreted to indicate variations in environmental dry vs. wet conditions over different periods. Compared to δ^{18}Os, the larger amplitude $\delta^{18}O_{FI}$ provides the most direct and pronounced evidence of evaporation in soils and epikarst zones, as well as in cave environments.

5.4.2 Variations in Hydroclimate in Southwest China Inferred From Fluid Inclusion Isotope Records

Millennial Scale Dry-wet Variations In the Mid-to Late Holocene

Our new record presents the consistency between the weakening of ASM and the reduction in precipitation during the Holocene, as revealed by the strong link between δ^{18}Os, δ^{13}Cs and $\delta^{18}O_{FI}$ (Figure 5.4). Phases with $\delta^{18}O_{FI}$ values significantly or consistently greater than the mean are defined as positive anomaly phases. The five $\delta^{18}O_{FI}$ positive anomaly phases, occurring around 950 yr, 1360 yr, 2260 yr, 3450 yr, and 5600 yr BP, correspond to weak ASM intervals during the mid- to late Holocene, as indicated by δ^{18}Os (Figure 5.4). Compared to the weak monsoon events identified by previous δ^{18}Os-based positive anomalies (Duan et al., 2023b), the $\delta^{18}O_{FI}$ -based positive anomaly phases are fewer and include some strong monsoon events. This difference partly arises from the lower resolution of $\delta^{18}O_{FI}$ which is insufficient to capture decadal to centennial scale changes. The $\delta^{18}O_{FI}$ positive anomaly phases shows an overall high mean value of δ^{18}Os, with very high internal variability and frequent positive excursions (Figure 5.4). $\delta^{18}O_{FI}$ positive anomaly phases reflects a long period (centennial to millennial scales) of weakened monsoon intensity and long-term environmental changes that promote stronger evaporation processes. These trends do not conflict with the short-term fluctuations in ASM intensity on decadal scales, as indicated by δ^{18}Os. This interpretation is further supported by the millennial scale IMF components of δ^{18}Os and δ^{13}Cs (IMF5, with a period of about 1000 years) (Figure S5.5 in Supplementary Information B.4). The trends of these components are nearly identical with $\delta^{18}O_{FI}$ highlighting the robustness of $\delta^{18}O_{FI}$ as an indicator of regional long-term evaporation and water balance variations. The $\delta^{18}O_{FI}$ positive anomaly phases are also evident in other δ^{13}Cs records from southern China (Figure 5.4), with δ^{13}Cs being higher during these positive anomaly phases (Figure 5.4). Given the stable regional environmental conditions of the mid-to-late Holocene, significant vegetation replacement due to natural factors is unlikely (Chen et al., 2021a,b). Instead, δ^{13}Cs reflects changes in vegetation density, soil CO_2 , and microbial activity (Li et al., 2018; Yang et al., 2017), indicating that these phases exhibit broad spatial correlation and contribute to widespread environmental degradation.

During the $\delta^{18}O_{FI}$ positive anomaly phases, $\delta^{18}O_{FI}$ exhibits larger amplitudes than δ^{18}Os and δ^{13}Cs , implying that inclusion water isotopes may be more sensitive to centennial-millennial hydroclimate shifts (Figure 5.4). This is because $\delta^{18}O_{FI}$ values reflect more significant evaporation processes in caves, karsts, and soils, which result from prolonged reductions in monsoon precipitation. The overall coefficient of variation (C.V = standard deviation/mean) of the $\delta^{18}O_{FI}$ sequence is 125% compared to only 5% for δ^{18}Os. Except for the 950 yr BP, the remaining four $\delta^{18}O_{FI}$ positive anomaly phases have variations of about 1‰

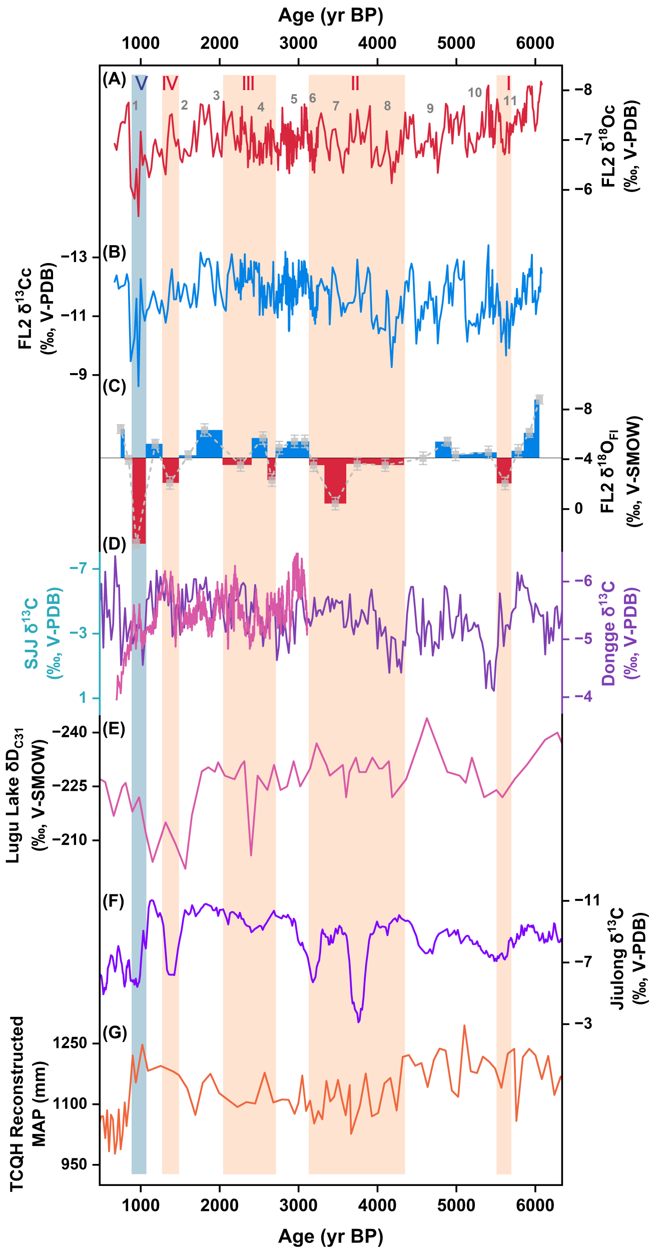

Figure 5.4. FL2 stalagmite calcite and fluid inclusion water stable isotope records and comparison with other records. (A) and (B) FL2 δ^{18}Os and δ^{13}Cs records from RN961. (C) FL2 $\delta^{18}O_{FI}$ record. Data potentially affected by analytical artifacts is removed, repeatedly measured samples from the same growth layer were averaged. The uncertainty of the mean value is calculated based on the error propagation principle, by summing the squares of the uncertainties of the two measurements, taking the square root, and then dividing by the number of measurements. (D) The δ^{13}Cs records of stalagmites from Dongge cave (purple) and Shijiangjun cave (pink) (Chen et al., 2021a; Yang et al., 2017). (E) Lugu lake δD_{C31} record (Zhao et al., 2021). (F) The δ^{13}Cs record of stalagmite from Jiulong cave (Zhang et al., 2021a). (G) Reconstructed mean annual precipitation (MAP) from Tengchongqinghai lake (Xiao et al., 2023). The orange and cyan bands indicate $\delta^{18}O_{FI}$ positive anomaly phases.

to 2‰ in δ^{18}Os and δ^{13}Cs, while $\delta^{18}O_{FI}$ records variations of 2‰ to 4‰ (Figure 5.4). Since inclusions remain sealed for much longer than the period of calcite deposition, the prolonged CO_2 degassing process resulting from reduced precipitation leads to more pronounced isotopic fractionation. Consequently, on centennial to millennial timescales, $\delta^{18}O_{FI}$ values may reflect amplified signals of climatic and environmental changes, exhibiting greater amplitudes than δ^{18}Os. Duan et al. (2023b) emphasise from δ^{18}Os-based reconstructions that the ENSO was an important driver of ASM variability during the Holocene on decadal to centennial scale. To investigate the factors influencing regional evaporation and water balance on centennial to millennial scales, the multi-indicator records were compared with reconstructions of solar activity and ENSO (Figure 5.5) (Figure S5.7 in Supplementary Information B.4). The results show that four $\delta^{18}O_{FI}$ positive anomaly phases (I-IV) in the mid- to late-Holocene were associated with reduced solar activity (Figure S5.7 in Supplementary Information B.4) and El Niño-like conditions (Chen et al., 2002) (Figure 5.5). ENSO regulates the intensity of ASM circulation and variations in moisture through water source areas ocean-atmosphere coupling (Jian et al., 2022). In southern China, during El Niño-like conditions, the Walker Circulation weakens and shifts eastward, causing its descending branch to extend over northeastern India and southwestern China, suppressing convection in the region (Kumar et al., 2006; Ropelewski and Halpert, 1987; Tan et al., 2017). El Niño has also led to the weakening of the Indian summer monsoon (ISM) and persistent negative sea surface temperature anomalies in the western tropical Pacific (Figure 5.4 and Figure 5.5). The ISM and the western tropical Pacific warm pool are significant moisture sources for ASM (Dang et al., 2020; Jian et al., 2022; Xue et al., 2023). These factors collectively contribute to a reduction in the transport of summer monsoon moisture to southwest China (Figure S5.8 in Supplementary Information B.4).

Solar activity is hypothesized to influence the ENSO and the ASM via changes in low-latitude processes (Lu et al., 2019a; Sun et al., 2024; Zhai et al., 2024). ENSO activity can amplify the impact of solar radiation on hydrological and climatic changes in the ASM region on centennial timescales (Chen et al., 2023; Reimer et al., 2020; Zhai et al., 2024). When solar radiation increases, the thermal contrast between the subtropical Asian continent and the Indian Ocean intensifies, leading to increased precipitation over India and the Bay of Bengal, as well as an easterly anomaly in the Indian Ocean-Pacific warm pool (Sun et al., 2024). Enhanced solar radiation also increases evaporation in the cloud-free regions of the subtropical Pacific, with moisture transported by easterlies to the equatorial western Pacific, increasing precipitation and strengthening the easterly anomaly (Meehl et al., 2008). These combined changes trigger a La Niña-like state and stronger monsoon circulation (Sun et al., 2024; Zhai et al., 2024). Conversely, a decrease in solar radiation may lead to the occurrence of an El Niño-like condition on a centennial scale. Previous studies have

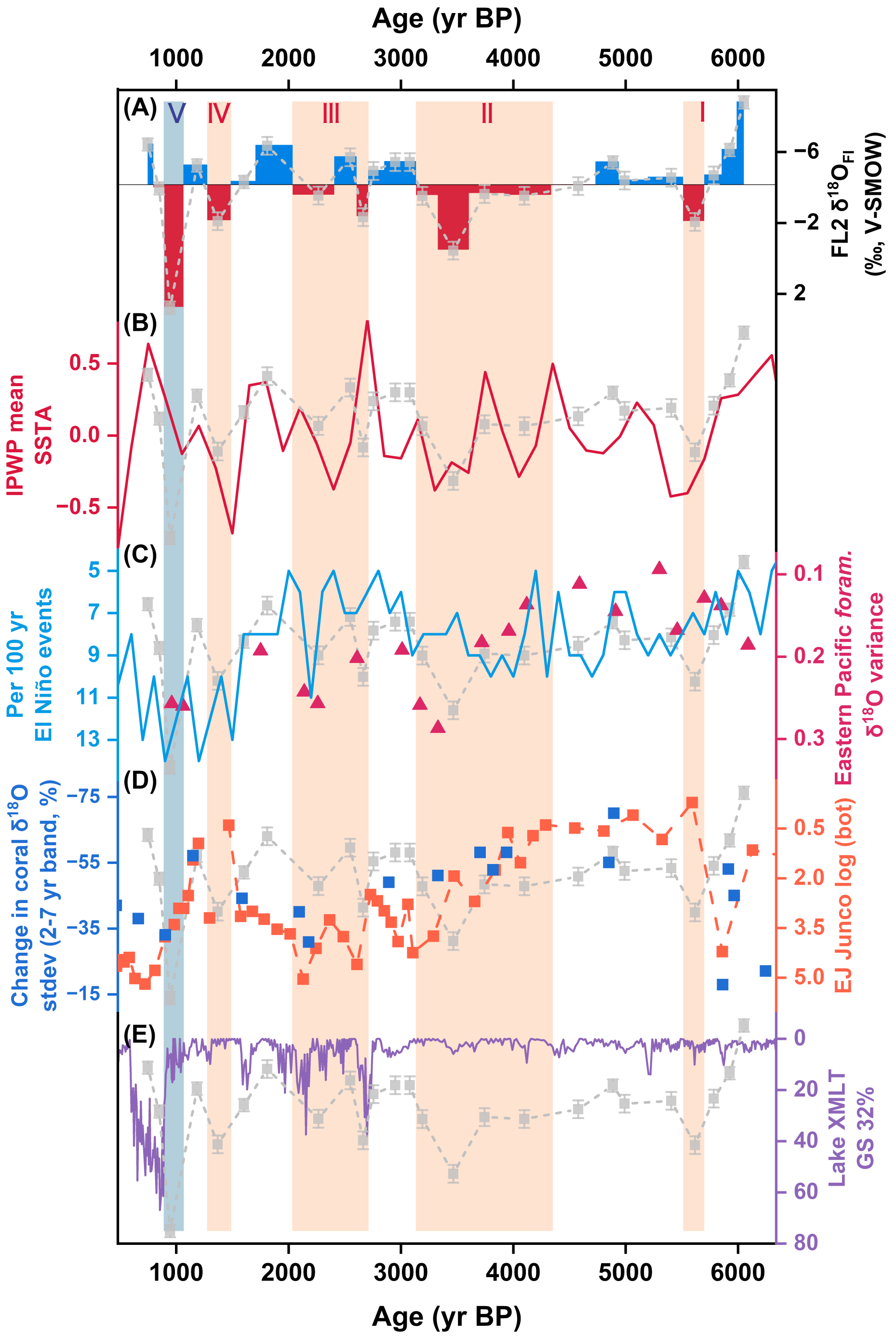

Figure 5.5. Comparison of fluid inclusion δ^{18}O records and forcing mechanisms from low latitudes. (A) FL2 $\delta^{18}O_{FI}$ records. (B) Mean sea surface temperature anomaly (SSTA) of the IPWP records (Dang et al., 2020). (C) The blue line indicates El Niño events per 100 years (Mark et al., 2022). The red triangles indicate estimates of ENSO variability from eastern equatorial Pacific foraminifera δ^{18}O variance (Koutavas and Joanides, 2012). (D) The blue square indicates changes in ENSO variance based on fossil coral δ^{18}O values in the Northern Line islands relative to 1968-1998 C.E. values (Cobb et al., 2013). The orange square indicates the log scale of botryococcene concentration in El Junco Lake sediments (Zhang et al., 2014). The grey records indicate FL2 $\delta^{18}O_{FI}$ records.

highlighted the influence of ENSO and Solar activity on ASM intensity (Duan et al., 2023b; Lu et al., 2019a; Zhai et al., 2024), such as significant solar activity cycles in δ^{18}Os and δ^{13}Cs (Figure S5.7 in Supplementary Information B.4). Our records provide new evidence that ENSO and solar activity regulate not only ASM circulation but also regional evaporation and water balance processes. With continued weakening of solar radiation in the future (Matthes et al., 2017), solar activity may induce more frequent centennial-scale fluctuations in regional water balance.

The short-term negative fluctuations in δ^{18}Os during the positive $\delta^{18}O_{FI}$ anomaly phases also indicate minor strong monsoon events. This suggests that intervals of prolonged dry hydrological conditions (i.e., local/regional water vapor deficits) are also accompanied by fluctuations in monsoon strength. This could be partly attributed to the measurement resolution of the fluid inclusions being lower than that of calcite powder. Secondly, shorter and less significant ENSO events also cause a weaking ASM circulation and decrease in δ^{18}Op and δ^{18}Os values, but the extent of regional precipitation reduction and its long-term effect on local water balance and sensitivity to evaporation in the soil/karst zone might be limited. While δ^{18}Os is highly sensitive to changes in large-scale monsoon circulation (Cheng et al., 2019; Duan et al., 2016; Liu et al., 2020), it may not accurately reflect long-term local evaporation and water balance compared to $\delta^{18}O_{FI}$. The $\delta^{18}O_{FI}$ values exhibit smoother and larger amplitude changes on centennial to millennial scales, suggesting that they better reflect gradual changes in vegetation, soil, karst, and cave environments over these time scales. For example, ENSO activity was stronger during the early and late compared to the middle Holocene, leading to a higher frequency of extreme hydroclimatic events in the Chinese monsoon region during these periods (Chen et al., 2016; Cobb et al., 2013; Mark et al., 2022; Yuan et al., 2023; Zhang et al., 2014; Zhu et al., 2017). In our record, the frequency of weak monsoon events recorded by δ^{18}Os appears similar between the middle and late Holocene (Figure 5.4). However, the frequency and magnitude of changes in $\delta^{18}O_{FI}$ are much smaller in the middle Holocene (about 2‰) than in the late Holocene (about 4‰) (Figure 5.5). Despite frequent decadal and centennial-scale fluctuations in δ^{18}Os indicative of ASM circulation strength in the middle Holocene, long-term region evaporation and water balance did not undergo significant changes due to stable ENSO activity. In contrast, during the late Holocene, as ENSO activity increased, the magnitude and frequency of changes in $\delta^{18}O_{FI}$ increased, reflecting larger fluctuations in regional water balance (Figure 5.5). Lake sediment records from southwestern China also show that enhanced ENSO activity in the Late Holocene led to more frequent extreme hydroclimatic events in the region (Figure 5.5) (Zhang et al., 2023a). The high-resolution δ^{18}Os record responds rapidly to short-term fluctuations in ASM intensity, while the $\delta^{18}O_{FI}$ values are more sensitive to the gradual changes in vegetation, soil, and karst environments. These changes may be influenced by factors such as ASM intensity, shifts in precipitation, and the frequency of drought events on shorter time scales.

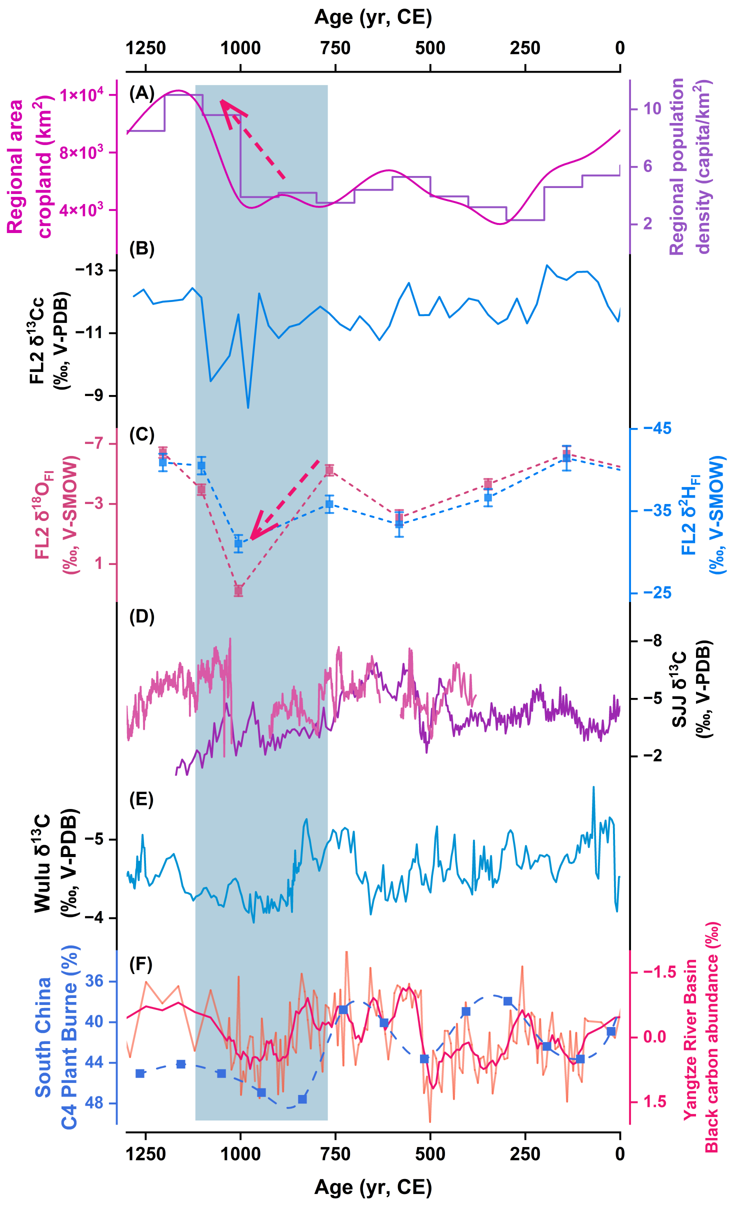

Figure 5.6. Influence of Late Holocene human activities on the regional environment. Variation in regional average population density and area cropland within the rectangle around Feilong cave (320×230 km, 7.36×104 km^2). Data from Klein Goldewijk et al. (2010). (B) FL2 δ^{13}Cs record from Duan et al. (2023b). (C) FL2 $\delta^{18}O_{FI}$ and $\delta^{2}H_{FI}$ records (this study). The cyan bar spans about 330 years. (D) The δ^{13}C records of stalagmites from Shijiangjun cave (Chen et al., 2021a). (E) The δ^{13}C records of stalagmite from Wulu cave (Zhao et al., 2020). (F) The red line indicates detrended ECMZ core black carbon abundance records (Pei et al., 2020). The red line indicates calculated south China C4 burned proportion form core ZK001 (Ju et al., 2024). For a more visual comparison the time unit is CE not BP.

Human Activities Trigger the Degradation of Regional Ecosystems

The most pronounced $\delta^{18}O_{FI}$ positive anomaly event occurs during 950-1150 CE (corresponding to a depth of 13±1.5 mm for stalagmite), with $\delta^{18}O_{FI}$ amplitudes exceeding 8‰ (Figure 5.6). This event is also prominently evident in FL2 δ^{13}Cs and other δ^{13}Cs records in south China (Figure 4 and 6). However, no significant precipitation and temperature anomalies were observed in southwest China during this time, and the magnitude of changes in IPWP, solar and ENSO activities were also comparable to the previous $\delta^{18}O_{FI}$ positive anomaly phases (Figure 4 and 5). These forcings explain the four previous $\delta^{18}O_{FI}$ positive anomaly phases (I-IV). This difference means that for this most enhanced regional evaporation and deterioration of water balance during phase V, it is not entirely attributable to changes in natural factors, such as monsoon intensity or precipitation. Increasing human activities in the mid-to late Holocene, especially large-scale population migration, could have also profoundly impacted the regional environment (Figure 5.6) (Chen et al., 2021a; Liu et al., 2011). During the Northern Song Dynasty, spanning from Emperor Taizu to Yingzong (about 976-1067 CE), the central government's policy of promoting agricultural development in border regions resulted in a notable migration of people from central China to the southwestern territories (Wu, 2000; Yang, 1996; Zhang and Peng, 2012). Around 1127 CE, due to prolonged warfare in northern China, known as the Jingkang event, approximately 5 million people migrated to southern China (Chen et al., 2021b; Wu, 2000; Zhang and Peng, 2012). The massive influx of people resulted in extensive land cultivation, destroying natural forests and grasslands (Chen et al., 2021b; Pei et al., 2020). The black carbon abundance record in the Yangtze River Basin and the pollen and charcoal records from western Guizhou also clearly document the far-reaching environmental impacts of population migration (Pei et al., 2020; Yue et al., 2024). The continuous increase in Yangtze River Basin black carbon abundance from 770 to 1000 CE indicates that human activities (Pei et al., 2020) (Figure 5.6), especially the intensification of land clearing, resulted in more frequent fires in southern China and an overall decline in the forest cover of the Yangtze River Basin (Pei et al., 2020).

According to long-term dynamic modelling of the global population and built-up area (Klein Goldewijk et al., 2010), during 800-1000 CE, the population density in the Feilong cave region remained relatively stable, about 6-8 caps/km^2 (Figure 5.6). However, from 1000 to 1100 CE, the population density more than doubled, reaching about 19 cap/km^2. Over the following century, it increased to about 22 cap/km^2 until a slight decrease around 1300 CE (about 17cap/km^2) (Figure S5.9 in Supplementary Information B.4). The significant population influx necessitated land cultivation to meet the growing demands for sustenance and food supply. The area of cropland in the study area increased from about 4×103 km^2 to about 1×104 km^2 from 1000 to 1100 CE (Figure 5.6). This expansion re-

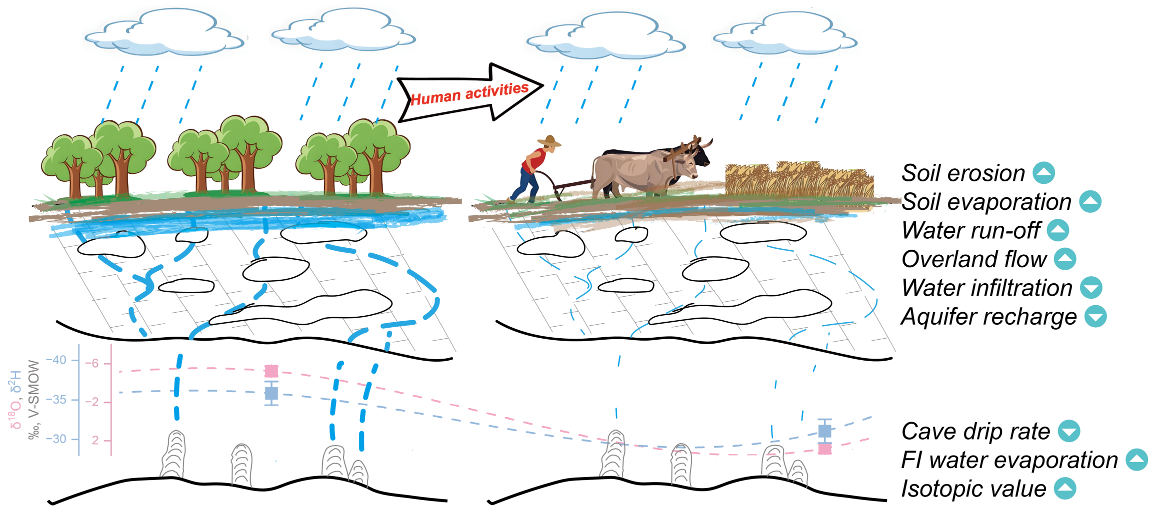

Figure 5.7. The impact of human activities on the surface hydrological environment and fluid inclusion water isotopes in karst regions. The left side illustrates the surface hydrological conditions in the absence of human activities. The right side represents the surface hydrological conditions after significant human impact. The original natural vegetation was extensively cleared, altering the evaporation-precipitation balance of surface water, while also exacerbating soil erosion and karst rocky desertification. Changes in arid and hydrological conditions led to a significant reduction in cave drip water supply. The enhanced evaporation in caves resulted in a notable increase in the isotopic values of fluid inclusion water.

sulted in the extensive clearing of native C3 vegetation, which was replaced by C4 crops for agricultural purposes (Figure 5.6) (Chen et al., 2021b; Ju et al., 2024; Liu et al., 2011). Other δ^{13}Cs records from southwest China also exhibit similarly significant positive shifts around 1000 CE (Figure 5.6), providing evidence that human activities during this period caused widespread surface environmental changes. The destruction of surface vegetation in the karst region will result in severe regional ecosystem degradation and soil erosion, i.e., rocky desertification (Figure 5.7) (Bai et al., 2013; Li et al., 2018). Surface exposure and land cultivation have altered the original balance of precipitation and evaporation on the land surface, resulting in rainfall experiencing more significant evaporation in the soil layer and epikarst zone (Jiang et al., 2014; Zhang et al., 2021a). Meanwhile, rocky desertification altered rainfall runoff, resulting in more frequent drought events (Guo et al., 2023; Jiang et al., 2014). Therefore, in this scenario, the supply of cave drip water is anticipated to be significantly reduced, degassing times will become more prolonged, resulting in more significant fractionation of $\delta^{18}O_{FI}$ (Figure 5.7).

5.5 Conclusions

Based on the development of glass tube measurements and the usage of Rayleigh fractionation models, our speleothem fluid inclusions measurement technique enables testing for significant evaporation of samples during preheating. Analytical artefacts in isotope results caused by heating in the measurement setup can be effectively identified and mitigated through meticulous petrographic examination and comparative measurements using glass tubes. Our reconstructed southwest China $\delta^{18}O_{FI}$ and $\delta^{2}H_{FI}$ records demonstrate sensitivity to evaporation processes in the epikarst zone and cave environment. It is suggested that the more significant evaporation experienced by fluid inclusions during formation may cause their isotopic composition to exhibit a greater amplitude of response to external climate and environmental changes, compared to the isotopic composition of calcite. The $\delta^{18}O_{FI}$ record reveals that during the Late Holocene, increased ENSO variability led to a higher frequency of drought events in southwest China. The $\delta^{18}O_{FI}$ record provides obvious and direct evidence for a regional environmental degradation event caused by human activities during the 950-1150 CE. The destruction and modification of the surface environment by human activities has resulted in the initial liquid of inclusions water experiencing more intense evaporation during transport through the soil layer, epikarst zone and cave environment. It is suggested that the combination of $\delta^{18}O_{FI}$ with carbonate stable isotopes contributes to a more accurate reconstruction of past regional environmental changes. It holds significant potential in distinguishing the impacts of human activities and natural factors on climate and environmental changes during the mid-to late Holocene.

Chapter 6

Northern Hemisphere Summer Insolation and Ice Volume Driven Variations in Hydrological Environment in Southwest China

Key Points:

- **Stalagmite trace elements are indicators of regional hydrological environmental variations in Southwestern China.**
- **Northern Hemisphere summer insolation and global ice volume modulate the phase and amplitude variations of regional hydrological environment.**
- **The meridional tripolar spatial pattern of precipitation in monsoon region in China on the orbital scale remains ambiguous.**

While it is well known that global changes have led to variations in the intensity and spatial distribution of Asian monsoon precipitation, the mechanisms behind these changes remain poorly understood. Paleoclimate records play a crucial role in uncovering the drivers behind monsoon variability. This chapter presents multiple indicator data sets from a stalagmite in southwestern China to explore variations in monsoon precipitation over the last 120,000 years. The findings indicate that fluctuations in Northern Hemisphere summer insolation are the primary drivers of the increase or decrease in Asian summer monsoon rainfall. Global ice volume modulates the magnitude of the rainfall response to insolation, with significant decreases in precipitation occurring during periods of high ice volume. Based on current paleo-precipitation records, the spatial pattern of increasing or decreasing rainfall in central China corresponding to opposite trends in northern and southern China remains unclear on orbital timescales, although this feature has been observed in some model simulations.

This work builds upon my Master's research, which reported the chronology and stable isotope data of the stalagmite (Wu et al., 2020). During my PhD, I conceptualized and carried out the extended study, including conducting trace element measurements, data analysis, and interpretation of the same stalagmite. The results of this work have been published in *Geophysical Research Letters* (https://doi.org/10.1029/2023GL105664). This chapter represents the published content, with the supplementary material placed as Section B.5 Supplementary information for Chapter 6. The data evaluation, visualization, and manuscript writing were all carried out by myself. The co-authors include Dr. Sophie Warken, Prof. Dr. Norbert Frank, Aaron Mielke, Dr. Chao-Jun Chen, Prof. Dr. Jun-Yun Li, and Prof. Dr. Ting-Yong Li. Aaron Mielke contributed to the trace element measurements, the others participated in the discussion and revisions of the manuscript.

6.1 Introduction

Oxygen isotope measurements in speleothem carbonate from the Asian monsoon region provide valuable climatic information for exploring of the driving mechanisms, the evolutionary processes, and intensity of the late Quaternary ASM (Cheng et al., 2016a, 2019). This concept encompasses several aspects of the ASM system, such as changes in moisture source and shifts in circulation patterns (Maher and Thompson, 2012; Tan, 2014), upstream Rayleigh fractionation (Hu et al., 2008), summer to winter precipitation ratio (Wang et al., 2001), and the variations in ASM circulation intensity or overall precipitation (Cheng et al., 2019). The interpretation of δ^{18}Os as an indicator of local rainfall amount in the monsoon region in China remains, however, controversial (e.g. Lachniet, 2020; Liu et al., 2020; Xue et al., 2023). For only a few of the δ^{18}Os records in China a correlation with local amount of precipitation was demonstrated (Liu et al., 2008a; Tan et al., 2014, 2015), while a relationship with the local instrumental rainfall record is often lacking (Xue et al., 2023; Yang et al., 2019b). δ^{18}Os may also be related to the strength of the large-scale atmospheric circulation and moisture transport, instead of providing direct measures of the regional precipitation quantity (Cheng et al., 2019; Liu et al., 2014).

There is significant spatial heterogeneity in precipitation across the monsoon region in China. In the modern era and the Holocene, precipitation in central China exhibits an inverse phase within southern and northern China. The increased rainfall in central China corresponds to a decrease in southern and northern China, also known as the "tripolar" pattern (Figure S6.1 in Supplementary Information B.5) (Chen et al., 2022; Chiang et al., 2020; Zhang et al., 2018). This pattern is difficult to observe in the δ^{18}Os records from the monsoon region in China because dynamical elements are not sufficiently well-constrained, limiting the ability of δ^{18}Os to capture the ASM thermodynamic nature and the rainfall amount (Zhao et al., 2023b). In respect to the driving mechanisms, compared to the ASM rhythms primarily controlled by NHSI (Cheng et al., 2016a, 2021b), the response of China summer precipitation to astronomical forcing and ice volume appears elusive. For example, summer precipitation in northern China is controlled by precession, showing significant 23 ka cycles, while in southern China 100 ka cycles are well present, indicating the dominant influence of the background climate state as for example, represented by the global ice volume (Dai et al., 2021; Lyu et al., 2021; Zhao et al., 2023a). In addition to NHSI and ice volume, it has also been hypothesized that the ASM is primarily driven by the Summer Inter-Tropical Insolation Gradient (SITIG) (Cheng et al., 2022a; Zhang et al., 2023c). During the precessional minima (Pmin), the increase in SITIG leads to a more pronounced northward shift of the ITCZ and enhanced western Pacific subtropical high and winter hemisphere trans-equatorial Hadley circulation (Beck et al., 2018). It eventually transports more oceanic moisture and latent heat to the Asian monsoon continent. This perspective emphasizes the "pull" and "push" forcing of ASM variations by inter-hemispheric temperature gradients, which is a more comprehensive theory than the traditional single factor driven view of ASM evolution (Cheng et al., 2022a). The discussion of the relationship between ASM and spatial heterogeneity in summer precipitation has focused on the Holocene, or millennial events of the last glacial period. On longer scales there is a heavy reliance on simulations (Dai et al., 2021; Lyu et al., 2021). Due to the absence of high-resolution precipitation reconstructions on glacial-interglacial periods, the existence of spatial precipitation heterogeneity and its forcing factors remain unclear for at orbital time scales.

Another aspect of our work is that the relationship between regional hydrological environment wet-dry variation and ASM intensity may not remain constant over different times scales. During the millennial-scale climate events of the LGM, the Yangtze River basin in central China experienced wet conditions during Heinrich event (H) 1 and Younger Dryas, although the ASM weakened significantly (Zhang et al., 2018). In contrast, the environment in the central Yangtze basin was dry and cold during H5 and H6, while it was wet and warm during Greenland Interstadials (GI) 9–18 (Wang et al., 2022a). In southwest China, the regional hydrological environment and effective rainfall during H4 and H5 were comparable to or even wetter than GIs (Liu et al., 2022a; Wu et al., 2023a). In summary, δ^{18}Os does not necessarily indicate regional precipitation variations, as circulation or moisture source effects may mask the less dominant local precipitation signals.

Currently, there are very few unambiguous regional rainfall or hydrological environment records spanning the glacial-interglacial cycle in southern China, with a resolution permitting to investigate individual millennial climate events. But some recent work has attempted to reconcile the relationship between ASM intensity and precipitation from the simulation perspective (Dai et al., 2021; Lyu et al., 2021; Zhao et al., 2023a). Here this dissertation report trace element records (Mg/Ca, Sr/Ca, Ba/Ca) for a stalagmite from Yangzi cave in southwest China spanning 116.09 to 4.07 ka BP. In combination with δ^{18}Os and δ^{13}Cs values, this record provides much clearer comparisons for assessing the relationship between ASM intensity and the regional hydrological environment.

6.2 Material and Methods

6.2.1 Study Area and Sample

Yangzi cave (29.78°N, 107.78°E, 400 m above sea level) is located on the lower reaches of Longhe River, which is a tributary of Yangtze River in Fengdu County, Chongqing City, southwestern China (Figure S6.1 in Supplementary Information B.5). Yangzi cave is about 500 m long, developed in lower Triassic limestone (Zhu et al., 2004). The region has a subtropical humid monsoon climate, which is affected by the ASM (Pu et al., 2015). Instrumental climate data from the nearest meteorological station (18 km northwest of Yangzi Cave), reveal that the mean annual temperature and precipitation amount are 18.3°C and 1018.6 mm, and the 1980–2010 averages June-October precipitation accounts for 70% of the entire year (http://www.cma.gov.cn/). The mean cave temperature is approximately constant at 16.0°C, and the humidity is close to 100% (Zhu et al., 2004). The modern vegetation above Yangzi cave primarily consists of subtropical perennial broad-leaved forests and shrubs (Pu et al., 2015). Details of the YZ1 stalagmite are described in Wu et al. (2020) and (Text S6.1 in Supplementary Information B.5).

6.2.2 Methods

The analytical setup and measurement protocol of trace elements follows the method described by Warken et al. (2021). The analysis of trace elements was performed at the Institute of Environmental Physics, Heidelberg University. A laser ablation system with a 193 nm ArF excimer laser (NWR193UC by New Wave Research) was used to ablate carbonate, which was analyzed for its major and trace element composition using an inductively coupled plasma quadrupole mass spectrometer (ICPMS) (Thermo Fisher iCAP-Q). Line scans were performed at a speed of 10 µm/s along the growth axis of YZ1 with a rectangular spot size of 15 × 150 µm. To remove possible surface contamination, the scan path was pre-ablated at a scan speed of 80 µm/s. The repetition rate of the laser pulses was 20 Hz, and each investigated isotope was measured every 100 ms on the mass spectrometer. Background counts were measured with the laser in off mode and subtracted from the raw data. To account for matrix effects, the blank corrected count rates of the analyzed isotopes (^{25}Mg, ^{88}Sr, ^{138}Ba) are calculated relative to the intensity of ^{43}Ca. The silicate glass NIST SRM 612 was analyzed for external calibration of the trace element to Ca ratios using the reference values by Jochum et al. (2011). Correlation analyses were performed in SPSS 25 software. Principal component analysis was performed in R. Ensemble empirical mode decomposition (EEMD), bandpass filters, and spectral analysis were performed on MATLAB 2022b platform.

6.3 Result

Measurement results for stalagmite trace element ratios (Sr/Ca, Mg/Ca and Ba/Ca; in the following referred to as X/Ca) are presented in g/g and shown in (Figure S6.2 in Supplementary Information B.5). The results of the Pearson correlation statistics revealed robust correlation coefficients between X/Ca of $0.46 < r < 0.75$ ($p < 0.01$) (Figure S6.3 in Supplementary Information B.5). Principal component analysis showed that totals of 76% and 18% of the variations in X/Ca data were explained by the first and second principal components (PCs) (Table S6.1 in Supplementary Information B.5). The results of the EEMD analyses suggests that the most relevant variability of X/Ca PC1 is captured by the component (IMF 7) that is coincident with precessional cycles ($\sim$23 ka) (Figure S6.4 and Tabls S5.2 in Supplementary Information B.5). On the orbital scale, X/Ca share substantial in-phase covariation to the oscillatory variations of δ^{18}O and δ^{13}C as reflected by the highly significant Pearson correlation coefficients ($0.23 < r < 0.53$, $p < 0.01$) (Figure S6.3 in Supplementary Information B.5). The values of X/Ca are generally elevated compared to the mean value during MIS5e, MIS5c, MIS4 and MIS2, and overall lower during MIS3 (Figure

S6.4 in Supplementary Information B.5).

6.4 Discussion

6.4.1 Climatic Significance of the Trace Element Ratios

The differential increase in the relative content of trace elements in stalagmites and positive correlation between all three elements was interpreted as prior calcite precipitation (PCP) (Fairchild et al., 2006; Shi et al., 2022; Stoll et al., 2023; Warken et al., 2018). Sinclair, Wassenburg, and their co-workers infer that predominance of PCP can be tested d through linear regression between ln(Sr/Ca) and ln(Mg/Ca) (Sinclair et al., 2012; Wassenburg et al., 2020). Here, the slopes of 1.0–1.2 between elemental ratios agree with model predictions (0.7–1.4) (Figure S6.5 in Supplementary Information B.5). During MIS5e and LGM, values of Mg/Ca and Sr/Ca are similar, while Sr/Ca is elevated in MIS5d (Figure S2 in Supplementary Information S1). This difference may reflect the partitioning coefficient dependencies for Mg and Sr during calcite growth (D(Mg) and (D(Sr)) (Text S6.2 in Supplementary Information B.5), including dependence on saturation state of drip water, cave P_{CO2}, and temperature. The D(Mg) increased with increasing temperature (Fairchild et al., 2006), whereas the D(Sr) is positively correlated with stalagmite growth rate and may be controlled by solution saturation under the influence of cave ventilation (Day and Henderson, 2013). During the LGM, lower temperatures may result in lower D(Mg), which contradict our findings (Figure S6.2 in Supplementary Information B.5). Although higher stalagmite growth rates lead to significant increases in D(Sr), no positive offset is found during the LGM, despite growth rates being twice as high during MIS 5e (Figure S6.2 in Supplementary Information B.5). There is, however, solely an effect on D(Sr) when growth rates are greater than 315 mm/ka (Gabitov et al., 2014), which is much lower for YZ1. In addition, the relative stable Sr/Mg ratios of YZ1 further suggest that both elements have common and relatively constant source to the drip water during bedrock weathering. Tremaine and Froelich propose to use the Mg/Ca and Sr/Ca ratio under such conditions as indicator of rainfall variation (Tremaine and Froelich, 2013). Therefore, factors such as temperature, growth rate are less likely to be the dominant factors controlling changes in trace elements compared to the strong indication for PCP.

Compared to Mg/Ca and Sr/Ca, Ba/Ca shows a low mean value of $0.04 \times 10-3$ but the variability is largest with variations of more than 500% (Figure S6.2 in Supplementary Information B.5). Hence, the variability and concentration of Mg, Sr, Ba follows inverse order with Mg/Ca > Sr/Ca > Ba/Ca and vice versa. The Ba/Ca is probably the most sensitive indicator of response to PCP. Given the strong synchronicity of the three trace element ratios on orbital-millennial time scales, and to avoid the uncertainties of using single trace element ratio record, this dissertation use PC 1 of the X/Ca time series as a robust, integrated hydroclimatic record, interpreted as the local precipitation amount or evapotranspiration variations. The high variance of PC1 (76%) means that it well identifies the main patterns of variation in the X/Ca. The lower X/Ca PC1 values indicate wetter conditions and vice versa for drier conditions.

Compare X/Ca PC1 with δ^{13}Cs and U concentrations from stalagmite chronology results to further validate our interpretation. δ^{13}Cs and U concentrations are also considered sensitive indicators of response to the external hydrological environment (Fohlmeister et al., 2020; Jamieson et al., 2016) . Additionally, X/Ca PC1 reveals similar trends throughout those of δ^{13}Cs and U concentration on orbital time scale (Figure S6.2 in Supplementary Information B.5). The extensive synchronisation of these multi-indicator records on orbital scales supports our interpretation of X/Ca PC1 as an indicator of regional hydroclimatic variations. Since the underlying PCP process is a non-linear Rayleigh process, this dissertation also use Mg/CaminMg/Casample to approximate the remaining fraction fCa in the drip water, which may serve as a more linear, that is, more direct proxy for regional precipitation amount variation than the X/Ca ratios (Stoll et al., 2023) (Figure S6.6 in Supplementary Information B.5).

6.4.2 Precessional Forcing of the Regional Hydrological Environment

During MIS2, MIS4 and MIS5c with lower-than-average NHSI, the positive shifted δ^{18}Os indicate the significant weakening of ASM intensity (Figure 6.1). Meanwhile, the higher δ^{13}Cs and X/Ca PC1 values associated with lower fCa values (Figure 6.1) (Figure S6.6 in Supplementary Information B.5) suggest substantial deterioration in the regional vegetation and soil carbon dynamics, and precipitation. Such changes may reflect the degradation of the hydrological environment forced by the weakening ASM in southwest China, including decreased temperature, drought, and changes in the ratio of C3/C4 plants (Fohlmeister et al., 2020; Tremaine and Froelich, 2013). Although the relative contribution of each factor is difficult to determine, this ratio captures the combined impact of environmental degradation. During periods of above-average NHSI, that is, MIS1, MIS3, and MIS5a, the opposite of the low NHSI periods was observed, with lower δ^{13}Cs and X/Ca PC1 values as well as higher fCa values (Figure 6.2). This implies that NHSI not only triggers variations in ASM intensity, but also controls local precipitation variations. Strong NHSI corresponds to stronger ASM circulation and thus enhanced monsoon-related precipitation as compared to periods of weaker NHSI. The EEMD and spectral analysis also confirms that the precession cycle is significant in both the X/Ca PC1 and fCa records (Schulz and Mudelsee, 2002)

(Figure S6.6 in Supplementary Information B.5). Recent precipitation simulations for the past 300 ka BP in northern China also show significant precession influence, highlighting the dominant role of insolation (Zhao et al., 2023a). Similar results are confirmed in the magnetic susceptibility record from lake sediments in southern China (Wang et al., 2022c). Our trace element-derived precipitation reconstruction from southwest China, now provides a continuous record even during the low NHSI (Figure 6.1).

The stalagmite δ^{13}Cs values in Zhenzhu cave from northern China are considered a sensitive indicator of response to variation in local precipitation (Figure 6.1) (Li et al., 2020). Zhenzhu Cave is in the monsoon edge region of northern China, which is most sensitive to ASM variations. Zhenzhu cave stalagmite halted growth during the periods of lowest solar insolation (MIS2, MIS4, MIS5b, and MIS5d), which is interpreted as an extreme weakening of the ASM, leading to a remarkable reduction in summer rainfall brought about by the southward retreat of the monsoon. This interpretation does not conflict with the insolation driven changes in ASM intensity and precipitation.

6.4.3 Low-Latitude Insolation Regulates Orbital-Scale ASM Precipitation

To assess the influence of forcing from low latitudes on ASM variation, this dissertation use the June 21 insolation difference between 30°N and 30°S to indicate variation in the Summer Inter-Tropical Insolation Gradient (SITIG). Our reconstructed precipitation variations point to a link with SITIG (Figure 6.1). Although, the NHSI and SITIG are nearly identical in phase, the decreasing NHSI is contrasting the elevated precipitation during MIS3, which is synchronous to SITIG (Figure 6.1). This finding supports the fact that inter-hemispheric heat contrasts also cause ASM precipitation variation (Beck et al., 2018; Zhang et al., 2023c). To validate this forcing, this dissertation compared our X/Ca PC1 record with marine proxies from ASM moisture source region (Figures 1b and 1g). The Indo-Pacific Warm Pool (IPWP) upper ocean heat content (OHC) variations exhibit significant precession cycles driven by the insolation-driven meridional gradients in the lower latitudes (Figure 6.1) (Jian et al., 2022). The OHC and YZ1 δ^{18}Os and X/Ca PC1 are in phase on the precession scale. This could be explained by the ASM dynamics and thermodynamics are influenced by the tropics warm pool ocean heat content. The increase in IPWP OHC during Pmin results in more evaporation, convergence, and transport of oceanic moisture to land (Jian et al., 2022). This process, while increasing East Asian monsoon precipitation, also produces more depleted δ^{18}O values in the speleothem records due to significant upstream moisture convergence and rainout (Figure 6.1) (Liu et al., 2014; Ruan et al., 2019). The above phenomena and processes have been confirmed in quantitatively reconstructed precipitation records on or-

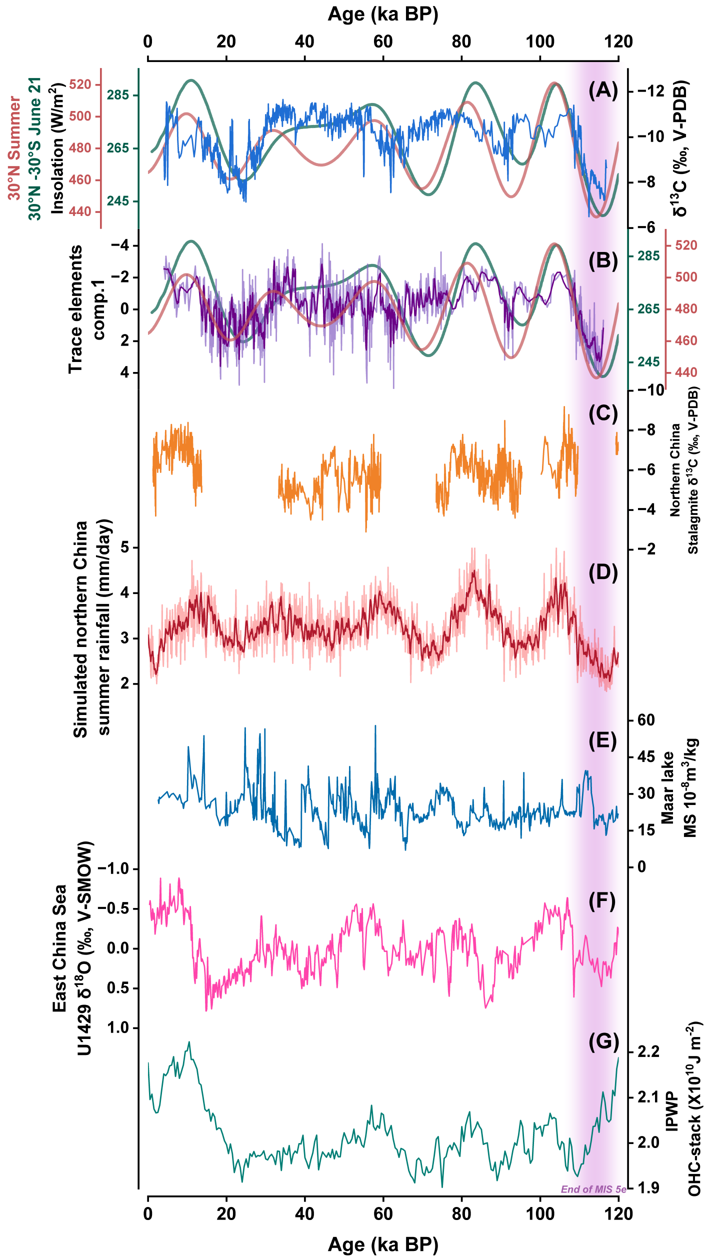

Figure 6.1. The YZ1 δ^{13}C and X/Ca PC1 records compared with climatic records for the Asian monsoon region. (a) YZ1 δ^{13}C (this study); (b) YZ1 X/Ca PC1 this study, the dark curve indicates 10-points smoothing; (c) Zhenzhu Cave stalagmite δ^{13}C (Li et al., 2020); (d) Summer rainfall in northern China as simulated by the full coupled NRAR-CCSM3 model (Zhao et al., 2023a); (e) Maar lake sediments Magnetic susceptibility (Wang et al., 2022c); (f) IODP U1429 planktonic foraminifer δ^{18}O (Clemens et al., 2018); (g) Indo-Pacific Warm Pool upper stacks ocean heat content variations (Jian et al., 2022). The brown and green curves represent 30°N summer and 30°N minus 30°S June 21 insolation, respectively (Laskar et al., 2004).

bital scales based on pollen in southern China and loess in the north China (Beck et al., 2018; Thomas et al., 2014; Zhang et al., 2023c). For the first time, this dissertation observe similar features in stalagmite trace element records from southern China. Our new record highlights that differences in insolation between the low-latitude tropics may be a more integrated forcing factor controlling monsoon precipitation phase variations (Cheng et al., 2022a).

Simulations have suggested that the “tripolar” precipitation pattern in the monsoon region of China during the modern and Holocene persists on orbital scales (Figure S6.7 in Supplementary Information B.5) (Dai et al., 2021; Lyu et al., 2021). However, our findings are broadly consistent with precipitation reconstructions in northern and southern China, that is, wet environments correspond to high NHSI or large SITIG, although there are differences in details (Figure 6.2). This dissertation observed antiphase only in loess δ^2H records near the edge of the Loess Plateau and in Taihu lake pollen proxies in the lower reaches of the Yangtze River (Figures 2d and 2e). These records show that the decrease in insolation sometimes corresponds to a wetter environment. The spatial heterogeneity of precipitation in the monsoon region in China is often interpreted as being related to Western Pacific Subtropical High (WPSH) (Chiang et al., 2020; Yuan et al., 2004). During high boreal summer insolation, a more La Niña-like state caused by the increased tropical east-west Pacific Sea surface temperature gradient will result in stronger and more active WPSH (Li et al., 2021a; Lu et al., 2019b). Enhanced and northwardly extending WPSH limits summer precipitation in east-central China while precipitation increases in north and south China (Zhang et al., 2020b). However, there is also evidence that strong WPSH can also lead to an east-west antiphase of summer precipitation in the mid-latitude monsoon region in China (Tian et al., 2022). Our results show high NHSI and La Niña-like situations correspond to increased precipitation (Lea et al., 2000; Zhang et al., 2017, 2021c) (Figure S6.6 in Supplementary Information B.5). Moreover, no similar antiphase is found in U1429 δ^{18}O, which is indicative of overall rainfall in the Yangtze River basin (Figure 6.2) (Clemens et al., 2018), suggesting that the generalized statement that central China is in antiphase with north-south precipitation may not be robust. The typical areas where high NHSI corresponds to negative precipitation anomalies are in the middle and lower reaches of the Yangtze River, which are more affected by WPSH (Dai et al., 2021; Jiang et al., 2021). The absence of continuous paleo precipitation records spanning the glacial-interglacial period in the middle and lower reaches of the Yangtze River also creates uncertainty in the interpretation (Figure S6.6 in Supplementary Information B.5). Therefore, its influencing range should be considered when discussing the spatial patterns of precipitation in the monsoon region in China on orbital scales. Also, caution should be exercised when discussing monsoon precipitation variations based on a single reconstructed record.

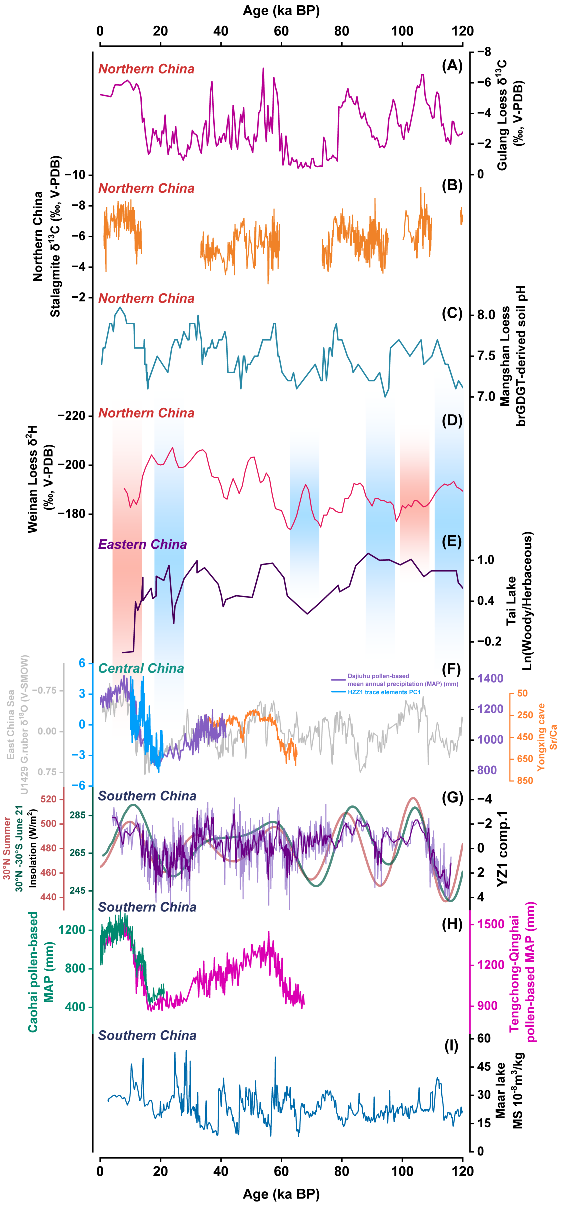

Figure 6.2. Comparison of the YZ1 X/Ca records with paleoclimate records from different regions of China. (a) Gulang loess δ^{13}C (Sun et al., 2015); (b) Zhenzhu Cave stalagmite δ^{13}C (Li et al., 2020); (c) Mangshan loess brGDGT-derived soil pH (Peterse et al., 2014); (d) Weinan loess δ^{2}H (Thomas et al., 2016); (e) Tai Lake pollen ratio of Woody/Herbaceous (Miao et al., 2015); (f) IODP U1429 planktonic foraminifer δ^{18}O (gray) (Clemens et al., 2018); Haozhu cave stalagmite trace elements PC1 (bule) (Zhang et al., 2018); Dajiuhu pollen-based mean annual precipitation (purple) (Zhang et al., 2023c); Yongxing cave stalagmite Sr/Ca (orange) (Wang et al., 2022a); (g) YZ1 X/Ca PC1 (this study); (h) Pollen-based MAP records of Caohai (green) and Tengchong-Qinghai (pink), respectively (Zhang et al., 2023c); (i) Maar lake sediments Magnetic susceptibility (Wang et al., 2022c). The red/blue bars indicate paleoclimatic records where increased/decreased insolation corresponds to decreased/increased precipitation.

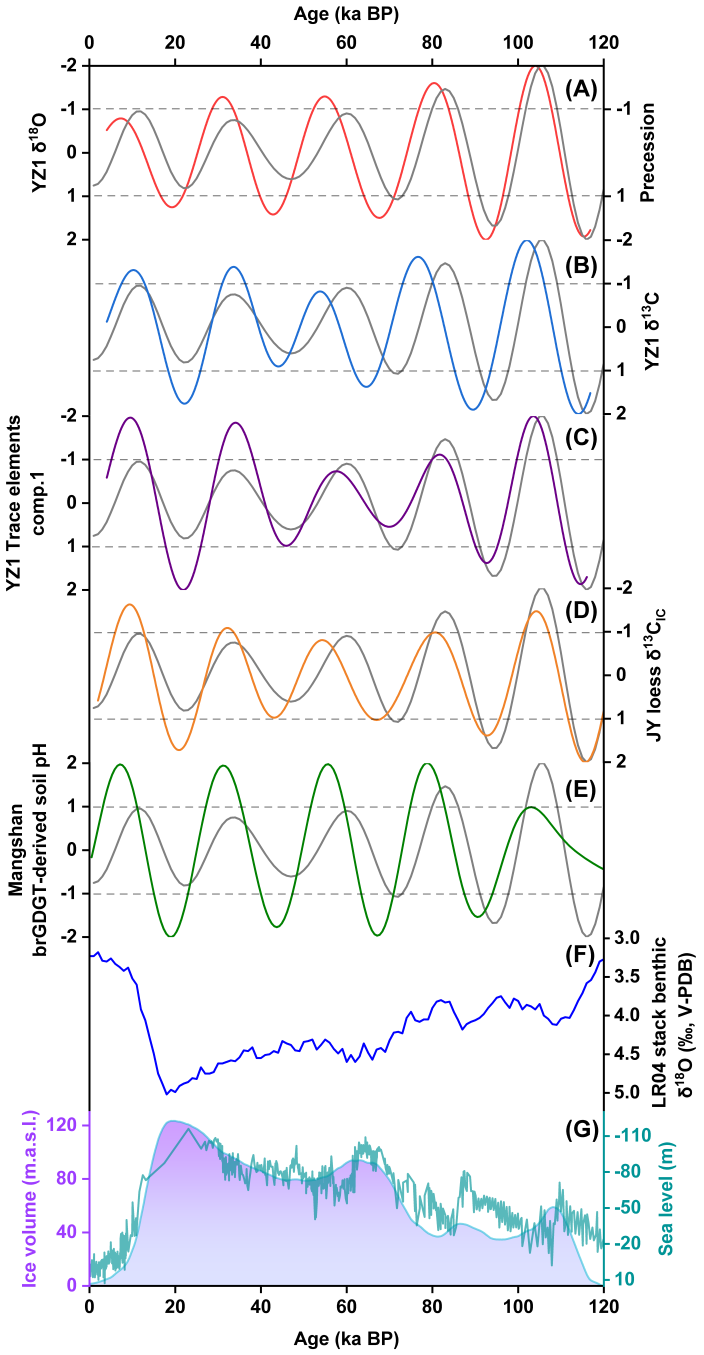

Figure 6.3. Influence of NHSI and ice sheet dynamics on ASM precipitation. (a–c) YZ1 δ^{18}O, δ^{13}C, and X/Ca PC1 records (this study); (d) The δ^{13}C of inorganic carbonate from the Chinese loess in northern China (Sun et al., 2019); (e) The brGDGT-derived soil pH for the Mangshan mountain (Peterse et al., 2014); (f) Global stack benthic foraminifer δ^{18}O sequence LR04 (Lisiecki and Raymo, 2005); (g) Global ice volume and sea level reconstructing records (Bintanja and van de Wal, 2008; Grant et al., 2014). The gray curve represents the variation in the precession. The frequency is 0.0434 ka^{-1} and the band width is 0.01 ka^{-1}, normalized to the interval −2 to 2.

6.4.4 The Global Ice Volume Forcing on Summer Monsoon Precipitation Amplitudes

The band bass filter analysis results show a long-term decreasing trend in δ^{18}Os from MIS5e to MIS1, with the phase and amplitude consistent with the precession (Figure 6.3). However, during the LGM, although the X/Ca PC1 record is in phase with the ASM and insolation, the amplitude is much larger, equivalent to strongly decreasing precipitation amounts as deduced from fCa estimates (Figure S6.6 in Supplementary Information B.5). Similar results are confirmed in different model simulations. The LGM annual precipitation in China was proposed to reduce by an average of 18%–25% compared to the pre-industrial period (Tian and Jiang, 2016). This suggests that the decrease in ASM precipitation during the LGM is exceeding the influence of ASM intensity, which is also captured by other precipitation records (Figure 6.3). The forcing of the intensely reduced precipitation during the LGM is not completely attributable to the decreasing insolation.

The decrease in monsoon precipitation may be related to the large global ice volume during the LGM (Figure 6.3). During the LGM, although the insolation decrease is minor compared to the MIS3, MIS4 and MIS5, the large-scale cooling of the NH continents due to the increased global ice volume produces high-pressure anomalies over Eurasia and low-pressure anomalies over the North Pacific, respectively, which further reduces the land-sea thermal contrast (Lyu et al., 2021; Tian and Jiang, 2016). Meanwhile, ocean cooling weakens local upward movement and air convection over the oceans, which leads to a weakening of the ASM and a reduction in ocean moisture fluxes. Strong cooling at NH high latitudes will lead to a strengthening and southward shift of NH subtropical westerlies, which limits the extent and intensity of summer monsoon penetrating deep into the East Asian continent (Chiang et al., 2020). On the other hand, the location of the ITCZ is sensitive to changes in ice volume in NH and the resulting differential heating between the two hemispheres (McGee et al., 2018). Thus, during the LGM, although the weakening of insolation is not significant, the large ice volume during this period amplified the magnitude of the reduction of monsoon precipitation. This feature has been captured in fully forced transient experiments (Lyu et al., 2021; Shi et al., 2019), which verify from the reconstructed record.

Another period of significantly reduced precipitation was during end of MIS5e. Almost all records indicate that precipitation reduced to the extent of the LGM during end of MIS5e, although this time ice volumes were much smaller (Figure 6.3). Modeling work suggests that the relationship between ASM precipitation and ice volume is non-linear (Yin et al., 2023b). Especially in the lower latitudes of 15°–25°N, precipitation does not entirely follow the change in ice volume, rainfall in southern China is less affected by ice volume in low insolation conditions (Lyu et al., 2021). Thus, forcing from ice volume is limited during end of MIS5e, and insolation dominates the monsoon precipitation variations.

The retreat of the coastline during the LGM resulted in an increase in the distance (100–300 km) from the study area to the ocean (De Groeve et al., 2022) (Figure S6.9 in Supplementary Information B.5), lengthening the distance between the oceanic moisture source and the cave site. The continuous condensation of monsoonal moisture in the transport path reduces monsoonal precipitation reaching the inland. The more significant Rayleigh fractionation process during moisture transport due to the retreating coastline will result in more negative precipitation δ^{18}O (δ^{18}Op) and thus δ^{18}Os downstream. This offsets the effect of positive δ^{18}Op due to positive seawater δ^{18}O ($\sim$1.7‰) during the LGM (Schrag et al., 1996), resulting in insignificant variation in δ^{18}Op over central and eastern China ($\sim$1.0–2.0‰) (Cai et al., 2015). Consequently, the relative magnitude of δ^{18}O variations is smaller than the amplitude of the trace element-derived precipitation reconstruction during the LGM. Our previous results also show that the enriched δ^{18}Os during MIS5d and end of MIS5e are attributed to the isotopic compositions of different moisture sources and the dynamics of the monsoon circulation (Wu et al., 2020). Therefore, δ^{18}Os primarily captures features of ASM dynamics, such as intensity, but caution is still advised when using it for precipitation reconstruction.

6.5 Conclusions

Based on high-resolution stalagmite trace element records, for the first time, this dissertation infer variations of the regional hydrological environment in southwest China during 4.07–116.09 ka BP. Our study highlights that the NHSI and differences in insolation in the interhemispheric tropics are the primary control on ASM precipitation phase variations. However, global ice volume moderates the magnitude of the response of monsoonal precipitation amount to changes in insolation. This dissertation suggest that discussions of the meridional tripolar distribution pattern in monsoon region in China on the orbital scale should be carefully considered regarding the range of its influence, although this pattern is highly significant during the modern and last glacial millennial events. This study provides a robust reference for precipitation variations in monsoon region in China, which can be used to validate the paleo precipitation simulation data.

Chapter 7

Conclusions and Outlook

7.1 Conclusions

Technological Advancements in Isotope Measurements of Fluid Inclusions water

This dissertation systematically enhances Heidelberg fluid inclusions water isotope measurement setup, incorporating numerous standard measurements and methodological optimizations. It quantifies the logarithmic trend in the deviation of the measured δ^{18}O and δ^{2}H values from the expected values under conditions of low water volume (less than 0.5 µl). To address this phenomenon, a novel calibration scheme is proposed to optimize isotope measurement results for small water volume samples. Through modifications to sample mixing cavity, improvements in the measurement process, and optimization of the data analysis protocol, the preheating and measurement times for individual samples have been shortened, while maintaining measurement accuracy. This approach also prevents potential evaporation and isotope fractionation of inclusion water caused by prolonged heating, and reduces the influence of background water vapor isotope values on fluid inclusion water isotope measurements.

Building upon these advancements, the newly developed method of encapsulating samples in glass tubes prevents the evaporation of inclusion water. It also minimizes the isotopic fractionation induced by high-temperature heating before crushing and measurement. The dissertation quantitatively assesses the isotopic fractionation caused by preheating-related evaporation during the isotopic analysis of fluid inclusion water in coral skeletons, using cold-water corals from Angola and Iceland, and applying the Rayleigh fractionation model. The results demonstrate that pre-crushing heating of coral samples—under varying temperature and duration conditions—induces significant fractionation effects on δ^{18}O and δ^{2}H values, leading to inconsistent measurements across different experimental setups and heating protocols. By introducing the glass tube encapsulation technique, both inclusion water evaporation and isotopic fractionation are effectively minimized, significantly improving measurement reproducibility. This advancement establishes a solid technical foundation for improving the reliability of isotopic analyses of fluid inclusion water in comparable experimental systems.

New Knowledge of the Water Fractionation Mechanism of Cold-Water Coral Skeleton Inclusions

Isotopic analyses of fluid inclusion water from Angola cold-water coral skeletons reveal no significant differences in δ^{18}O or δ^{2}H between the Holocene and the Last Glacial Period. The δ^{18}O values are like the values of seawater, whereas δ^{2}H values are markedly depleted (−55‰ to −70‰), which may reflect biological regulation during calcification or mixing between calcifying fluids and seawater. Immersion experiments further demonstrate the presence of an exchangeable water reservoir within the coral skeleton, which undergoes variable exchange with surrounding seawater and becomes progressively evaporated following separation from the marine environment. While current methodologies are insufficient to fully resolve the primary hydrogen and oxygen isotopic signatures of coral skeletons inclusion water, the experimental framework and measurement protocols developed here establish a robust basis for interpreting their environmental significance. These findings advance the mechanistic understanding of isotopic fractionation in cold-water coral inclusion water and provide essential methodological support for paleoceanographic reconstructions based on coral skeletons fluid inclusions water isotopic composition.

Interlaboratory Comparison Reveals the Accuracy and Limitations of Fluid Inclusion Water Isotope Measurements

In this dissertation, the precision and accuracy characteristics of fluid inclusion water isotope measurements are systematically assessed through an inter-laboratory comparison experiment involving 13 laboratories. δ^{18}O measurements deviate from standard water δ^{18}O values by less than 1‰ in most reports, whereas δ^{2}H deviations typically range from 2 to 5‰, highlighting the greater technical challenges associated with hydrogen isotope analysis. Water volume is a key factor affecting measurement accuracy. For water volumes ≥1 µl, the standard deviations of δ^{18}O and δ^{2}H stabilize at 0.2-1.0‰ and 0.2-2.0‰, respectively. However, when the water volume decreases to ≤0.5 µl, the standard deviations increase significantly (up to 3‰ for δ^{18}O and over 10‰ for δ^{2}H), indicating substantial uncertainties in the analysis of low-volume samples. Most reports observe water volume effects on isotope values, with δ^{18}O and δ^{2}H showing systematic shifts of 2-5‰ as water volume decreases. The direction of these shifts may be influenced by factors such as experimental setup. Taken together, isotope results for water volumes in the 0.5-1 µl range are closest to expected values for most laboratories and exhibit good internal reproducibility.

Hydrological and Environmental Changes in Southwestern China During the Middle and Late Holocene in Relation to ENSO and Human Activities

This dissertation reconstructs mid-to-late Holocene hydroclimatic variations in southwestern China using δ^{18}O and δ^{2}H time-series from fluid inclusion water in Holocene stalagmites. By applying the Rayleigh fractionation model and the glass tube encapsulation technique, evaporation-induced isotopic fractionation during measurement was effectively minimized, leading to robust isotopic datasets. Analytical results indicate that weakened ASM intensities during the mid-to-late Holocene correspond to significantly elevated δ^{18}O and δ^{2}H values in fluid inclusion water, demonstrating a high hydrological sensitivity to ASM variability. Late Holocene $\delta^{18}O_{FI}$ fluctuations suggest intensified ENSO activity, with four major drought events (1.36, 2.26, 3.45, and 5.60 ka BP) occurring in strong synchronicity with persistent El Niño events. Furthermore, a rapid $\delta^{18}O$ positive episode between 950 and 1150 BP correlates with agricultural expansion driven by population migration, marking early anthropogenic hydrological degradation. These findings conclusively demonstrate that pre-industrial human activities had already exerted profound impacts on regional environmental systems.

Driving Mechanisms of Monsoon Orbital-Scale Precipitation Variations in the Asian Monsoon Region

This dissertation presents a high-resolution reconstruction of regional hydrological variations in southwestern China over orbital timescales (4.07–116.09 ka BP) through an integrated analysis of stalagmite trace element ratios, $\delta^{18}O$ and $\delta^{13}C$ records. The results indicate that NHSI and the interhemispheric insolation gradient across tropical latitudes are primary controls on the phase variations of EASM precipitation. Enhanced EASM rainfall occurred during periods of higher NHSI and greater tropical interhemispheric insolation contrasts. In addition to solar forcing, global ice volume modulated the magnitude of precipitation responses to NHSI. During the LGM, the high ice volume resulted in a significant reduction in monsoon precipitation. Although climate simulations suggest a persistent meridional tripolar spatial pattern over orbital timescales in the Chinese monsoon region, characterized by anti-phase rainfall variations between central China and northern/southern China, our trace element ratio records show broad consistency with paleoprecipitation reconstructions from both southern and northern China. This highlights remaining uncertainties regarding the meridional tripolar spatial pattern of Chinese monsoon precipitation. This dissertation underscores the need for caution when interpreting spatial characteristics of orbital-scale monsoon rainfall variations based solely on single-proxy reconstruction records.

7.2 Outlook

While this dissertation has advanced fluid inclusion water isotope analysis techniques and provided new insights into the mechanisms driving multi-scale hydroclimatic variability in the Asian monsoon region, several challenges remain. Future research could be pursued along the following directions:

First, continued innovation in isotopic measurement techniques for fluid inclusions is essential, particularly for low water volume samples. Stalagmite fluid inclusions often contain minimal water (typically 0 – 1 µl/g). Despite substantial improvements in isotopic accuracy and measurement efficiency with CRDS and IRMS setups, pronounced volume-dependent isotopic shift persists at low water volumes, undermining analytical accuracy and precision. To address this, future work could focus on refining empirical calibration models for volume-dependent isotopic offsets through extensive replicate measurements under low water volume conditions. Additionally, reducing the background water vapor concentration represents another promising approach to improving the signal-to-noise ratio of isotope measurements. While the source of isotopic fractionation is not yet fully understood, it may primarily originate from the background vapor, or alternatively, be related to the integration process of water vapor and isotope signals during data processing. For instance, if the integration surface area is systematically underestimated, the calculated isotopic values may shift accordingly. Therefore, future research should aim to optimize background signal correction and evaluate the influence of signal integration methods on isotopic results, thereby further enhancing the accuracy and reliability of fluid inclusion water isotope measurements.

Another critical issue requiring attention is the control of isotopic fractionation during sample measurements, especially the preheating of the sample prior to crushing. Although the use of glass tube encapsulation in this dissertation effectively minimizes isotopic fractionation during the heating stage, further validation is needed to assess the potential influence of water vapor adsorption on sample surfaces and the contribution of moisture from trapped air under laboratory conditions (i.e., temperature and humidity). Our experiments, involving the measurement of small capillary tube filled with standard water and Iceland Spar, suggest that under a water content of 1 µl/g, these effects may be negligible. Nevertheless, further evaluation is necessary to assess the potential impact of vapor adsorption and atmospheric moisture on samples with lower water content. Additionally, future studies should thoroughly investigate possible interference from water background signals and adsorption effects caused by the large number of glass fragments generated during the crushing process in glass tubes, as well as their influence on final isotopic measurements.

The second aspect relates to findings from inter-laboratory comparisons of fluid inclusion isotope measurements, which reveal ongoing challenges in δ^{18}O and δ^{2}H analyses of inclusion water. Significant discrepancies in isotope results are common across laboratories, likely due to differences in instruments, procedures, heating settings, and data processing. Clarifying the influence of these factors on measurements and improving data consistency through optimized workflows or standardized protocols should be key goals for future work. Moreover, some laboratories observe higher standard deviations and systematic shifts in isotopic values under low water volume conditions, especially when volumes are below 0.5 µl. Future studies should investigate the cause of this volume effect and its impact on the accuracy and reproducibility of δ^{18}O and δ^{2}H measurements. There is also a need to improve or develop more sensitive techniques for small water content sample analyses. Finally, using Iceland Spar to simulate sample crushing does not fully capture the possible effects of water adsorption on freshly broken calcite surfaces. Future studies should use real speleothem samples to better assess how adsorption might affect isotope results.

The third aspect should focus on the mechanisms of hydrogen and oxygen isotope fractionation in fluid inclusions in cold-water coral skeletons, particularly the significant negative shift in δ^2H relative to seawater δ^2H. Combining precise isotope measurements techniques with studies of coral biomineralization will help clarify how isotopic fractionation occurs during water inclusion formation and preservation. Investigating water exchange between different “reservoirs” in coral skeletons and surrounding seawater—as well as the effects of drying and heating on isotopic signals—may provide important insights for improving data interpretation.

Understanding the interactions between regional hydroclimatic changes and human activities since the Holocene—particularly the relative roles of natural forcing and anthropogenic influences in extreme hydrological events—remains a key focus for future research. This could be achieved by developing multi-proxy approaches based on indicators sensitive to surface hydrological conditions, combined with cross-validation against other climate and environmental archives, including historical documentary records. In particular, isotopic compositions of stalagmite fluid inclusion water can trace past hydrological changes and detect subtle climatic fluctuations, thus enhancing the precision of paleoenvironmental reconstructions. It well help to clarify the interplay between climate change and human activities, including agricultural expansion and population migration.

To further advance our understanding of Asian monsoon dynamics, three key areas merit additional attention. First, the role of low-latitude solar insolation gradients in modulating monsoonal precipitation should be systematically analyzed. Second, the impact of ice volume fluctuations on low-latitude precipitation needs to be quantitatively assessed, particularly under conditions of reduced solar insolation. Third, integrating multiple climate proxies—such as lake sediments and loess records—can help clarify precipitation heterogeneity across the Chinese monsoon region and test their consistency with climate model simulations.

List of publications

Published as (co-)first/corresponding author:

1. **Wu, Y***., Hölkermann, D., Grund, A., Warken, S., & Frank, N. (2025). Environmental and calcification impacts on the δ^{18}O and δ^{2}H values of cold-water coral skeleton fluid inclusions. *Geochemistry, Geophysics, Geosystems*, e2024GC011981. https://doi.org/10.1029/2024GC011981

2. Xue, Y.-X., **Wu, Y**, Chen, C.-L., Fan, T., Su, H., Li, H.-Y., Cheng, H., Yin, J.-J., Li, J.-Y., Ning, Y.-F., & Li, T.-Y*. (2025). Stalagmite Multi-Proxy Records Reveal Spatial Complexity of Precipitation and Monsoon Variability in China Over the Past 60 Years. (co-first author). *Quaternary Science Reviews, 353*, 109240. https://doi.org/10.1016/j.quascirev.2025.109240

3. Xue, Y.-X., **Wu, Y***, Chen, C.-L., Li, J.-Y., Cheng, H., Shen, C.-C., Zhang, J., & Li, T.-Y*. (2025). Evolution of the Asian Summer Monsoon During the Heinrich Events 1–6. *Global and Planetary Change, 245*, 104680. (co-first and co-corresponding author). https://doi.org/10.1016/j.gloplacha.2024.104680

4. **Wu, Y***, Warken, S., Frank, N., Mielke, A., Chen, C., Li, J.-Y., & Li, T.-Y*. (2023). Northern Hemisphere Summer Insolation and Ice Volume Driven Variations in Hydrological Environment in Southwest China. *Geophysical Research Letters, 50(23)*, e2023GL105664. https://doi.org/10.1029/2023GL105664

5. **Wu, Y**, Li, T.-Y.* , Cheng, H., Ning, Y.-F., Shen, C.-C., Yang, Y., Zhao, J.-Y., Chen, C.-J., Liang, M.-Q., Xiao, S.-Y., Qiu, H.-Y., Xu, Y.-Z., Huang, Y.-Y., Yu, T.-L., & Edwards, R. L. (2023). Variations in Asian Summer Monsoon and Hydroclimate During Heinrich Stadials 4 Revealed by Stalagmite Stable Isotopes and Trace Elements. *Quaternary Science Reviews, 299,* 107869. https://doi.org/10.1016/j.quascirev.2022.107869

6. **Wu, Y**, Li, T.-Y*., Yu, T., Shen, C.-C., Chen, C.-L., Zhang, J., Li, J.-Y., Wang, T., Huang, R., & Xiao, S.-Y. (2020). Variation of the Asian Summer Monsoon Since the

Last Glacial-Interglacial Recorded in a Stalagmite from Southwest China. *Quaternary Science Reviews, 234*, 106261. https://doi.org/10.1016/j.quascirev.2020.106261

7. **Wu, Y**, Li, T.-Y*., Chen, C.-J., Huang, R., Wang, T., Xiao, S.-Y., Qiu, H.-Y., Xu, Y.-Z., Huang, Y.-Y., & Li, J.-Y. (2020). Application of stalagmite laminae in paleoclimate reconstructions of China. *Quaternary Sciences, 40(4)*, 1008–1024. [In Chinese with English abstract] https://doi.org/10.11928/j.issn.1001-7410.2020.04.15

Published as co-authors:

8. Chen, C.-J., **Wu, Y**, Li, J.-Y., Zhang, H.-W., Cheng, H., Shen, C.-C., Ning, Y.-F., Yuan, D.-X., Edwards, R. L., Zhang, J., & Li, T.-Y. (2025). Hydrological changes in the East Asian monsoon region around 4.2 ka precisely reconstructed from multiproxy stalagmites. *Quaternary Science Reviews, 320*, 109321. https://doi.org/10.1016/j.quascirev.2025.109321

9. Wang, C.-Y., Li, J.-Y., Chen, C.-J., **Wu, Y**, Su, Z., Liang, Q.-S., Li, H.-Y., Zhang, J., & Li, T.-Y. (2025). Evolution of the Asian summer monsoon and regional karst ecological environment since the middle ages in Southwest China. *Scientific Reports, 15*, 8091. https://doi.org/10.1038/s41598-025-92634-0

10. Li, J.-Y., Li, T.-Y., Li, H.-C., Spötl, C., Chen, C.-J., Zhang, J., **Wu, Y**, Li, H.-Y., Jin, Y., Zhao, M., Li, H.-K., & Dong, Y.-M. (2024). The influence of hydrogeology and carbon sources on speleothem δ^{13}C based on long-term monitoring in Furong Cave, southwest China. *Chemical Geology, 642*, 122210. https://doi.org/10.1016/j.chemgeo.2024.122210

11. Xue, Y.-X., Zhang, J., Su, Z., **Wu, Y**, Liang, Q.-S., Liang, M.-Q., Liu, X.-Z., Chen, C.-J., Qiu, H.-Y., Li, J.-Y., & Li, T.-Y. (2023). Quantifying source effects based on rainwater δ^{18}O from 10-year monitoring records in Southwest China. *Applied Geochemistry, 145*, 105706. https://doi.org/10.1016/j.apgeochem.2023.105706

12. Weissbach, T., Kluge, T..*, Affolter, S., Leuenberger, M. C., Vonhof, H., Riechelmann, D. F. C., Fohlmeister, J., Juhl, M.-C., Hemmer, B., **Wu, Y**, Warken, S. F., Schmidt, M., Frank, N., & Aeschbach, W. (2023). Constraints for Precise and Accurate Fluid Inclusion Stable Isotope Analysis Using Water-Vapor Saturated CRDS Techniques. *Chemical Geology, 617*, 121268. https://doi.org/10.1016/j.chemgeo.2022.121268

13. Huang, Y.-Y., Li, T.-Y., Chen, C.-L., Huang, R., Wang, T., **Wu, Y**, Xiao, S.-Y., Xu, Y.-Z., Qiu, H.-Y., Yang, Y., & Li, J.-Y. (2022). Testing the Isotopic Equilibrium Frac-

tionation on Active Speleothem Based on Cave Monitoring. *Journal of Earth System Science, 120*, 40-01845-W. https://doi.org/10.1007/s12040-022-01845-w

14. Li, T.-Y..*, Xiao, S.-Y., Shen, C.-C., Zhang, J., Chen, C.-J., Cheng, H., Spötl, C., Huang, R., Wang, T., Li, J.-Y., **Wu, Y**, Liu, Z.-Q., Yu, T.-L., & Edwards, R. L. (2021). Little Ice Age Climate Changes in Southwest China from a Stalagmite δ^{18}O Record. *Palaeogeography, Palaeoclimatology, Palaeoecology, 562*, 110167. https://doi.org/10.1016/j.palaeo.2020.110167

15. Li, T.-Y..*, Li, T.-Y., Wang, X., Chen, C.-L., Tan, M., & **Wu, Y** (2022). Testing the Initial ^{230}Th/^{232}Th for ”Known Age Carbonate” and Its Significance for ^{230}Th Dating and Paleoclimate Research. *Quaternary International, 670*, 113-119. https://doi.org/10.1016/j.quaint.2021.07.020

16. Li, T.-Y..*, Baker, J. L*., Wang, T., Zhang, J., **Wu, Y**, Li, H.-C., Blakharchuk, T., Yu, T.-L., Shen, C.-C., Cheng, H., Kong, X.-G., Xie, W.-L., & Edwards, R. L. (2021). Early Holocene Permafrost Retreat in West Siberia Amplified by Reorganization of Westerly Wind Systems. *Communications Earth & Environment, 4*, 3247-00238-2. https://doi.org/10.1038/s43247-021-00238-z

17. Li, J.-Y*., Li, T.-Y., Shen, C.-C., Yu, T.-L., Zhang, T.-T., **Wu, Y**, Zhou, J.-L., Chen, C.-L., & Zhang, J. (2021). Variations and Significance of Mg/Sr and ^{87}Sr/^{86}Sr in a Karst Cave System in Southwest China. *Journal of Hydrology, 596*, 126140. https://doi.org/10.1016/j.jhydrol.2021.126140

18. Chen, C.-J., Yuan, D.-X., Cheng, H., Yu, T.-L., Shen, C.-C., Edwards, R. L., **Wu, Y**, Xiao, S.-Y., Zhang, J., Wang, T., Huang, R., Liu, Z.-Q., Li, T.-Y., & Li, J.-Y*. (2021). Human Change Triggered the Expansion of Rocky Desertification in Southwestern China. *Science China Earth Sciences, 64*, 1674-7313. https://doi.org/10.1007/s11430-020-9760-7

19. Qiu, H.-Y., Li, T.-Y*., Chen, C.-L., Huang, R., Wang, T., **Wu, Y**, Xiao, S.-Y., Xu, Y.-Z., Huang, Y.-Y., & Zhang, J. (2021). Significance of Active Speleothem δ^{18}O at Annual-Decadal Timescale: A Case Study from Monitoring in Furgng Cave. *Applied Geochemistry, 126*, 104873. https://doi.org/10.1016/j.apgeochem.2021.104873

20. Li, T.-Y*., **Wu, Y**, Shen, C.-C., Lin, K., Tan, L.-C., Jiang, X.-Y., Cheng, H., & Edwards, R.L. (2021). High Precision Dating on the Variation of the Asian Summer Monsoon Since 37 Ka BP. *Scientific Reports, 11*, 9375. https://doi.org/10.1038/s41598-021-88597-7

21. Chen, C.-J., Huang, R., Yuan, D.-X., Zhang, J., Cheng, H., Ning, Y.-F., Yu, T.-L., Shen, C.-C., Edwards, R. L., Long, X.-Y., Wang, T., Xiao, S.-Y., **Wu, Y**, Liu, Z.-Q., Li, T.-Y., & Li, J.-Y*. (2021). Karst Hydrological Changes During the Late Holocene in Southwestern China. *Quaternary Science Reviews, 258*, 106865. https://doi.org/10.1016/j.quascirev.2021.106865

22. Xiao, S.-Y., Li, T.-Y., Chen, C.-J., Huang, R., Wang, T., **Wu, Y**, Xu, Y.-Z., Qiu, H.-Y., Huang, Y.-Y., & Li, J.-Y. (2021). Pattern of precipitation changes in southern China during the Little Ice Age. *Geological Review, 67(1)*, 56–67. [In Chinese with English abstract]. https://doi.org/10.16509/j.georeview.2021.01.005

23. Huang, R., Chen, C.-J., Li, T.-Y., **Wu, Y**, Xiao, S.-Y., Zhang, J., Wang, T., & Li, J.-Y. (2019). Comparison of climatic events in the Late Holocene, based on stalagmite records from monsoon regions near the east and west Pacific. *Quaternary Sciences, 39(3)*, 742–754. [In Chinese with English abstract]. https://doi.org/10.11928/j.issn.1001-7410.2019.03.19

Bibliography

Affolter, S., Fleitmann, D., and Leuenberger, M. (2014). New online method for water isotope analysis of speleothem fluid inclusions using laser absorption spectroscopy (WS-CRDS). *Climate of the Past* 10, 1291–1304. https://doi.org/10.5194/cp-10-1291-2014

Affolter, S., Hauselmann, A., Fleitmann, D., Edwards, R. L., Cheng, H., and Leuenberger, M. (2019). Central europe temperature constrained by speleothem fluid inclusion water isotopes over the past 14,000 years. *Science Advances* 5, 9. https://doi.org/10.1126/sciadv.aav3809

Affolter, S., Häuselmann, A. D., Fleitmann, D., Häuselmann, P., and Leuenberger, M. (2015). Triple isotope (δD, δ^{17}O, δ^{18}O) study on precipitation, drip water and speleothem fluid inclusions for a western central european cave (NW Switzerland). *Quaternary Science Reviews* 127, 73–89. https://doi.org/10.1016/j.quascirev.2015.08.030

Affolter, S., Kipfer, T., Hofmeister, E., Leuenberger, M., and Fleitmann, D. (2025). Paleoclimatic significance of water isotopes in speleothem fluid inclusions. *Earth-Science Reviews* 261, 105026. https://doi.org/10.1016/j.earscirev.2024.105026

Affolter, S. and Leuenberger, M. C. (2021). Challenges in the direct determination of $^{17}\mathrm{O}_{excess}$ in microliter amount of water extracted from speleothem fluid inclusions. *Frontiers in Earth Science* 9. https://doi.org/10.3389/feart.2021.612436

Allemand, D., Tambutté, É., Zoccola, D., and Tambutté, S. (2011). Coral calcification, cells to reefs. In *Coral Reefs: An Ecosystem in Transition*, eds. Z. Dubinsky and N. Stambler (Springer). 119–150

An, Z. S., Clemens, S. C., Shen, J., Qiang, X., Jin, Z., Sun, Y., et al. (2011). Glacial-interglacial Indian summer monsoon dynamics. *Science* 333, 719–723. https://dx.doi.org/10.1126/science.1203752

An, Z. S., Porter, S. C., Kutzbach, J. E., Xihao, W., Suming, W., Xiaodong, L., et al. (2000). Asynchronous Holocene optimum of the east Asian monsoon. *Quaternary Science Reviews* 19, 743–762. https://doi.org/10.1016/S0277-3791(99)00031-1

An, Z. S., Wu, G. X., Li, J. P., Sun, Y. B., Liu, Y. M., Zhou, W. J., et al. (2015). Global monsoon dynamics and climate change. *Annual Review of Earth and Planetary Sciences* 43, 29–77. https://doi.org/10.1146/annurev-earth-060313-054623

Andrews, J. T. and Voelker, A. H. L. (2018). ”Heinrich events” (& sediments): A history of terminology and recommendations for future usage. *Quaternary Science Reviews* 187, 31–40. https://doi.org/10.1016/j.quascirev.2018.03.017

Arienzo, M. M., Swart, P. K., and Vonhof, H. B. (2013). Measurement of δ^{18}O and δ^{2}H values of fluid inclusion water in speleothems using cavity ring-down spectroscopy compared with isotope ratio mass spectrometry. *Rapid Communications in Mass Spectrometry* 27, 2616–2624. https://doi.org/10.1002/rcm.6723

Azharuddin, S., Omine, K., Masaka, K., Asami, R., Lone, M. A., Chou, Y.-C., et al. (2025). Multidecadal hydroclimate responses to volcanic forcing in the Mid-Holocene. *Communications Earth & Environment* 6, 101. https://doi.org/0.1038/s43247-025-02047-0

Bai, X. Y., Wang, S. J., and Xiong, K. N. (2013). Assessing spatial-temporal evolution processes of karst rocky desertification land: Indications for restoration strategies. *Land Degradation & Development* 24, 47–56. https://doi.org/10.1002/ldr.1102

Baker, A. and Genty, D. (1998). Environmental pressures on conserving cave speleothems: effects of changing surface land use and increased cave tourism. *Journal of Environmental Management* 53, 165–175. https://dx.doi.org/10.1006/jema.1998.0208

Baker, A., Hartmann, A., Duan, W., Hankin, S., Comas-Bru, L., Cuthbert, M. O., et al. (2019). Global analysis reveals climatic controls on the oxygen isotope composition of cave drip water. *Nature Communications* 10, 2984. https://doi.org/10.1038/s41467-019-11027-w

Baker, A., Smith, C. L., Catherine, J., Fairchild, I. J., Dominique, G., and Lisa, F. (2008). Annually laminated speleothems: a review. *International Journal of Speleology* 37, 193–206. http://dx.doi.org/10.5038/1827-806X.37.3.4

Barker, S., Chen, J., Gong, X., Jonkers, L., Knorr, G., and Thornalley, D. (2015). Icebergs not the trigger for North Atlantic cold events. *Nature* 520, 333–336. https://doi.org/10.1038/nature14330

Bassis, J. N., Petersen, S. V., and Mac Cathles, L. (2017). Heinrich events triggered by ocean forcing and modulated by isostatic adjustment. *Nature* 542, 332–334. https://doi.org/10.1038/nature21069

Beck, J. W., Zhou, W. J., Li, C., Wu, Z. K., White, L., Xian, F., et al. (2018). A 550,000-year record of east Asian monsoon rainfall from ^{10}Be in loess. *Science* 360, 877–881. https://doi.org/10.1126/science.aam5825

Berger, A. (1988). Milankovitch theory and climate. *Reviews of Geophysics* 26, 624–657. https://doi.org/10.1029/RG026i004p00624

Bintanja, R. and van de Wal, R. S. W. (2008). North American ice-sheet dynamics and the onset of 100,000-year glacial cycles. *Nature* 454, 869–872. https://doi.org/10.1038/0.1038/nature07158

Blyth, A. J., Baker, A., Collins, M. J., Penkman, K. E. H., Gilmour, M. A., Moss, J. S., et al. (2008). Molecular organic matter in speleothems and its potential as an environmental proxy. *Quaternary Science Reviews* 27, 905–921. https://doi.org/10.1016/j.quascirev.2008.02.002

Brand, W. A., Geilmann, H., Crosson, E. R., and Rella, C. W. (2009). Cavity ring-down spectroscopy versus high-temperature conversion isotope ratio mass spectrometry; a case study on δ^2H and δ^{18}O of pure water samples and alcohol/water mixtures. *Rapid Communications in Mass Spectrometry* 23, 1879–1884. https://doi.org/10.1002/rcm.4083

Burns, S. J., Matter, A., Frank, N., and Mangini, A. (1998). Speleothem-based paleoclimate record from northern oman. *Geology* 26, 499–502. https://doi.org/10.1130/0091-7613(1998)026<0499:SBPRFN>2.3.CO;2

Cai, Y. J., An, Z. S., Cheng, H., Edwards, R. L., Kelly, M. J., Liu, W. G., et al. (2006). High-resolution absolute-dated Indian monsoon record between 53 and 36 ka from Xiaobailong cave, southwestern China. *Geology* 34, 621. https://doi.org/10.1130/G22567.1

Cai, Y. J., Cheng, H. A. I., Cheng, X., Shi, Z. G., Lu, Y. B., Ma, L. E., et al. (2023). Orbital-to millennial-scale variation of the speleothem δ^{18}O record during marine isotope stages 5 to 3 on the southeast Chinese loess plateau and its climatic and environmental implications. *Journal of Quaternary Science* 38, 295–307. https://doi.org/10.1002/jqs.3489. Https://doi.org/10.1002/jqs.3489

Cai, Y. J., Fung, I. Y., Edwards, R. L., An, Z. s., Cheng, H., Lee, J.-E., et al. (2015). Variability of stalagmite-inferred Indian monsoon precipitation over the past 252,000 y. *Proceedings of the National Academy of Sciences* 112, 2954–2959. https://dx.doi.org/10.1073/pnas.1424035112

Cai, Z. Y., Tian, L. D., and Bowen, G. J. (2018). Spatial-seasonal patterns reveal large-scale atmospheric controls on Asian monsoon precipitation water isotope ratios. *Earth and Planetary Science Letters* 503, 158–169. https://doi.org/10.1016/j.epsl.2018.09.028

Caley, T., Zaragosi, S., Bourget, J., Martinez, P., Malai, B., Eynaud, F., et al. (2013). Southern hemisphere imprint for Indo–Asian summer monsoons during the last glacial period as revealed by arabian sea productivity records. *Biogeosciences* 10, 7347–7359. https://doi.org/10.5194/bg-10-7347-2013

Cao, J. T., Chen, F. J., Chu, G. Q., and Jia, G. D. (2024). A persistent coast mode of precipitation in southeast China over the last millennium. *Geophysical Research Letters* 51, e2024GL109379. https://doi.org/10.1029/2024GL109379

Cerling, T. E. (1984). The stable isotopic composition of modern soil carbonate and its relationship to climate. *Earth and Planetary Science Letters* 71, 229–240. https://doi.org/10.1016/0012-821X(84)90089-X

Chen, C., Zheng, Y. W., Zheng, Z., Zong, Y. Q., Huang, K. Y., Rolett, B. V., et al. (2023). Holocene millennial-scale megaflood events point to ENSO-driven extreme climate changes. *Science China Earth Sciences* 66, 2530–2545. https://doi.org/10.1007/s11430-023-1196-y

Chen, C.-J., Huang, R., Yuan, D.-X., Zhang, J., Cheng, H., Ning, Y.-F., et al. (2021a). Karst hydrological changes during the late-Holocene in southwestern China. *Quaternary Science Reviews* 258, 106865. https://doi.org/10.1016/j.quascirev.2021.106865

Chen, C.-J. and Li, T.-Y. (2018). Geochemical characteristics of cave drip water respond to ENSO based on a 6-year monitoring work in Yangkou cave, southwest China. *Journal of Hydrology* 561, 896–907. https://doi.org/10.1016/j.jhydrol.2018.04.061

Chen, C.-J., Yuan, D. X., Cheng, H., Yu, T.-L., Shen, C.-C., Edwards, R. L., et al. (2021b). Human activity and climate change triggered the expansion of rocky desertification in the karst areas of southwestern China. *Science China Earth Sciences* 64, 1761–1773. https://doi.org/10.1007/s11430-020-9760-7

Chen, J. S., Zhao, K., Wang, Y. J., Cui, Y. F., Liang, Y. J., Shao, Q. F., et al. (2022). ENSO effect on hydroclimate changes in southeastern China over the past two millennia. *Quaternary Science Reviews* 285, 107539. https://doi.org/10.1016/j.quascirev.2022.107539

Chen, M. Y., Xie, P. P., Janowiak, J. E., and Arkin, P. A. (2002). Global land precipitation: A 50-yr monthly analysis based on gauge observations. *Journal of Hydrometeorology* 3, 249–266. https://doi.org/10.1175/1525-7541(2002)003<0249:GLPAYM>2.0.CO;2

Chen, S., Hoffmann, S. S., Lund, D. C., Cobb, K. M., Emile-Geay, J., and Adkins, J. F. (2016). A high-resolution speleothem record of western equatorial Pacific rainfall: Implications for Holocene ENSO evolution. *Earth and Planetary Science Letters* 442, 61–71. https://doi.org/10.1016/j.epsl.2016.02.050

Cheng, H., Edwards, R. L., Sinha, A., Sptl, C., Yi, L., Chen, S. T., et al. (2016a). The Asian monsoon over the past 640,000 years and ice age terminations. *Nature* 534, 640–646. https://doi.org/10.1038/nature18591

Cheng, H., Lawrence Edwards, R., Shen, C. C., Polyak, V. J., Asmerom, Y., Woodhead, J., et al. (2013). Improvements in ^{230}Th dating, ^{230}Th and ^{234}U half-life values, and U-Th isotopic measurements by multi-collector inductively coupled plasma mass spectrometry. *Earth Planetary Science Letters* 371-372, 82–91. https://doi.org/10.1016/j.epsl.2013.04.006

Cheng, H., Li, H. Y., Sha, L. J., Sinha, A., Shi, Z. G., Yin, Q. Z., et al. (2022a). Milankovitch theory and monsoon. *The Innovation* 3, 100338. https://doi.org/10.1016/j.xinn.2022.100338

Cheng, H., Spötl, C., Breitenbach, S. F. M., Sinha, A., Wassenburg, J. A., Jochum, K. P., et al. (2016b). Climate variations of central Asia on orbital to millennial timescales. *Scientific Reports* 6, 36975. https://doi.org/10.1038/srep36975

Cheng, H., Xu, Y., Dong, X. Y., Zhao, J. Y., Li, H. Y., Baker, J., et al. (2021a). Onset and termination of Heinrich stadial 4 and the underlying climate dynamics. *Communications Earth & Environment* 2, 230. https://doi.org/10.1038/s43247-021-00304-6

Cheng, H., Zhang, H. W., Cai, Y. J., Shi, Z. G., Yi, L., Deng, C. L., et al. (2021b). Orbital-scale Asian summer monsoon variations: Paradox and exploration. *Science China Earth Sciences* 64, 529–544. https://doi.org/10.1007/s11430-020-9720-y

Cheng, H., Zhang, H. W., Zhao, J. Y., Li, H. Y., Ning, Y., and Kathayat, G. (2019). Chinese stalagmite paleoclimate researches: A review and perspective. *Science China Earth Sciences* 62, 1489–1513. https://doi.org/10.1007/s11430-019-9478-3

Cheng, K., Wang, Q., Liu, S. H., Liu, Y. F., Yang, Y., Zhan, C., et al. (2022b). Different response of trace elements in the drip-water of Kaiyuan cave on Shandong peninsula (coastal north China) to hydroclimatic changes from 2012 to 2014. *Journal of Hydrology* 608, 127616. https://doi.org/10.1016/j.jhydrol.2022.127616

Chiang, J. C. H. and Bitz, C. M. (2005). Influence of high latitude ice cover on the marine intertropical convergence zone. *Climate Dynamics* 25, 477–496. https://doi.org/10.1007/s00382-005-0040-5

Chiang, J. C. H., Fung, I. Y., Wu, C.-H., Cai, Y. J., Edman, J. P., Liu, Y. W., et al. (2015). Role of seasonal transitions and westerly jets in east Asian paleoclimate. *Quaternary Science Reviews* 108, 111–129. https://doi.org/10.1016/j.quascirev.2014.11.009

Chiang, J. C. H., Herman, M. J., Yoshimura, K., and Fung, I. Y. (2020). Enriched east Asian oxygen isotope of precipitation indicates reduced summer seasonality in regional climate and westerlies. *Proceedings of the National Academy of Sciences* 117, 14745–14750. https://doi.org/10.1073/pnas.1922602117

Chiang, J. C. H., Swenson, L. M., and Kong, W. (2017). Role of seasonal transitions and the westerlies in the interannual variability of the east Asian summer monsoon precipitation: Seasonal transitions in easm variability. *Geophysical Research Letters* 44, 3788–3795. https://doi.org/10.1002/2017GL072739

Clemens, S. C., Holbourn, A., Kubota, Y., Lee, K. E., Liu, Z., Chen, G., et al. (2018). Precession-band variance missing from east Asian monsoon runoff. *Nature Communications* 9, 3364. https://doi.org/10.1038/s41467-018-05814-0

Cobb, K. M., Westphal, N., Sayani, H. R., Watson, J. T., Di Lorenzo, E., Cheng, H., et al. (2013). Highly variable El Niño–Southern Oscillation throughout the Holocene. *Science* 339, 67–70. https://doi.org/10.1126/science.1228246

Cohen, A. L. and Gaetani, G. A. (2006). Compositional variability in the cold-water coral lophelia pertusa is driven by temperature and aragonite precipitation “efficiency”. *Geochimica et Cosmochimica Acta* 70, A107. https://doi.org/10.1016/j.gca.2006.06.127

Cohen, A. L., Gaetani, G. A., Lundälv, T., Corliss, B. H., and George, R. Y. (2006). Compositional variability in a cold-water scleractinian, lophelia pertusa: New insights into “vital effects”. *Geochemistry, Geophysics, Geosystems* 7. https://doi.org/10.1029/2006GC001354

Cosford, J., Qing, H. R., Mattey, D., Eglington, B., and Zhang, M. L. (2009). Climatic and local effects on stalagmite δ^{13}C values at lianhua cave, China. *Palaeogeography, Palaeoclimatology, Palaeoecology* 280, 235–244. https://doi.org/10.1016/j.palaeo.2009.05.020

Cuif, J.-P. and Dauphin, Y. (2005). The environment recording unit in coral skeletons – a synthesis of structural and chemical evidences for a biochemically driven, stepping-growth process in fibres. *Biogeosciences* 2, 61–73. https://doi.org/10.5194/bg-2-61-2005

Cuif, J.-P., Dauphin, Y., Berthet, P., and Jegoudez, J. (2004). Associated water and organic compounds in coral skeletons: Quantitative thermogravimetry coupled to infrared absorption spectrometry. *Geochemistry, Geophysics, Geosystems* 5. https://doi.org/10.1029/2004GC000783

Dai, G. W., Zhang, Z. S., Otterå, O. H., Langebroek, P., Yan, Q., and Zhang, R. (2022). Simulated cycles of east Asian temperature and precipitation over the past 425 ka. *Journal of Geophysical Research: Atmospheres* 127, e2022JD036802. https://doi.org/10.1029/2022JD036802

Dai, G. W., Zhang, Z. S., Otterå, O. H., Langebroek, P. M., Yan, Q., and Zhang, R. (2021). A modeling study of the tripole pattern of east China precipitation over the past 425 ka. *Journal of Geophysical Research: Atmospheres* 126, e2020JD033513. https://doi.org/10.1029/2020JD033513

Dang, H. W., Jian, Z. M., Wang, Y., Mohtadi, M., Rosenthal, Y., Ye, L. M., et al. (2020). Pacific warm pool subsurface heat sequestration modulated Walker circulation and ENSO activity during the Holocene. *Science Advances* 6, eabc0402. https://doi.org/10.1126/sciadv.abc0402

Day, C. C. and Henderson, G. M. (2013). Controls on trace-element partitioning in cave-analogue calcite. *Geochimica et Cosmochimica Acta* 120, 612–627. https://doi.org/10.1016/j.gca.2013.05.044

Daëron, M., Drysdale, R. N., Peral, M., Huyghe, D., Blamart, D., Coplen, T. B., et al. (2019). Most earth-surface calcites precipitate out of isotopic equilibrium. *Nature Communications* 10, 429. https://doi.org/10.1038/s41467-019-08336-5

de Graaf, S., Vonhof, H. B., Reijmer, J. J. G., Feenstra, E., Mienis, F., Prud'Homme, C., et al. (2022). Analytical artefacts preclude reliable isotope ratio measurement of internal water in coral skeletons. *Geostandards and Geoanalytical Research* 46, 563–577. https://doi.org/10.1111/ggr.12445

de Graaf, S., Vonhof, H. B., Weissbach, T., Wassenburg, J. A., Levy, E. J., Kluge, T., et al. (2020). A comparison of isotope ratio mass spectrometry and cavity ring-down spectroscopy techniques for isotope analysis of fluid inclusion water. *Rapid Communications in Mass Spectrometry* 34, e8837. https://doi.org/10.1002/rcm.8837

De Groeve, J., Kusumoto, B., Koene, E., Kissling, W. D., Seijmonsbergen, A. C., Hoeksema, B. W., et al. (2022). Global raster dataset on historical coastline positions and shelf sea extents since the last glacial maximum. *Global Ecology and Biogeography* 31, 2162–2171. https://doi.org/10.1111/geb.13573

de Wet, C. B., Griffith, E. M., Erhardt, A. M., and Oster, J. L. (2024). A comparative study of cave system calcium isotope ratios: Implications for quantitative reconstruction of paleorainfall from speleothems. *Geochemistry, Geophysics, Geosystems* 25, e2024GC011691. https://doi.org/10.1029/2024GC011691

Deininger, M., Fohlmeister, J., Scholz, D., and Mangini, A. (2012). Isotope disequilibrium effects: The influence of evaporation and ventilation effects on the carbon and oxygen isotope composition of speleothems – a model approach. *Geochimica et Cosmochimica Acta* 96, 57–79. https://doi.org/10.1016/j.gca.2012.08.013

Dennis, P. F., Rowe, P. J., and Atkinson, T. C. (2001). The recovery and isotopic measurement of water from fluid inclusions in speleothems. *Geochimica et Cosmochimica Acta* 65, 871–884. https://doi.org/10.1016/S0016-7037(00)00576-7

Dever, L., Durand, R., Fontes, J. C., and Vachier, P. (1982). Geochimie et teneurs isotopiques des systèmes saisonniers de dissolution de la calcite dans un sol sur craie. *Geochimica Et Cosmochimica Acta* 46, 1947–1956. https://doi.org/10.1016/0016-7037(82)90132-6

Ding, Y. H. and Chan, J. C. L. (2005). The east Asian summer monsoon: an overview. *Meteorology and Atmospheric Physics* 89, 117–142. https://doi.org/10.1007/s00703-005-0125-z

Ding, Y. H., Liang, P., Liu, Y. J., and Zhang, Y. C. (2020a). Multiscale variability of Meiyu and its prediction: A new review. *Journal of Geophysical Research: Atmospheres* 125, e2019JD031496. https://doi.org/10.1029/2019JD031496

Ding, Y. H., Liu, Y. J., and Song, Y. F. (2020b). East Asian summer monsoon moisture transport belt and its impact on heavy rainfalls and floods in China. *Advances in Water Science* 31, 629–643. https://doi.org/10.14042/j.cnki.32.1309.2020.05.001. [In Chinese with English abstract]

Ding, Y. H., Si, D., and Liu, Y. J. (2018). On the characteristics, driving forces and interdecadal variability of the east Asian summer monsoon. *Chinese Journal of Atmospheric Science* 42, 533–558. https://doi.org/10.3878/j.issn.1006-9895.1712.17261

Dong, X. Y., Kathayat, G., Rasmussen, S. O., Svensson, A., Severinghaus, J. P., Li, H. Y., et al. (2022). Coupled atmosphere-ice-ocean dynamics during Heinrich stadial 2. *Nature Communications* 13, 5867. https://doi.org/10.1038/s41467-022-33583-4

Dorale, J. A., Edwards, R. L., Ito, E., and González, L. A. (1998). Climate and vegetation history of the midcontinent from 75 to 25 ka: A speleothem record from Crevice Cave, Missouri, USA. *Science* 282, 1871–1874. https://doi.org/10.1126/science.282.5395.1871

Dorale, J. A. and Liu, Z. (2009). Limitations of hendy test criteria in judging the paleoclimatic suitability of speleothems and the need for replication. *Journal of Cave & Karst Studies the National Speleological Society Bulletin* 71, 73–80. https://caves.org/wp-content/uploads/Publications/JCKS/v71/cave-71-01-73.pdf

Dreybrodt, W. and Scholz, D. (2011). Climatic dependence of stable carbon and oxygen isotope signals recorded in speleothems: From soil water to speleothem calcite. *Geochimica et Cosmochimica Acta* 75, 734–752. https://dx.doi.org/10.1016/j.gca.2010.11.002

Duan, P. Z., Li, H. Y., Ma, Z. B., Zhao, J. Y., Dong, X. Y., Sinha, A., et al. (2023a). Interdecadal to centennial climate variability surrounding the 8.2 ka event in north China revealed through an annually resolved speleothem record from Beijing. *Geophysical Research Letters* 50, e2022GL101182. https://doi.org/10.1029/2022GL101182

Duan, R., Li, T.-Y., Li, J.-Y., Spötl, C., Li, H.-C., Wang, H.-B., et al. (2023b). Karst-ecological changes during the middle and late Holocene in southwest China revealed by δ^{18}O and δ^{13}C records in a stalagmite. *Palaeogeography, Palaeoclimatology, Palaeoecology* 615, 111437. https://doi.org/10.1016/j.palaeo.2023.111437

Duan, W. H., Cai, B. G., Tao, T., Yang, X., and Tan, M. (2023c). Multi-timescale variations of δ^{18}O-δ^{13}C in stalagmites: Insights into isotopic disequilibrium and human activities. *Journal of Geophysical Research: Atmospheres* 128, e2023JD039607. https://doi.org/10.1029/2023JD039607

Duan, W. H., Ruan, J. Y., Luo, W. J., Li, T. Y., Tian, L. J., Zeng, G. N., et al. (2016). The transfer of seasonal isotopic variability between precipitation and drip water at eight caves in the monsoon regions of China. *Geochimica et Cosmochimica Acta* 183, 250–266. https://dx.doi.org/10.1016/j.gca.2016.03.037

Duan, W. H., Wu, S. T., Wang, X. F., Shen, J. H., Xiao, Z. Y., Cui, L. L., et al. (2024). Ma/Ca ratio in stalagmites as a potential palaeo-temperature indicator. *Geophysical Research Letters* 51, e2024GL108498. https://doi.org/10.1029/2024GL108498

Dublyansky, Y. V. and Spötl, C. (2009). Hydrogen and oxygen isotopes of water from inclusions in minerals: design of a new crushing system and on-line continuous-flow isotope ratio mass spectrometric analysis. *Rapid Communications in Mass Spectrometry* 23, 2605–2613. https://doi.org/10.1002/rcm.4155

Duplessy, J.-C., Labeyrie, L., and Waelbroeck, C. (2002). Constraints on the ocean oxygen isotopic enrichment between the last glacial maximum and the Holocene: Paleoceanographic implications. *Quaternary Science Reviews* 21, 315–330. https://doi.org/10.1016/S0277-3791(01)00107-X

D'Olivo, J. P. and McCulloch, M. T. (2017). Response of coral calcification and calcifying fluid composition to thermally induced bleaching stress. *Scientific Reports* 7, 2207. https://doi.org/10.1038/s41598-017-02306-x

EPICA Community Members (2006). One-to-one coupling of glacial climate variability in Greenland and Antarctica. *Nature* 444, 195. https://doi.org/10.1038/nature05301

Fairchild, I. J. and Baker, A. (2012). *The Architecture of Speleothems* (Wiley-Blackwell), chap. 7. 205–244. https://doi.org/10.1002/9781444361094.ch7

Fairchild, I. J., Baker, A., Borsato, A., Frisia, S., Hinton, R., McDermott, F., et al. (2001). Annual to sub-annual resolution of multiple trace-element trends in speleothems. *Journal of The Geological Society* 158, 831–841. https://doi.org/10.1144/jgs.158.5.831

Fairchild, I. J., Smith, C. L., Baker, A., Fuller, L., Spötl, C., Mattey, D., et al. (2006). Modification and preservation of environmental signals in speleothems. *Earth-Science Reviews* 75, 105–153. https://dx.doi.org/10.1016/j.earscirev.2005.08.003

Fairchild, I. J. and Treble, P. C. (2009). Trace elements in speleothems as recorders of environmental change. *Quaternary Science Reviews* 28, 449–468. https://dx.doi.org/10.1016/j.quascirev.2008.11.007

Fan, H. W., Hu, Z. Y., Liu, Y. H., Wang, M. Y., and Hu, C. Y. (2024). Holocene variability of the atlantic multidecadal oscillation and the Pacific decadal oscillation inferred from Chinese speleothem δ^{18}O records. *Paleoceanography and Paleoclimatology* 39, e2023PA004800. https://doi.org/10.1029/2023PA004800

Fernandez, A., Løland, M. H., Maccali, J., Krüger, Y., Vonhof, H. B., Sodemann, H., et al. (2023). Characterization and correction of evaporative artifacts in speleothem fluid inclusion isotope analyses as applied to a stalagmite from Borneo. *Geochemistry, Geophysics, Geosystems* 24, e2023GC010857. https://doi.org/10.1029/2023GC010857

Fleitmann, D., Burns, S. J., Matter, A., Cheng, H., and Affolter, S. (2022). Moisture and seasonality shifts recorded in Holocene and pleistocene speleothems from southeastern Arabia. *Geophysical Research Letters* 49, e2021GL097255. https://doi.org/10.1029/2021GL097255

Fleitmann, D., Burns, S. J., Neff, U., Mangini, A., and Matter, A. (2003). Changing moisture sources over the last 330,000 years in Northern Oman from fluid-inclusion evidence in speleothems. *Quaternary Research* 60, 223–232. https://doi.org/10.1016/S0033-5894(03)00086-3

Fohlmeister, J., Voarintsoa, N. R. G., Lechleitner, F. A., Boyd, M., Brandtstätter, S., Jacobson, M. J., et al. (2020). Main controls on the stable carbon isotope composition of speleothems. *Geochimica et Cosmochimica Acta* 279, 67–87. https://doi.org/10.1016/j.gca.2020.03.042

Gabitov, R. I., Sadekov, A., and Leinweber, A. (2014). Crystal growth rate effect on Mg/Ca and Sr/Ca partitioning between calcite and fluid: An in situ approach. *Chemical Geology* 367, 70–82. https://doi.org/10.1016/j.chemgeo.2013.12.019

Gaffey, S. J. (1988). Water in skeletal carbonates. *Journal of Sedimentary Research* 58, 397–414. https://doi.org/10.1306/212F8DA5-2B24-11D7-8648000102C1865D

Genty, D., Baker, A., Massault, M., Proctor, C., Gilmour, M., Pons-Branchu, E., et al. (2001). Dead carbon in stalagmites: carbonate bedrock paleodissolution vs. ageing of soil organic matter. implications for δ^{13}C variations in speleothems. *Geochimica et Cosmochimica Acta* 65, 3443–3457. https://doi.org/10.1016/S0016-7037(01)00697-4

Genty, D., Blamart, D., Ouahdi, R., Gilmour, M., Baker, A., Jouzel, J., et al. (2003). Precise dating of Dansgaard-Oeschger climate oscillations in western Europe from stalagmite data. *Nature* 421, 833–837. https://doi.org/10.1038/nature01391

Genty, D., Plagnes, V., Causse, C., Cattani, O., Stievenard, M., Falourd, S., et al. (2002). Fossil water in large stalagmite voids as a tool for paleoprecipitation stable isotope composition reconstitution and paleotemperature calculation. *Chemical Geology* 184, 83–95. https://doi.org/10.1016/S0009-2541(01)00356-4

Goede, A., Green, D. C., and Harmon, R. S. (1986). Late Pleistocene paleotemperature record from a Tasmanian speleothem. *Australian Journal of Earth Sciences* 33, 333–342. https://doi.org/10.1080/08120098608729370

Gonfiantini, R., Wassenaar, L. I., Araguas-Araguas, L., and Aggarwal, P. K. (2018). A unified Craig-Gordon isotope model of stable hydrogen and oxygen isotope fractionation during fresh or saltwater evaporation. *Geochimica et Cosmochimica Acta* 235, 224–236. https://doi.org/10.1016/j.gca.2018.05.020

Grant, K. M., Rohling, E. J., Ramsey, C. B., Cheng, H., Edwards, R. L., Florindo, F., et al. (2014). Sea-level variability over five glacial cycles. *Nature Communications* 5, 5076. https://doi.org/10.1038/ncomms6076

Griffiths, M. L., Drysdale, R. N., Vonhof, H. B., Gagan, M. K., Zhao, J.-x., Ayliffe, L. K., et al. (2010). Younger Dryas–Holocene temperature and rainfall history of southern indonesia from δ^{18}O in speleothem calcite and fluid inclusions. *Earth and Planetary Science Letters* 295, 30–36. https://doi.org/10.1016/j.epsl.2010.03.018

Guo, B., Yang, F., Fan, Y. W., and Zang, W. Q. (2023). The dominant driving factors of rocky desertification and their variations in typical mountainous karst areas of southwest China in the context of global change. *Catena* 220, 106674. https://doi.org/10.1016/j.catena.2022.106674

Guo, W., Li, D. H., and Yang, W. C. (2006). Comparative research on mollusca, arthropoda and chordata communities in Xia cave, Feilong cave and Bailong cave in Xingyi. *Guizhou Science* 24. https://doi.org/CNKI:SUN:GZKX.0.2006-02-012. [In Chinese with English abstract]

Gupta, P., Noone, D., Galewsky, J., Sweeney, C., and Vaughn, B. H. (2009). Demonstration of high-precision continuous measurements of water vapor isotopologues in laboratory and remote field deployments using wavelength-scanned cavity ring-down spectroscopy (WS-CRDS) technology. *Rapid Communications in Mass Spectrometry* 23, 2534–2542. https://doi.org/10.1002/rcm.4100

Harmon, R. S., Schwarcz, H. P., and Ford, D. C. (1978). Stable isotope geochemistry of speleothems and cave waters from the Flint Ridge-Mammoth Cave System, Kentucky: Implications for terrestrial climate change during the period 230,000 to 100,000 years b.p. *The Journal of Geology* 86, 373–384. https://doi.org/10.1086/649697

Hays, J. D., Imbrie, J., and Shackleton, N. J. (1976a). Variations in the earth's orbit: Pacemaker of the ice ages. *Science* 194, 1121–1132. https://doi.org/10.1126/science.194.4270.1121

Hays, J. D., Imbrie, J., and Shackleton, N. J. (1976b). Variations in the earth's orbit: Pacemaker of the ice ages. *Science* 194, 1121–1132. https://doi.org/10.1126/science.194.4270.1121

Hebbeln, D., Wienberg, C., Bender, M., Bergmann, F., Dehning, K., Dullo, W.-C., et al. (2017). *ANNA Cold-Water Coral Ecosystems off Angola and Namibia - Cruise No. M122 - December 30, 2015 - January 31, 2016 - Walvis Bay (Namibia) - Walvis Bay (Namibia)*. Techreport 2195-8475, DFG-Senatskommission für Ozeanographie. https://doi.org/10.2312/cr_m122

Helama, S. (2024). The 4.2 ka event: A review of palaeoclimate literature and directions for future research. *The Holocene* 34, 1408–1415. https://doi.org/10.1177/09596836241254486

Held, F., Cheng, H., Edwards, R. L., Tüysüz, O., Koç, K., and Fleitmann, D. (2024). Dansgaard-Oeschger cycles of the penultimate and last glacial period recorded in stalagmites from Türkiye. *Nature Communications* 15, 1183. https://doi.org/10.1038/s41467-024-45507-5

Hemming, S. R. (2004). Heinrich events: Massive late pleistocene detritus layers of the North Atlantic and their global climate imprint. *Reviews of Geophysics* 42, RG1005. https://doi.org/10.1029/2003rg000128

Hendy, C. H. (1971). The isotopic geochemistry of speleothems; 1, the calculation of the effects of different modes of formation on the isotopic composition of speleothems and their applicability as paleoclimatic indicators. *Geochimica et Cosmochimica Acta* 35, 801–824. https://doi.org/10.1016/0016-7037(71)90127-X

Herzschuh, U., Cao, X., Laepple, T., Dallmeyer, A., Telford, R. J., Ni, J., et al. (2019). Position and orientation of the westerly jet determined Holocene rainfall patterns in China. *Nature Communications* 10, 2376. https://doi.org/10.1038/s41467-019-09866-8

Horita, J., Rozanski, K., and Cohen, S. (2008). Isotope effects in the evaporation of water: a status report of the Craig–Gordon model. *Isotopes in Environmental and Health Studies* 44, 23–49. https://doi.org/10.1080/10256010801887174

Horita, J. and Wesolowski, D. J. (1994). Liquid-vapor fractionation of oxygen and hydrogen isotopes of water from the freezing to the critical temperature. *Geochimica et Cosmochimica Acta* 58, 3425–3437. https://doi.org/10.1016/0016-7037(94)90096-5

Hu, C. Y., Henderson, G. M., Huang, J. H., Xie, S. C., Sun, Y., and Johnson, K. R. (2008). Quantification of Holocene Asian monsoon rainfall from spatially separated cave records. *Earth and Planetary Science Letters* 266, 221–232. https://doi.org/10.1016/j.epsl.2007.10.015

Hu, P., Chen, W., Wang, L., Chen, S. F., Liu, Y. Y., and Chen, L. Y. (2022). Revisiting the ENSO–monsoonal rainfall relationship: new insights based on an objective determination of the Asian summer monsoon duration. *Environmental Research Letters* 17, 104050. https://doi.org/10.1088/1748-9326/ac97ad

Huang, J. P., Chen, W., Wen, Z. P., Zhang, G. J., Li, Z. X., Zuo, Z. Y., et al. (2019). Review of Chinese atmospheric science research over the past 70 years: Climate and climate change. *Science China Earth Sciences* 62, 1514–1550. https://doi.org/10.1007/s11430-019-9483-5

Huang, Y. M. and Fairchild, I. J. (2001). Partitioning of Sr^{2+} and Mg^{2+} into calcite under karst-analogue experimental conditions. *Geochimica et Cosmochimica Acta* 65, 47–62. https://doi.org/10.1016/s0016-7037(00)00513-5

Jamieson, R. A., Baldini, J. U. L., Brett, M. J., Taylor, J., Ridley, H. E., Ottley, C. J., et al. (2016). Intra- and inter-annual uranium concentration variability in a belizean stalagmite controlled by prior aragonite precipitation: A new tool for reconstructing hydro-climate using aragonitic speleothems. *Geochimica et Cosmochimica Acta* 190, 332–346. https://doi.org/10.1016/j.gca.2016.06.037

Jian, Z. M., Wang, Y., Dang, H. W., Mohtadi, M., Rosenthal, Y., Lea, D. W., et al. (2022). Warm pool ocean heat content regulates ocean–continent moisture transport. *Nature* 612, 92–99. https://doi.org/10.1038/s41586-022-05302-y

Jiang, N. X., Yan, Q., Xu, Z. Q., and Wang, H. J. (2023). Divergent response of eastern China precipitation to the Pacific decadal oscillation during the last interglacial. *Quaternary Science Reviews* 319, 108344. https://doi.org/10.1016/j.quascirev.2023.108344

Jiang, S. W., Zhou, X., Sachs, J. P., Luo, W. H., Tu, L. Y., Liu, X. Q., et al. (2021). Central eastern China hydrological changes and ENSO-like variability over the past 1800 yr. *Geology* 49, 1386–1390. https://doi.org/10.1130/G48894.1

Jiang, Z. C., Lian, Y. Q., and Qin, X. Q. (2014). Rocky desertification in southwest China: Impacts, causes, and restoration. *Earth-Science Reviews* 132, 1–12. https://doi.org/10.1016/j.earscirev.2014.01.005

Jochum, K. P., Scholz, D., Stoll, B., Weis, U., Wilson, S. A., Yang, Q. C., et al. (2012). Accurate trace element analysis of speleothems and biogenic calcium carbonates by LA-ICP-MS. *Chemical Geology* 318-319, 31–44. https://doi.org/10.1016/j.chemgeo.2012.05.009

Jochum, K. P., Weis, U., Stoll, B., Kuzmin, D., Yang, Q. C., Raczek, I., et al. (2011). Determination of reference values for NIST SRM 610–617 glasses following ISO guidelines. *Geostandards and Geoanalytical Research* 35, 397–429. https://doi.org/10.1111/j.1751-908X.2011.00120.x

Johnston, V. E., Borsato, A., Spötl, C., Frisia, S., and Miorandi, R. (2013). Stable isotopes in caves over altitudinal gradients: fractionation behaviour and inferences for speleothem sensitivity to climate change. *Climate of the Past* 9, 99–118. https://doi.org/10.5194/cp-9-99-2013

Ju, M., Wan, S., Clift, P. D., Pei, W., Jiao, D., Zhang, J., et al. (2024). History of human activity in south china since 7 cal ka bp: Evidence from a sediment record in the south china sea. *Quaternary Science Reviews* 333, 108683. https://doi.org/10.1016/j.quascirev.2024.108683

Kalnay, E., Kanamitsu, M., Kistler, R., Collins, W., Deaven, D., Gandin, L., et al. (1996). The NCEP/NCAR 40-year reanalysis project. *Bulletin of the American Meteorological Society* 77, 437–472. https://doi.org/10.1175/1520-0477(1996)077<0437:TNYRP>2.0.CO;2

Kendall, A. C. and Broughton, P. L. (1978). Origin of fabrics in speleothems composed of columnar calcite crystals. *Journal of Sedimentary Petrology* 48, 519–538. https://doi.org/10.1306/212f74c3-2b24-11d7-8648000102c1865d

Kim, S. T. and O’neil, J. R. (1997). Equilibrium and nonequilibrium oxygen isotope effects in synthetic carbonates. *Geochimica Et Cosmochimica Acta* 61, 3461–3475. https://doi.org/10.1016/S0016-7037(97)00169-5

Kim, S.-T., O’Neil, J. R., Hillaire-Marcel, C., and Mucci, A. (2007). Oxygen isotope fractionation between synthetic aragonite and water: Influence of temperature and Mg^{2+} concentration. *Geochimica et Cosmochimica Acta* 71, 4704–4715. https://doi.org/10.1016/j.gca.2007.04.019

Klein Goldewijk, K., Beusen, A., and Janssen, P. (2010). Long-term dynamic modeling of global population and built-up area in a spatially explicit way: HYDE 3.1. *The Holocene* 20, 565–573. https://doi.org/10.1177/0959683609356587

Kluge, T., Marx, T., Scholz, D., Niggemann, S., Mangini, A., and Aeschbach-Hertig, W. (2008). A new tool for palaeoclimate reconstruction: Noble gas temperatures from fluid inclusions in speleothems. *Earth and Planetary Science Letters* 269, 408–415. https://doi.org/10.1016/j.epsl.2008.02.030

Koutavas, A. and Joanides, S. (2012). El niño–southern oscillation extrema in the Holocene and last glacial maximum. *Paleoceanography* 27, PA4208. https://doi.org/10.1029/2012PA002378

Krief, S., Hendy, E. J., Fine, M., Yam, R., Meibom, A., Foster, G. L., et al. (2010). Physiological and isotopic responses of scleractinian corals to ocean acidification. *Geochimica et Cosmochimica Acta* 74, 4988–5001. https://doi.org/10.1016/j.gca.2010.05.023

Kumar, K. K., Rajagopalan, B., Hoerling, M., Bates, G., and Cane, M. (2006). Unraveling the mystery of Indian monsoon failure during El Niño. *Science* 314, 115–119. https://doi.org/10.1126/science.1131152

Lachniet, M. S. (2020). Illuminating the meaning of Asian monsoon cave speleothem records. *Paleoceanography and Paleoclimatology* 35, e2019PA003841. https://doi.org/10.1029/2019PA003841

Laskar, J., Robutel, P., Joutel, F., Gastineau, M., Correia, A. C. M., and Levrard, B. (2004). A long-term numerical solution for the insolation quantities of the earth. *Astronomy & Astrophysics* 428, 261–285. https://doi.org/10.1051/0004-6361:20041335

Lea, D. W., Pak, D. K., and Spero, H. J. (2000). Climate impact of late quaternary equatorial Pacific sea surface temperature variations. *Science* 289, 1719–1724. https://doi.org/10.1126/science.289.5485.1719

Leng, G. Y., Tang, Q. H., and Rayburg, S. (2015). Climate change impacts on meteorological, agricultural and hydrological droughts in China. *Global and Planetary Change* 126, 23–34. https://doi.org/10.1016/j.gloplacha.2015.01.003

Li, J. Y. and Li, T. Y. (2018). Seasonal and annual changes in soil/cave air p_{co_2} and the $\delta^{13}\mathrm{C}_{\mathrm{DIC}}$ of cave drip water in response to changes in temperature and rainfall. *Applied Geochemistry* 93, 94–101. https://doi.org/10.1016/j.apgeochem.2018.04.002

Li, N. N., Sharifi, A., Chambers, F. M., Ge, Y., Dubois, N., Gao, G. Z., et al. (2021a). Linking Holocene east Asian monsoon variability to solar forcing and ENSO activity: Multi-proxy evidence from a peatland in northeastern China. *The Holocene* 31, 966–982. https://doi.org/10.1177/0959683621994662

Li, T.-Y., Huang, C.-X., Tian, L.-J., Suarez, M., and Gao, Y.-L. (2018). Variation of δ^{13}C in plant-soil-cave systems in karst regions with different degrees of rocky desertification in southwest China. *Journal of Cave and Karst Studies* 80, 212–228. https://doi.org/10.4311/2018ES0107

Li, T.-Y., Xiao, S.-Y., Shen, C.-C., Zhang, J., Chen, C.-J., Cheng, H., et al. (2021b). Little ice age climate changes in southwest China from a stalagmite δ^{18}O record. *Palaeogeography, Palaeoclimatology, Palaeoecology* 562, 110167. https://doi.org/10.1016/j.palaeo.2020.110167

Li, X. S., Zhou, Y. W., Han, Z. Y., Yuan, X. K., Yi, S. W., Zeng, Y. Q., et al. (2024). Loess deposits in the low latitudes of east Asia reveal the 20-kyr precipitation cycle. *Nature Communications* 15, 1023. https://doi.org/10.1038/s41467-024-45379-9

Li, Y.-B., Shao, J.-A., Yang, H., and Bai, X.-Y. (2009). The relations between land use and karst rocky desertification in a typical karst area, China. *Environmental Geology* 57, 621–627. https://doi.org/10.1007/s00254-008-1331-z

Li, Y. X., Rao, Z. G., Xu, Q. H., Zhang, S. R., Liu, X. K., Wang, Z. L., et al. (2020). Interrelationship and environmental significance of stalagmite δ^{13}C and δ^{18}O records from Zhenzhu Cave, north China, over the last 130 ka. *Earth and Planetary Science Letters* 536, 116149. https://doi.org/10.1016/j.epsl.2020.116149

Liang, Q.-S., Sha, L.-J., Li, J.-Y., Zhang, J., Wang, X.-J., Zhou, S.-L., et al. (2024). Seasonal variations and controls on triple oxygen and hydrogen isotopes in precipitation—a case study from monitoring in southwest China. *Journal of Geophysical Research: Atmospheres* 129, e2023JD040654. https://doi.org/10.1029/2023JD040654

Liang, Y.-J., Chen, S.-T., Wang, Y.-J., Zhao, K., Yang, S.-H., Wang, Z.-J., et al. (2022). Asian monsoon intensity coupled to antarctic climate during Dansgaard–Oeschger 8 and Heinrich 4 glacial intervals. *Communications Earth & Environment* 3, 298. https://doi.org/10.1038/s43247-022-00633-0

Lin, F. Y., Zhang, Q., Sinha, A., Wang, Z. Q., Axelsson, J., Chen, L. F., et al. (2024). Seasonal to decadal variations of precipitation oxygen isotopes in northern China linked to the moisture source. *npj Climate and Atmospheric Science* 7, 14. https://doi.org/10.1038/s41612-024-00564-x

Lisiecki, L. E. and Raymo, M. E. (2005). A pliocene-pleistocene stack of 57 globally distributed benthic δ^{18}O records. *Paleoceanography* 20. https://doi.org/110.1029/2004PA001071

Liu, D. B., Mi, X., Liu, S. S., and Wang, Y. J. (2022a). Multi-phased Asian hydroclimate variability during Heinrich Stadial 5. *Climate Dynamics* 60, 4003–4016. https://doi.org/10.1007/s00382-022-06566-w

Liu, H. Y., Gu, Y. S., Qin, Y. M., Yu, Z. X., Huang, X. Y., Xie, S. C., et al. (2021). The elemental enrichments at Dajiuhu peatland in the middle Yangtze valley in response to changes in east Asian monsoon and human activity since 20,000 cal yr BP. *Science of The Total Environment* 757, 143990. https://doi.org/10.1016/j.scitotenv.2020.143990

Liu, J. B., Chen, J. H., Zhang, X. J., Li, Y., Rao, Z. G., and Chen, F. H. (2015). Holocene east Asian summer monsoon records in northern China and their inconsistency with Chinese stalagmite δ^{18}O records. *Earth-Science Reviews* 148, 194–208. https://doi.org/10.1016/j.earscirev.2015.06.004

Liu, J. H., Zhang, P. Z., Cheng, H., Chen, F. H., Yang, X. L., Zhang, D. Z., et al. (2008a). Asian summer monsoon precipitation recorded by stalagmite oxygen isotopic composition in the western loess plateau during AD1875–2003 and its linkage with ocean-atmosphere system. *Chinese Science Bulletin* 53, 2041–2049. https://doi.org/10.1007/s11434-008-0286-5

Liu, S. S., Liu, D. B., Wang, Y. J., Zou, L. Z., and Gao, H. (2022b). Spatio-temporal expressions of precessional-scale stalagmite δ^{18}O variations from the Asian monsoon area. *Palaeogeography, Palaeoclimatology, Palaeoecology* 585, 110720. https://doi.org/10.1016/j.palaeo.2021.110720

Liu, T. and Ding, Z. (1998). Chinese loess and the paleomonsoon. *Annual Review of Earth and Planetary Sciences* 26, 111–145. https://doi.org/10.1146/annurev.earth.26.1.111

Liu, X. D., Xie, X. X., Guo, Z. T., Yin, Z.-Y., and Chen, G. S. (2022c). Model-based orbital-scale precipitation δ^{18}O variations and distinct mechanisms in Asian monsoon and arid regions. *National Science Review* 9, nwac182. https://doi.org/10.1093/nsr/nwac182

Liu, X. K., Liu, J. B., Chen, S. Q., Chen, J. H., Zhang, X., Yan, J. J., et al. (2020). New insights on Chinese cave δ^{18}O records and their paleoclimatic significance. *Earth-Science Reviews* 207, 103216. https://doi.org/10.1016/j.earscirev.2020.103216

Liu, Z. H., Sun, H. L., Li, H. C., and Wan, N. J. (2011). δ^{13}C , δ^{18}O and deposition rate of tufa in Xiangshui river, sw China: implications for land-cover change caused by climate and human impact during the late Holocene. *Geological Society, London, Special Publications* 352, 85–96. https://doi.org/10.1144/SP352.7

Liu, Z. Q., Li, H.-C., Xiong, K. N., Yuan, D. X., Ying, B., Xu, X. M., et al. (2008b). Implication for sampling paleo-climate indicators by monitoring seasonal variations of δD and δ^{18}O in cave waters. *Carsologica Sinica* 27, 139–144. https://doi.org/10.3969/j.issn.1001-4810.2008.02.007. [In Chinese with English abstract]

Liu, Z. Y., Wen, X. Y., Brady, E. C., Otto-Bliesner, B., Yu, G., Lu, H. Y., et al. (2014). Chinese cave records and the east Asia summer monsoon. *Quaternary Science Reviews* 83, 115–128. https://doi.org/10.1016/j.quascirev.2013.10.021

Lopez-Elorza, M., Muñoz-García, M. B., González-Acebrón, L., and Martín-Chivelet, J. (2021). Fluid-inclusion petrography in calcite stalagmites: Implications for entrapment processes. *Journal of Sedimentary Research* 91, 1206–1226. https://doi.org/10.2110/jsr.2021.016

Lu, F. Z., Lu, H. Y., Gu, Y., Lin, P. Y., Lu, Z. Y., Zhang, Q., et al. (2025). Tipping point-induced abrupt shifts in East Asian hydroclimate since the Last Glacial Maximum. *Nature Communications* 16, 477. https://doi.org/10.1038/s41467-025-55888-w

Lu, F. Z., Ma, C. M., Zhu, C., Lu, H. Y., Zhang, X. J., Huang, K. Y., et al. (2019a). Variability of east Asian summer monsoon precipitation during the Holocene and possible forcing mechanisms. *Climate Dynamics* 52, 969–989. https://doi.org/10.1007/s00382-018-4175-6

Lu, Z. Y., Liu, Z. Y., Chen, G. S., and Guan, J. (2019b). Prominent precession band variance in ENSO intensity over the last 300,000 years. *Geophysical Research Letters* 46, 9786–9795. https://doi.org/10.1029/2019gl083410

Lyu, A. Q., Yin, Q. Z., Crucifix, M., and Sun, Y. B. (2021). Diverse regional sensitivity of summer precipitation in east Asia to ice volume, CO_2 and astronomical forcing. *Geophysical Research Letters* 48, e2020GL092005. https://doi.org/10.1029/2020GL092005

Lyu, Y. N., Luo, W. J., Zeng, G. N., Wang, Y. W., Chen, J., and Wang, S. J. (2024). The effect of cave ventilation on carbon and oxygen isotopic fractionation between calcite and drip water. *Science of The Total Environment* 915, 169967. https://doi.org/10.1016/j.scitotenv.2024.169967

Lécuyer, C. and O'Neil, J. R. (1994). Stable isotope compositions of fluid inclusions in biogenic carbonates. *Geochimica et Cosmochimica Acta* 58, 353–363. https://doi.org/10.1016/0016-7037(94)90469-3

Løland, M. H., Krüger, Y., Fernandez, A., Buckingham, F., Carolin, S. A., Sodemann, H., et al. (2022). Evolution of tropical land temperature across the last glacial termination. *Nature Communications* 13, 5158. https://doi.org/10.1038/s41467-022-32712-3

Maccali, J., Meckler, A. N., Lauritzen, S. E., Brekken, T., Rokkan, H. A., Fernandez, A., et al. (2023). Multi-proxy speleothem-based reconstruction of mid-MIS 3 climate in South Africa. *Climate of the Past* 19, 1847–1862. https://doi.org/10.5194/cp-19-1847-2023

Maher, B. A. and Thompson, R. (2012). Oxygen isotopes from Chinese caves: records not of monsoon rainfall but of circulation regime. *Journal of Quaternary Science* 27, 615–624. https://doi.org/10.1002/jqs.2553

Mark, S. Z., Abbott, M. B., Rodbell, D. T., and Moy, C. M. (2022). XRF analysis of Laguna Pallcacocha sediments yields new insights into Holocene El Niño development. *Earth and Planetary Science Letters* 593, 117657. https://doi.org/10.1016/j.epsl.2022.117657

Martin, K. C., Buizert, C., Edwards, J. S., Kalk, M. L., Riddell-Young, B., Brook, E. J., et al. (2023). Bipolar impact and phasing of Heinrich-type climate variability. *Nature* 617, 100–104. https://doi.org/10.1038/s41586-023-05875-2

Mass, T., Giuffre, A. J., Sun, C.-Y., Stifler, C. A., Frazier, M. J., Neder, M., et al. (2017). Amorphous calcium carbonate particles form coral skeletons. *Proceedings of the National Academy of Sciences* 114, E7670–E7678. https://doi.org/10.1073/pnas.1707890114

Matthes, K., Funke, B., Andersson, M. E., Barnard, L., Beer, J., Charbonneau, P., et al. (2017). Solar forcing for CMIP6 (v3.2). *Geoscientific Model Development* 10, 2247–2302. https://doi.org/10.5194/gmd-10-2247-2017

Matthews, A., Affek, H. P., Ayalon, A., Vonhof, H. B., and Bar-Matthews, M. (2021). Eastern Mediterranean climate change deduced from the Soreq Cave fluid inclusion stable isotopes and carbonate clumped isotopes record of the last 160 ka. *Quaternary Science Reviews* 272, 107223. https://doi.org/10.1016/j.quascirev.2021.107223

Matthews, A., Ayalon, A., and Bar-Matthews, M. (2000). D/H ratios of fluid inclusions of Soreq cave (Israel) speleothems as a guide to the Eastern Mediterranean Meteoric Line relationships in the last 120 ky. *Chemical Geology* 166, 183–191. https://doi.org/10.1016/S0009-2541(99)00192-8

McCulloch, M., Falter, J., Trotter, J., and Montagna, P. (2012). Coral resilience to ocean acidification and global warming through pH up-regulation. *Nature Climate Change* 2, 623–627. https://doi.org/10.1038/nclimate1473

McDermott, F. (2004). Palaeo-climate reconstruction from stable isotope variations in speleothems: a review. *Quaternary Science Reviews* 23, 901–918. https://doi.org/10.1016/j.quascirev.2003.06.021

McGarry, S., Bar-Matthews, M., Matthews, A., Vaks, A., Schilman, B., and Ayalon, A. (2004). Constraints on hydrological and paleotemperature variations in the Eastern Mediterranean region in the last 140ka given by the δD values of speleothem fluid inclusions. *Quaternary Science Reviews* 23, 919–934. https://doi.org/10.1016/j.quascirev.2003.06.020

McGee, D., Moreno-Chamarro, E., Green, B., Marshall, J., Galbraith, E., and Bradtmiller, L. (2018). Hemispherically asymmetric trade wind changes as signatures of past ITCZ shifts. *Quaternary Science Reviews* 180, 214–228. https://doi.org/10.1016/j.quascirev.2017.11.020

McKay, N. P., Kaufman, D. S., Arcusa, S. H., Kolus, H. R., Edge, D. C., Erb, M. P., et al. (2024). The 4.2 ka event is not remarkable in the context of Holocene climate variability. *Nature Communications* 15, 6555. https://doi.org/10.1038/s41467-024-50886-w

Meckler, A. N., Affolter, S., Dublyansky, Y. V., Krüger, Y., Vogel, N., Bernasconi, S. M., et al. (2015). Glacial–interglacial temperature change in the tropical west Pacific: A comparison of stalagmite-based paleo-thermometers. *Quaternary Science Reviews* 127, 90–116. https://doi.org/10.1016/j.quascirev.2015.06.015

Meehl, G. A., Arblaster, J. M., Branstator, G., and van Loon, H. (2008). A coupled air–sea response mechanism to solar forcing in the Pacific region. *Journal of Climate* 21, 2883–2897. https://doi.org/10.1175/2007JCLI1776.1

Meng, X. Q., Zhang, C., Li, G. K., Cheng, J. R., Cai, J., Liu, Y. L., et al. (2024). Rapid wet-dry climatic oscillations and large-scale social unrest in ancient China. *Science Bulletin* 69, 314–318. https://doi.org/10.1016/j.scib.2023.12.010

Miao, Y. F., Zhang, P., Lu, S. M., Wu, X. Y., Li, L. L., Chen, H. G., et al. (2015). Late quaternary pollen records from the Yangtze River delta, east China, and its implications for the Asian monsoon evolution. *Arabian Journal of Geosciences* 8, 7845–7854. https://doi.org/10.1007/s12517-015-1777-8

Mickler, P. J., Banner, J. L., Stern, L., Asmerom, Y., Edwards, R. L., and Ito, E. (2004). Stable isotope variations in modern tropical speleothems: Evaluating equilibrium vs. kinetic isotope effects 1 1associate editor: E. m. ripley. *Geochimica et Cosmochimica Acta* 68, 4381–4393. https://doi.org/10.1016/j.gca.2004.02.012

Milankovitch, M. (1941). *Kanon der Erdbestrahlungen und seine Anwendung auf das Eiszeitenproblem*, vol. 33 (Belgrade: Royal Serbian Academy, Section of Mathematical and Natural Sciences)

Millo, C., Strikis, N. M., Vonhof, H. B., Deininger, M., da Cruz, F. W., Wang, X. F., et al. (2017). Last glacial and Holocene stable isotope record of fossil dripwater from subtropical Brazil based on analysis of fluid inclusions in stalagmites. *Chemical Geology* 468, 84–96. https://doi.org/10.1016/j.chemgeo.2017.08.018

Nash, M. C., Diaz-Pulido, G., Harvey, A. S., and Adey, W. (2019). Coralline algal calcification: A morphological and process-based understanding. *Plos One* 14, e0221396. https://doi.org/10.1371/journal.pone.0221396

NGRIP Members (2004). High-resolution record of Northern Hemisphere climate extending into the last interglacial period. *Nature* 431, 147–151. https://doi.org/10.1038/nature02805

Niu, X. W., Wang, J., Kang, L., Li, Y. W., Zhang, H. W., Dong, X. Y., et al. (2025). Millennial-scale climate variability of the Asian summer monsoon over the last 690,000 years: insights from cave records. *Science Bulletin* https://doi.org/10.1016/j.scib.2025.02.011

Nooitgedacht, C. W., van der Lubbe, H. J. L., Ziegler, M., and Staudigel, P. T. (2021). Internal water facilitates thermal resetting of clumped isotopes in biogenic aragonite. *Geochemistry, Geophysics, Geosystems* 22, e2021GC009730. https://doi.org/10.1029/2021GC009730

O'Neil, J. R., Clayton, R. N., and Mayeda, T. K. (1969). Oxygen isotope fractionation in divalent metal carbonates. *Journal of Chemical Physics* 51, 5547–5558. https://doi.org/10.1063/1.1671982

Pan, L. K., Zhao, J. Y., Yang, Y., Wang, K. X., Pérez-Mejías, C., Cui, J. H., et al. (2023). Different responses of precipitation patterns to the east Asian summer monsoon weakening: The 7.2 and 8.2 ka events. *Quaternary Science Reviews* 319, 108329. https://doi.org/10.1016/j.quascirev.2023.108329

Patterson, W. P., Smith, G. R., and Lohmann, K. C. (1993). *Continental Paleothermometry and Seasonality Using the Isotopic Composition of Aragonitic Otoliths of Freshwater Fishes* (American Geophysical Union (AGU)). 191–202. https://doi.org/10.1029/GM078p0191

Pausata, F. S. R., Battisti, D. S., Nisancioglu, K. H., and Bitz, C. M. (2011). Chinese stalagmite δ^{18}O controlled by changes in the Indian monsoon during a simulated Heinrich event. *Nature Geoscience* 4, 474–480. https://doi.org/10.1038/ngeo1169

Pederson, C. L., Weiss, L., Mavromatis, V., Rollion-Bard, C., Dietzel, M., Neuser, R., et al. (2019). Significance of fluid chemistry throughout diagenesis of aragonitic porites corals – an experimental approach. *The Depositional Record* 5, 592–612. https://doi.org/10.1002/dep2.82

Pei, W. Q., Wan, S. M., Clift, P. D., Dong, J., Liu, X. T., Lu, J., et al. (2020). Human impact overwhelms long-term climate control of fire in the Yangtze River Basin since 3.0 ka BP. *Quaternary Science Reviews* 230, 106165. https://doi.org/10.1016/j.quascirev.2020.106165

Peterse, F., Martínez-García, A., Zhou, B., Beets, C. J., Prins, M. A., Zheng, H., et al. (2014). Molecular records of continental air temperature and monsoon precipitation variability in east Asia spanning the past 130,000 years. *Quaternary Science Reviews* 83, 76–82. https://doi.org/10.1016/j.quascirev.2013.11.001

Pu, J. B., Wang, A. Y., Yin, J. J., Shen, L. C., Sun, Y. C., Yuan, D. X., et al. (2015). Processes controlling dripwater hydrochemistry variations in Xueyu Cave, SW China: implications for speleothem palaeoclimate signal interpretations. *Boreas* 44, 603–617. https://doi.org/10.1111/bor.12117

Qiu, H.-Y., Li, T.-Y., Chen, C.-J., Huang, R., Wang, T., Wu, Y., et al. (2021). Significance of active speleothem δ^{18}O at annual-decadal timescale——a case study from monitoring in Furong cave. *Applied Geochemistry* 126, 104873. https://doi.org/10.1016/j.apgeochem.2021.104873

Qiu, W. Y., Yang, Y. Y., Jiang, X. Y., Wang, X. F., Wang, Y., Cai, J. R., et al. (2023). Oxygen isotope variability in precipitation, dripwater, and modern calcite responding to ENSO based on 11 years' monitoring in Yuhua Cave, southeast China. *Journal of Hydrology* 624, 129937. https://doi.org/10.1016/j.jhydrol.2023.129937

Reimer, P. J., Austin, W. E. N., Bard, E., Bayliss, A., Blackwell, P. G., Bronk Ramsey, C., et al. (2020). The IntCal20 Northern hemisphere radiocarbon age calibration curve (0–55 cal kbp). *Radiocarbon* 62, 725–757. https://doi.org/10.1017/RDC.2020.41

Roche, D., Paillard, D., and Cortijo, E. (2004). Constraints on the duration and freshwater release of Heinrich event 4 through isotope modelling. *Nature* 432, 379–382. https://doi.org/10.1038/nature03059

Rollion-Bard, C., Blamart, D., Cuif, J.-P., and Dauphin, Y. (2010). In situ measurements of oxygen isotopic composition in deep-sea coral, lophelia pertusa: Re-examination of the current geochemical models of biomineralization. *Geochimica et Cosmochimica Acta* 74, 1338–1349. https://doi.org/10.1016/j.gca.2009.11.011

Ropelewski, C. F. and Halpert, M. S. (1987). Global and regional scale precipitation patterns associated with the El Niño/Southern Oscillation. *Monthly Weather Review* 115, 1606–1626. https://doi.org/10.1175/1520-0493(1987)115<1606:GARSPP>2.0.CO;2

Rowe, P. J., Mason, J. E., Andrews, J. E., Marca, A. D., Thomas, L., van Calsteren, P., et al. (2012). Speleothem isotopic evidence of winter rainfall variability in northeast Turkey between 77 and 6 ka. *Quaternary Science Reviews* 45, 60–72. https://doi.org/10.1016/j.quascirev.2012.04.013

Ruan, J. Y., Zhang, H. Y., Cai, Z. Y., Yang, X. Q., and Yin, J. (2019). Regional controls on daily to interannual variations of precipitation isotope ratios in southeast China: Implications for paleomonsoon reconstruction. *Earth and Planetary Science Letters* 527, 115794. https://doi.org/10.1016/j.epsl.2019.115794

Ruddiman, W. F., Fuller, D. Q., Kutzbach, J. E., Tzedakis, P. C., Kaplan, J. O., Ellis, E. C., et al. (2016). Late Holocene climate: Natural or anthropogenic? *Reviews of Geophysics* 54, 93–118. https://doi.org/10.1002/2015RG000503

Saenger, C., Affek, H. P., Felis, T., Thiagarajan, N., Lough, J. M., and Holcomb, M. (2012). Carbonate clumped isotope variability in shallow water corals: Temperature dependence and growth-related vital effects. *Geochimica et Cosmochimica Acta* 99, 224–242. https://doi.org/10.1016/j.gca.2012.09.035

Sakai, M., Hori, M., Uemura, R., Ghaleb, B., Pinti, D. L., Yumiba, M., et al. (2024). A snapshot of the climate in the Middle Pleistocene inferred from a stalagmite from central Japan. *Geoscience Letters* 11, 41. https://doi.org/10.1186/s40562-024-00357-3

[Dataset] Schneider, U., Becker, A., Finger, P., Elke;, R., and Ziese, M. (2020). GPCC monitoring product: Near real-time monthly land-surface precipitation from rain-gauges based on synop and climat data. http://dx.doi.org/10.5676/DWD_GPCC/MP_M_V2020_100

Scholz, D. and Hoffmann, D. L. (2011). Stalage – an algorithm designed for construction of speleothem age models. *Quaternary Geochronology* 6, 369–382. https://doi.org/10.1016/j.quageo.2011.02.002

Scholz, D., Mühlinghaus, C., and Mangini, A. (2009). Modelling δ^{13}C and δ^{18}O in the solution layer on stalagmite surfaces. *Geochimica et Cosmochimica Acta* 73, 2592–2602. https://doi.org/10.1016/j.gca.2009.02.015

Schrag, D. P., Adkins, J. F., McIntyre, K., Alexander, J. L., Hodell, D. A., Charles, C. D., et al. (2002). The oxygen isotopic composition of seawater during the last glacial maximum. *Quaternary Science Reviews* 21, 331–342. https://doi.org/10.1016/S0277-3791(01)00110-X

Schrag, D. P., Hampt, G., and Murray, D. W. (1996). Pore fluid constraints on the temperature and oxygen isotopic composition of the glacial ocean. *Science* 272, 1930–1932. https://doi.org/10.1126/science.272.5270.1930

Schulz, H., von Rad, U., Erlenkeuser, H., and von Rad, U. (1998). Correlation between arabian sea and Greenland climate oscillations of the past 110,000 years. *Nature* 393, 54–57. https://doi.org/10.1038/31750

Schulz, M. and Mudelsee, M. (2002). Redfit: estimating red-noise spectra directly from unevenly spaced paleoclimatic time series. *Computers Geosciences* 28, 421–426. https://doi.org/10.1016/S0098-3004(01)00044-9

Schwarcz, H. P., Harmon, R. S., Thompson, P., and Ford, D. C. (1976). Stable isotope studies of fluid inclusions in speleothems and their paleoclimatic significance. *Geochimica et Cosmochimica Acta* 40, 657–665. https://doi.org/10.1016/0016-7037(76)90111-3

Sevilgen, D. S., Venn, A. A., Hu, M. Y., Tambutté, E., de Beer, D., Planas-Bielsa, V., et al. (2019). Full in vivo characterization of carbonate chemistry at the site of calcification in corals. *Science Advances* 5, eaau7447. https://doi.org/10.1126/sciadv.aau7447

Shao, H., Zhang, Y. D., Gu, F. X., Shi, C. M., Miao, N., and Liu, S. R. (2021). Impacts of climate extremes on ecosystem metrics in southwest China. *Science of The Total Environment* 776, 145979. https://doi.org/10.1016/j.scitotenv.2021.145979

Shao, S., Wu, D., Wang, T., Guo, S. L., Xiao, Q. L., Li, Y. M., et al. (2024). Holocene extreme flood events in the middle reaches of the Lancang–Mekong River basin recorded by a high-altitude lake in southwestern China. *Quaternary Science Reviews* 343, 108918. https://doi.org/10.1016/j.quascirev.2024.108918

Shi, F., Lu, H. Y., Guo, Z. T., Yin, Q. Z., Wu, H. B., Xu, C. X., et al. (2021). The position of the current warm period in the context of the past 22,000 years of summer climate in China. *Geophysical Research Letters* 48, e2020GL091940. https://doi.org/10.1029/2020GL091940

Shi, X., Yang, Y., Cheng, H., Zhao, J., Li, T.-Y., Lei, L., et al. (2022). Influences on Asian summer monsoon during Dansgaard-Oeschger events 19 to 25 (70–115 kyr B.P.). *Palaeogeography, Palaeoclimatology, Palaeoecology* 587, 110798. https://doi.org/10.1016/j.palaeo.2021.110798

Shi, Z. G., Xie, X. N., Ren, X., Li, X. Z., Yang, L., Lei, J., et al. (2019). Radiative effect of mineral dust on east Asian summer monsoon during the last glacial maximum: Role of snow-albedo feedback. *Geophysical Research Letters* 46, 10901–10909. https://doi.org/10.1029/2019GL084211

Sinclair, D. J., Banner, J. L., Taylor, F. W., Partin, J., Jenson, J., Mylroie, J., et al. (2012). Magnesium and strontium systematics in tropical speleothems from the western Pacific. *Chemical Geology* 294-295, 1–17. https://doi.org/10.1016/j.chemgeo.2011.10.008

Song, Y. P., Xu, H., Lan, J. H., Zhang, J., Zhou, K. E., Shi, S. W., et al. (2022). Enhanced human activity altered the late Holocene vegetation composition in subtropical east Asia. *Global and Planetary Change* 214, 103850. https://doi.org/10.1016/j.gloplacha.2022.103850

Spratt, R. M. and Lisiecki, L. E. (2016). A late pleistocene sea level stack. *Climate of the Past* 12, 1079–1092. https://doi.org/10.5194/cp-12-1079-2016

Spötl, C., Fairchild, I. J., and Tooth, A. F. (2005). Cave air control on dripwater geochemistry, obir caves (Austria): Implications for speleothem deposition in dynamically ventilated caves. *Geochimica et Cosmochimica Acta* 69, 2451–2468. https://doi.org/10.1016/j.gca.2004.12.009

Spötl, C. and Mattey, D. (2006). Stable isotope microsampling of speleothems for palaeoenvironmental studies: A comparison of microdrill, micromill and laser ablation techniques. *Chemical Geology* 235, 48–58. https://doi.org/10.1016/j.chemgeo.2006.06.003

Stoll, H. M., Day, C., Lechleitner, F., Kost, O., Endres, L., Sliwinski, J., et al. (2023). Distinguishing the combined vegetation and soil component of δ^{13}C variation in speleothem records from subsequent degassing and prior calcite precipitation effects. *Climate of the Past* 19, 2423–2444. https://doi.org/10.5194/cp-19-2423-2023

Sun, W. Y., Ma, Y. N., Liu, J., Chen, D. L., Ning, L., Yan, M., et al. (2024). Multi-centennial ENSO-like variability response to solar activity during the Holocene. *Climate Dynamics* 62, 6189–6201. https://doi.org/10.1007/s00382-024-07198-y

Sun, Y. B., Clemens, S. C., Guo, F., Liu, X. X., Wang, Y., Yan, Y., et al. (2021). High-sedimentation-rate loess records: A new window into understanding orbital- and millennial-scale monsoon variability. *Earth-Science Reviews* 220, 103731. https://doi.org/10.1016/j.earscirev.2021.103731

Sun, Y. B., Kutzbach, J., An, Z. S., Clemens, S., Liu, Z. Y., Liu, W. G., et al. (2015). Astronomical and glacial forcing of East Asian summer monsoon variability. *Quaternary Science Reviews* 115, 132–142. https://doi.org/10.1016/j.quascirev.2015.03.009

Sun, Y. B., Wang, T., Yin, Q. Z., Lyu, A. Q., Crucifix, M., Cai, Y. J., et al. (2022). A review of orbital-scale monsoon variability and dynamics in East Asia during the Quaternary. *Quaternary Science Reviews* 288, 107593. https://doi.org/10.1016/j.quascirev.2022.107593

Sun, Y. B., Yin, Q. Z., Crucifix, M., Clemens, S. C., Araya-Melo, P., Liu, W. G., et al. (2019). Diverse manifestations of the mid-Pleistocene climate transition. *Nature Communications* 10, 352. https://doi.org/10.1038/s41467-018-08257-9

Tambutté, S., Holcomb, M., Ferrier-Pagès, C., Reynaud, S., Tambutté, E., Zoccola, D., et al. (2011). Coral biomineralization: From the gene to the environment. *Journal of Experimental Marine Biology and Ecology* 408, 58–78. https://doi.org/10.1016/j.jembe.2011.07.026

Tan, L. C., An, Z. S., Huh, C.-A., Cai, Y. J., Shen, C.-C., Shiau, L.-J., et al. (2014). Cyclic precipitation variation on the western Loess Plateau of China during the past four centuries. *Scientific Reports* 4, 6381. https://doi.org/10.1038/srep06381

Tan, L. C., Cai, Y. J., An, Z. S., Cheng, H., Shen, C.-C., Gao, Y. L., et al. (2017). Decreasing monsoon precipitation in southwest China during the last 240 years associated with the warming of tropical ocean. *Climate Dynamics* 48, 1769–1778. https://doi.org/10.1007/s00382-016-3171-y

Tan, L. C., Cai, Y. J., Cheng, H., Lawrence Edwards, R., Shen, C.-C., Gao, Y. L., et al. (2015). Climate significance of speleothem δ^{18}O from central China on decadal timescale. *Journal of Asian Earth Sciences* 106, 150–155. https://doi.org/10.1016/j.jseaes.2015.03.008

Tan, M. (2014). Circulation effect: response of precipitation δ^{18}O to the ENSO cycle in monsoon regions of China. *Climate Dynamics* 42, 1067–1077. https://doi.org/10.1007/s00382-013-1732-x

Tan, M., Baker, A., Genty, D., Smith, C., Esper, J., and Cai, B. (2006). Applications of stalagmite laminae to paleoclimate reconstructions: Comparison with dendrochronology/climatology. *Quaternary Science Reviews* 25, 2103–2117. https://doi.org/10.1016/j.quascirev.2006.01.034

Thomas, E. K., Clemens, S. C., Prell, W. L., Herbert, T. D., Huang, Y. S., Liu, Z. Y., et al. (2014). Temperature and leaf wax δ^2H records demonstrate seasonal and regional controls on Asian monsoon proxies. *Geology* 42, 1075–1078. https://doi.org/10.1130/G36289.1

Thomas, E. K., Clemens, S. C., Sun, Y., Prell, W. L., Huang, Y. S., Gao, L., et al. (2016). Heterodynes dominate precipitation isotopes in the east Asian monsoon region, reflecting interaction of multiple climate factors. *Earth and Planetary Science Letters* 455, 196–206. https://doi.org/10.1016/j.epsl.2016.09.044

Thomas, E. R., Wolff, E. W., Mulvaney, R., Steffensen, J. P., Johnsen, S. J., Arrowsmith, C., et al. (2007). The 8.2ka event from Greenland ice cores. *Quaternary Science Reviews* 26, 70–81. https://doi.org/10.1016/j.quascirev.2006.07.017

Tian, S. H., Dai, G. W., Yin, Q. Z., Meng, X. Q., Zhang, Z. S., Zhu, Z. M., et al. (2022). Spatial differences in east Asian climate transition at ~260 ka and their links to ENSO. *Quaternary Science Reviews* 296, 107805. https://doi.org/10.1016/j.quascirev.2022.107805

Tian, Y., Zhang, H. W., Zong, B. Y., Duan, P. Z., Vonhof, H., Dublyansky, Y., et al. (2020). Measurement of oxygen and hydrogen isotopic ratios of speleothem fluid inclusion water using Picarro. *Chinese Science Bulletin* 65, 3626–3634. https://doi.org/10.1360/TB-2020-0201. [In Chinese with English abstract]

Tian, Z. P. and Jiang, D. B. (2016). Revisiting last glacial maximum climate over China and east Asian monsoon using PMIP3 simulations. *Palaeogeography, Palaeoclimatology, Palaeoecology* 453, 115–126. https://doi.org/10.1016/j.palaeo.2016.04.020

Treble, P. C., Chappell, J., and Shelley, J. M. G. (2005). Complex speleothem growth processes revealed by trace element mapping and scanning electron microscopy of annual layers. *Geochimica et Cosmochimica Acta* 69, 4855–4863. https://doi.org/10.1016/j.gca.2005.06.008

Tremaine, D. M. and Froelich, P. N. (2013). Speleothem trace element signatures: A hydrologic geochemical study of modern cave dripwaters and farmed calcite. *Geochimica et Cosmochimica Acta* 121, 522–545. https://doi.org/10.1016/j.gca.2013.07.026

Tremaine, D. M., Froelich, P. N., and Wang, Y. (2011). Speleothem calcite farmed in situ: Modern calibration of δ^{18}O and δ^{13}C paleoclimate proxies in a continuously-monitored natural cave system. *Geochimica et Cosmochimica Acta* 75, 4929–4950. https://doi.org/10.1016/j.gca.2011.06.005

Uemura, R., Kina, Y., Shen, C. C., and Omine, K. (2020). Experimental evaluation of oxygen isotopic exchange between inclusion water and host calcite in speleothems. *Climate of the Past* 16, 17–27. https://doi.org/10.5194/cp-16-17-2020

Uemura, R., Nakamoto, M., Asami, R., Mishima, S., Gibo, M., Masaka, K., et al. (2016). Precise oxygen and hydrogen isotope determination in nanoliter quantities of speleothem inclusion water by cavity ring-down spectroscopic techniques. *Geochimica et Cosmochimica Acta* 172, 159–176. https://doi.org/10.1016/j.gca.2015.09.017

Venn, A., Tambutté, E., Holcomb, M., Allemand, D., and Tambutté, S. (2011). Live tissue imaging shows reef corals elevate pH under their calcifying tissue relative to seawater. *PloS one* 6, e20013. https://doi.org/10.1371/journal.pone.0020013

Verheyden, S., Genty, D., Cattani, O., and van Breukelen, M. R. (2008). Water release patterns of heated speleothem calcite and hydrogen isotope composition of fluid inclusions. *Chemical Geology* 247, 266–281. https://doi.org/10.1016/j.chemgeo.2007.10.019

Vieten, R., Winter, A., Warken, S. F., Schröder-Ritzrau, A., Miller, T. E., and Scholz, D. (2016). Seasonal temperature variations controlling cave ventilation processes in Cueva Larga, Puerto Rico. *International Journal of Speleology* 45, 259–273. http://doi.org/10.5038/1827-806X.45.3.1983

Vonhof, H. B., van Breukelen, M. R., Postma, O., Rowe, P. J., Atkinson, T. C., and Kroon, D. (2006). A continuous-flow crushing device for on-line δ^2H analysis of fluid inclusion water in speleothems. *Rapid Communications in Mass Spectrometry* 20, 2553–2558. https://doi.org/10.1002/rcm.2618

Wainer, K., Genty, D., Blamart, D., Daëron, M., Bar-Matthews, M., Vonhof, H., et al. (2011). Speleothem record of the last 180 ka in villars cave (SW France): Investigation of a large δ^{18}O shift between MIS6 and MIS5. *Quaternary Science Reviews* 30, 130–146. https://doi.org/10.1016/j.quascirev.2010.07.004

Wang, L., Chen, W., Haung, G., Wang, T., Wang, Q. L., Su, X. Y., et al. (2024). Characteristics of super drought in southwest China and the associated compounding effect of multiscalar anomalies. *Science China Earth Sciences* 67, 2084–2102. https://doi.org/10.1007/s11430-023-1341-4

Wang, M., Chen, S. T., Wang, Y. J., Zhao, K., Wang, X. F., Liang, Y. J., et al. (2022a). Stalagmite multi-proxy evidence of wet and dry intervals in the middle Yangtze valley during the last glacial period. *Palaeogeography, Palaeoclimatology, Palaeoecology* 586, 110764. https://doi.org/10.1016/j.palaeo.2021.110764

Wang, P. X. (2021). Low-latitude forcing: A new insight into paleo-climate changes. *The Innovation* 2, 100145. https://doi.org/10.1016/j.xinn.2021.100145

Wang, P. X., Wang, B., Cheng, H., Fasullo, J., Guo, Z. T., Kiefer, T., et al. (2014). The global monsoon across timescales: coherent variability of regional monsoons. *Climate of the Past* 10, 2007–2052. http://doi.org/10.5194/cp-10-2007-2014

Wang, P. X., Wang, B., Cheng, H., Fasullo, J., Guo, Z. T., Kiefer, T., et al. (2017). The global monsoon across time scales: Mechanisms and outstanding issues. *Earth-Science Reviews* 174, 84–121. https://doi.org/10.1016/j.earscirev.2017.07.006

Wang, S. Y., Lu, H. Y., Han, J. T., Chu, G. Q., Liu, J. Q., and Negendank, J. F. W. (2012). Palaeovegetation and palaeoclimate in low-latitude southern during the Last Glacial Maximum. *Quaternary International* 248, 79–85. https://doi.org/10.1016/j.quaint.2010.07.030

Wang, T. L., Li, D., Cheng, X., Lan, J. H., Edwards, R. L., Cheng, H., et al. (2022b). Hydroclimatic changes in south-central China during the 4.2 ka event and their potential impacts on the development of Neolithic culture. *Quaternary Research* , 1–14 https://doi.org/10.1017/qua.2022.11

Wang, Y., Lu, H. Y., Yi, S. W., Huber, M., Yang, F., Gu, Y., et al. (2022c). Tropical forcing orbital-scale precipitation variations revealed by a maar lake record in South China. *Climate Dynamics* 58, 2269–2280. https://doi.org/10.1007/s00382-021-06004-3

Wang, Y. J., Cheng, H., Edwards, R. L., An, Z. S., Wu, J. Y., Shen, C. C., et al. (2001). A high-resolution absolute-dated late pleistocene monsoon record from Hulu cave, China. *Science* 294, 2345–2348. https://doi.org/10.1126/science.1064618

Wang, Y. J., Cheng, H., Edwards, R. L., Kong, X. G., Shao, X. H., Chen, S. T., et al. (2008). Millennial- and orbital-scale changes in the east Asian monsoon over the past 224,000 years. *Nature* 451, 1090–1093. https://doi.org/10.1038/nature06692

Wang, Y. Z., Hu, C. Y., Ruan, J. Y., and Johnson, K. R. (2020). East Asian precipitation δ^{18}O relationship with various monsoon indices. *Journal of Geophysical Research: Atmospheres* 125, e2019JD032282. https://doi.org/10.1029/2019JD032282

Wang, Z. J., Chen, S. T., Wang, Y. J., Zhao, K., Liang, Y. J., Li, X. L., et al. (2022d). Climatic implication of stalagmite δ^{13}C in the middle reaches of the Yangtze River since the Last Glacial Maximum and coupling with δ^{18}O. *Palaeogeography, Palaeoclimatology, Palaeoecology* 608, 111290. https://doi.org/10.1016/j.palaeo.2022.111290

Wanner, H., Beer, J., Bütikofer, J., Crowley, T. J., Cubasch, U., Flückiger, J., et al. (2008). Mid- to late Holocene climate change: an overview. *Quaternary Science Reviews* 27, 1791–1828. https://doi.org/10.1016/j.quascirev.2008.06.013

Warken, S. F., Fohlmeister, J., Schröder-Ritzrau, A., Constantin, S., Spötl, C., Gerdes, A., et al. (2018). Reconstruction of late Holocene autumn/winter precipitation variability in sw romania from a high-resolution speleothem trace element record. *Earth and Planetary Science Letters* 499, 122–133. https://doi.org/10.1016/j.epsl.2018.07.027

Warken, S. F., Riechelmann, D. F. C., Fohlmeister, J., Schröder-Ritzrau, A., Frank, N., Scholz, D., et al. (2024). Dynamic processes determine precipitation variability in Eastern Central Europe since the Last Glacial Maximum. *Communications Earth & Environment* 5, 694. https://doi.org/10.1038/s43247-024-01876-99

Warken, S. F., Schmitt, A. K., Scholz, D., Hertwig, A., Weber, M., Mertz-Kraus, R., et al. (2025). Discovery of Laacher See eruption in speleothem record synchronizes Greenland and central European Late Glacial climate change. *Science Advances* 11, eadt4057. https://doi.org/10.1126/sciadv.adt4057

Warken, S. F., Schorndorf, N., Stinnesbeck, W., Hennhoefer, D., Stinnesbeck, S. R., Förstel, J., et al. (2021). Solar forcing of early Holocene droughts on the Yucatán peninsula. *Scientific Reports* 11, 13885. https://doi.org/10.1038/s41598-021-93417-z

Warken, S. F., Weißbach, T., Kluge, T., Vonhof, H., Scholz, D., Vieten, R., et al. (2022). Last glacial millennial-scale hydro-climate and temperature changes in Puerto Rico constrained by speleothem fluid inclusion δ^{18}O and δ^{2}H values. *Climate of the Past* 18, 167–181. https://doi.org/10.5194/cp-18-167-2022

Wassenburg, J. A., Riechelmann, S., Schröder-Ritzrau, A., Riechelmann, D. F. C., Richter, D. K., Immenhauser, A., et al. (2020). Calcite Mg and Sr partition coefficients in cave environments: Implications for interpreting prior calcite precipitation in speleothems. *Geochimica et Cosmochimica Acta* 269, 581–596. https://doi.org/10.1016/j.gca.2019.11.011

Wassenburg, J. A., Samanta, A., Sha, L. J., Lee, H., Scholz, D., Cheng, H., et al. (2024). Trace element partitioning controls on cave drip water compositions through prior calcite and aragonite precipitation. *Communications Earth & Environment* 5, 488. https://doi.org/10.1038/s43247-024-01648-5

Weber, S. L. and Tuenter, E. (2011). The impact of varying ice sheets and greenhouse gases on the intensity and timing of boreal summer monsoons. *Quaternary Science Reviews* 30, 469–479. https://doi.org/10.1016/j.quascirev.2010.12.009

Wefer, G. and Berger, W. H. (1991). Isotope paleontology: growth and composition of extant calcareous species. *Marine Geology* 100, 207–248. https://doi.org/10.1016/0025-3227(91)90234-U

Weissbach, T., Kluge, T., Affolter, S., Leuenberger, M. C., Vonhof, H., Riechelmann, D. F. C., et al. (2023). Constraints for precise and accurate fluid inclusion stable isotope analysis using water-vapour saturated CRDS techniques. *Chemical Geology* 617, 121268. https://doi.org/10.1016/j.chemgeo.2022.121268

Wilcox, P. S., Honiat, C., Trüssel, M., Edwards, R. L., and Spötl, C. (2020). Exceptional warmth and climate instability occurred in the european alps during the last interglacial period. *Communications Earth & Environment* 1, 57. https://doi.org/10.1038/s43247-020-00063-w

Wortham, B. E., Montañez, I. P., Swart, P. K., Vonhof, H., and Tabor, C. (2022). Variability in effective moisture inferred from inclusion fluid δ^{18}O and δ^{2}H values in a central Sierra Nevada stalagmite (CA). *Quaternary Science Reviews* 279, 107399. https://doi.org/10.1016/j.quascirev.2022.107399

Wu, G. X., Liu, Y. M., He, B., Bao, Q., Duan, A. M., and Jin, F.-F. (2012). Thermal controls on the Asian summer monsoon. *Scientific Reports* 2, 404. https://doi.org/10.1038/srep00404

Wu, S. D. (2000). *The history of population of China: Liao, Song, Jin and Yuan Dynasties (in Chinese)*, vol. Liao, Song, Jin and Yuan Dynasties (Shanghai: Fudan University Press)

Wu, Y., Li, T.-Y., Li, J.-Y., Cheng, H., Ning, Y.-F., Shen, C.-C., et al. (2023a). Variations in Asian summer monsoon and hydroclimate during Heinrich stadials 4 revealed by stalagmite stable isotopes and trace elements. *Quaternary Science Reviews* 299, 107869. https://doi.org/10.1016/j.quascirev.2022.107869

Wu, Y., Li, T.-Y., Yu, T.-L., Shen, C.-C., Chen, C.-J., Zhang, J., et al. (2020). Variation of the Asian summer monsoon since the last glacial-interglacial recorded in a stalagmite from southwest China. *Quaternary Science Reviews* 234, 106261. https://doi.org/10.1016/j.quascirev.2020.106261

Wu, Y., Warken, S., Frank, N., Mielke, A., Chen, C.-J., Li, J.-Y., et al. (2023b). Northern hemisphere summer insolation and ice volume driven variations in hydrological environment in southwest China. *Geophysical Research Letters* 50, e2023GL105664. https://doi.org/10.1029/2023GL105664

Wu, Z. H. and Huang, N. E. (2009). Ensemble empirical mode decomposition: a noiseassisted data analysis method. *Advances in Adaptive Data Analysis* 01, 1–41. https://doi.org/10.1142/S1793536909000047

Xiao, X. Y., Zhao, Y., Chi, C. T., Zheng, Z., Ma, C. M., Liang, C., et al. (2023). Quantitative pollen-based paleoclimate reconstructions for the past 18.5 ka in southwestern Yunnan province, China. *Global and Planetary Change* 230, 104288. https://doi.org/10.1016/j.gloplacha.2023.104288

Xue, J. B., Zhong, W., Xie, L. C., and Unkel, I. (2015). Vegetation responses to the last glacial and early Holocene environmental changes in the northern Leizhou Peninsula, south China. *Quaternary Research* 84, 223–231. https://doi.org/10.1016/j.yqres.2015.08.001

Xue, Y.-X., Zhang, J., Su, Z., Wu, Y., Liang, Q.-S., Liang, M.-Q., et al. (2023). Quantifying source effects based on rainwater δ^{18}O from 10-year monitoring records in southwest China. *Applied Geochemistry* 155, 105706. https://doi.org/10.1016/j.apgeochem.2023.105706

Yang, H., Johnson, K. R., Griffiths, M. L., and Yoshimura, K. (2016). Interannual controls on oxygen isotope variability in Asian monsoon precipitation and implications for paleoclimate reconstructions. *Journal of Geophysical Research: Atmospheres* 121, 8410–8428. https://doi.org/10.1002/2015jd024683

Yang, S. H., Chen, S. T., Wang, Y. J., Qiu, Z. Z., and Zeng, Y. L. (2017). Comparison of oxygen-carbon isotopes from a Holocene stalagmite by EEMD method. *Geographical Research* 36, 1455–1466. https://doi.org/10.11821/dlyj201708005. [In Chinese with English abstract]

Yang, X. L., Yang, H., Wang, B. Y., Huang, L. J., Shen, C. C., Edwards, R. L., et al. (2019a). Early-Holocene monsoon instability and climatic optimum recorded by Chinese stalagmites. *The Holocene* 29, 1059–1067. https://doi.org/10.1177/0959683619831433

Yang, Y., Yang, R., Cao, J., Zhao, J., Cheng, H., and Wang, J. (2019b). Relationship between the Asian summer monsoon circulation and speleothem δ^{18}O of Xiaobailong cave. *Climate Dynamics* 53, 6351–6362. https://doi.org/10.1007/s00382-019-04935-6

Yang, Z. H. (1996). *China Historical Population Data and the Relavant Studies* (Benjing: Reform Press). [In Chinese]

Yatagai, A., Kamiguchi, K., Arakawa, O., Hamada, A., Yasutomi, N., and Kitoh, A. (2012). Aphrodite: Constructing a long-term daily gridded precipitation dataset for Asia based on a dense network of rain gauges. *Bulletin of the American Meteorological Society* 93, 1401–1415. https://doi.org/10.1175/BAMS-D-11-00122.1

Yin, J.-J., Wang, Z. J., Shi, W. Q., Shao, Q. F., Wu, X., Tang, W., et al. (2023a). Spatial pattern and cause of centennial-scale hydroclimatic variability over eastern China during the last millennium. *Palaeogeography, Palaeoclimatology, Palaeoecology* 627, 111753. https://doi.org/10.1016/j.palaeo.2023.111753

Yin, J.-J., Wang, Z. J., Yuan, D. X., Tang, W., Wu, X., Zhang, T., et al. (2023b). The severe drought event of 2009–2010 over southwest China as recorded by a cave stalagmite from southeast Yunnan: Implication for stalagmite δ^{18}O interpretation in the Asian monsoon region. *Quaternary Science Reviews* 302, 107967. https://doi.org/10.1016/j.quascirev.2023.107967

Yuan, D. X., Cheng, H., R Lawrence, E., Dykoski, C. A., Kelly, M. J., Zhang, M. L., et al. (2004). Timing, duration, and transitions of the last interglacial Asian monsoon. *Science* 304, 575–578. https://doi.org/10.1126/science.1091220

Yuan, S. F., Chiang, H.-W., Liu, G. X., Bijaksana, S., He, S. N., Jiang, X. Y., et al. (2023). The strength, position, and width changes of the intertropical convergence zone since the Last Glacial Maximum. *Proceedings of the National Academy of Sciences* 120, e2217064120. https://doi.org/10.1073/pnas.2217064120

Yue, Y. F., He, L. Y., Zheng, Z., Chen, C., Wan, Q. C., Tang, Y. J., et al. (2024). Late Holocene vegetation succession, climate change, and fire history in western Guizhou (in Chinese). *Quaternary Sciences* 44, 112–127. http://doi.org/10.11928/j.issn.1001-7410.2024.01.09

Zhai, X. M., Zhang, J. W., Chen, X. M., Chen, J. S., Gao, K., Liang, Y. J., et al. (2024). Middle to late Holocene hydroclimate variability revealed by multi-proxy stalagmite records from Jinfo cave, central-west China. *Palaeogeography, Palaeoclimatology, Palaeoecology* 642, 112151. https://doi.org/10.1016/j.palaeo.2024.112151

Zhang, E. L., Meng, X. Q., Ning, D. L., Shulmeister, J., Sun, W. W., Zhang, W. F., et al. (2023a). Holocene extreme hydroclimate events in the Asian monsoon region were more frequent during cooler intervals. *Communications Earth & Environment* 4, 344. https://doi.org/10.1038/s43247-023-00997-x

Zhang, H. B., Griffiths, M. L., Chiang, J. C. H., Kong, W. W., Wu, S. T., Atwood, A., et al. (2018). East Asian hydroclimate modulated by the position of the westerlies during Termination I. *Science* 362, 580–583. https://doi.org/10.1126/science.aat9393

Zhang, H. W., Cheng, H., Cai, Y. J., Spotl, C., Sinha, A., Kathayat, G., et al. (2020a). Effect of precipitation seasonality on annual oxygen isotopic composition in the area of spring persistent rain in southeastern China and its paleoclimatic implication. *Climate of the Past* 16, 211–225. https://doi.org/10.5194/cp-16-211-2020

Zhang, H. W., Cheng, H., Sinha, A., Spötl, C., Cai, Y. J., Liu, B., et al. (2021a). Collapse of the Liangzhu and other Neolithic cultures in the lower Yangtze region in response to climate change. *Science Advances* 7, eabi9275. https://doi.org/10.1126/sciadv.abi9275

Zhang, H. W., Zhang, X., Cai, Y. J., Sinha, A., Spötl, C., Baker, J., et al. (2021b). A data-model comparison pinpoints Holocene spatiotemporal pattern of east Asian summer monsoon. *Quaternary Science Reviews* 261, 106911. https://doi.org/10.1016/j.quascirev.2021.106911

Zhang, J. and Li, T.-Y. (2019). Seasonal and interannual variations of hydrochemical characteristics and stable isotopic compositions of drip waters in Furong cave, southwest China based on 12 years' monitoring. *Journal of Hydrology* 572, 40–50. https://doi.org/10.1016/j.jhydrol.2019.02.052

Zhang, J. P., Lu, H. Y., Jia, J. W., Shen, C. M., Wang, S. Y., Chu, G. Q., et al. (2020b). Seasonal drought events in tropical east Asia over the last 60,000 y. *Proceedings of the National Academy of Sciences* 117, 30988–30922. https://doi.org/10.1073/pnas.2013802117

Zhang, P. Z., Cheng, H., Edwards, R. L., Chen, F. H., Wang, Y. J., Yang, X. L., et al. (2008). A test of climate, sun, and culture relationships from an 1810-year Chinese cave record. *Science* 322, 940–942. https://doi.org/10.1126/science.1163965

Zhang, S., Li, T. G., Chang, F. M., Yu, Z. F., Xiong, Z. F., and Wang, H. X. (2017). Correspondence between the ENSO-like state and glacial-interglacial condition during the past 360 kyr. *Chinese Journal of Oceanology and Limnology* 35, 1018–1031. https://doi.org/10.1007/s00343-017-6082-9

Zhang, S., Yu, Z. F., Gong, X., Wang, Y., Chang, F. M., Lohmman, G., et al. (2021c). Precession cycles of the El Niño/Southern oscillation-like system controlled by Pacific upper-ocean stratification. *Communications Earth & Environment* 2, 239. https://doi.org/10.1038/s43247-021-00305-5

Zhang, S. Y. and Peng, R. F. (2012). On the Song dynasty population migration to the national blend promote in the Wujiang river basin. *Guizhou Ethnic Studies* 33, 122–127. https://doi.org/10.13965/j.cnki.gzmzyj10026959.2012.03.029. [In Chinese with English abstract]

Zhang, W. H., Chen, S. T., Shao, Q. F., and Chen, J. S. (2023b). Hydroclimatic variation over central China during the 4.2 ka event and its implications for cultural transformation. *Palaeogeography, Palaeoclimatology, Palaeoecology* 615, 111441. https://doi.org/10.1016/j.palaeo.2023.111441

Zhang, X., Jiang, X. Y., Xiao, H. Y., Cai, B. G., Yu, T.-L., and Shen, C.-C. (2021d). A gradual transition into Greenland interstadial 14 in southeastern China based on a sub-decadally-resolved stalagmite record. *Quaternary Science Reviews* 253, 106769. https://doi.org/10.1016/j.quascirev.2020.106769

Zhang, X., Qiu, W. Y., Jiang, X. Y., Hu, H.-M., Xiao, H. Y., Cai, B. G., et al. (2021e). Three-phase structure of the east Asia summer monsoon during Heinrich stadial 4 recorded in Xianyun cave, southeastern China. *Quaternary Science Reviews* 274, 107267. https://doi.org/10.1016/j.quascirev.2021.107267

Zhang, X., Xiao, H., Chou, Y.-C., Cai, B., Lone, M. A., Shen, C.-C., et al. (2020c). A detailed east Asian monsoon history of Greenland interstadial 21 in southeastern China. *Palaeogeography, Palaeoclimatology, Palaeoecology* 552, 109752. https://doi.org/10.1016/j.palaeo.2020.109752

Zhang, X., Zheng, Z., Huang, K. Y., Cheng, J., Cheddadi, R., Zhao, Y., et al. (2023c). Quantification of Asian monsoon variability from 68 ka BP through pollen-based climate reconstruction. *Science Bulletin* 68, 713–722. https://doi.org/10.1016/j.scib.2023.03.013

Zhang, Z. H., Leduc, G., and Sachs, J. P. (2014). El niño evolution during the Holocene revealed by a biomarker rain gauge in the Galápagos islands. *Earth and Planetary Science Letters* 404, 420–434. https://doi.org/10.1016/j.epsl.2014.07.013

Zhang, Z. M., Huang, X. F., and Zhou, Y. C. (2021f). Factors influencing the evolution of human-driven rocky desertification in karst areas. *Land Degradation & Development* 32, 817–829. https://doi.org/10.1002/ldr.3731

Zhang, Z. P., Liu, J. B., Chen, J., Chen, S. Q., Shen, Z. W., Chen, J., et al. (2021g). Holocene climatic optimum in the east Asian monsoon region of China defined by climatic stability. *Earth-Science Reviews* 212, 103450. https://doi.org/10.1016/j.earscirev.2020.103450

Zhao, C., Cheng, J., Wang, J. J., Yan, H., Leng, C. C., Zhang, C., et al. (2021). Paleoclimate significance of reconstructed rainfall isotope changes in Asian monsoon region. *Geophysical Research Letters* 48, e2021GL092460. https://doi.org/10.1029/2021GL092460

Zhao, D. B., Lu, Z. Y., Wan, S. M., Cheng, H., Shi, X. F., and Li, A. C. (2023a). Quaternary rainfall variability is governed by insolation in northern China and ice-sheet forcing in the south. *Communications Earth & Environment* 4, 7. https://doi.org/10.1038/s43247-022-00670-9

Zhao, J. Y., Cheng, H., Cao, J., Sinha, A., Dong, X. Y., Pan, L. K., et al. (2023b). Orchestrated decline of Asian summer monsoon and Atlantic meridional overturning circulation in global warming period. *The Innovation Geoscience* 1, 100011. https://doi.org/10.59717/j.xinn-geo.2023.100011

Zhao, J. Y., Cheng, H., Pan, L. K., Wang, K. X., Cui, J. H., Liang, M.-Q., et al. (2025). Putting the recent 100-year of asian summer monsoon weakening into context. *Science Bulletin* https://doi.org/10.1016/j.scib.2025.05.006. [In Press]

Zhao, K., Wang, Y. J., Edwards, R. L., Cheng, H., Kong, X. G., Liu, D. B., et al. (2020). Late Holocene monsoon precipitation changes in southern China and their linkage to northern hemisphere temperature. *Quaternary Science Reviews* 232, 106191. https://doi.org/10.1016/j.quascirev.2020.106191

Zhao, K., Wang, Y. J., Edwards, R. L., Cheng, H., Liu, D. B., and Kong, X. G. (2015). A high-resolved record of the Asian summer monsoon from Dongge cave, China for the past 1200 years. *Quaternary Science Reviews* 122, 250–257. https://doi.org/10.1016/j.quascirev.2015.05.030

Zhao, Y., Yu, Z., Chen, F., Zhang, J., and Yang, B. (2009). Vegetation response to Holocene climate change in monsoon-influenced region of China. *Earth-Science Reviews* 97, 242–256. https://doi.org/10.1016/j.earscirev.2009.10.007

Zheng, Y. K., Liu, H. Y., Yang, H., Wang, H. Y., Zhao, W. J., Zhang, Z. Y., et al. (2022). Decoupled Asian monsoon intensity and precipitation during glacial-interglacial transitions on the Chinese loess plateau. *Nature Communications* 13, 5397. https://doi.org/10.1038/s41467-022-33105-2

Zhou, H., Zhang, X. P., Yao, T. C., Hua, M. Q., Wang, X. J., Rao, Z. G., et al. (2019). Variation of δ^{18}O in precipitation and its response to upstream atmospheric convection and rainout: A case study of changsha station, south-central China. *Science of The Total Environment* 659, 1199–1208. https://doi.org/10.1016/j.scitotenv.2018.12.396

Zhou, X., Sun, L. G., Zhan, T., Huang, W., Zhou, X. Y., Hao, Q. Z., et al. (2016). Time-transgressive onset of the Holocene optimum in the east Asian monsoon region. *Earth and Planetary Science Letters* 456, 39–46. https://doi.org/10.1016/j.epsl.2016.09.052

Zhou, Y. X. and McManus, J. F. (2024). Heinrich event ice discharge and the fate of the Atlantic Meridional Overturning Circulation. *Science* 384, 983–986. https://doi.org/10.1126/science.adh8369

Zhu, X. W., Zhang, Y. H., Han, D. S., Wen, R. P., and Chen, B. Q. (2004). Cave characteristics and speleothems in Xueyu Cave group, Fengdu, Chongqing city. *Carsologica Sinica* 23, 85–90. https://doi.org/10.3969/j.issn.1001-4810.2004.02.001. [In Chinese with English abstract]

Zhu, Z. M., Feinberg, J. M., Xie, S. C., Bourne, M. D., Huang, C. J., Hu, C. Y., et al. (2017). Holocene ENSO-related cyclic storms recorded by magnetic minerals in speleothems of central China. *Proceedings of the National Academy of Sciences* 114, 852–857. https://doi.org/10.1073/pnas.1610930114

Apppendix

A. Lists Figures and Tables

List of Figures

List of Tables

B. Supplementary Information

B.1 Supplementary Information for Chapter 2

Supplementary Tables

Table S2.1. The isotope results of standard water injection measurements used to detect the water volume effect on isotope values and their corrected values. Isotopic values are presented relative to V-SMOW. The measurement uncertainty is 0.5‰ for δ^{18}O and 1.5‰ for δ^{2}H.

Standard Water	Water Volume (μl)	$\delta^{18}O_{original}$, ‰	$\delta^{2}H_{original}$, ‰	$\delta^{18}O_{correction}$, ‰	$\delta^{2}H_{correction}$, ‰
VE	0.04	-6.71	-57.88	-7.76	-60.09
VE	0.05	-5.97	-55.55	-6.87	-57.43
VE	0.05	-8.31	-54.93	-9.23	-56.79
VE	0.19	-7.58	-60.26	-7.91	-60.96
VE	0.05	-6.45	-55.53	-7.34	-57.38
VE	0.08	-6.99	-59.16	-7.72	-60.69
VE	0.08	-7.55	-56.79	-8.28	-58.30
VE	0.19	-7.70	-57.58	-8.04	-58.26
VE	0.08	-6.83	-58.88	-7.55	-60.39
VE	0.09	-7.89	-57.01	-8.59	-58.44
VE	0.09	-7.10	-58.76	-7.79	-60.21
VE	0.12	-7.71	-57.53	-8.27	-58.68
VE	0.15	-7.44	-59.33	-7.87	-60.23
VE	0.17	-7.22	-59.43	-7.61	-60.23
VE	0.17	-7.60	-57.00	-7.98	-57.79
VE	0.18	-7.61	-60.26	-7.96	-61.01
VE	0.19	-8.00	-59.80	-8.35	-60.51
VE	0.19	-8.22	-59.69	-8.56	-60.41
VE	0.19	-7.46	-60.13	-7.80	-60.84
VE	0.19	-8.10	-59.48	-8.43	-60.17
VE	0.19	-8.05	-58.17	-8.38	-58.85
VE	0.19	-8.20	-58.56	-8.53	-59.23
VE	0.26	-8.10	-59.94	-8.29	-60.33
VE	0.26	-8.20	-59.03	-8.39	-59.43
VE	0.29	-8.43	-57.89	-8.57	-58.18
VE	0.29	-8.08	-59.81	-8.22	-60.10
VE	0.30	-7.96	-59.50	-8.10	-59.78

Table S2.1 Continued

Standard Water	**Water Volume (μl)**	δ^{18}**O**$_{\textbf{original}}$, **‰**	δ^{2}**H**$_{\textbf{original}}$, **‰**	δ^{18}**O**$_{\textbf{correction}}$, **‰**	δ^{2}**H**$_{\textbf{correction}}$, **‰**
VE	0.30	-8.24	-59.54	-8.37	-59.82
VE	0.30	-7.86	-59.76	-7.98	-60.03
VE	0.31	-8.36	-59.03	-8.49	-59.28
VE	0.33	-7.92	-59.73	-8.00	-59.91
VE	0.39	-7.99	-59.89	-7.99	-59.90
VE	0.40	-8.00	-59.04	-7.99	-59.03
VE	0.41	-8.01	-59.53	-8.01	-59.52
VE	0.41	-8.14	-58.01	-8.14	-58.00
VE	0.41	-7.97	-59.16	-7.96	-59.13
VE	0.44	-7.85	-59.44	-7.81	-59.36
VE	0.45	-7.83	-59.27	-7.78	-59.16
VE	0.47	-8.12	-58.35	-8.04	-58.19
VE	0.49	-8.15	-59.31	-8.06	-59.12
VE	0.51	-7.96	-58.55	-7.86	-58.33
VE	0.51	-8.17	-59.04	-8.06	-58.81
VE	0.51	-8.14	-59.67	-8.02	-59.44
VE	0.54	-7.94	-58.89	-7.80	-58.60
VE	0.60	-8.36	-59.38	-8.17	-59.00
VE	0.60	-8.39	-59.93	-8.20	-59.54
VE	0.61	-8.16	-59.47	-7.97	-59.07
VE	0.61	-8.17	-59.56	-7.98	-59.17
VE	0.61	-8.03	-58.58	-7.84	-58.18
VE	0.62	-8.09	-59.57	-7.89	-59.16
VE	0.62	-8.16	-59.56	-7.96	-59.14
VE	0.63	-8.23	-59.34	-8.02	-58.91
VE	0.72	-8.13	-59.90	-7.86	-59.35
VE	0.72	-8.18	-59.89	-7.91	-59.33
VE	0.72	-8.28	-59.90	-8.00	-59.34
VE	0.73	-8.29	-59.93	-8.02	-59.36
VE	0.74	-8.29	-59.73	-8.01	-59.15
VE	0.80	-8.26	-59.79	-7.94	-59.13
VE50%	0.05	5.83	-17.81	5.07	-19.47
VE50%	0.06	5.64	-16.33	4.93	-17.88
VE50%	0.06	5.23	-18.03	4.55	-19.51

Table S2.1 Continued

Standard Water	**Water Volume (μl)**	δ^{18}**O**$_{\mathbf{original}}$, **‰**	δ^{2}**H**$_{\mathbf{original}}$, **‰**	δ^{18}**O**$_{\mathbf{correction}}$, **‰**	δ^{2}**H**$_{\mathbf{correction}}$, **‰**
VE50%	0.08	4.82	-19.39	4.23	-20.66
VE50%	0.09	4.99	-18.03	4.44	-19.21
VE50%	0.13	4.60	-16.94	4.19	-17.81
VE50%	0.15	4.36	-19.95	4.01	-20.71
VE50%	0.19	5.04	-18.68	4.76	-19.29
VE50%	0.19	4.70	-18.68	4.43	-19.27
VE50%	0.19	4.70	-17.85	4.43	-18.44
VE50%	0.22	4.73	-19.11	4.52	-19.57
VE50%	0.23	4.74	-18.86	4.53	-19.31
VE50%	0.24	4.87	-18.69	4.68	-19.09
VE50%	0.29	4.73	-18.69	4.61	-18.95
VE50%	0.31	4.32	-20.26	4.23	-20.45
VE50%	0.34	4.75	-20.59	4.69	-20.72
VE50%	0.35	4.23	-19.68	4.18	-19.78
VE50%	0.36	4.76	-19.47	4.71	-19.56
VE50%	0.37	4.06	-18.83	4.03	-18.89
VE50%	0.38	4.39	-18.83	4.37	-18.88
VE50%	0.39	4.65	-18.67	4.65	-18.68
VE50%	0.40	4.31	-19.07	4.31	-19.08
VE50%	0.41	4.41	-19.77	4.41	-19.76
VE50%	0.44	4.48	-20.15	4.51	-20.07
VE50%	0.46	4.39	-19.87	4.45	-19.76
VE50%	0.46	4.28	-20.23	4.33	-20.11
VE50%	0.47	4.57	-19.71	4.63	-19.59
VE50%	0.48	4.04	-19.07	4.11	-18.92
VE50%	0.50	4.57	-19.34	4.65	-19.16
VE50%	0.50	4.55	-19.47	4.64	-19.29
VE50%	0.51	4.35	-19.84	4.44	-19.65
VE50%	0.51	4.44	-20.30	4.53	-20.10
VE50%	0.51	4.39	-19.55	4.48	-19.35
VE50%	0.51	4.57	-18.92	4.67	-18.72
VE50%	0.56	4.62	-19.24	4.74	-18.97
VE50%	0.59	4.68	-19.77	4.83	-19.46
VE50%	0.60	4.49	-19.56	4.64	-19.24

Table S2.1 Continued

Standard Water	**Water Volume (μl)**	δ^{18}**O**$_{\mathbf{original}}$**, ‰**	δ^{2}**H**$_{\mathbf{original}}$**, ‰**	δ^{18}**O**$_{\mathbf{correction}}$**, ‰**	δ^{2}**H**$_{\mathbf{correction}}$**, ‰**
VE50%	0.61	4.35	-19.66	4.51	-19.32
VE50%	0.61	4.51	-20.02	4.67	-19.68
VE50%	0.62	4.28	-20.69	4.45	-20.34
VE50%	0.63	4.25	-20.10	4.42	-19.73
VE50%	0.67	4.57	-19.78	4.77	-19.36
VE50%	0.71	4.46	-19.51	4.67	-19.06
VE50%	0.71	4.39	-19.56	4.61	-19.10
VE50%	0.72	4.45	-19.50	4.67	-19.03
VE50%	0.73	4.45	-19.70	4.67	-19.21
VE50%	0.75	4.11	-19.71	4.35	-19.21
VE50%	0.77	4.32	-18.99	4.56	-18.47
VE50%	0.79	4.36	-19.50	4.62	-18.96
VE50%	0.81	4.20	-18.89	4.47	-18.33
VE50%	0.81	4.12	-20.14	4.38	-19.57
CC	0.04	-14.06	-106.15	-15.20	-108.71
CC	0.04	-13.53	-108.09	-14.66	-110.65
CC	0.08	-12.95	-109.22	-13.76	-111.09
CC	0.09	-14.25	-107.71	-14.99	-109.37
CC	0.10	-14.24	-108.91	-14.95	-110.52
CC	0.11	-13.45	-108.82	-14.09	-110.28
CC	0.15	-14.50	-109.32	-14.98	-110.39
CC	0.20	-14.87	-109.19	-15.23	-109.99
CC	0.20	-14.70	-109.01	-15.06	-109.81
CC	0.20	-14.49	-108.86	-14.83	-109.62
CC	0.27	-14.82	-109.81	-15.01	-110.25
CC	0.30	-14.41	-109.62	-14.57	-109.95
CC	0.30	-14.88	-109.80	-15.03	-110.12
CC	0.31	-15.08	-109.57	-15.21	-109.86
CC	0.32	-14.62	-109.46	-14.74	-109.73
CC	0.36	-14.66	-110.17	-14.72	-110.29
CC	0.36	-15.00	-109.34	-15.06	-109.46
CC	0.36	-14.97	-110.39	-15.02	-110.50
CC	0.39	-14.89	-110.64	-14.90	-110.66
CC	0.41	-14.85	-110.70	-14.84	-110.69

Table S2.1 Continued

Standard Water	**Water Volume (µl)**	δ^{18}**O**$_{\textbf{original}}$, **‰**	δ^{2}**H**$_{\textbf{original}}$, **‰**	δ^{18}**O**$_{\textbf{correction}}$, **‰**	δ^{2}**H**$_{\textbf{correction}}$, **‰**
CC	0.41	-15.02	-110.00	-15.00	-109.97
CC	0.41	-14.88	-110.45	-14.86	-110.41
CC	0.42	-15.01	-110.17	-14.99	-110.13
CC	0.42	-14.98	-109.95	-14.97	-109.91
CC	0.44	-14.58	-110.39	-14.54	-110.29
CC	0.44	-14.70	-110.24	-14.65	-110.13
CC	0.46	-14.87	-109.87	-14.79	-109.70
CC	0.50	-15.10	-110.71	-14.99	-110.46
CC	0.50	-14.66	-110.46	-14.54	-110.21
CC	0.52	-14.92	-109.86	-14.79	-109.58
CC	0.52	-14.83	-110.48	-14.69	-110.19
CC	0.60	-14.84	-110.24	-14.63	-109.78
CC	0.61	-14.91	-110.24	-14.70	-109.76
CC	0.62	-14.99	-110.33	-14.77	-109.83
CC	0.63	-14.91	-110.52	-14.68	-110.01
CC	0.63	-14.86	-110.41	-14.63	-109.91
CC	0.64	-14.87	-110.81	-14.63	-110.29
CC	0.69	-14.99	-110.81	-14.71	-110.19

Table S2.2. Standard water isotope measurements using 0.4 l and 0.1 l sample mixing chambers. Isotopic values are presented relative to V-SMOW. The measurement uncertainty is 0.5‰ for δ^{18}O and 1.5‰ for δ^{2}H. The unit of water volume is microliter.

Standard Water	**Water Volume**	**δ^{18}O ‰**	**δ^{2}H ‰**	**Standard Water**	**Water Volume**	**δ^{18}O ‰**	**δ^{2}H ‰**
CC 0.4 l	0.02	-15.23	-103.74	VE 0.4 l	0.24	-6.88	-57.37
CC 0.4 l	0.04	-13.95	-110.83	VE 0.4 l	0.24	-7.42	-57.23
CC 0.4 l	0.04	-15.28	-105.23	VE 0.4 l	0.26	-8.10	-59.94
CC 0.4 l	0.04	-14.06	-106.15	VE 0.4 l	0.26	-8.20	-59.03
CC 0.4 l	0.04	-14.46	-112.77	VE 0.4 l	0.29	-8.89	-61.31
CC 0.4 l	0.04	-13.53	-108.09	VE 0.4 l	0.29	-8.43	-57.89
CC 0.4 l	0.07	-14.57	-110.09	VE 0.4 l	0.29	-8.08	-59.81
CC 0.4 l	0.08	-12.95	-109.22	VE 0.4 l	0.30	-7.96	-59.50
CC 0.4 l	0.08	-12.62	-109.82	VE 0.4 l	0.30	-7.08	-57.09
CC 0.4 l	0.08	-14.03	-109.42	VE 0.4 l	0.30	-7.99	-60.60
CC 0.4 l	0.08	-13.97	-111.50	VE 0.4 l	0.30	-8.24	-59.54
CC 0.4 l	0.09	-14.54	-112.50	VE 0.4 l	0.30	-7.98	-60.21
CC 0.4 l	0.09	-14.26	-110.86	VE 0.4 l	0.30	-7.86	-59.76
CC 0.4 l	0.09	-14.25	-107.71	VE 0.4 l	0.31	-8.36	-59.03
CC 0.4 l	0.09	-14.90	-106.62	VE 0.4 l	0.31	-7.14	-58.34
CC 0.4 l	0.09	-14.85	-111.12	VE 0.4 l	0.32	-7.11	-58.05
CC 0.4 l	0.09	-13.95	-110.59	VE 0.4 l	0.33	-7.92	-59.73
CC 0.4 l	0.10	-14.24	-108.91	VE 0.4 l	0.37	-7.99	-61.34
CC 0.4 l	0.10	-14.24	-108.91	VE 0.4 l	0.39	-7.99	-59.89
CC 0.4 l	0.11	-13.45	-108.82	VE 0.4 l	0.40	-8.21	-60.21
CC 0.4 l	0.12	-14.01	-110.61	VE 0.4 l	0.40	-8.00	-59.04
CC 0.4 l	0.12	-15.06	-108.67	VE 0.4 l	0.41	-8.01	-59.53
CC 0.4 l	0.14	-14.03	-112.33	VE 0.4 l	0.41	-8.14	-58.01
CC 0.4 l	0.15	-14.65	-110.59	VE 0.4 l	0.41	-7.97	-59.16
CC 0.4 l	0.15	-14.50	-109.32	VE 0.4 l	0.41	-7.19	-56.76
CC 0.4 l	0.18	-14.30	-110.50	VE 0.4 l	0.43	-7.48	-58.44
CC 0.4 l	0.19	-14.81	-111.20	VE 0.4 l	0.44	-7.85	-59.44
CC 0.4 l	0.19	-14.45	-110.46	VE 0.4 l	0.45	-7.83	-59.27
CC 0.4 l	0.19	-14.14	-110.49	VE 0.4 l	0.47	-8.12	-58.35
CC 0.4 l	0.19	-14.63	-110.65	VE 0.4 l	0.49	-8.15	-59.31
CC 0.4 l	0.20	-14.70	-109.01	VE 0.4 l	0.50	-8.29	-60.30

Table S2.2 Continued

Standard Water	Water Volume	$\delta^{18}O$ ‰	$\delta^{2}H$ ‰	Standard Water	Water Volume	$\delta^{18}O$ ‰	$\delta^{2}H$ ‰
CC 0.4 l	0.20	-14.87	-109.19	VE 0.4 l	0.50	-8.42	-60.02
CC 0.4 l	0.20	-14.49	-108.86	VE 0.4 l	0.51	-7.96	-58.55
CC 0.4 l	0.24	-15.01	-110.13	VE 0.4 l	0.51	-8.09	-60.61
CC 0.4 l	0.24	-15.09	-108.98	VE 0.4 l	0.51	-8.17	-59.04
CC 0.4 l	0.24	-15.06	-110.93	VE 0.4 l	0.51	-7.96	-60.74
CC 0.4 l	0.24	-13.69	-106.90	VE 0.4 l	0.51	-8.14	-59.67
CC 0.4 l	0.27	-14.82	-109.81	VE 0.4 l	0.52	-8.02	-60.20
CC 0.4 l	0.28	-14.79	-111.58	VE 0.4 l	0.52	-7.41	-57.95
CC 0.4 l	0.30	-14.41	-109.62	VE 0.4 l	0.53	-7.32	-58.05
CC 0.4 l	0.30	-14.88	-109.80	VE 0.4 l	0.54	-7.76	-57.29
CC 0.4 l	0.31	-14.98	-112.75	VE 0.4 l	0.54	-7.94	-58.89
CC 0.4 l	0.31	-15.08	-109.57	VE 0.4 l	0.60	-8.36	-59.38
CC 0.4 l	0.31	-14.78	-110.60	VE 0.4 l	0.60	-8.39	-59.93
CC 0.4 l	0.32	-14.62	-109.46	VE 0.4 l	0.61	-8.16	-59.47
CC 0.4 l	0.35	-14.59	-108.74	VE 0.4 l	0.61	-8.17	-59.56
CC 0.4 l	0.36	-14.66	-110.17	VE 0.4 l	0.61	-8.03	-58.58
CC 0.4 l	0.36	-15.00	-109.34	VE 0.4 l	0.62	-8.09	-59.57
CC 0.4 l	0.36	-14.97	-110.39	VE 0.4 l	0.62	-8.16	-59.56
CC 0.4 l	0.38	-14.53	-106.79	VE 0.4 l	0.63	-8.23	-59.34
CC 0.4 l	0.39	-15.29	-104.90	VE 0.4 l	0.72	-8.13	-59.90
CC 0.4 l	0.39	-14.96	-109.06	VE 0.4 l	0.72	-8.33	-59.36
CC 0.4 l	0.39	-15.14	-108.53	VE 0.4 l	0.72	-8.18	-59.89
CC 0.4 l	0.39	-14.80	-109.44	VE 0.4 l	0.72	-8.28	-59.90
CC 0.4 l	0.39	-14.89	-110.64	VE 0.4 l	0.73	-8.29	-59.93
CC 0.4 l	0.40	-14.47	-109.34	VE 0.4 l	0.73	-7.76	-58.40
CC 0.4 l	0.40	-15.08	-111.29	VE 0.4 l	0.74	-8.62	-60.78
CC 0.4 l	0.40	-14.85	-110.70	VE 0.4 l	0.74	-8.29	-59.73
CC 0.4 l	0.41	-15.02	-110.00	VE 0.4 l	0.79	-8.22	-59.08
CC 0.4 l	0.41	-14.51	-111.33	VE 0.4 l	0.80	-8.26	-59.79
CC 0.4 l	0.41	-14.88	-109.27	VE 0.4 l	0.80	-8.00	-59.76
CC 0.4 l	0.41	-14.88	-109.27	VE 0.4 l	0.81	-7.83	-58.99
CC 0.4 l	0.41	-14.72	-110.45	VE 0.4 l	0.82	-8.27	-60.00
CC 0.4 l	0.41	-15.01	-109.30	VE 0.4 l	0.82	-8.30	-60.29
CC 0.4 l	0.41	-14.98	-110.17	VE 0.4 l	0.83	-8.25	-59.57

Table S2.2 Continued

Standard Water	**Water Volume**	δ^{18}**O ‰**	δ^{2}**H ‰**	**Standard Water**	**Water Volume**	δ^{18}**O ‰**	δ^{2}**H ‰**
CC 0.4 l	0.43	-14.58	-109.95	VE 0.4 l	0.83	-8.34	-59.70
CC 0.4 l	0.43	-14.69	-108.48	VE 0.4 l	0.83	-8.42	-59.64
CC 0.4 l	0.44	-14.70	-110.39	VE 0.4 l	0.92	-8.07	-59.15
CC 0.4 l	0.46	-15.00	-110.24	VE 0.4 l	0.93	-8.28	-59.64
CC 0.4 l	0.46	-14.87	-109.20	VE 0.4 l	0.93	-8.32	-59.51
CC 0.4 l	0.46	-15.01	-109.87	VE 0.4 l	0.93	-8.26	-59.86
CC 0.4 l	0.47	-14.87	-109.22	VE 0.4 l	0.94	-8.20	-59.67
CC 0.4 l	0.49	-14.90	-109.25	VE 0.4 l	0.94	-8.16	-59.13
CC 0.4 l	0.49	-15.10	-109.46	VE 0.4 l	0.95	-8.28	-59.63
CC 0.4 l	0.49	-14.98	-110.71	VE 0.4 l	0.99	-7.37	-62.79
CC 0.4 l	0.50	-15.12	-111.19	VE 0.4 l	1.00	-8.25	-59.77
CC 0.4 l	0.50	-14.66	-109.35	VE 0.4 l	1.01	-8.14	-59.66
CC 0.4 l	0.51	-14.75	-108.94	VE 0.4 l	1.02	-8.35	-60.10
CC 0.4 l	0.51	-15.22	-110.99	VE 0.4 l	1.02	-8.19	-59.90
CC 0.4 l	0.52	-14.92	-110.46	VE 0.4 l	1.02	-8.35	-59.94
CC 0.4 l	0.52	-14.83	-109.86	VE 0.4 l	1.02	-8.38	-60.08
CC 0.4 l	0.53	-15.04	-110.94	VE 0.4 l	1.02	-8.36	-59.53
CC 0.4 l	0.53	-14.68	-109.66	VE 0.4 l	1.03	-8.30	-60.25
CC 0.4 l	0.54	-15.32	-110.68	VE 0.4 l	1.04	-8.41	-59.69
CC 0.4 l	0.57	-14.86	-111.42	VE 0.4 l	1.04	-8.30	-59.43
CC 0.4 l	0.59	-14.65	-108.38	VE 0.4 l	1.04	-8.41	-59.14
CC 0.4 l	0.60	-14.42	-106.51	VE 0.4 l	1.04	-8.11	-59.51
CC 0.4 l	0.60	-15.47	-111.72	VE 0.4 l	1.04	-8.14	-59.60
CC 0.4 l	0.60	-14.84	-110.48	VE 0.4 l	1.05	-8.44	-60.43
CC 0.4 l	0.61	-14.91	-110.24	VE 0.4 l	1.05	-8.25	-59.28
CC 0.4 l	0.62	-14.99	-110.24	VE 0.4 l	1.06	-8.11	-59.64
CC 0.4 l	0.63	-14.91	-110.33	VE 0.4 l	1.06	-8.38	-59.53
CC 0.4 l	0.63	-14.86	-110.52	VE 0.4 l	1.06	-8.44	-59.86
CC 0.4 l	0.64	-14.87	-110.41	VE 0.4 l	1.22	-8.38	-60.29
CC 0.4 l	0.66	-14.68	-109.53	VE 0.4 l	1.43	-8.28	-59.62
CC 0.4 l	0.69	-14.99	-110.81	VE 0.4 l	1.90	-8.18	-59.83
CC 0.4 l	0.75	-15.23	-110.54	VE 0.4 l	2.07	-8.26	-60.07
CC 0.4 l	0.75	-15.25	-111.58	VE 0.4 l	2.09	-8.42	-59.97
CC 0.4 l	0.76	-14.62	-109.50	VE 0.4 l	2.17	-8.29	-59.76

Table S2.2 Continued

Standard Water	Water Volume	δ^{18}O ‰	δ^{2}H ‰	Standard Water	Water Volume	δ^{18}O ‰	δ^{2}H ‰
CC 0.4 l	0.78	-15.32	-111.16	VE 0.4 l	2.17	-8.29	-59.76
CC 0.4 l	0.78	-15.14	-112.08	VE 0.4 l	2.49	-8.20	-60.05
CC 0.4 l	0.79	-15.33	-110.07	VE 0.4 l	2.49	-8.20	-60.05
CC 0.4 l	1.38	-14.73	-110.29	VE 0.4 l	2.69	-8.32	-59.47
CC 0.4 l	3.65	-14.97	-110.77	VE 0.4 l	3.16	-8.34	-59.46
VE 0.4 l	0.03	-8.07	-61.72	VE 0.4 l	3.17	-8.30	-59.64
VE 0.4 l	0.04	-7.63	-60.42	VE 0.4 l	3.17	-8.28	-59.63
VE 0.4 l	0.04	-6.71	-57.88	VE 0.4 l	3.19	-8.28	-59.72
VE 0.4 l	0.05	-5.97	-55.55	CC 0.1 l	0.24	-14.22	-107.35
VE 0.4 l	0.05	-8.31	-54.93	CC 0.1 l	0.38	-14.66	-108.96
VE 0.4 l	0.05	-6.45	-55.53	CC 0.1 l	0.59	-14.83	-110.68
VE 0.4 l	0.07	-8.62	-61.44	CC 0.1 l	0.11	-14.91	-106.88
VE 0.4 l	0.08	-6.99	-59.16	CC 0.1 l	0.57	-15.08	-110.12
VE 0.4 l	0.08	-7.55	-56.79	CC 0.1 l	0.64	-15.11	-110.97
VE 0.4 l	0.08	-6.83	-58.88	CC 0.1 l	1.74	-15.15	-111.38
VE 0.4 l	0.08	-7.47	-56.12	CC 0.1 l	0.57	-15.16	-110.58
VE 0.4 l	0.08	-7.71	-60.82	CC 0.1 l	0.36	-15.17	-109.91
VE 0.4 l	0.09	-7.89	-57.01	CC 0.1 l	0.82	-15.20	-111.11
VE 0.4 l	0.09	-7.10	-58.76	CC 0.1 l	1.09	-15.35	-111.62
VE 0.4 l	0.11	-8.68	-60.97	CC 0.1 l	1.19	-15.34	-111.96
VE 0.4 l	0.11	-8.68	-60.97	CC 0.1 l	1.00	-15.24	-111.64
VE 0.4 l	0.12	-7.71	-57.53	CC 0.1 l	0.19	-15.11	-110.13
VE 0.4 l	0.12	-8.70	-59.88	VE 0.1 l	0.66	-8.28	-60.86
VE 0.4 l	0.12	-8.70	-59.88	VE 0.1 l	0.49	-8.37	-60.50
VE 0.4 l	0.15	-7.44	-59.33	VE 0.1 l	0.49	-8.37	-60.71
VE 0.4 l	0.17	-7.22	-59.43	VE 0.1 l	0.78	-8.44	-60.72
VE 0.4 l	0.17	-7.60	-57.00	VE 0.1 l	0.67	-8.48	-61.29
VE 0.4 l	0.18	-7.61	-60.81	VE 0.1 l	0.37	-8.50	-61.05
VE 0.4 l	0.19	-8.00	-59.80	VE 0.1 l	0.37	-8.50	-61.05
VE 0.4 l	0.19	-8.22	-59.69	VE 0.1 l	0.26	-8.51	-61.72
VE 0.4 l	0.19	-7.46	-60.13	VE 0.1 l	0.12	-8.52	-61.60
VE 0.4 l	0.19	-7.96	-61.00	VE 0.1 l	0.53	-8.52	-60.87
VE 0.4 l	0.19	-7.70	-57.58	VE 0.1 l	0.70	-8.53	-60.35
VE 0.4 l	0.19	-8.10	-59.48	VE 0.1 l	0.26	-8.62	-61.09

Table S2.2 Continued

Standard Water	**Water Volume**	**δ^{18}O ‰**	**δ^{2}H ‰**	**Standard Water**	**Water Volume**	**δ^{18}O ‰**	**δ^{2}H ‰**
VE 0.4 l	0.19	-8.05	-58.17	VE 0.1 l	0.65	-8.64	-60.98
VE 0.4 l	0.19	-7.58	-60.26	VE 0.1 l	1.17	-8.74	-61.83
VE 0.4 l	0.19	-8.05	-60.13	VE 0.1 l	1.04	-8.65	-61.34
VE 0.4 l	0.19	-8.20	-58.56	VE 0.1 l	1.64	-8.47	-61.32
VE 0.4 l	0.19	-7.73	-59.51	VE 0.1 l	1.41	-8.46	-61.11
VE 0.4 l	0.20	-7.92	-58.31	VE 0.1 l	0.19	-8.34	-60.25
VE 0.4 l	0.21	-8.50	-59.00				

Table S2.3. Deviation of injected isotope measurements from standard values. Isotope results are presented relative to V-SMOW.

Water Backgrounds	**δ^{18}O, ‰**	**δ^{2}H, ‰**	**Water Backgrounds**	**δ^{18}O, ‰**	**δ^{2}H, ‰**
VE 50%	-0.1	-0.442	VE	-0.054	-0.664
VE50%	-0.094	-0.811	VE	-0.039	-0.537
VE50%	-0.063	-0.538	VE	0.017	-0.32
VE50%	-0.047	-0.438	VE	0.049	-0.498
VE50%	-0.024	-0.706	VE	0.056	-0.364
CC	-0.084	-0.55	NG a	-0.073	-0.859
CC	-0.02	-0.759	NG a	-0.012	-0.023
CC	-0.004	-0.617	NG a	0.017	0.081
CC	0.025	0.164	NG a	0.042	-0.438
CC	0.091	-0.332	NG a	0.059	-0.683

Supplementary Jupyter script

The Jupyter script here shows how to correct isotope data for water volumes less than 0.8 µl. An explanation of some of these correction parameters can be found in the main text.

```
# The data used and imported here are all raw data, i.e., data that have not been isotope-corrected.
# Correction for low water volume (<0.8 µl) in the Heidelberg FI line
import matplotlib.pyplot as plt
import numpy as np
import csv

# Import data
with open('...', 'r') as csvfile:
r = csv.reader(csvfile, delimiter=',')
data = [i for i in r]
headings = data.pop(0)  # Extract headers
data = np.array([[np.float64(j) for j in i] for i in data])

# Extract data columns
water_amount = data.T[0]
Oraw = data.T[1]
Hraw = data.T[2]

# Create two subplots
fig, axs = plt.subplots(2, 1, figsize=(8, 10))  # Create 2-row, 1-column subplots with defined size

# Plot first subplot - Oraw vs. water_amount (scatter plot)
axs[0].scatter(water_amount, Oraw, label=headings[1], color='blue', alpha=0.7)
axs[0].set_xlabel(headings[0])  # X-axis label
axs[0].set_ylabel(headings[1])  # Y-axis label
axs[0].set_title(f'{headings[1]}␣vs.␣{headings[0]}')  # Title
axs[0].legend()  # Legend
axs[0].grid()  # Add grid

# Plot second subplot - Hraw vs. water_amount (scatter plot)
axs[1].scatter(water_amount, Hraw, label=headings[2], color='green', alpha=0.7)
axs[1].set_xlabel(headings[0])  # X-axis label
axs[1].set_ylabel(headings[2])  # Y-axis label
axs[1].set_title(f'{headings[2]}␣vs.␣{headings[0]}')  # Title
```

```
axs[1].legend()  # Legend
axs[1].grid()  # Add grid

# Adjust layout and display
plt.tight_layout()
plt.show()

# Check data
print(Oraw)
print(Hraw)
print(water_amount)

# Reverse correction (only applicable to corrected data) #
    Correction parameters for a specific period
d18WJZ = (Oraw - 2.04429) / 1.00195
d2HWJZ = (Hraw + 9.94473) / 0.98245

# Input logarithmic function linear fitting parameters
Oslop = 0.00688
Ointercept = -0.40354
Hslop = 0.00363
Hintercept = -0.72665

# Calculate correction factors
Ocorr = (Oslop * d18WJZ + Ointercept) / ((1 / (np.log(
    water_amount)-np.log(0.4)) - Oslop))
Hcorr = (Hslop * d2HWJZ + Hintercept) / ((1 / (np.log(
    water_amount)-np.log(0.4)) - Hslop))

# Absolute value of correction factors
ABSOcorr = abs(Ocorr)
ABSHcorr = abs(Hcorr)

# Check correction factors
print(ABSOcorr)
print(ABSHcorr)

# Linear correction parameters
linearity_d18O = 1.00195  # Linear data
linearity_d2H = 0.98245  # Linear data
intercept_d18O = 2.04429  # Linear data 0.98127
intercept_d2H = -9.94473  # Linear data -9.09120

# Linear correction
```

```
d18O_correct = (d18WJZ - Ocorr) * linearity_d18O +
    intercept_d18O
d2H_correct = (d2HWJZ - Hcorr) * linearity_d2H +
    intercept_d2H

# Final corrected data
print(d18O_correct, d2H_correct)

# Create two subplots
fig, axs = plt.subplots(2, 1, figsize=(8, 12))  # Create 2-
    row, 1-column subplots with defined size

# First subplot - Oraw vs. water_amount and d18O_correct vs.
    water_amount
axs[0].scatter(water_amount, Oraw, label='Original␣' +
    headings[1], color='blue', alpha=0.7)
axs[0].scatter(water_amount, d18O_correct, label='Correct␣' +
     headings[1], color='red', alpha=0.7)
axs[0].set_xlabel(headings[0])  # X-axis label
axs[0].set_ylabel(headings[1])  # Y-axis label
axs[0].set_title(f'{headings[1]}␣Comparison␣(Original␣vs.␣
    Processed)')  # Title
axs[0].legend()  # Legend
axs[0].grid()  # Add grid

# Second subplot - Hraw vs. water_amount and d2H_correct vs.
    water_amount
axs[1].scatter(water_amount, Hraw, label='Original␣' +
    headings[2], color='green', alpha=0.7)
axs[1].scatter(water_amount, d2H_correct, label='Correct␣' +
    headings[2], color='orange', alpha=0.7)
axs[1].set_xlabel(headings[0])  # X-axis label
axs[1].set_ylabel(headings[2])  # Y-axis label
axs[1].set_title(f'{headings[2]}␣Comparison␣(Original␣vs.␣
    Processed)')  # Title
axs[1].legend()  # Legend
axs[1].grid()  # Add grid

# Adjust layout and display
plt.tight_layout()
plt.show()

# Export data
import csv
import os
```

```
def main():
current_dir = os.path.abspath('...')
file_name = os.path.join(current_dir, "output.csv")
csvfile = open(file_name, 'wt', newline='')

writer = csv.writer(csvfile, delimiter=",")
header = ['water', 'd18O_correct', 'd2H_correct']
writer.writerow(header)
writer.writerows(zip(water_amount, d18O_correct, d2H_correct)
    )

csvfile.close()

if __name__ == '__main__':
main()
```

B.2 Supplementary Information for Chapter 3

Supplementary Figures

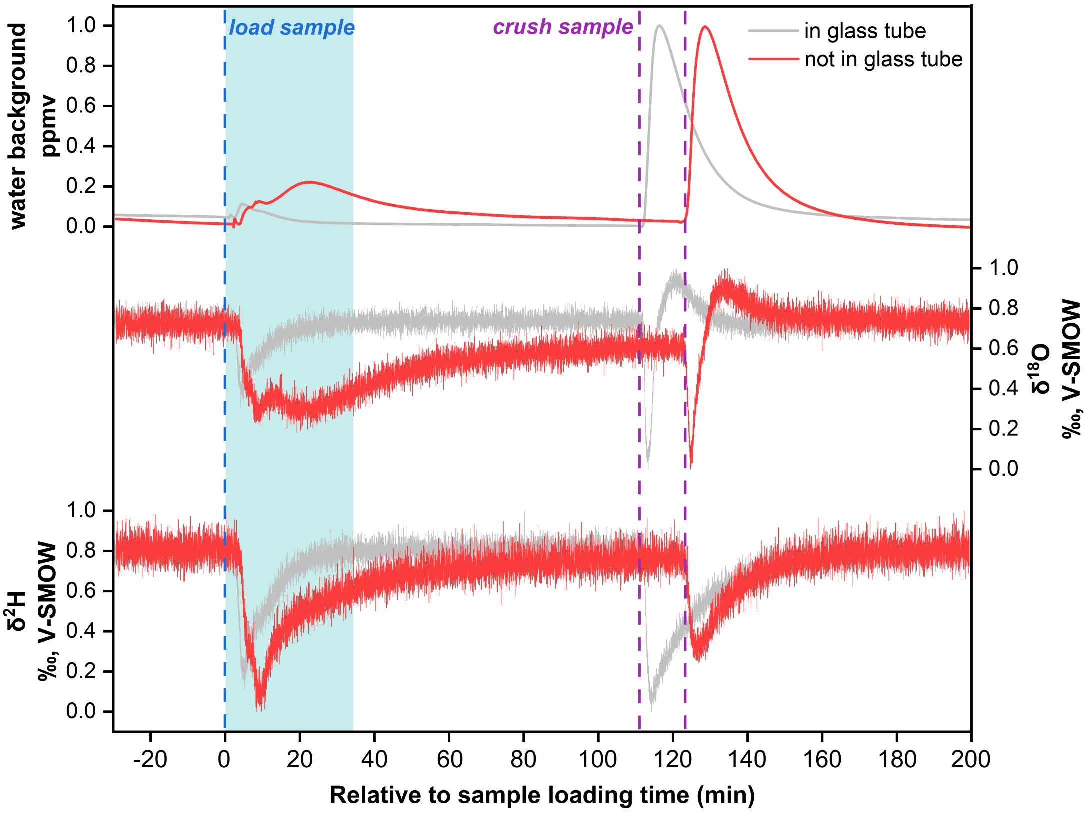

Figure S3.1. Effects of glass tube enclosure on water concentration and isotopic background during sample heating. Variation in water concentration, $\delta^{18}O$ and $\delta^{2}H$ background induced by heating of samples enclosed in glass tube versus not enclosed in glass tube. The grey/red curves indicate coral fragments heated in and out of the glass tube, respectively. With the glass tube, a slight fluctuation in the background was caused by the line opening after loading the samples, and the line background returned to normal after 20-30 minutes. In the case without glass tube, additional perturbations in the water and isotopic backgrounds were caused by the continued evaporation of water from the coral samples, which took longer to stabilise.

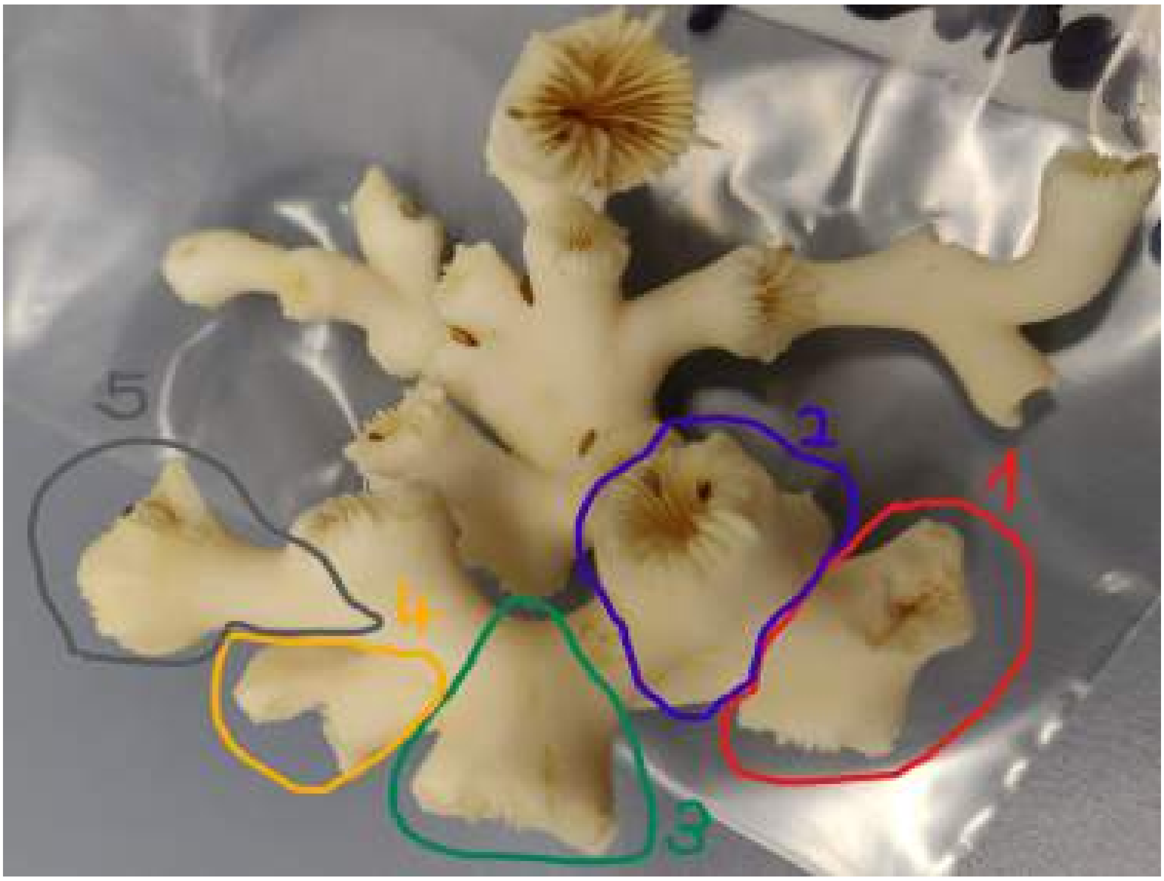

Figure S3.2. Icelandic coral used for heating leading to isotope fractionation experiments. Circles of different colours indicate where different samples were taken.

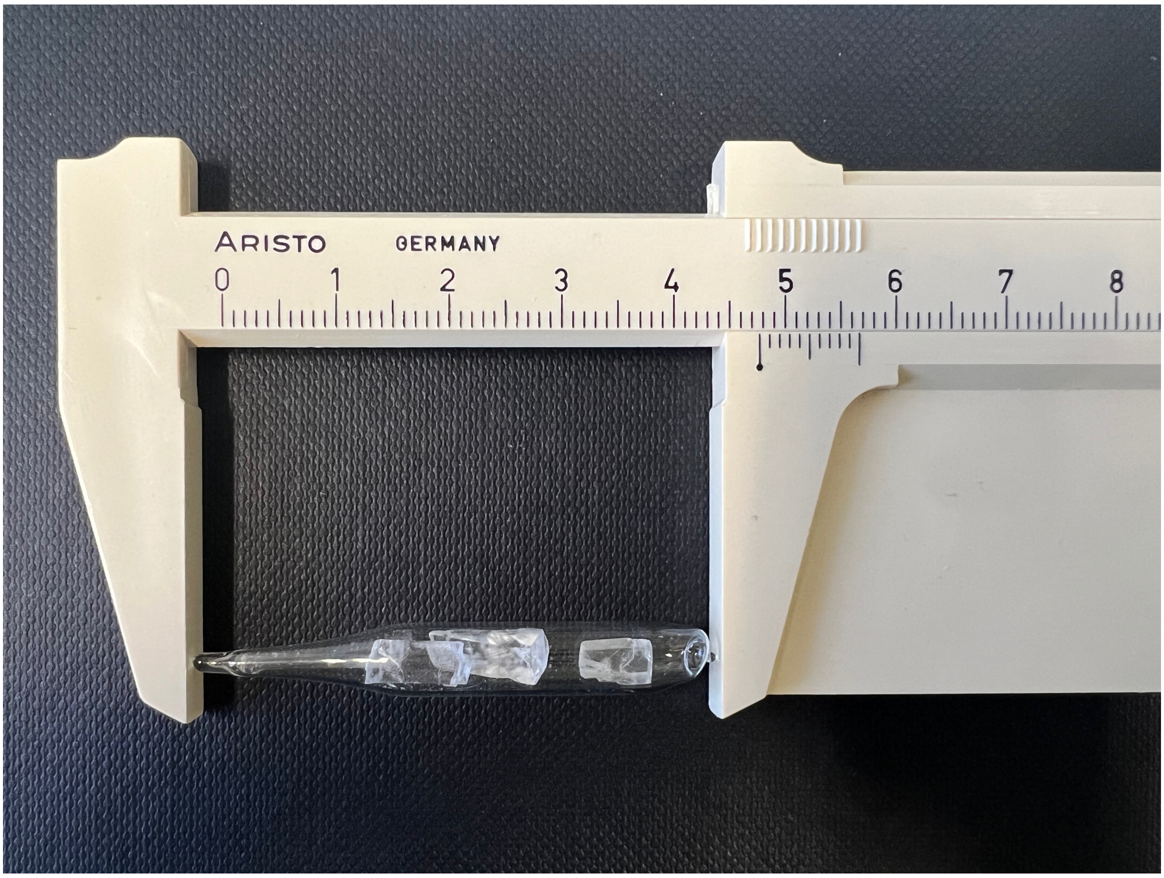

Figure S3.3. The sample was enclosed in a glass tube ready for measurement. The figure shows the black experiment with transparent Iceland spar and small capillary enclosed in glass tube.

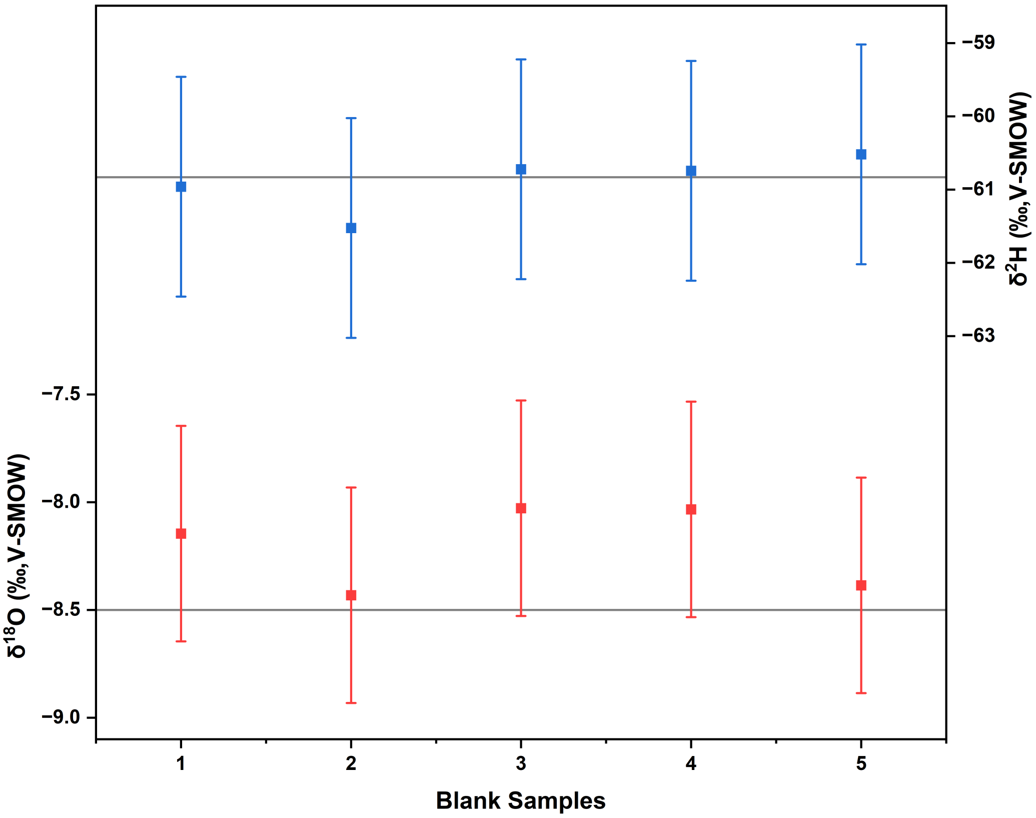

Figure S3.4. Isotope measurements from the blank experiment. The 5 measurements were consistent with the expected values within the error range. The horizontal line in the graph represents the expected value.

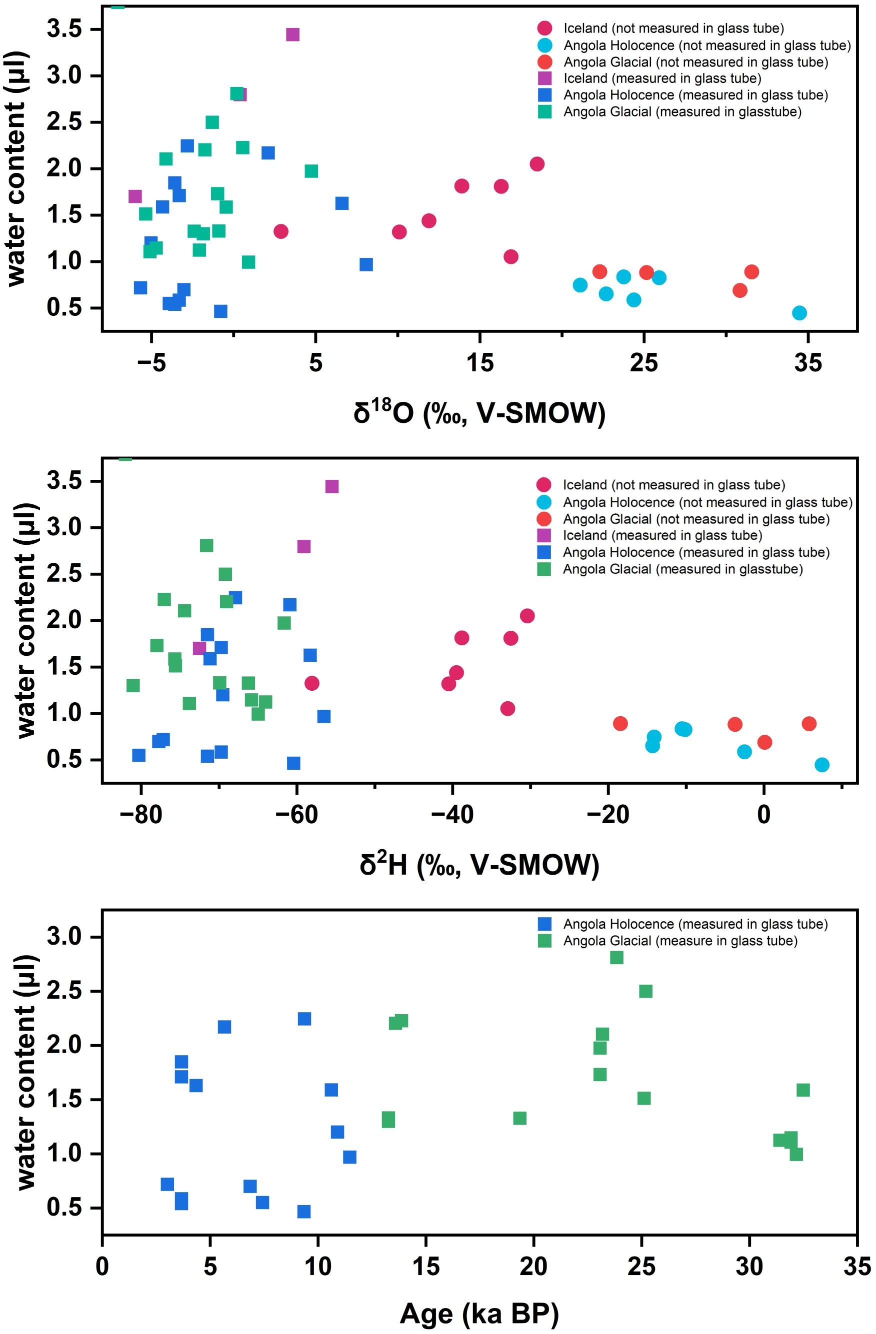

Figure S3.5. Measured water content of coral skeleton in relation to isotopic values and age. (A) The relationship between water content and δ^{18}O values. The circular and square data points indicate samples measured without and in glass tubes, respectively. (B) The relationship between water content and δ^{2}H values. (C) The relationship between water content and coral age (only Angolan glacial and Holocene coral samples measured in glass tubes are shown here).

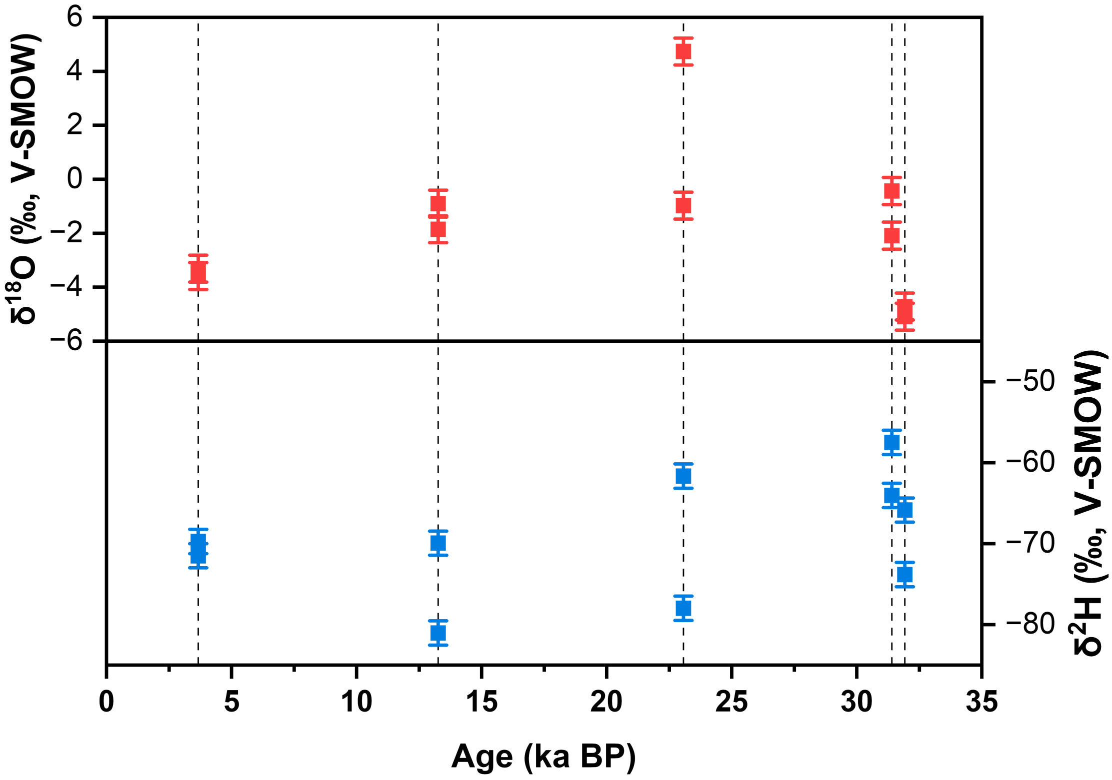

Figure S3.6. Repeated measurements of stable isotopes of skeleton inclusion water of Angolan corals. All samples were enclosed in glass tubes and crushed after being heated at 120°C for approximately 40 minutes.

Supplementary Tables

Table S3.1. Sources and chronological results of coral samples.

Sample source	Lab. No.	GeoB No.	Latitude	Longitude	Depth (m)	Coral species	Age (ka)	Error (ka)
Iceland	/	ICEFI PL500 A3	62°36.493’ N	24°59.190’ W	685	*Desmophyllum pertusum*	0.01	0.01
Angola	IUP-7919	GeoB20933-1	9°49.331’ S	12°46.565’ E	338	*Desmophyllum pertusum*	3.01	0.01
Angola	IUP-10742	GeoB20908-2	9°43.605’ S	12°42.893’ E	439	*Desmophyllum pertusum*	3.33	0.03
Angola	IUP-7920	GeoB20933-1	9°49.331’ S	12°46.566’ E	338	*Desmophyllum pertusum*	3.67	0.01
Angola	IUP-10757	GeoB20908-2	9°43.605’ S	12°42.894’ E	440	*Desmophyllum pertusum*	4.35	0.04
Angola	IUP-10761	GeoB20908-2	9°43.605’ S	12°42.895’ E	441	*Desmophyllum pertusum*	5.66	0.12
Angola	IUP-7922	GeoB20933-1	9°49.331’ S	12°46.567’ E	338	*Desmophyllum pertusum*	6.85	0.02
Angola	IUP-7923	GeoB20933-1	9°49.331’ S	12°46.568’ E	338	*Desmophyllum pertusum*	7.42	0.05
Angola	IUP-7924	GeoB20933-1	9°49.332’ S	12°46.569’ E	338	*Desmophyllum pertusum*	9.35	0.02
Angola	IUP-7925	GeoB20933-1	9°49.331’ S	12°46.568’ E	208.5	*Desmophyllum pertusum*	9.37	0.05
Angola	IUP-7927	GeoB20933-1	9°49.331’ S	12°46.568’ E	273	*Desmophyllum pertusum*	10.62	0.03
Angola	IUP-7929	GeoB20933-1	9°49.331’ S	12°46.568’ E	329.5	*Desmophyllum pertusum*	10.90	0.04
Angola	IUP-7931	GeoB20933-1	9°49.331’ S	12°46.569’ E	338	*Desmophyllum pertusum*	11.46	0.04
Angola	IUP-7932	GeoB20933-1	9°49.331’ S	12°46.570’ E	338	*Desmophyllum pertusum*	13.26	0.04
Angola	IUP-7934	GeoB20933-1	9°49.331’ S	12°46.568’ E	522.5	*Desmophyllum pertusum*	13.59	0.05
Angola	IUP-7935	GeoB20933-1	9°49.331’ S	12°46.571’ E	338	*Desmophyllum pertusum*	13.87	0.04
Angola	IUP-7936	GeoB20933-1	9°49.331’ S	12°46.572’ E	338	*Desmophyllum pertusum*	19.36	0.05
Angola	IUP-7938	GeoB20933-1	9°49.331’ S	12°46.573’ E	338	*Desmophyllum pertusum*	23.07	0.08

Table S3.1 Continued

Sample source	**Lab. No.**	**GeoB No.**	**Latitude**	**Longitude**	**Depth (m)**	**Coral species**	**Age (ka)**	**Error (ka)**
Angola	IUP-7937	GeoB20933-1	9°49.331’ S	12°46.568’ E	630	*Desmophyllum pertusum*	23.18	0.10
Angola	IUP-10727	GeoB20928-1	9°43.388’ S	12°42.900’ E	457	*Desmophyllum pertusum*	23.84	0.05
Angola	IUP-7939	GeoB20933-1	9°49.331’ S	12°46.568’ E	684.5	*Desmophyllum pertusum*	25.11	0.08
Angola	IUP-10728	GeoB20928-1	9°43.388’ S	12°42.901’ E	457	*Desmophyllum pertusum*	25.11	0.06
Angola	IUP-10725	GeoB20928-1	9°43.388’ S	12°42.899’ E	457	*Desmophyllum pertusum*	25.19	0.05
Angola	IUP-10729	GeoB20928-1	9°43.388’ S	12°42.902’ E	457	*Desmophyllum pertusum*	25.31	0.09
Angola	IUP-7942	GeoB20933-1	9°49.331’ S	12°46.568’ E	761	*Desmophyllum pertusum*	31.41	0.10
Angola	IUP-7945	GeoB20933-1	9°49.331’ S	12°46.568’ E	834.5	*Desmophyllum pertusum*	31.92	0.09
Angola	IUP-7946	GeoB20933-1	9°49.331’ S	12°46.574’ E	338	*Desmophyllum pertusum*	32.17	0.14
Angola	IUP-7947	GeoB20933-1	9°49.331’ S	12°46.575’ E	338	*Desmophyllum pertusum*	32.49	0.07
Angola	IUP-7948	GeoB20933-1	9°49.331’ S	12°46.568’ E	916	*Desmophyllum pertusum*	32.72	0.15

Table S3.2. Result of isotope fractionation experiments with different heating times in Iceland cold water corals.

Sample ID	Heating time (min)	Weight (g)	Water (µl)	Water content (µl/g)	δ^{18}O ‰ V-SMOW	Error	δ^{2}H ‰ V-SMOW	Error	Note
ICEFI1.1	30	0.78	1.33	1.70	-6.00	0.50	-72.51	1.50	in glass tube
ICEFI3.1	110	0.72	2.48	3.44	3.60	0.50	-55.50	1.50	in glass tube
ICEFI4	80	0.79	2.21	2.80	0.40	0.50	-59.10	1.50	in glass tube
ICEFI1	68	1.07	1.54	1.44	11.90	0.50	-39.50	1.50	not in glass tube
ICEFI5.1	84	0.57	0.64	1.12	16.90	0.50	-32.90	1.50	not in glass tube
ICEFI2.1	98	1.16	1.53	1.32	10.10	0.50	-40.50	1.50	not in glass tube
ICEFI5.2	109	0.59	1.07	1.81	13.90	0.50	-38.80	1.50	not in glass tube
ICEFI2.2	120	1.00	1.81	1.81	16.30	0.50	-32.50	1.50	not in glass tube
ICEFI3.2	150	1.00	2.05	2.05	18.50	0.50	-30.40	1.50	not in glass tube
ICEFI1.2	30	0.80	1.06	1.33	2.89	0.50	-58.07	1.50	not in glass tube

Table S3.3. Sources and chronological results of coral samples. The Y in the notes indicates that the sample is measured in the glass tube, and N indicates that it is not measured in the glass tube.

Lab. No.	GeoB No.	Heating time (min)	weight (g)	water (µl)	water content (µl/g)	δ^{18}O ‰ V-SMOW	Error	δ^{2}H ‰ V-SMOW	Error	Note
IUP-7919	GeoB20933-1	40	0.58	0.81	1.39	-5.67	0.50	-77.17	1.50	Y
IUP-7920	GeoB20933-1	60	0.67	1.15	1.71	-3.32	0.50	-69.73	1.50	Y
IUP-7920	GeoB20933-1	40	0.43	0.80	1.85	-3.59	0.50	-71.49	1.50	Y
IUP-10757	GeoB20908-2	100	0.70	1.14	1.63	6.60	0.50	-58.30	1.50	Y
IUP-10761	GeoB20908-2	80	0.76	1.65	2.17	2.10	0.50	-60.90	1.50	Y
IUP-7922	GeoB20933-1	40	0.61	0.87	1.43	-3.03	0.50	-77.75	1.50	Y
IUP-7923	GeoB20933-1	60	0.50	0.91	1.82	-3.92	0.50	-80.31	1.50	Y
IUP-7925	GeoB20933-1	30	0.59	1.33	0.45	-2.83	0.50	-67.89	1.50	Y
IUP-7927	GeoB20933-1	33	0.75	1.19	0.63	-4.33	0.50	-71.17	1.50	Y
IUP-7929	GeoB20933-1	31	0.71	0.85	0.83	-5.04	0.50	-69.52	1.50	Y
IUP-7934	GeoB20933-1	33	0.51	1.12	0.45	-1.76	0.50	-69.05	1.50	Y
IUP-7937	GeoB20933-1	30	0.43	0.91	0.48	-4.13	0.50	-74.44	1.50	Y
IUP-7939	GeoB20933-1	32	0.49	0.74	0.66	-5.36	0.50	-75.61	1.50	Y
IUP-7942	GeoB20933-1	48	0.41	0.60	0.68	-0.44	0.50	-57.49	1.50	Y
IUP-7942	GeoB20933-1	36	0.40	0.45	0.89	-2.09	0.50	-64.04	1.50	Y
IUP-7945	GeoB20933-1	31	0.43	0.48	0.90	-5.09	0.50	-73.82	1.50	Y
IUP-7945	GeoB20933-1	31	0.41	0.47	0.87	-4.72	0.50	-65.85	1.50	Y

Table S3.3 Continued

Lab. No.	**GeoB No.**	**Heating time (min)**	**weight (g)**	**water (µl)**	**water content (µl/g)**	**δ^{18}O ‰ V-SMOW**	**Error**	**δ^{2}H ‰ V-SMOW**	**Error**	**Note**
IUP-7948	GeoB20933-1	33	0.57	2.16	0.26	-7.06	0.50	-82.04	1.50	Y
IUP-7924	GeoB20933-1	40	0.78	1.68	2.15	-0.79	0.50	-60.42	1.50	Y
IUP-7931	GeoB20933-1	40	0.71	0.73	1.03	8.08	0.50	-57.92	1.50	Y
IUP-7932	GeoB20933-1	40	0.59	0.79	1.33	-0.90	0.50	-69.94	1.50	Y
IUP-7932	GeoB20933-1	50	0.58	0.75	1.30	-1.85	0.50	-81.04	1.50	Y
IUP-7935	GeoB20933-1	40	0.54	1.20	2.23	0.55	0.50	-77.04	1.50	Y
IUP-7936	GeoB20933-1	40	0.74	0.98	1.33	-2.41	0.50	-66.24	1.50	Y
IUP-7938	GeoB20933-1	40	0.58	1.00	1.73	-0.98	0.50	-77.99	1.50	Y
IUP-7938	GeoB20933-1	40	0.60	1.19	1.98	4.73	0.50	-61.65	1.50	Y
IUP-10727	GeoB20928-1	60	0.79	2.22	2.81	0.20	0.50	-71.60	1.50	Y
IUP-10725	GeoB20928-1	80	0.96	2.40	2.50	-1.30	0.50	-69.20	1.50	Y
IUP-7946	GeoB20933-1	50	0.55	0.55	0.99	0.91	0.50	-64.97	1.50	Y
IUP-7947	GeoB20933-1	40	0.57	0.91	1.59	-0.46	0.50	-75.69	1.50	Y
IUP-10742	GeoB20908-2	130	0.80	0.67	0.84	23.76	0.50	-10.51	1.50	N
IUP-10742	GeoB20908-2	90	0.81	0.67	0.83	25.93	0.50	-10.15	1.50	N
IUP-10757	GeoB20908-2	120	0.55	0.25	0.45	34.48	0.50	7.46	1.50	N
IUP-10757	GeoB20908-2	130	0.90	0.53	0.59	24.39	0.50	-2.51	1.50	N
IUP-10761	GeoB20908-2	100	0.79	0.59	0.75	21.12	0.50	-14.10	1.50	N
IUP-10761	GeoB20908-2	90	0.80	0.52	0.65	22.70	0.50	-14.31	1.50	N

Table S3.3 Continued

Lab. No.	**GeoB No.**	**Heating time (min)**	**weight (g)**	**water (µl)**	**water content (µl/g)**	**δ^{18}O ‰ V-SMOW**	**Error**	**δ^{2}H ‰ V-SMOW**	**Error**	**Note**
IUP-10725	GeoB20928-1	180	0.76	0.52	0.69	30.85	0.50	0.12	1.50	N
IUP-10725	GeoB20928-1	330	0.78	0.69	0.89	31.56	0.50	5.82	1.50	N
IUP-10727	GeoB20928-1	70	0.68	0.61	0.89	22.31	0.50	-18.43	1.50	N
IUP-10728	GeoB20928-1	110	0.55	0.30	0.54	42.83	0.50	20.85	1.50	N
IUP-10729	GeoB20928-1	200	0.62	0.55	0.88	25.16	0.50	-3.72	1.50	N

Table S3.4. Isotopic results of coral skeleton inclusions from immersion experiment. The detailed explanation of the label in the immersion experiment can be found in section 2.2.4. The error of the isotope measurement is 0.5‰ for δ^{18}O and 1.5‰ for δ^{2}H.

Label	**GeoB Nr.**	**coral Nr.**	**Weight (g)**	**Water content (µl/g)**	**Heating time (min)**	**δ^{18}O ‰ V-SMOW**	**δ^{2}H ‰ V-SMOW**	**Immersion time in seawater (hr)**	**Drying time after immersion (hr)**
NimA	GeoB20917-1	IUP-ROV-2b	0.58	2.00	36	-2.04	-61.22	/	/
NimB	GeoB20951-1	IUP-Rov Bulk	0.36	1.92	46	-7.34	-80.73	/	/
NimC	GeoB20933-1	IUP-7927	0.75	1.59	33	-4.33	-71.17	/	/
imA	GeoB20917-1	IUP-ROV-2b	0.55	2.37	31	0.70	-33.27	117	23
imB	GeoB20951-1	IUP-Rov Bulk	0.53	1.99	33	-0.21	-54.42	117	23
imC1	GeoB20933-1	IUP-7927	0.69	1.47	33	6.82	-24.09	117	23
imC2	GeoB20933-1	IUP-7927	0.60	0.77	30	13.11	9.68	815	164

B.3 Supplementary Information for Chapter 4

Supplementary Figures

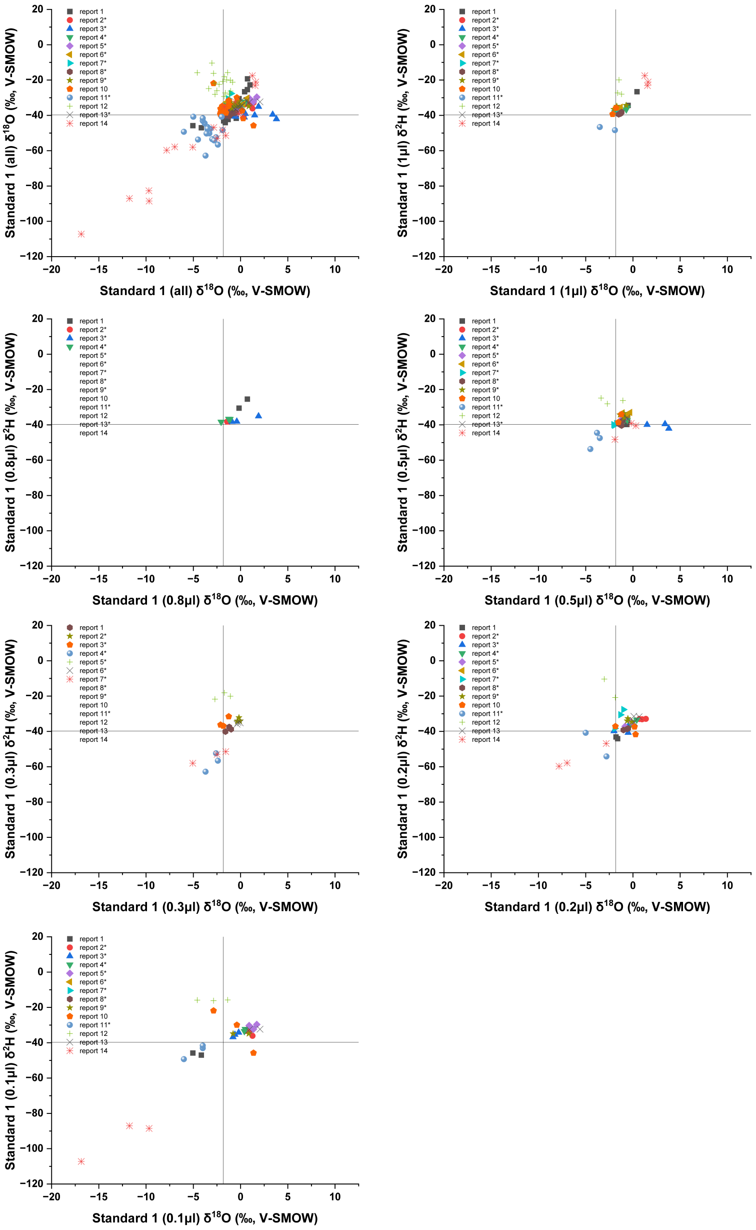

Figure S4.1. The δ^{18}O and δ^{2}H measurements of standard water 1 in each report. The * denotes reports where Iceland spar was crushed together with capillaries. Solid lines indicate δ^{18}O and δ^{2}H values for standard water.

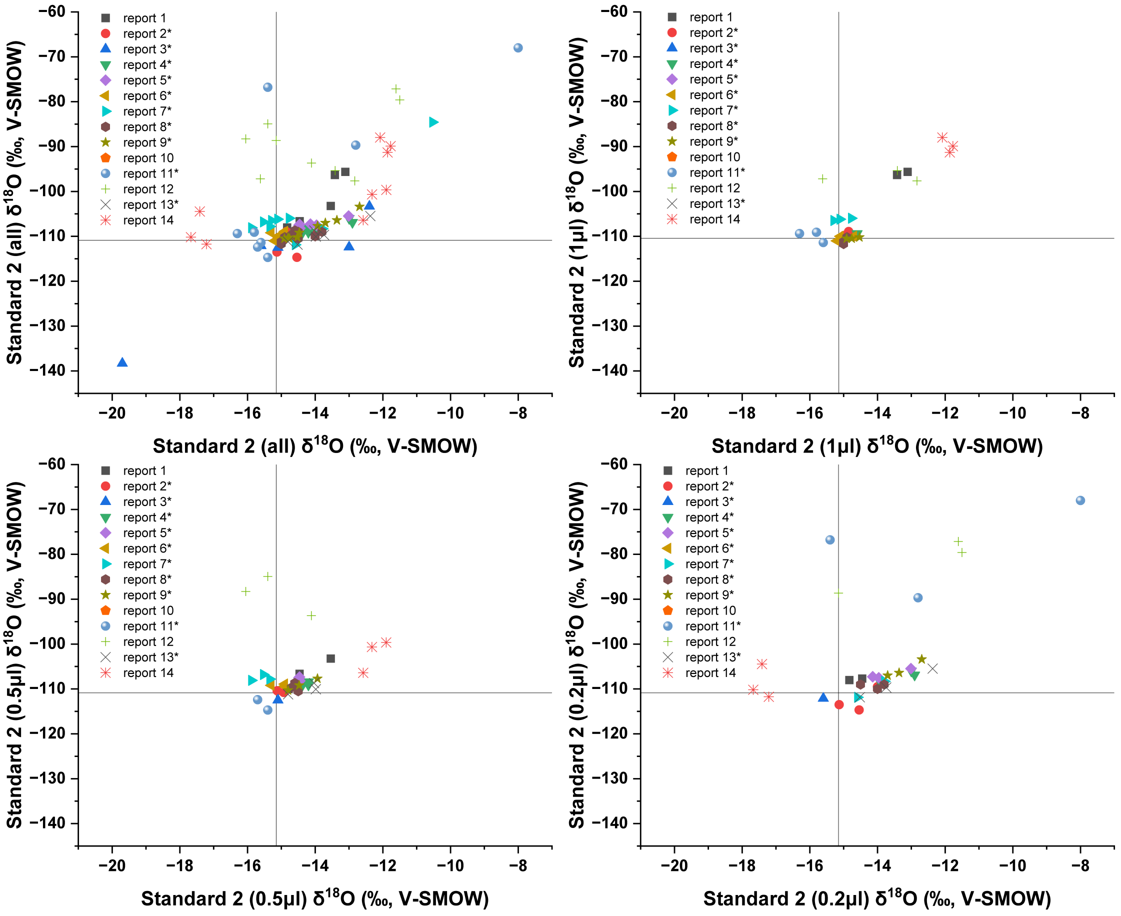

Figure S4.2. The δ^{18}O and δ^{2}H measurements of standard water 2 in each report. The * denotes reports where Iceland spar was crushed together with capillaries. Solid lines indicate δ^{18}O and δ^{2}H values for standard water.

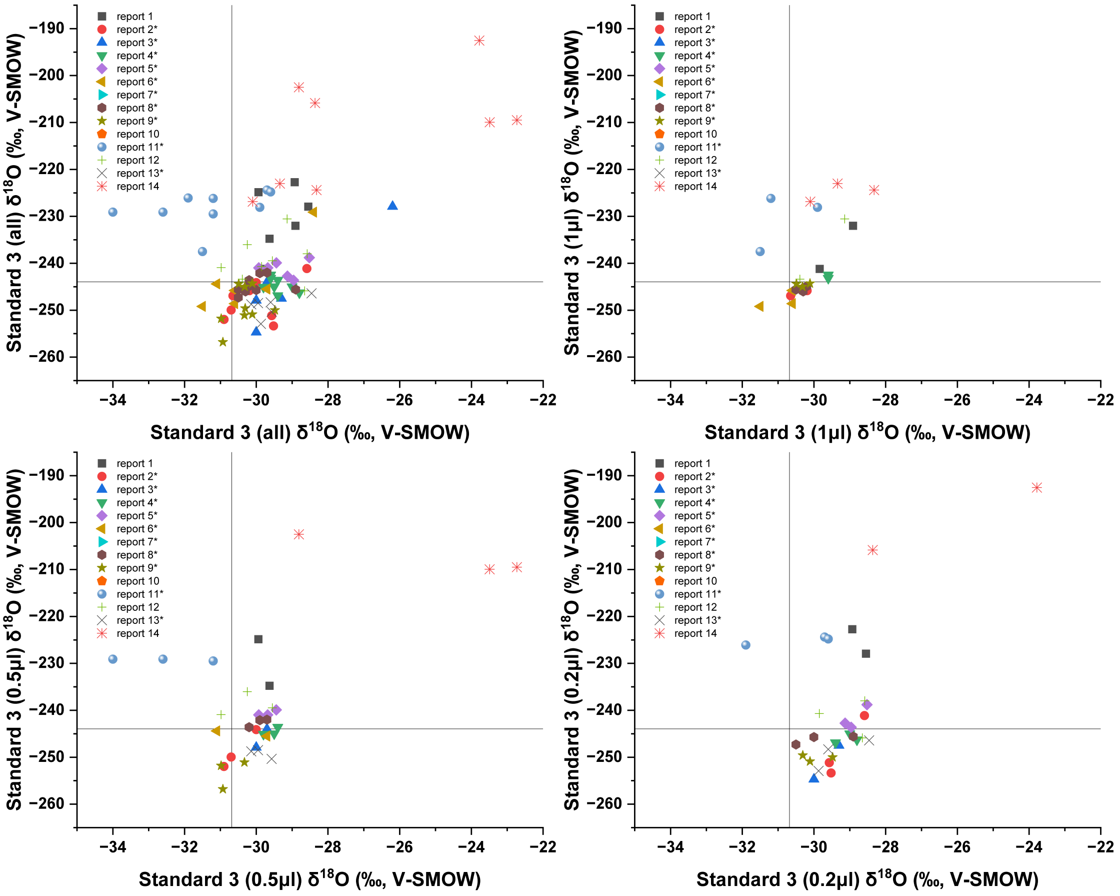

Figure S4.3. The δ^{18}O and δ^{2}H measurements of standard water 3 in each report. The * denotes reports where Iceland spar was crushed together with capillaries. Solid lines indicate δ^{18}O and δ^{2}H values for standard water.

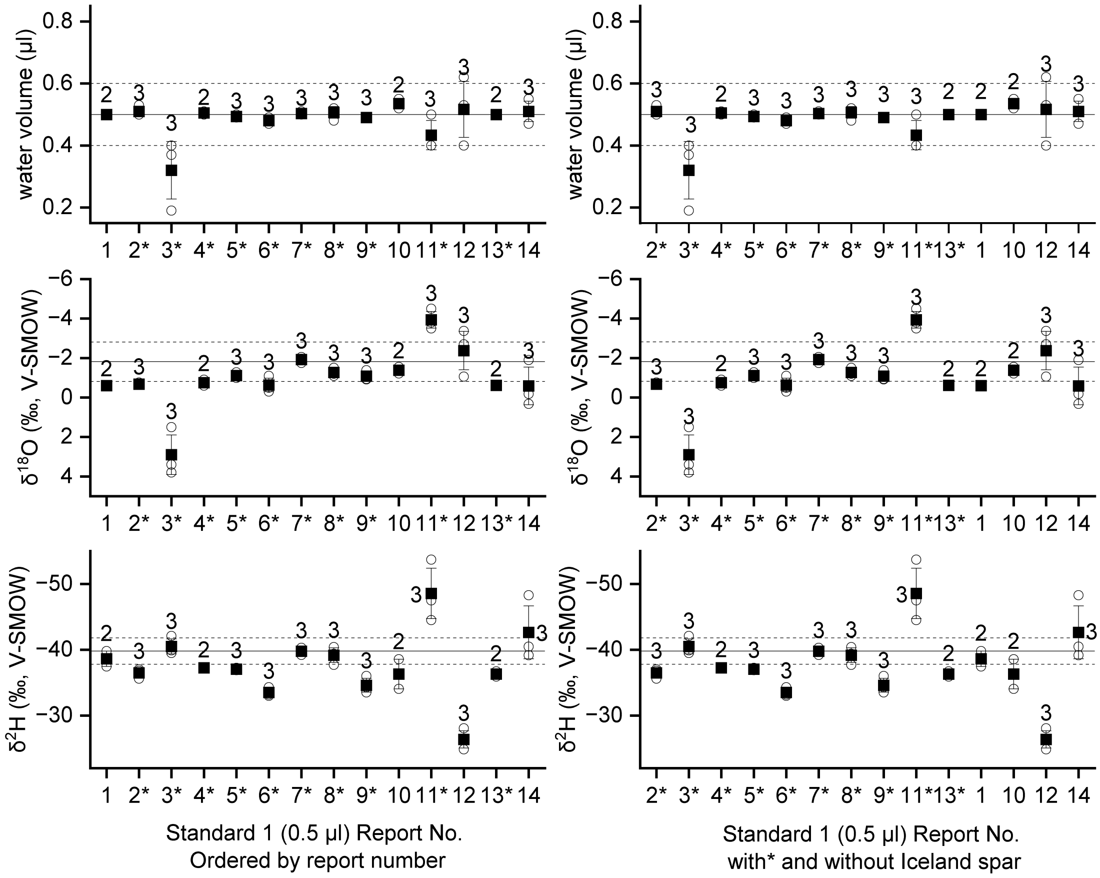

Figure S4.4. Mean values and SD (1σ) for water volume and isotope measurements of 0.5 µl standard water 1 from various reports. The left side is organized by report number, while the right side is arranged by whether the capillary tube is crushed together with the Iceland spar. The hollow dots indicate individual measurement data. The * denotes reports where Iceland spar was crushed together with capillaries. The dotted lines indicate ±0.1 µl of filled water volume, ±1‰ for δ^{18}O and ±2‰ for δ^{2}H respectively.

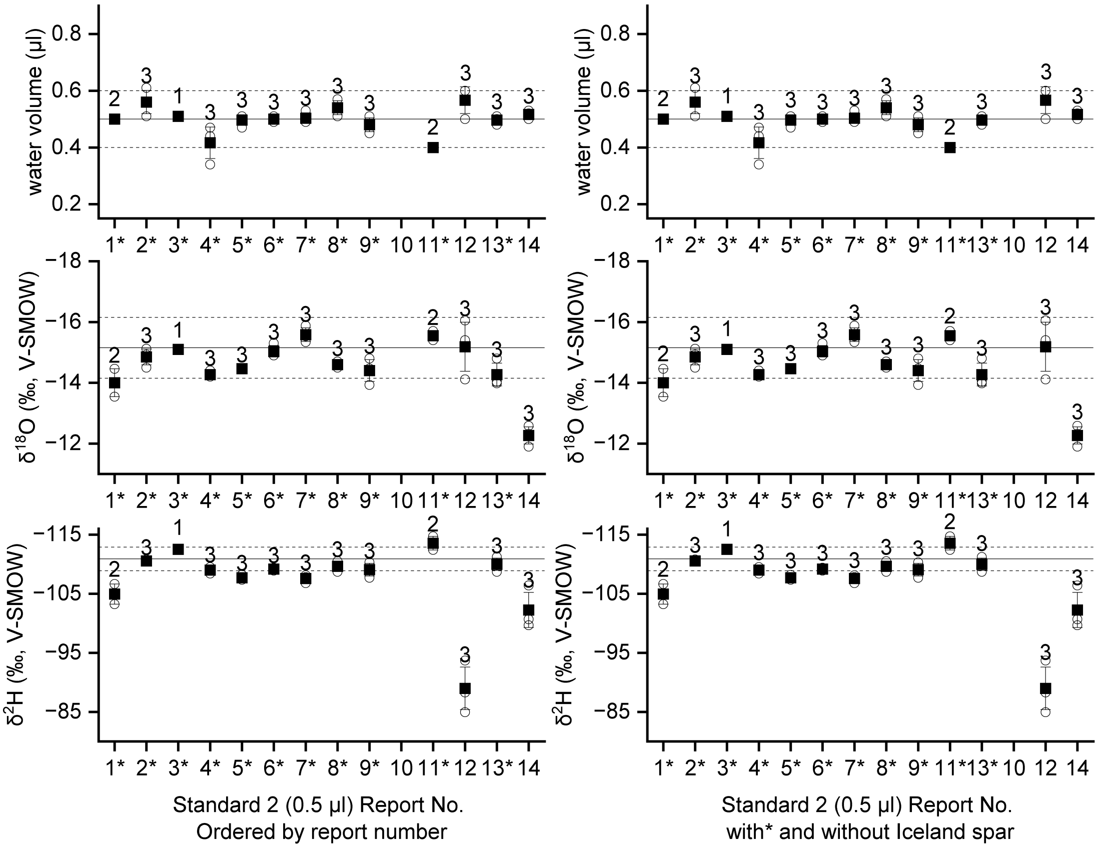

Figure S4.5. Mean values and SD (1σ) for water volume and isotope measurements of 0.5 µl standard water 2 from various reports. The left side is organized by report number, while the right side is arranged by whether the capillary tube is crushed together with the Iceland spar. The hollow dots indicate individual measurement data. The * denotes reports where Iceland spar was crushed together with capillaries. The dotted lines indicate ±0.1 µl of filled water volume, ±1‰ for δ^{18}O and ±2‰ for δ^{2}H respectively.

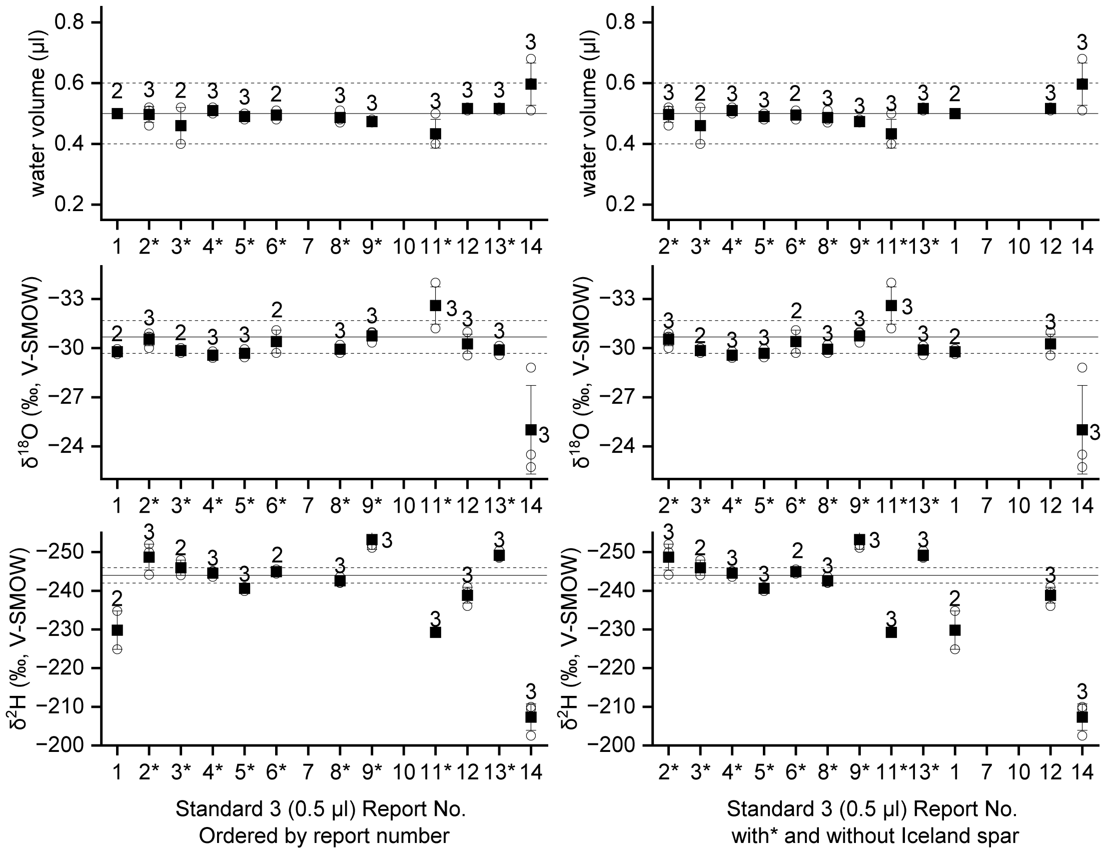

Figure S4.6. Mean values and SD (1σ) for water volume and isotope measurements of 0.5 µl standard water 3 from various reports. The left side is organized by report number, while the right side is arranged by whether the capillary tube is crushed together with the Iceland spar. The hollow dots indicate individual measurement data. The * denotes reports where Iceland spar was crushed together with capillaries. The dotted lines indicate ±0.1 µl of filled water volume, ±1‰ for δ^{18}O and ±2‰ for δ^{2}H respectively.

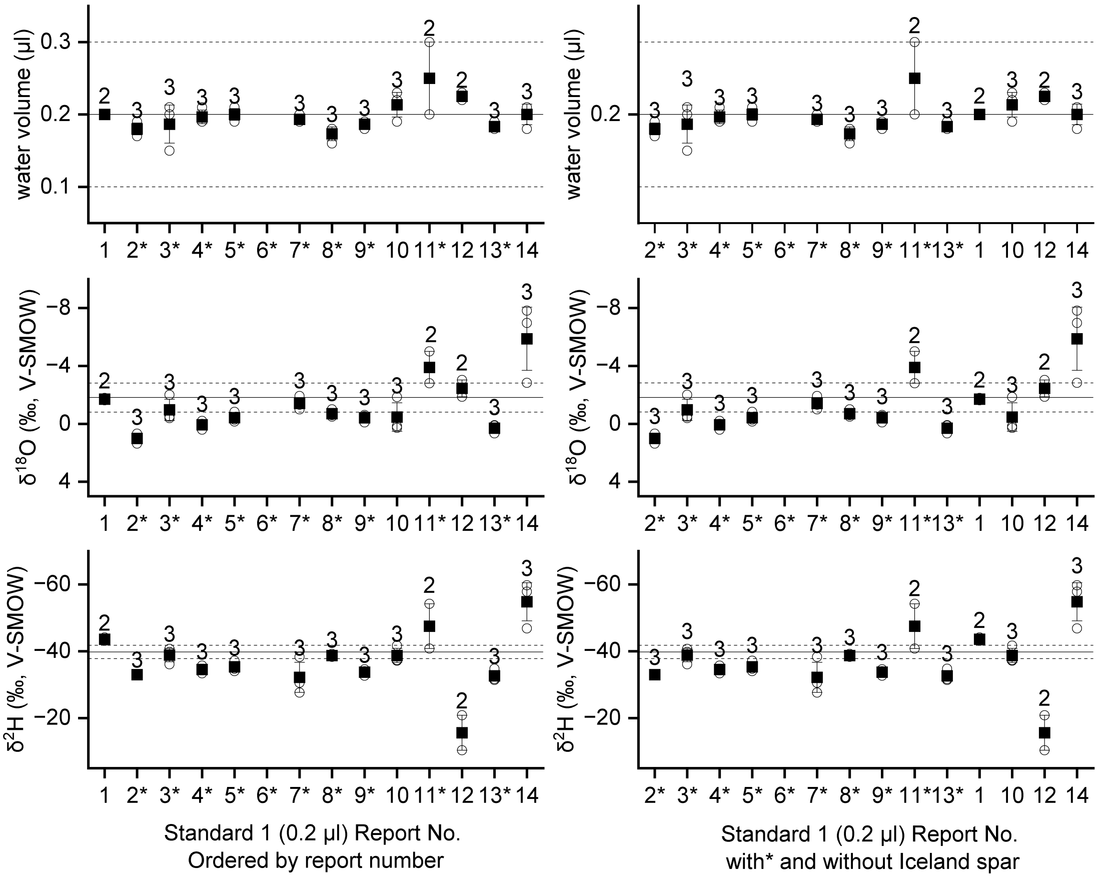

Figure S4.7. Mean values and SD (1σ) for water volume and isotope measurements of 0.2 µl standard water 1 from various reports. The left side is organized by report number, while the right side is arranged by whether the capillary tube is crushed together with the Iceland spar. The hollow dots indicate individual measurement data. The * denotes reports where Iceland spar was crushed together with capillaries. The dotted lines indicate ±0.1 µl of filled water volume, ±1‰ for δ^{18}O and ±2‰ for δ^{2}H respectively.

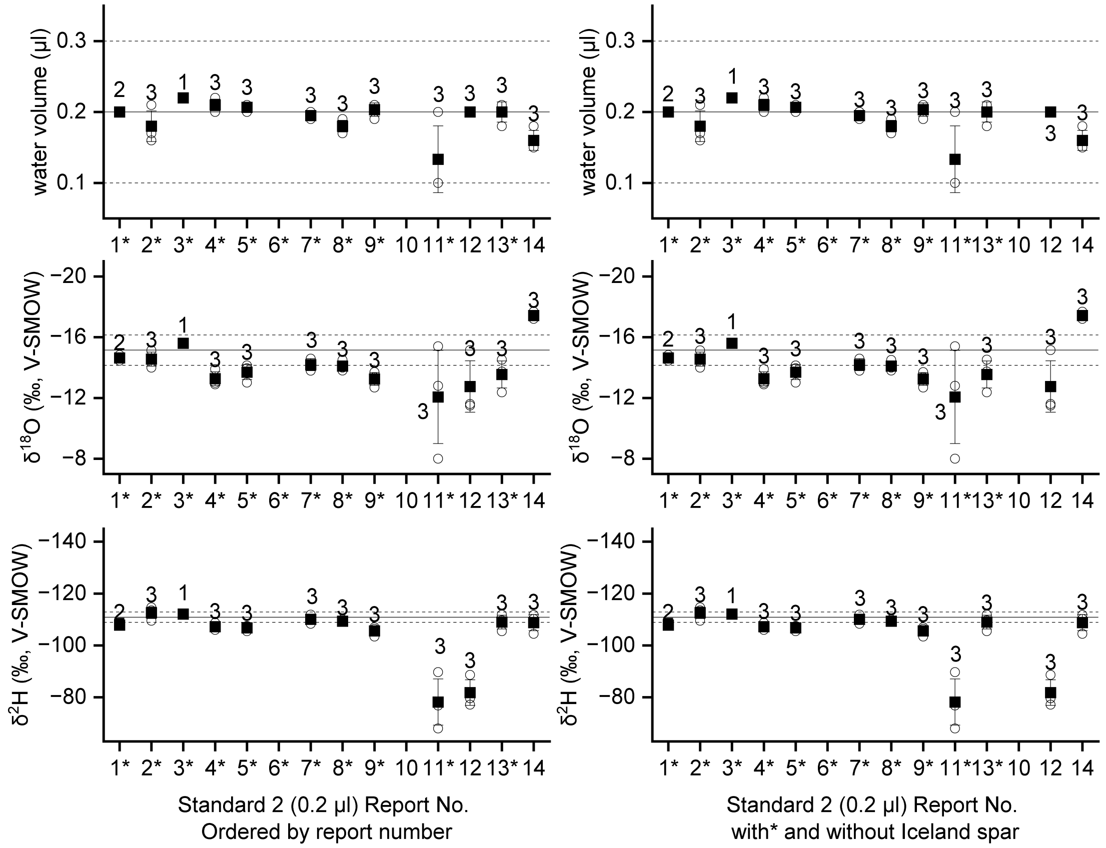

Figure S4.8. Mean values and SD (1σ) for water volume and isotope measurements of 0.2 µl standard water 2 from various reports. The left side is organized by report number, while the right side is arranged by whether the capillary tube is crushed together with the Iceland spar. The hollow dots indicate individual measurement data. The * denotes reports where Iceland spar was crushed together with capillaries. The dotted lines indicate ±0.1 µl of filled water volume, ±1‰ for δ^{18}O and ±2‰ for δ^{2}H respectively.

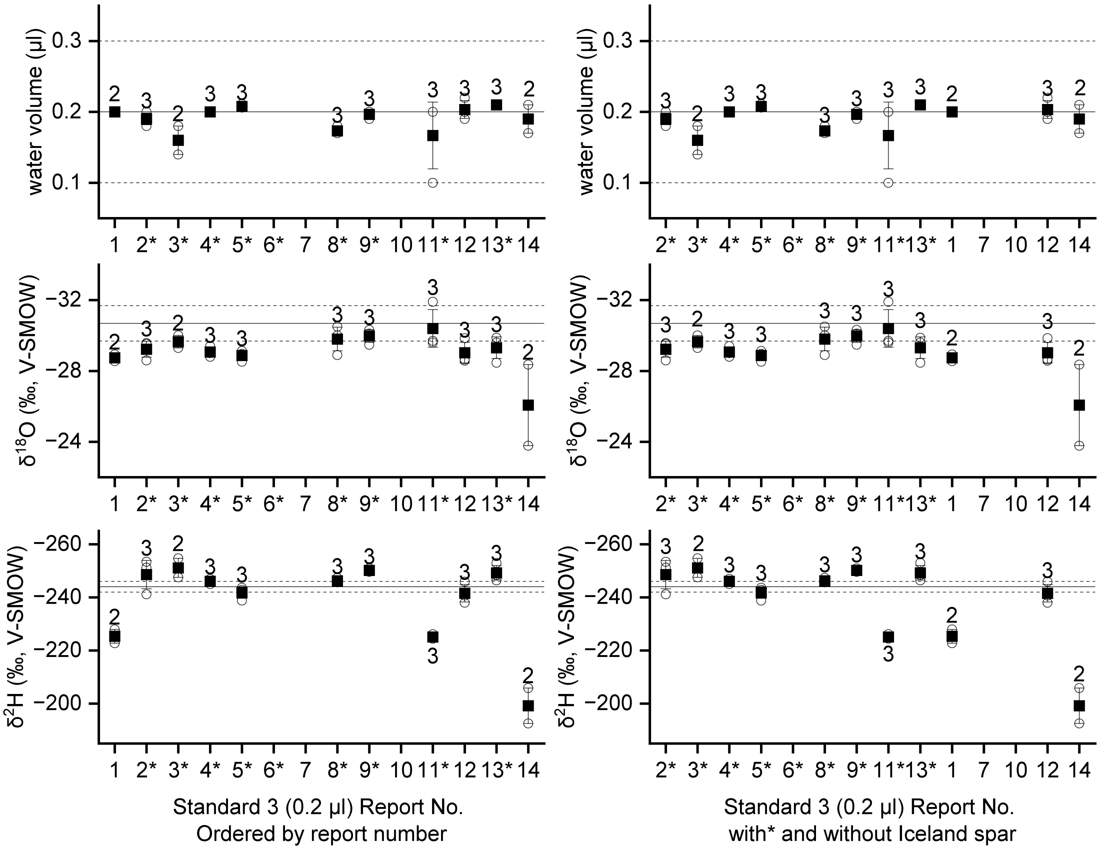

Figure S4.9. Mean values and SD (1σ) for water volume and isotope measurements of 0.2 µl standard water 3 from various reports. The left side is organized by report number, while the right side is arranged by whether the capillary tube is crushed together with the Iceland spar. The hollow dots indicate individual measurement data. The * denotes reports where Iceland spar was crushed together with capillaries. The dotted lines indicate ±0.1 µl of filled water volume, ±1‰ for δ^{18}O and ±2‰ for δ^{2}H respectively.

B.4 Supplementary Information for Chapter 5

Supplementary Figures

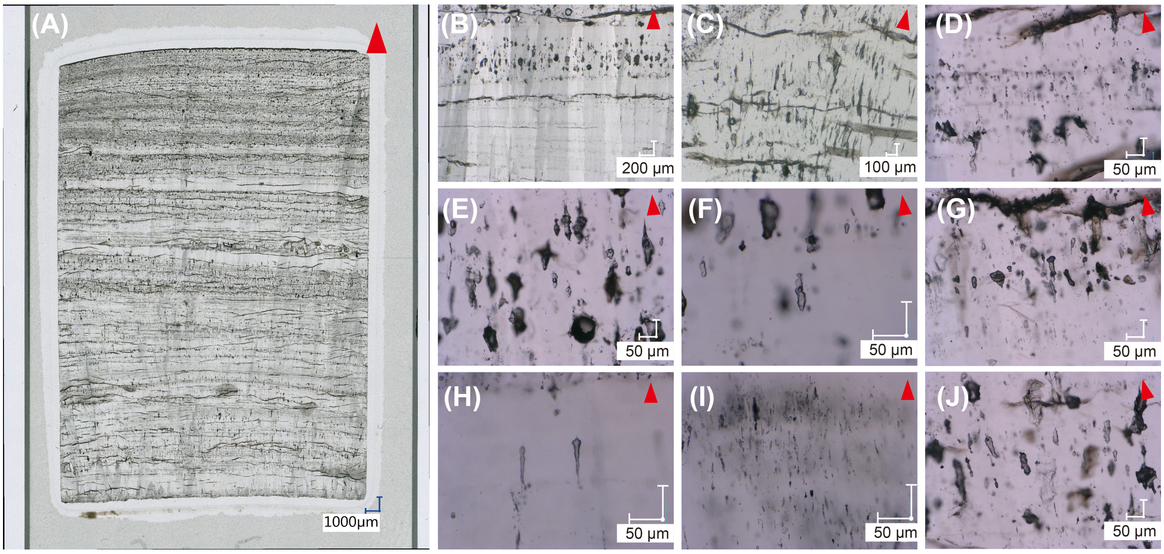

Figure S5.1. Transmitted light photographs of polished thin sections of stalagmite FL2. Petrographic images show the typical shapes and distribution of fluid inclusions at different depths within the FL2 stalagmite. Numerous small and elongated fluid inclusions are dispersed throughout the stalagmite. (A) Images of the entire thin section of the FL2 stalagmite (350-380 mm), depicting the calcite structure of the stalagmite. (B-J) High-magnification micrographs of stalagmites at different depths show various forms of inclusions. Red arrows indicate the direction of stalagmite growth.

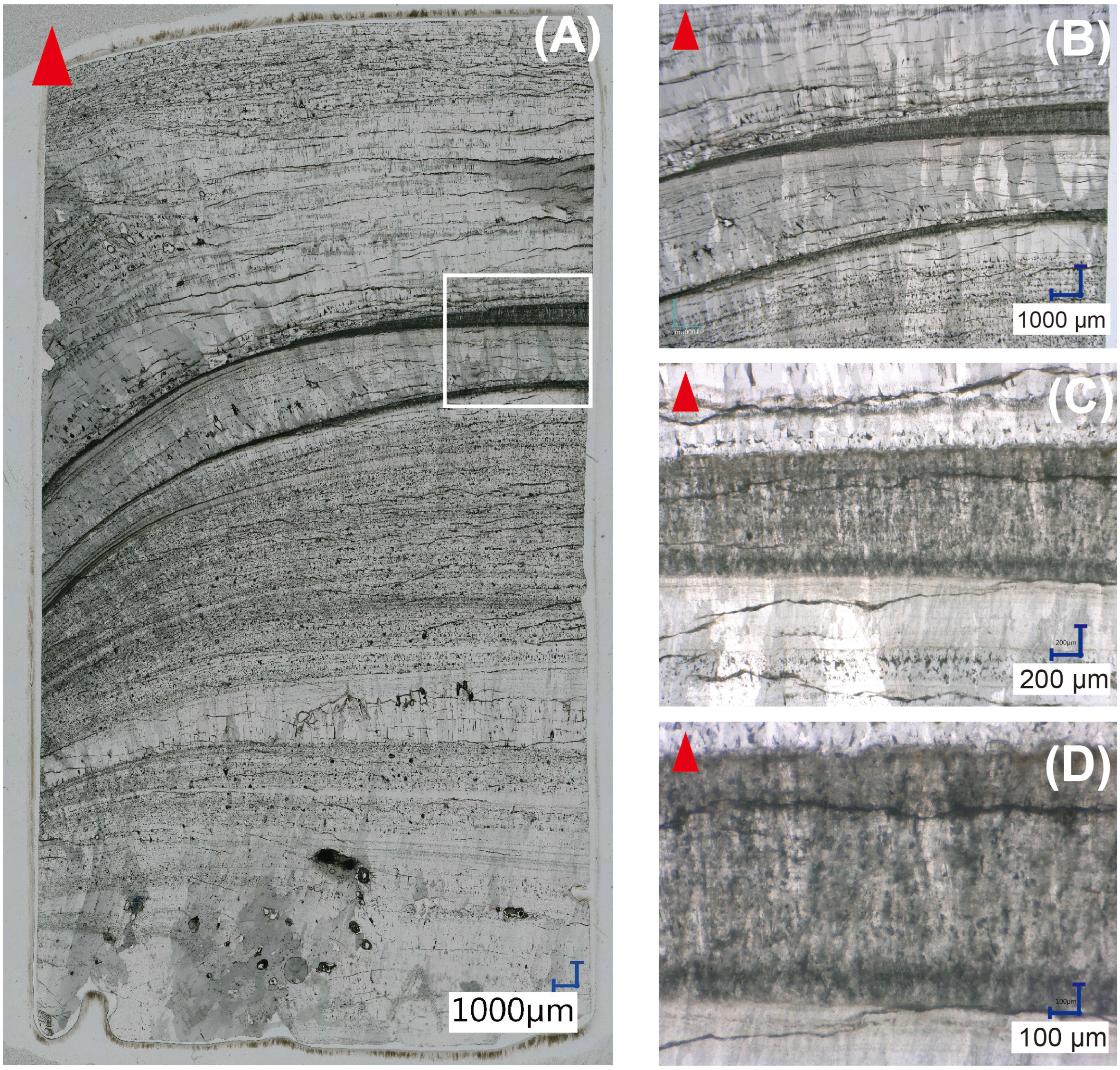

Figure S5.2. Transmitted light photographs of polished thin sections of stalagmite FL2. (A) The distinct dark layer appears 13mm from the top of the stalagmite, corresponding to a $\delta^{18}O_{FI}$ positive anomaly event (amplitudes exceeding 7‰) around 950-1150 CE. (B-D) The thin section images about 13mm of the stalagmite are enlarging of the dark layer in (A).

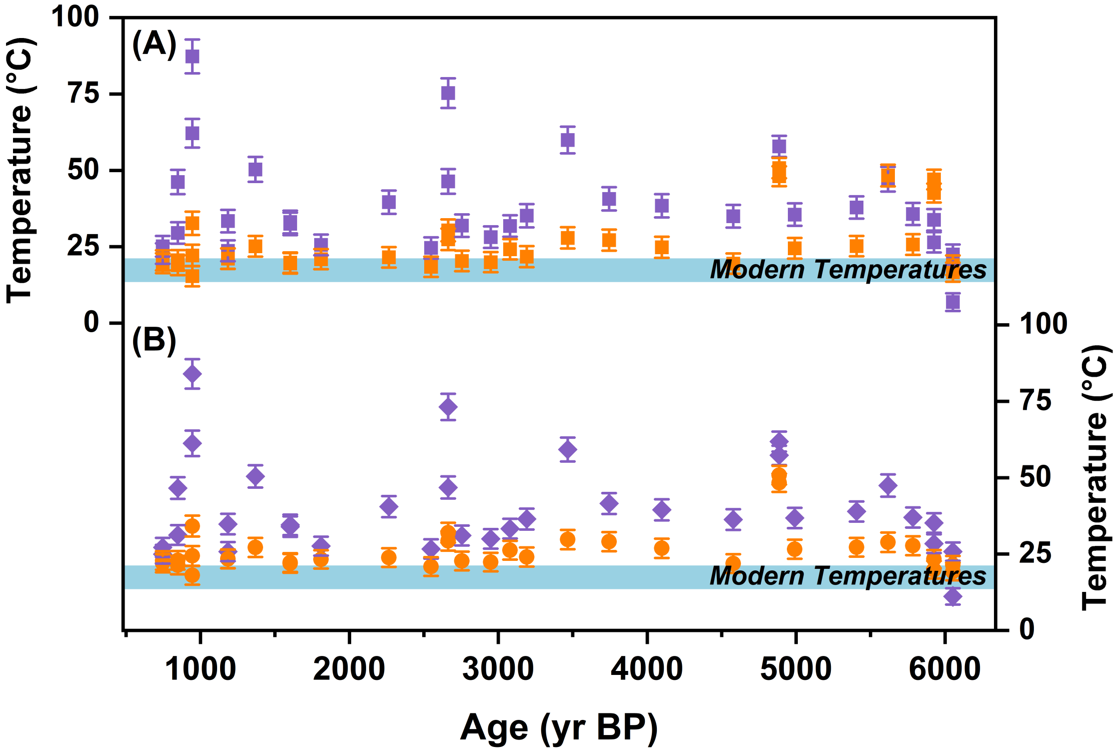

Figure S5.3. Palaeotemperature calculations based on isotopic values of FL2 stalagmite inclusions water and calcite. (A) Calculation of palaeotemperatures based on the empirical equations of Tremaine et al. (2011) (A) and Daëron et al. (2019) (B). The violet points indicate the temperature results calculated using $\delta^{18}O_{FI}$ and $\delta^{18}Os$. The orange indicates the temperature results calculated using $\delta^{18}O_{FI}$ (using $\delta^{2}H_{FI}$ and LMWL inversion) and $\delta^{18}Os$.

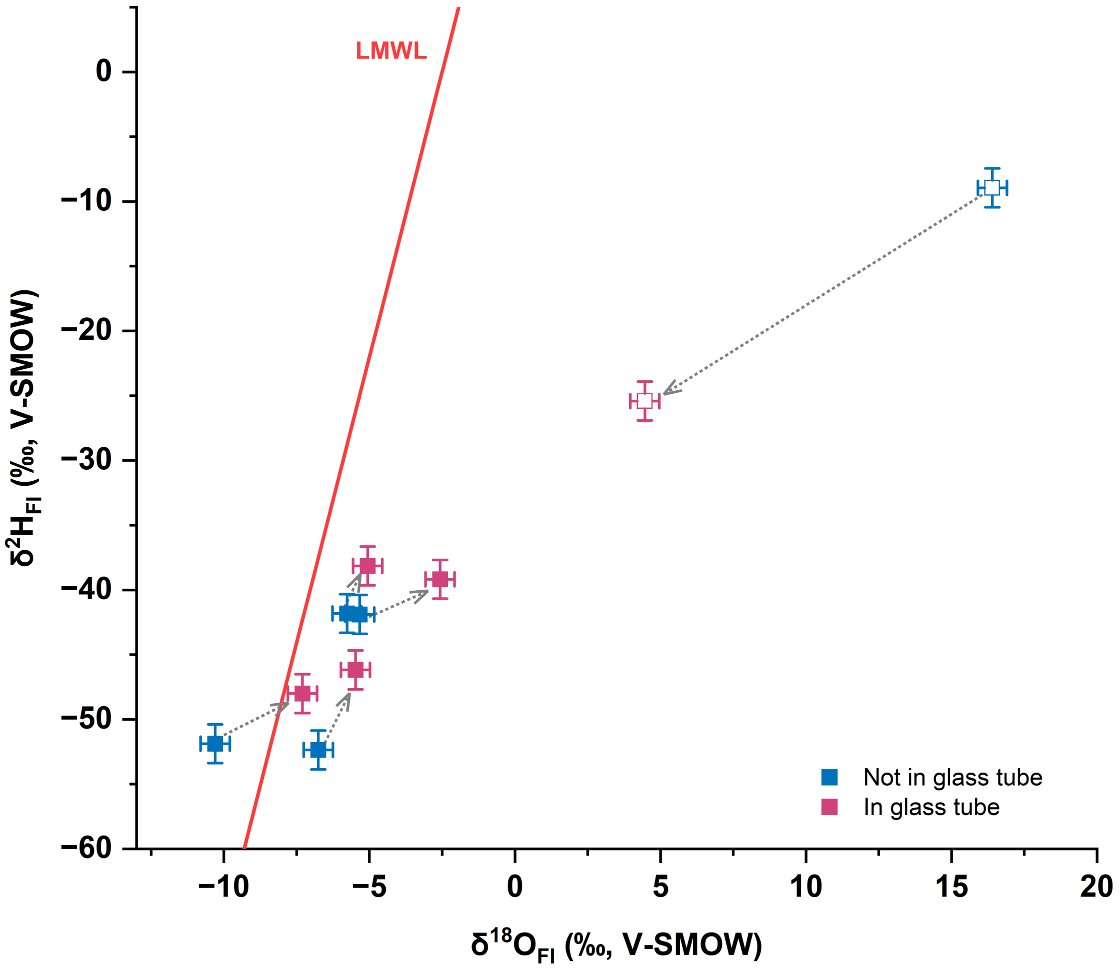

Figure S5.4. Comparison of fluid inclusion water $\delta^{18}O_{FI}$ and δ^2H_{FI} measured in and out of glass tubes. Each layer's samples were split into two parts for comparative measurements. Samples from only one growth layer (at about 13 mm) show very large differences in isotope values (hollow data points).

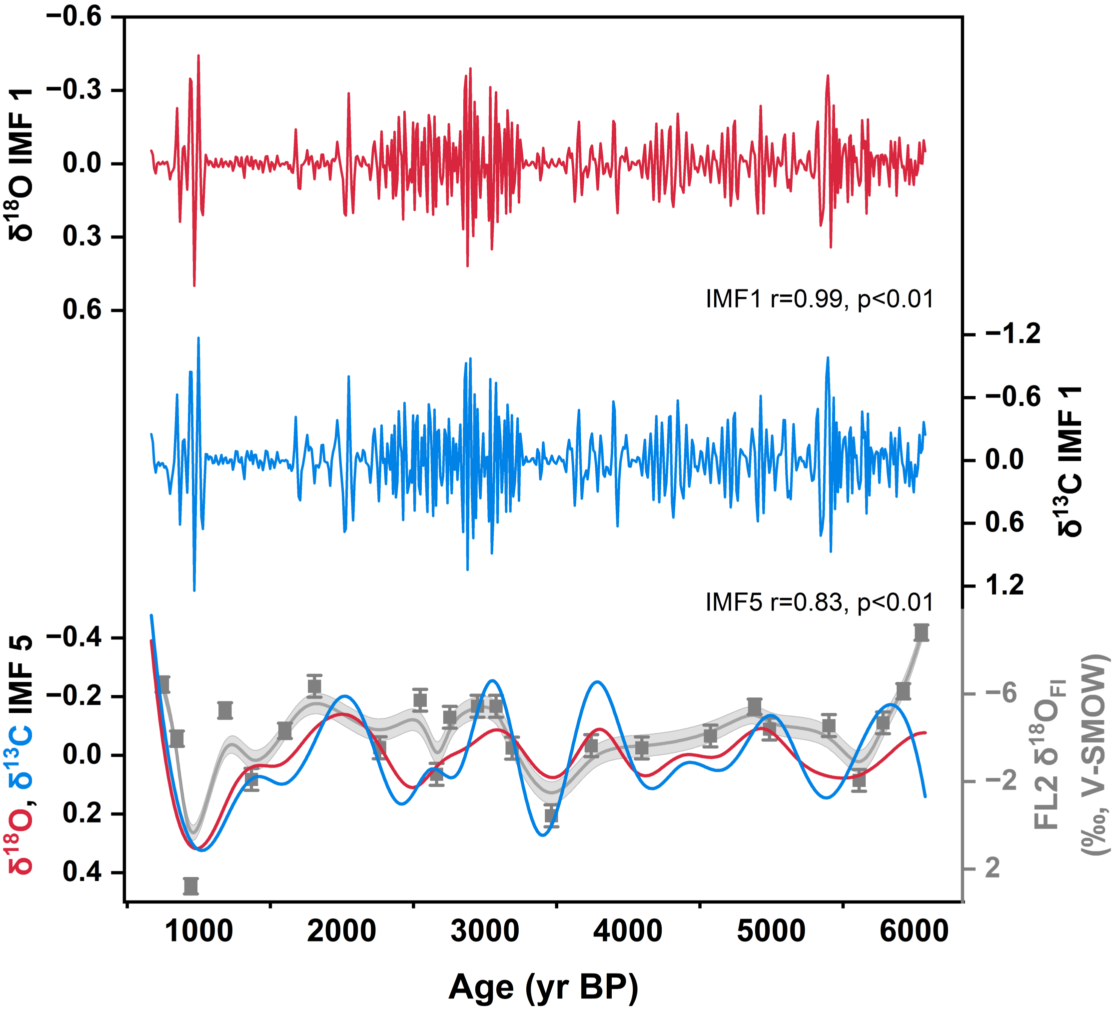

Figure S5.5. The intrinsic mode functions (IMF1 and IMF5) of the ensemble empirical mode decomposition of the FL2 $\delta^{18}O_S$ and $\delta^{13}C_S$ records. EEMD is a signal analysis method suitable for nonlinear and non-stationary signals, which can effectively extract signals, trends, and cycles at different time scales of a time series (Wu and Huang, 2009).

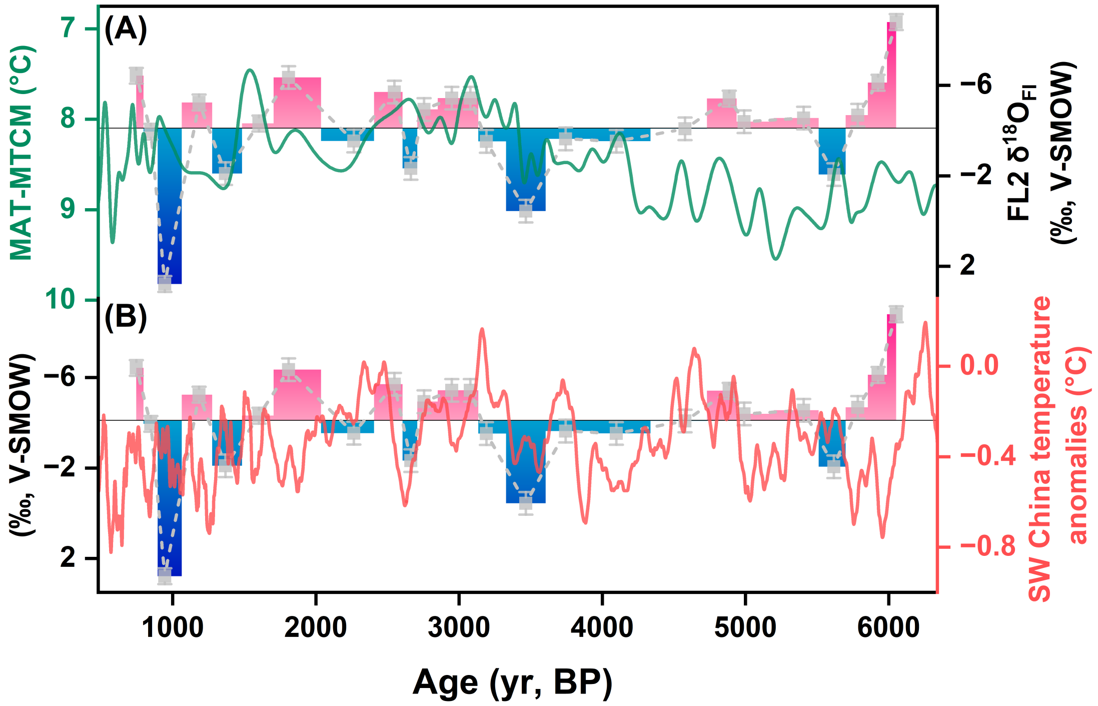

Figure S5.6. Comparison of FL2 $\delta^{18}O_{FI}$ and temperature variations in southwest China based on reconstruction and modelling. (A) The green curve represents the difference between the mean annual temperature and the mean annual coldest month temperature (Xiao et al., 2023). (B) Model simulated temperature anomalies in southwest China (Shi et al., 2021). The $\delta^{18}O_{FI}$ and temperature variations did not show a consistent pattern.

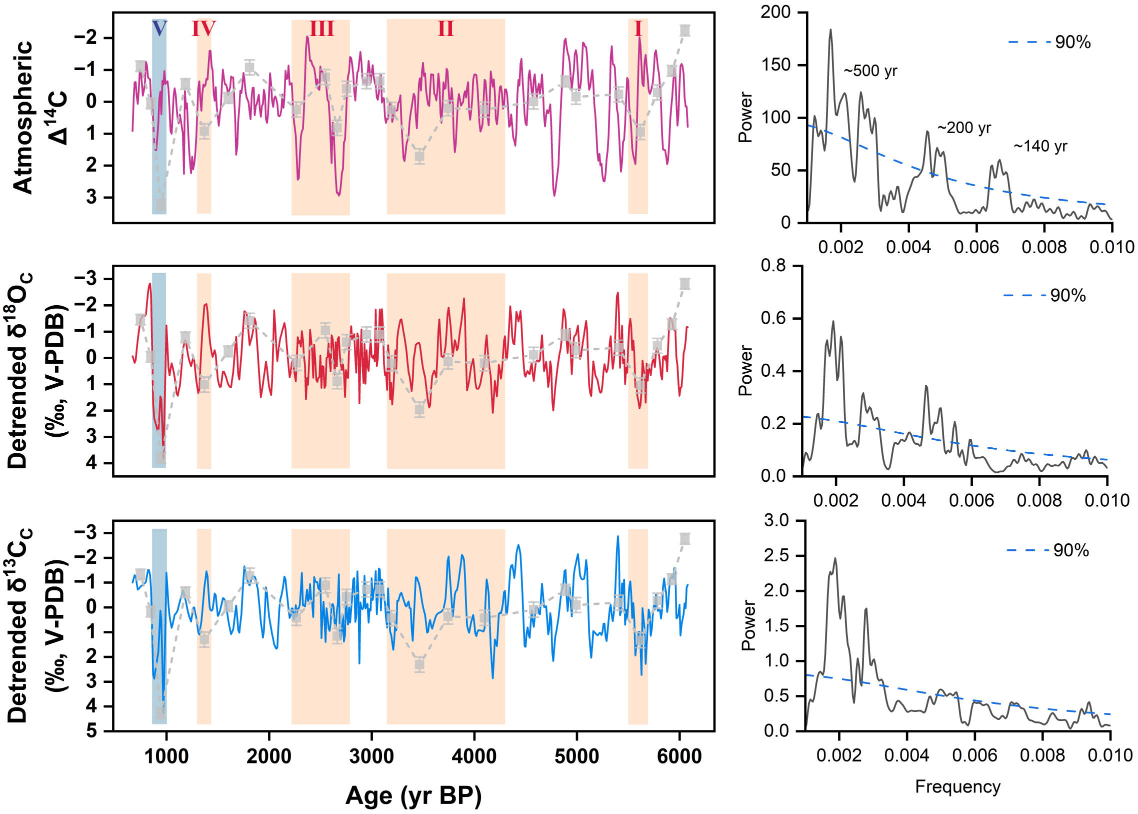

Figure S5.7. FL2 stalagmite records in comparison to atmospheric Δ^{14}C as indicator of solar activity. δ^{18}Os, δ^{13}Cs and atmospheric Δ^{14}C was detrended (Reimer et al., 2020).

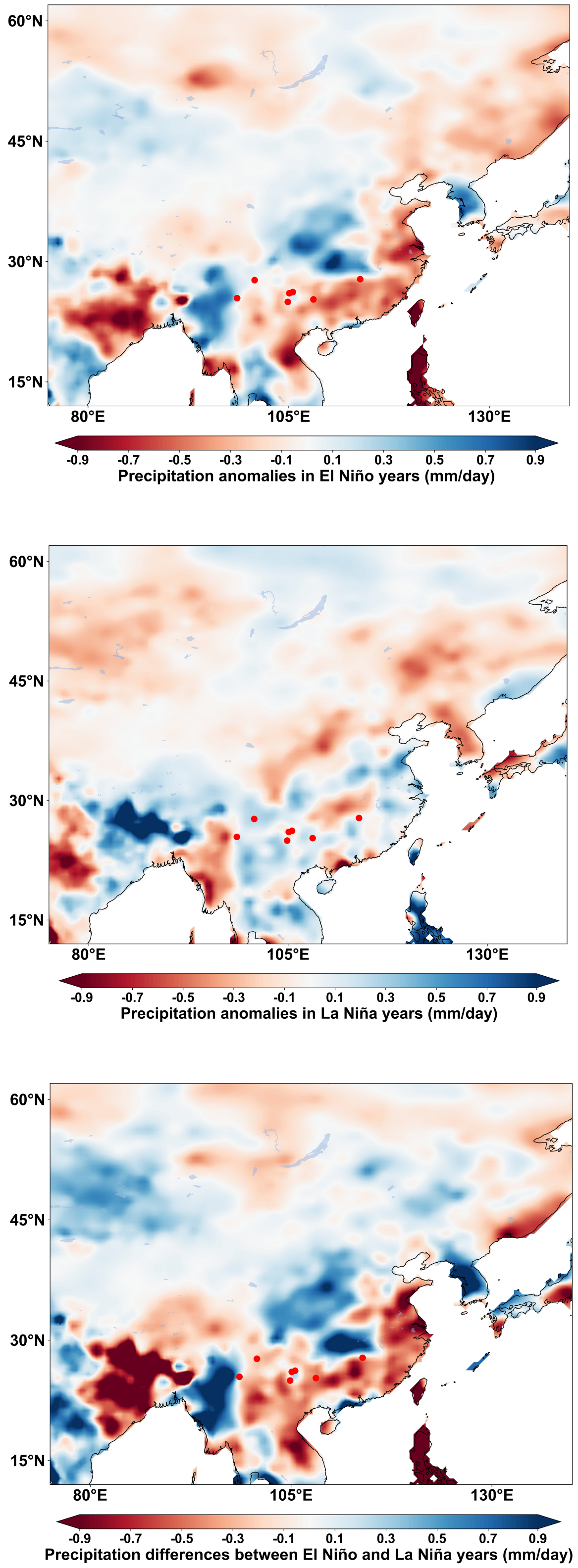

Figure S5.8. The summer precipitation (MJJA) anomalies in the ASM region during the of El Niño and La Niña years during 1950-2020 CE. Precipitation data from NOAA's Precipitation Reconstruction over Land database (Chen et al., 2002). The El Niño years and La Niña years are determined based on peak years in the historical statistics of ENSO events as defined by the National Climate Centre of China.

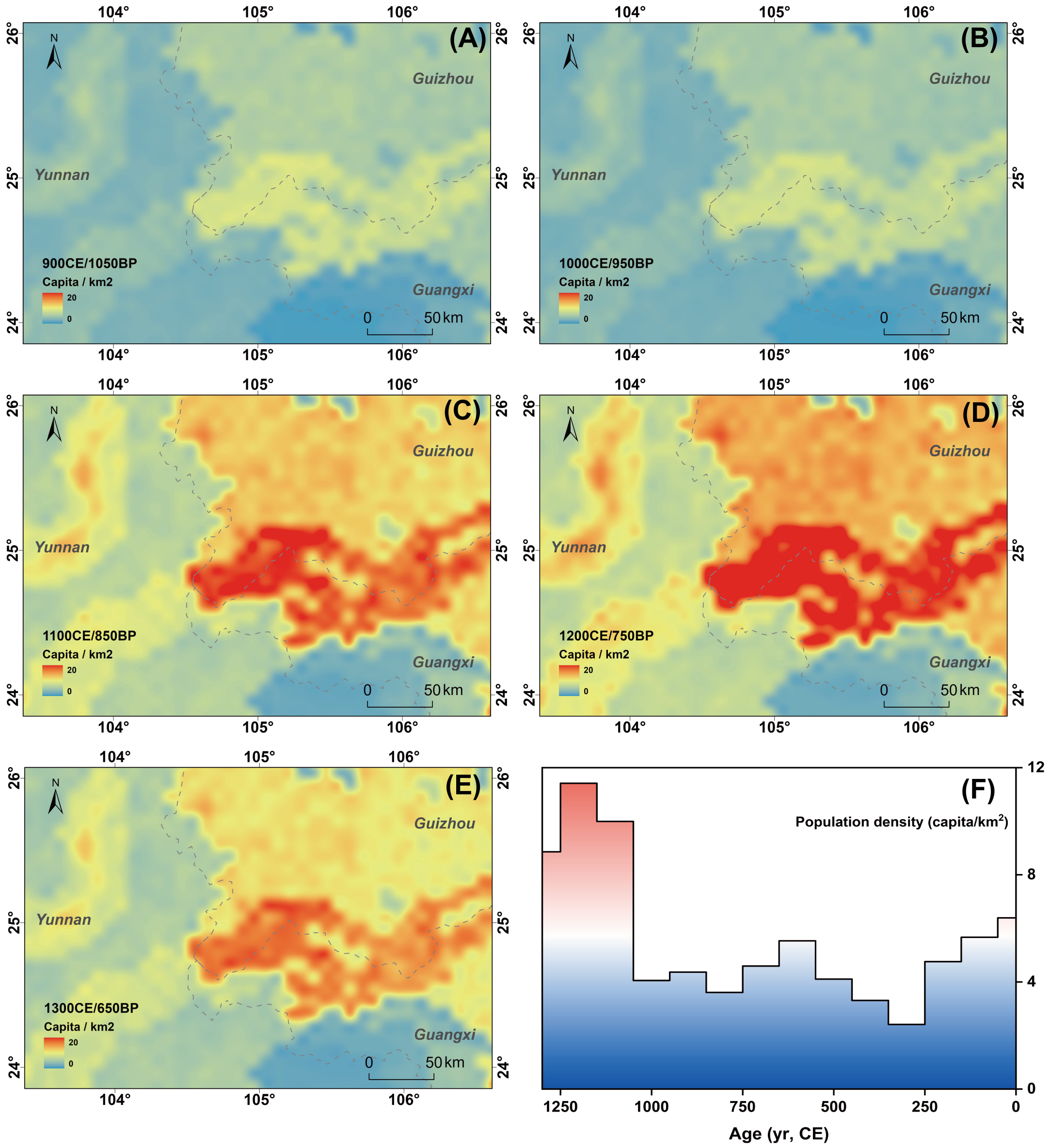

Figure S5.9. Variation in population density within the rectangle around Feilong cave (380 × 270 km). (A-E) Population density variations around Feilong cave during 900, 1000, 1100, 1200, 1300 CE. (H) Variation in average population density around Feilong cave over the 0-1300 CE interval. Data from the History Database of the Global Environment (HYDE, v 3.3) (Klein Goldewijk et al., 2010).

Supplementary Text S5.1

We use the Craig-Gordon (C-G) model to predict the line internal fractionation process. Fractionation is assumed to happen at 120°C with a relative humidity of 0.42%-0.49% (relative to a water vapour concentration of 6000-7000 ppm, T=120°C, P=1400 hPa). The equilibrium fractionation factor is calculated using the relationship proposed by Horita and Wesolowski (1994), 1994. Diffusion fractionation factors ranged from 1 to 0.8, corresponding to processes dominated by molecular diffusion (Gonfiantini et al., 2018; Horita et al., 2008). The isotopic composition of water vapour in the air in the model uses isotopic values of laboratory standard water used as the water vapour background for the measurement line (δ^{18}O= -8.53‰, δ^{2}H= -60.41‰). We used measurements close to the GMWL (δ^{18}O=-6.39‰, δ^{2}H=-41.08‰) as the isotope values of the initial fluid inclusion, assuming that these samples did not experience significant evaporation.

Given the limited temperature variations in southwest China during the mid-to late Holocene (Figure S6), we used the modern annual mean temperature (16.4°C) from study area as the range for temperature fluctuations. For relative humidity in the cave, the range of values is 50-95%, which includes the ideal state where the cave is close to saturation with water vapour and the extreme conditions associated with enhanced cave ventilation. Equilibrium fractionation factors are calculated using the relationship proposed by Horita and Wesolowski (1994). The diffusion fractionation factor ranges from 0.5 to 1 and covers all possible conditions that can occur in the cave Fernandez et al. (2023); Gonfiantini et al. (2018). The δ^{18}O and δ^{2}H values of water vapour in cave air are assumed to be in equilibrium with the mean $\delta^{18}\mathrm{O}_{\mathrm{FI}}$ and $\delta^{2}\mathrm{H}_{\mathrm{FI}}$ value close to the GMWL (δ^{18}O=-16.29‰, δ^{2}H=-118.39‰).

The effective fractionation factors α_{eff} for ^{18}O and ^{2}H during evaporation are expressed as follows:

$$\alpha_{\text{eff}} = \frac{\alpha(T) - h \cdot \left(\frac{R_a}{R_l}\right)}{1 - h \cdot \left(\frac{1}{D^n}\right)}$$

where:

- h is the relative humidity, - D is the ratio of molecular diffusivities of the heavy to the light isotopologues, - R_a is the isotope ratio in air, - R_l is the isotope ratio in liquid.

The equilibrium vapor-liquid isotope fractionation factor $\alpha(T)$ depends on temperature $T(K)$ and is derived from experimental relationships:

$$\alpha(T) = \exp\left(\frac{A}{T^2} + \frac{B}{T} + C\right)$$

Using the Rayleigh distillation model, the isotopic ratio of the residual liquid is related to the fraction of remaining liquid (f) as follows:

$$R_l = R_o \cdot f^{(\alpha_{\text{eff}}-1)}$$

where:

- R_l is the isotope ratio of the liquid at each step of an evaporative process, - R_o is the isotope ratio of the initial liquid, - f is the fraction of liquid remaining at each step, and - α_{eff} is the effective fractionation factor.

Iterating with a 2% reduction in the proportion of liquid remaining each time, the relationship between $\delta^{18}O$ ($\delta^{18}O_l$) and δ^2H (δ^2H_l) in the remaining liquid was fitted to obtain the slope, assuming a linear relationship:

$$\delta^2H_l = m \cdot \delta^{18}O_l + b$$

Supplementary Table

Table S5.1. Results of analyses of FL2 fluid inclusion water isotopic. NG and G indicate samples measured not in and in glass tubes, respectively. Depth starts from the top. The units for water volume and water content are µl and µl/g, respectively.

Sample ID	**Depth (mm)**	**Error**	**Age (yr, BP)**	**Age Δ (yr, BP)**	**Weight (g)**	**Water volume**	**Water content**	δ^{18}O **(‰, V-SMOW)**	**Error**	δ^{2}H **(‰, V-SMOW)**	**Error**	**Note**
FL2-1A	5	2	746	77	0.57	0.61	1.08	-6.64	0.5	-41.69	1.5	NG
FL2-1B	5	2	746	77	0.56	0.50	0.89	-6.21	0.5	-40.13	1.5	NG
FL2-2A	9	2	847	123	0.58	0.45	0.77	-5.34	0.5	-41.90	1.5	NG
FL2-2B	9	2	847	123	0.54	0.49	0.91	-2.57	0.5	-39.18	1.5	G
FL2-3A	13	1.5	944	78	0.49	0.12	0.24	16.40	0.5	-8.95	1.5	NG
FL2-3B	13	1.5	944	78	0.51	0.23	0.45	4.46	0.5	-25.41	1.5	G
FL2-3C	13	1.5	944	78	0.44	0.16	0.36	1.11	0.5	-36.66	1.5	G
FL2-4A	23	1.5	1184	79	0.50	0.64	1.29	-4.39	0.5	-35.88	1.5	G
FL2-4B	23	1.5	1184	79	0.49	0.66	1.34	-6.10	0.5	-35.81	1.5	G
FL2-5	30	1.5	1368	77	0.64	0.41	0.64	-2.10	0.5	-33.38	1.5	NG
FL2-6A	40	1.5	1602	77	0.34	0.26	0.77	-4.37	0.5	-36.44	1.5	G
FL2-6B	40	1.5	1602	77	0.40	0.29	0.72	-4.26	0.5	-36.85	1.5	G
FL2-7	49	1	1809	52	0.64	0.97	1.52	-6.35	0.5	-41.44	1.5	NG
FL2-8	70	1.5	2265	7	0.60	0.22	0.37	-3.54	0.5	-36.83	1.5	NG
FL2-9	112	1.5	2548	25	0.75	0.79	1.05	-5.71	0.5	-38.34	1.5	NG
FL2-10	126	1.5	2664	33	0.52	1.18	2.26	-2.33	0.5	-26.39	1.5	G
FL2-11	141	1.5	2756	23	0.75	1.50	2.00	-4.93	0.5	-35.77	1.5	NG

Table S5.1 Continued

Sample ID	**Depth (mm)**	**Error**	**Age (yr, BP)**	**Age Δ (yr, BP)**	**Weight (g)**	**Water volume**	**Water content**	δ^{18}O **(‰, V-SMOW)**	**Error**	δ^{2}H **(‰, V-SMOW)**	**Error**	**Note**
FL2-12	190	2	2949	20	0.60	3.14	5.23	-5.44	0.5	-38.97	1.5	NG
FL2-13	220	1.5	3079	19	0.52	0.54	1.03	-5.44	0.5	-37.76	1.5	NG
FL2-14	246	2	3191	19	0.94	1.13	1.20	-3.53	0.5	-29.85	1.5	NG
FL2-15	268	1	3466	67	0.42	0.13	0.31	-0.43	0.5	-26.97	1.5	G
FL2-16	280	2	3745	90	0.56	0.55	0.98	-3.64	0.5	-30.26	1.5	NG
FL2-17	296	2	4098	82	0.54	1.86	3.44	-3.53	0.5	-29.79	1.5	NG
FL2-18	320	1.5	4577	80	0.47	0.63	1.33	-4.08	0.5	-38.22	1.5	G
FL2-19A	335	1.5	4886	81	0.60	0.56	0.94	-5.77	0.5	-41.82	1.5	NG
FL2-19B	335	1.5	4886	81	0.46	0.77	1.68	-5.06	0.5	-38.15	1.5	G
FL2-20	339.5	1.5	4991	82	0.49	1.14	2.32	-4.39	0.5	-33.64	1.5	G
FL2-21	360	1.5	5407	54	0.60	0.94	1.57	-4.55	0.5	-37.30	1.5	NG
FL2-22	383	1.5	5617	37	0.68	1.63	2.39	-2.05	0.5	-25.70	1.5	NG
FL2-23	400	1.5	5785	38	0.42	1.16	2.77	-4.68	0.5	-34.49	1.5	G
FL2-24A	414	2	5925	41	0.60	1.15	1.92	-6.76	0.5	-52.36	1.5	NG
FL2-24B	414	1.5	5925	41	0.46	1.25	2.71	-5.48	0.5	-46.18	1.5	G
FL2-25A	427	1.5	6053	34	0.51	0.41	0.81	-10.30	0.5	-51.88	1.5	NG
FL2-25B	427	1.5	6053	34	0.40	0.35	0.88	-7.30	0.5	-48.01	1.5	G

Table S5.2. Mean isotopic value of repeated measurements. Depth starts from the top.

Number of repeated measurements	**Depth (mm)**	**Error**	**Age (yr, BP)**	δ^{18}O **(‰, V-SMOW)**	**Error**	δ^{2}H **(‰, V-SMOW)**	**Error**
2	5	2	746	-6.43	0.35	-40.91	1.06
2	9	2	847	-3.95	0.35	-40.54	1.06
2	13	1.5	944	2.79	0.35	-31.04	1.06
2	23	1.5	1184	-5.24	0.35	-35.84	1.06
1	30	1.5	1368	-2.10	0.50	-33.38	1.50
2	40	1.5	1602	-4.31	0.35	-36.65	1.06
1	49	1	1809	-6.35	0.50	-41.44	1.50
1	70	1.5	2265	-3.54	0.50	-36.83	1.50
1	112	1.5	2548	-5.71	0.50	-38.34	1.50
1	126	1.5	2664	-2.33	0.50	-26.39	1.50
1	141	1.5	2756	-4.93	0.50	-35.77	1.50
1	190	2	2949	-5.44	0.50	-38.97	1.50
1	220	1.5	3079	-5.44	0.50	-37.76	1.50
1	246	2	3191	-3.53	0.50	-29.85	1.50
1	268	1	3466	-0.43	0.50	-26.97	1.50
1	280	2	3745	-3.64	0.50	-30.26	1.50
1	296	2	4098	-3.53	0.50	-29.79	1.50
1	320	1.5	4577	-4.08	0.50	-38.22	1.50

Table S5.2 Continued

Number of repeated measurements	**Depth (mm)**	**Error**	**Age (yr, BP)**	δ^{18}O **(‰, V-SMOW)**	**Error**	δ^{2}H **(‰, V-SMOW)**	**Error**
2	335	1.5	4886	-5.41	0.35	-39.98	1.06
1	339.5	1.5	4991	-4.39	0.50	-33.64	1.50
1	360	1.5	5407	-4.55	0.50	-37.30	1.50
1	383	1.5	5617	-2.05	0.50	-25.70	1.50
1	400	1.5	5785	-4.68	0.50	-34.49	1.50
2	414	2	5925	-6.12	0.35	-49.27	1.06
2	427	1.5	6053	-8.80	0.35	-49.95	1.06

B.5 Supplementary Information for Chapter 6

Supplementary Figures

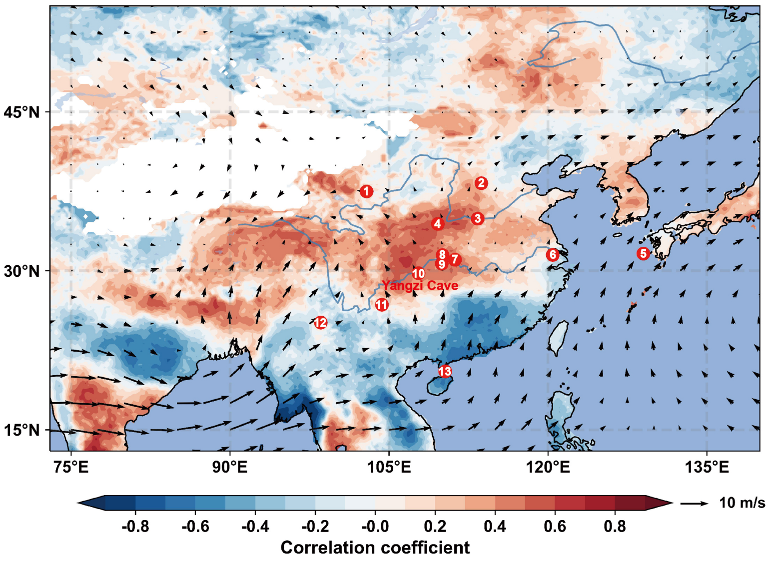

Figure S6.1. Study sites, modern spatial distribution of precipitation in China and general circulation pattern of the ASM. The first empirical orthogonal function (EOF) model for June-July-August (JJA) precipitation for 1980-2007 C.E. Analysis of Asian Precipitation-Highly-Resolved Observational Data Integration Towards Evaluation (APHRODITE) gridded rainfall data set using the eofs: Version 1.1.0 Python package (Yatagai et al., 2012). The mode explains 14.5% of the total variance. Monsoonal precipitation in China shows the tripolar pattern, whereby rainfall decreases in east-central China and increases in the northern and southern China. Arrows indicate the summer (June–August) 850 hPa wind field. Wind data are derived from NCEP/NCAR reanalysis datasets (Kalnay et al., 1996), with averages calculated over the period from 1981–2020 C.E. The red circles indicate the locations of 1 Gulang Loess (Sun et al., 2019), 2 Zhenzhu Cave (Li et al., 2020), 3 Mangshan Loess (Peterse et al., 2014), 4 Weinan Loess (Thomas et al., 2014), 5 IODP U1429 (Clemens et al., 2018), 6 Tai Lake (Miao et al., 2015), 7 Yongxing Cave (Wang et al., 2022a) (Wang et al., 2022a), 8 Dajiuhu mountain Wetland (Zhang et al., 2023c), 9 Haozhu Cave (Zhang et al., 2018), 10 Yangzi Cave (this study), 11 Caohai mountain Wetland (Zhang et al., 2023c), 12 Tengchong–Qinghai Volcanic Lake (Zhang et al., 2023c), and 13 Maar Lake (Wang et al., 2022c), respectively.

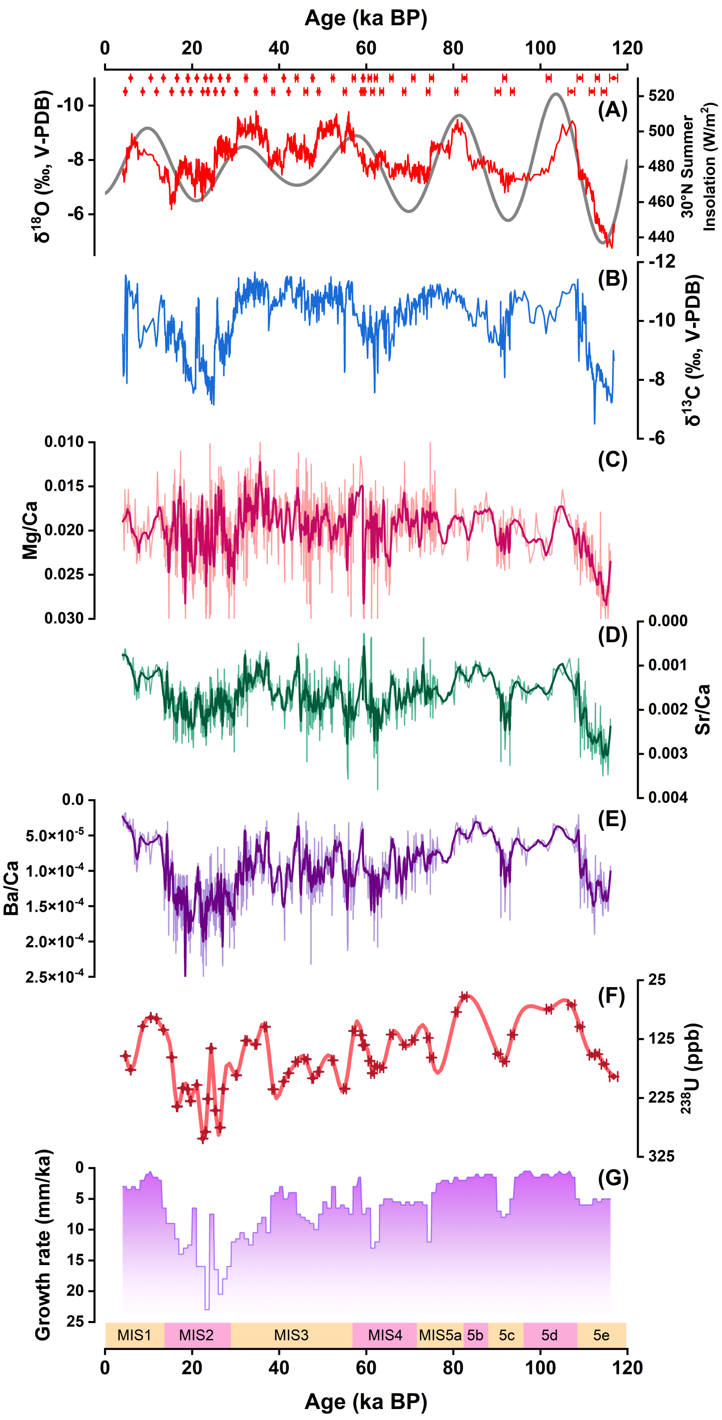

Figure S6.2. δ^{18}O, δ^{13}C and X/Ca records of YZ1 stalagmite. (A) The red curve indicates the δ^{18}O record of YZ1, and the grey curve indicates the NHSI at 30°N; (B) δ^{13}C record of YZ1; (C) Mg/Ca record of YZ1; (D) Sr/Ca record of YZ1; (E) Ba/Ca record of YZ1; (F) ^{238}U concentration (ppb) record for the YZ1 stalagmite dating sample; (G) growth rate of YZ1. Trace element records are linearly interpolated to stable isotope resolution. The dark curves of the trace element records indicate the respective 10-point smoothing. MIS X indicates the stage of Marine Isotope Stages (Lisiecki and Raymo, 2005).

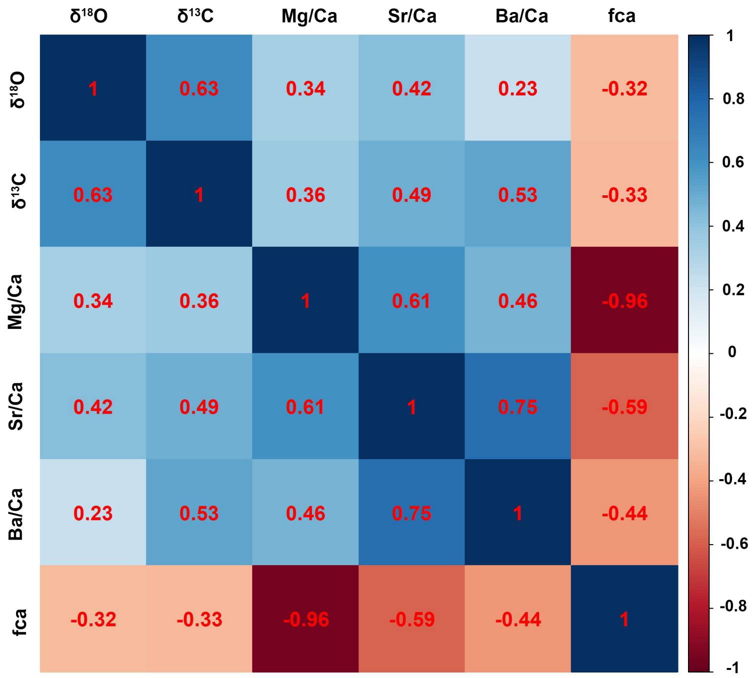

	$\delta^{18}O$	$\delta^{13}C$	Mg/Ca	Sr/Ca	Ba/Ca	fca
$\delta^{18}O$	1	0.63	0.34	0.42	0.23	-0.32
$\delta^{13}C$	0.63	1	0.36	0.49	0.53	-0.33
Mg/Ca	0.34	0.36	1	0.61	0.46	-0.96
Sr/Ca	0.42	0.49	0.61	1	0.75	-0.59
Ba/Ca	0.23	0.53	0.46	0.75	1	-0.44
fca	-0.32	-0.33	-0.96	-0.59	-0.44	1

Figure S6.3. Correlation of δ^{18}O, δ^{13}C and Sr/Ca, Mg/Ca, Ba/Ca, fCa of stalagmite YZ1 (p<0.01).

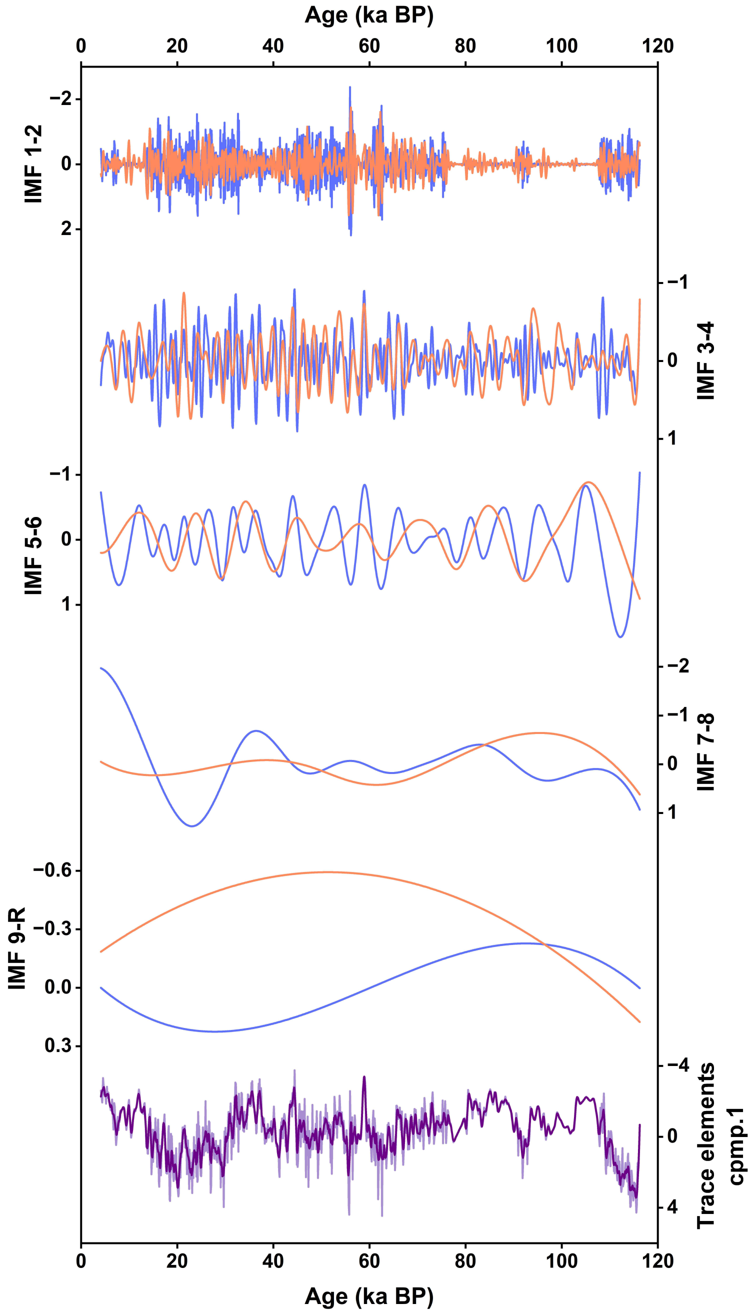

Figure S6.4. The intrinsic mode functions (IMF1–IMF9 and R) of the ensemble empirical mode decomposition (EEMD) of the YZ1 X/Ca PC1 record. The purple curve indicates the X/Ca PC1 record of YZ1, the dark curve indicates 10-points smoothing. These nine components extend the period from orbital to suborbital, millennial, and centennial time scales. IMF7 captures the precession cycle. We performed the EEMD analysis using the MATLAB 2022b platform. The EEMD is a noise-assisted data analysis method favorable method for extracting signals and trends on different scales of time series (Wu and Huang, 2009). This approach extracts the patterns of variation from multivariate time series datasets that best describe the overall variability of these datasets by reducing the dimensionality of large datasets.

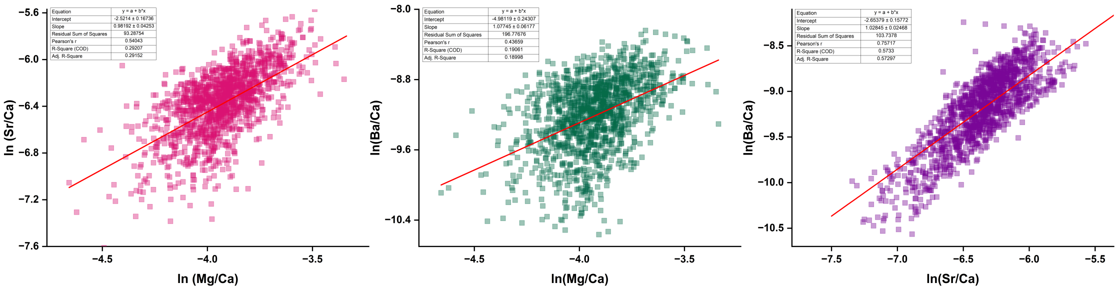

Equation	y = a + b*x
Intercept	-2.5214 ± 0.16736
Slope	0.98192 ± 0.04253
Residual Sum of Squares	93.28754
Pearson's r	0.54043
R-Square (COD)	0.29207
Adj. R-Square	0.29152

Equation	y = a + b*x
Intercept	-4.98119 ± 0.24307
Slope	1.07745 ± 0.06177
Residual Sum of Squares	196.77676
Pearson's r	0.43659
R-Square (COD)	0.19061
Adj. R-Square	0.18998

Equation	y = a + b*x
Intercept	-2.65379 ± 0.15772
Slope	1.02845 ± 0.02468
Residual Sum of Squares	103.7378
Pearson's r	0.75717
R-Square (COD)	0.5733
Adj. R-Square	0.57297

Figure S6.5. Cross plots of element to calcium ratios in YZ1 shown as ln(Sr/Ca) vs. ln(Mg/Ca) (left), ln(Ba/Ca) vs. ln(Mg/Ca) (middle), and ln(Ba/Ca) vs. ln(Sr/Ca) (right).

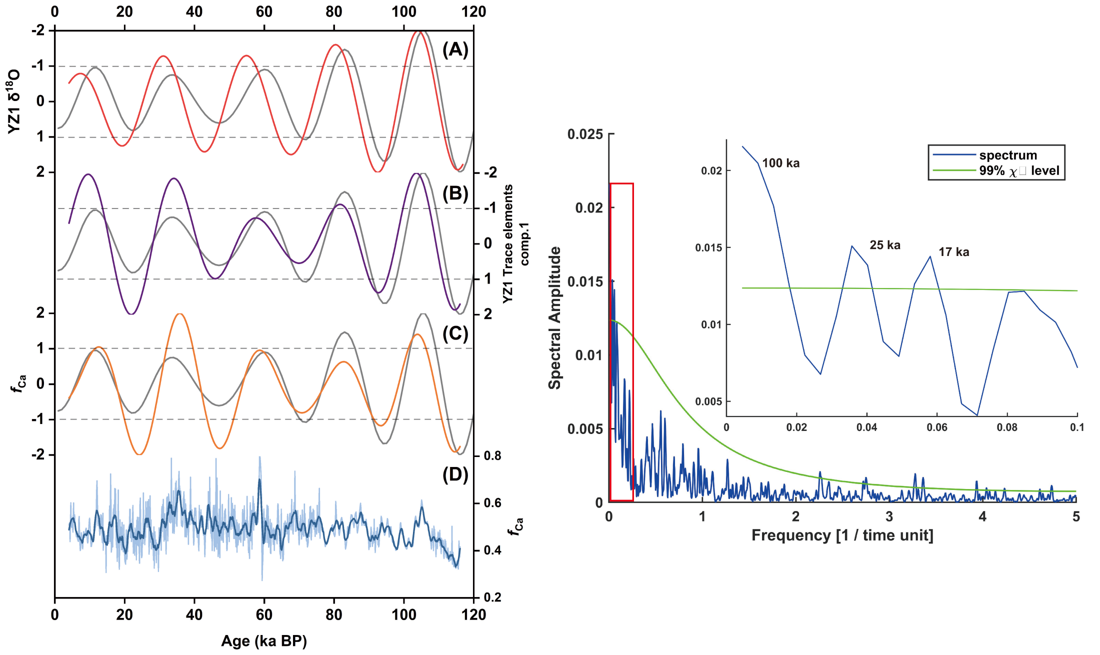

Figure S6.6. YZ1 δ^{18}O, X/Ca PC1 and fCa band pass filters results (left). (A) δ^{18}O; (B) X/Ca PC1; (C) fCa; (D) fCa using the Mg/Camin/Mg/Ca sample approximation, the dark blue curve indicates 10-point smoothing of the original record. The band pass filters were calculated using the Acycle 2.4.1 software on the MATLAB 2022b platform. The frequency is 0.0434 ka^{-1} and the band width is 0.01 ka^{-1}, normalized to the interval -2 to 2. The right side indicates the results of the spectral analysis of the fCa records using the REDFIT GUI (Schulz and Mudelsee, 2002). The green curve is 99% confidence limits, the time unit is ka. The grey curve indicates the variation in the precession (Laskar et al., 2004).

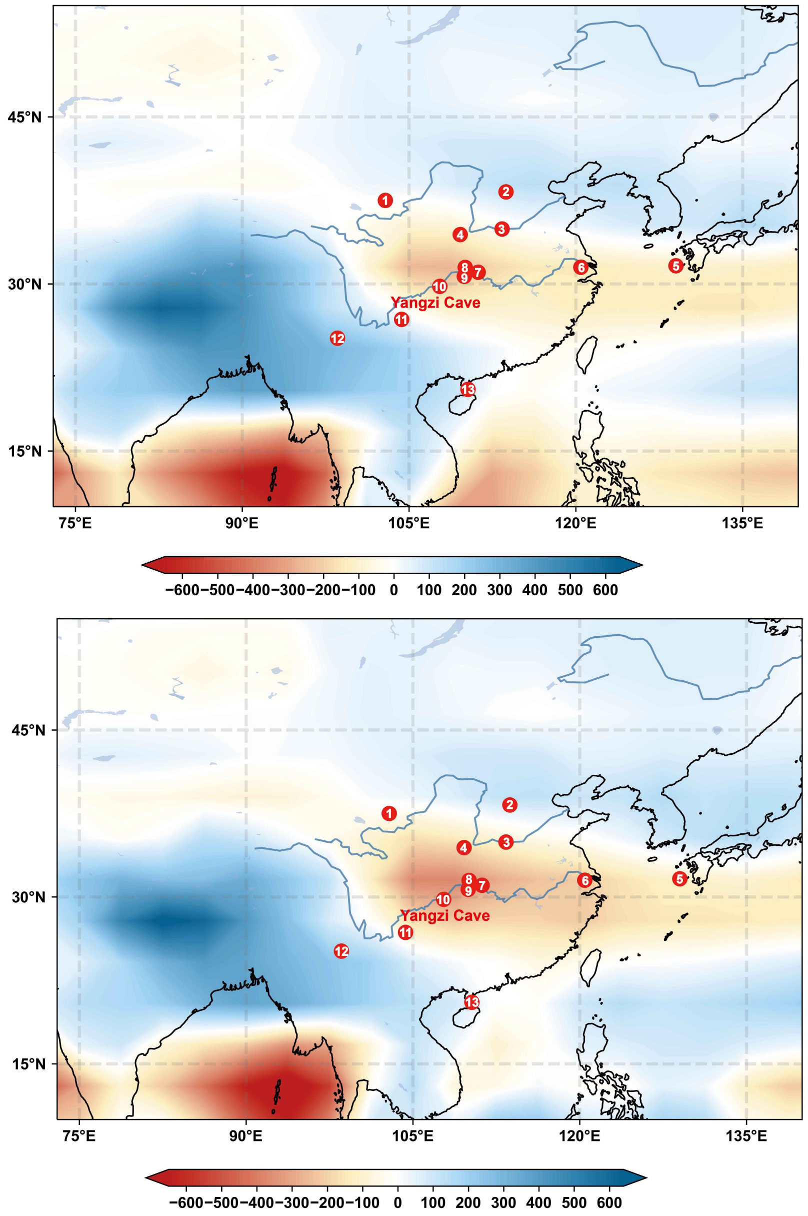

Figure S6.7. The changes in ensemble mean precipitation (unit: mm, shading colors) due to intensified summer monsoon (6 insolation maxima minus 6 insolation minima) (data from Dai et al. (2021)). The top panel shows precipitation anomalies from May to September; the bottom panel shows anomalies in annual mean precipitation. Only changes that are significant at the 95% confidence level are shown. The red circles indicate the locations of 1 Gulang Loess (Sun et al., 2019), 2 Zhenzhu Cave (Li et al., 2020), 3 Mangshan Loess (Peterse et al., 2014), 4 Weinan Loess (Thomas et al., 2014), 5 IODP U1429 (Clemens et al., 2018), 6 Tai Lake (Miao et al., 2015), 7 Yongxing Cave (Wang et al., 2022a), 8 Dajiuhu mountain Wetland (Zhang et al., 2023c), 9 Haozhu Cave (Zhang et al., 2018), 10 Yangzi Cave (this study), 11 Caohai mountain Wetland (Zhang et al., 2023c), 12 Tengchong–Qinghai Volcanic Lake (Zhang et al., 2023c), and 13 Maar Lake (Wang et al., 2022c), respectively.

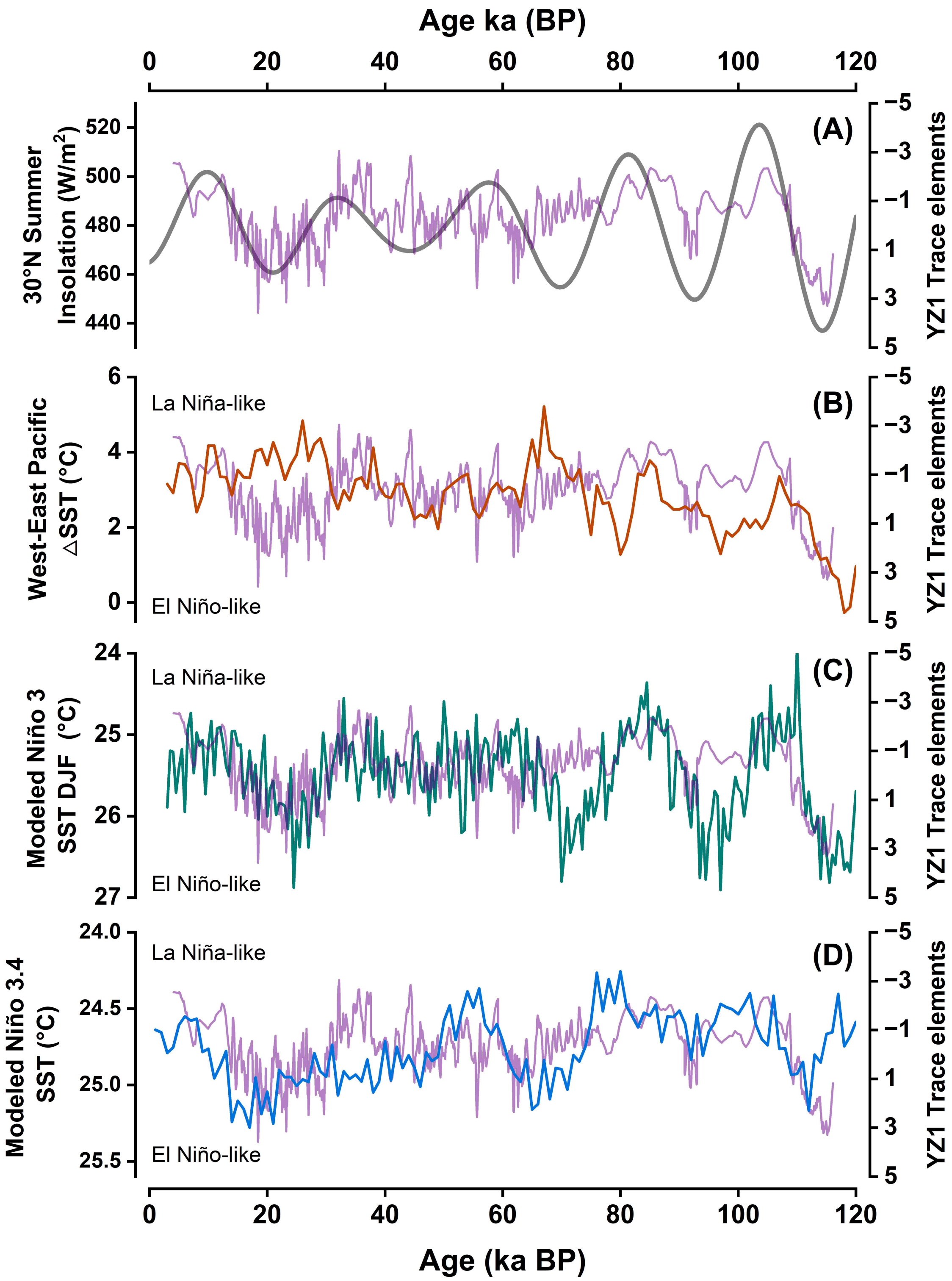

Figure S6.8. Comparison of YZ1 stalagmite X/Ca PC1 and ENSO indicators. (A) The purple curve indicates YZ1 X/Ca PC1 (this study) and the grey curve indicates NHSI at 30°N; (B) SST difference between the Western equatorial pacific (core KX97322-415) and Eastern equatorial pacific (core TR163−19) (Lea et al., 2000; Zhang et al., 2017, 2021c); (C) Simulates Niño3 SST for December - January - February (Zhang et al., 2021c) ; (D) Modeled Niño 3.4 annual mean SST (Lu et al., 2019b).

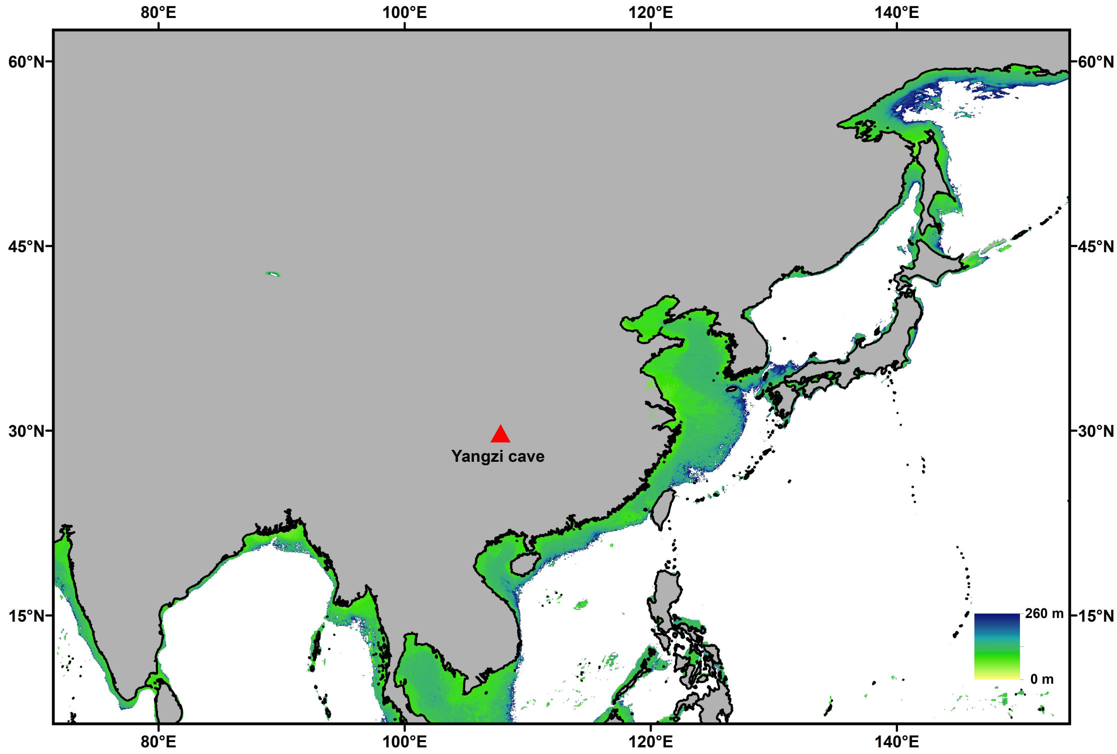

Figure S6.9. Global map of historical coastline positions since 26 ka BP (De Groeve et al., 2022).

Supplementary Table

Table S6.1. Principal component analysis results of Mg/Ca, Sr/Ca, and Ba/Ca in YZ1 stalagmite.

	Comp.1	Comp.2	Comp.3
Standard deviation	1.51	0.75	0.41
Proportion of Variance	0.76	0.18	0.06
Cumulative Proportion	0.76	0.94	1.00

Comp.1, Comp.2, Comp.3 represent the calculated principal components;
Standard deviation represents the standard deviation of each principal component;
Proportion of Variance represents the contribution rate of each principal component;
Cumulative Proportion represents the cumulative contribution rate of each principal component.

Table S6.2. The Periods and Contribution Rates (CRs) of the IMF and R.

	IMF1	IMF2	IMF3	IMF4	IMF5	IMF6	IMF7	IMF8	IMF9	R
Period (yr)	0.32	0.72	1.45	2.85	7.10	13.96	25.20	52.83	111.96	R
CR (%)	16.06	9.34	6.35	6.29	15.05	9.73	24.99	7.37	1.91	2.93

Supplementary Text S6.1

Stalagmite YZ1 was collected about 200 meters from the entrance of the cave. The stalagmite is 690 mm long and is approximately 100 mm and 65 mm in diameter at the bottom and top. YZ1 is composed of pure, dense calcite, but shows few clearly visible growth contaminations and minor detrital layers (Figure S6.10). Wu et al. (2020) reported the U/Th dating and age-depth model, as well as the δ^{18}O and δ^{13}C results for the YZ1 stalagmite. In short, YZ1 covers the period 116.09 to 4.07 ka BP continuously with growth rates varying between 0.5 and 23 µm/year. The average uncertainty of the age model is in the range of ±0.7 ka at 100ka, and ±0.27 ka at 10 ka BP.

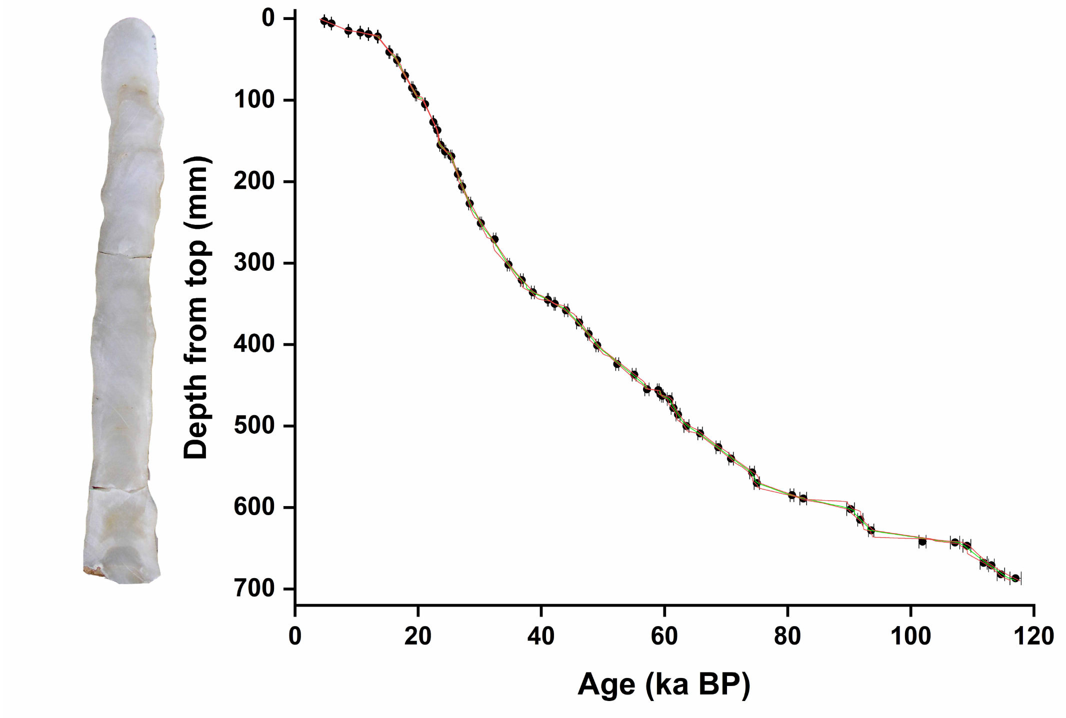

Figure S6.10. YZ1 stalagmite profile and age model. The black dots are the depths and ages of the U-Th dating samples, and the error bars indicate the dating error (±2σ) (modified from Wu et al. (2020)). The green line is a StalAge age model for YZ1, the red line indicates the 95% confidence limit (Scholz and Hoffmann, 2011).

Supplementary Text S6.2

The previous calcite precipitation promotes the degassing of CO2 from the solution and affects the trace element to Ca ratio of the drip water. Because trace element incorporation is not proportional to Ca incorporation, trace element incorporation can be described by the concept of trace element distribution coefficient (D), which is defined as:

$$D_x = \frac{(\mathrm{X/Ca})_{\text{prec}}}{(\mathrm{X/Ca})_{\text{drip}}}$$

where $(\mathrm{X/Ca})_{\text{prec}}$ is the trace element-to-Ca ratio of the precipitate, and $(\mathrm{X/Ca})_{\text{drip}}$ is the trace element-to-Ca ratio of the drip water.

The trace-element to Ca ratios can be used to semi-quantitatively assess relative changes in precipitation amount by estimating the remaining fraction of Ca in the solution, fCa via a Rayleigh fractionation equation (Stoll et al., 2023).The relationship between the remaining fraction fCa of the initial Ca in solution during karst carbonate deposition and the partition coefficient DMg, initial drip water Mg/Caini, measured solution Mg/Ca can be described by a Rayleigh process equation process. Eq. 1 shows how the fraction of initial Ca remaining in solution (fCa) can be calculated from the initial drip water Mg/Cainil (e.g., prior to degassing) and measured solution Mg/Ca, when the partitioning coefficient DMg is known:

Eq.1:

$$f_{\text{Ca}} = \left(\frac{(\mathrm{Mg/Ca})_{\text{spel}}}{D_{\text{Mg}} \cdot (\mathrm{Mg/Ca})_{\text{ini}}} \right)^{\frac{1}{(D_{\text{Mg}}-1)}}$$

With the assumption, that the minimum Mg/Ca value of the speleothem, Mg/Caspel,min is the closest approximation of the bedrock Mg/Ca ratio, equation (1) can be approximated by the following:

Eq.2:

$$f_{\text{Ca}} = \left(\frac{(\mathrm{Mg/Ca})_{\text{spel}}}{(\mathrm{Mg/Ca})_{\text{spel,min}}} \right)^{\frac{1}{(D_{\text{Mg}}-1)}}$$

To first order, the minimum Mg/Ca of a stalagmite corresponds to a situation of negligible degassing and PCP, and that the partitioning coefficient DMg is constant. Therefore, the initial Mg/Ca can be approximated by the minimum Mg/Ca of the stalagmite (compare also Stoll et al. (2023)):

Eq.3:

$$f_{\text{Ca\_MgCa}} = \frac{(\mathrm{Mg/Ca})_{\text{min}}}{(\mathrm{Mg/Ca})_{\text{sample}}}$$

C. Main Abbreviations

Abbreviation	Definition
ASM	Asian Summer Monsoon
CRDS	Cavity Ring-Down Spectroscopy
D/O event	Dansgaard–Oeschger event
EASM	East Asian Summer Monsoon
EOF	Empirical Orthogonal Function
ENSO	El Niño–Southern Oscillation
GMWL	Global Meteoric Water Line
H events	Heinrich events
HOC	Holocene Optimum Climate
IRMS	Isotope Ratio Mass Spectrometry
ISM	Indian Summer Monsoon
ITCZ	Intertropical Convergence Zone
LGM	Last Glacial Maximum
LMWL	Local Meteoric Water Line
NH	Northern Hemisphere
NHSI	Northern Hemisphere Summer Insolation
PCP	Prior Calcite Precipitation
SH	Southern Hemisphere
SITIG	Summer Inter-Tropical Insolation Gradient
WPSH	Subtropical Western Pacific High
WRI	Water–rock interaction
X/Ca	Trace element ratios
δ^{13}Cs	Speleothem δ^{13}C
δ^{18}Os	Speleothem δ^{18}O
$\delta^{18}O_{FI}$	Fluid inclusion δ^{18}O
$\delta^{2}H_{FI}$	Fluid inclusion δ^{2}H

Data Availability Statement

All data used in this dissertation, as well as newly developed codes for data analysis, have been explicitly provided in the main text, supplementary materials, or this statement. The specific availability of data is as follows:

Chapter 2: All quantitative injection measurement results for isotopes have been included in the main text and tables in Supplementary Material B.1. Additionally, a Jupyter code example for correcting water volume effects is provided in the supplementary scripts of Supplementary Materials B.1.

Chapter 3: Chronological data of coral samples, water volume measurements of fluid inclusions in coral skeletons, and isotopic measurement results are provided in Supplementary Materials B.2.

Chapter 4: Water volume and isotopic measurement results from capillary samples across different laboratories are available upon reasonable request.

Chapter 5: Measured water volumes and isotopic results of fluid inclusions are provided in Supplementary Materials B.4.

Chapter 6: All trace element data interpolated to oxygen and carbon isotope resolutions, as well as raw LA-ICP-MS data, are available upon reasonable request.

All external data cited in this dissertation have been clearly referenced in the respective citations and are accessible through their original sources.

Acknowledgements

I am honored to present this dissertation. Throughout this research journey, I have been incredibly fortunate to receive the support and guidance of many people, for which I am deeply grateful. The experiences I have shared with them have been invaluable.

My deepest gratitude goes to my supervisor, Prof. Dr. Norbert Frank, whose constant encouragement and optimistic, positive attitude have been a source of great inspiration throughout this entire process. He not only provided meticulous academic guidance but also lent an attentive ear during times of confusion, offering the confidence I needed to persevere. His passion for research and rigorous approach have left a lasting impact, and he has truly been one of the most influential mentors in my academic journey. Every conversation with him was invaluable, and the trust and support he offered helped me grow through challenges. Completing this research under his mentorship has been one of the most rewarding experiences of my career.

My heartfelt thanks go to Dr. Sophie Warken for her steadfast support and invaluable guidance throughout my research. Her dedication, patience, and extensive knowledge were invaluable in helping me navigate challenges in experimental procedures, data analysis, and thesis writing. Her supportive and professional approach was instrumental in advancing my research skills. I truly appreciate her collaboration and the valuable insights she shared.

Dr. Martina Schmidt deserves my heartfelt thanks for her immense support, particularly in sample calibration and data analysis. Her expert advice and meticulous attention to detail were crucial in ensuring the accuracy and reliability of my experiments. Her patience and guidance were indispensable, and I am deeply honored to have received her assistance throughout this dissertation process.

My sincere gratitude extends to Jenny Maccali, Alvaro Fernandez Bremer, Sam Nicholson, Stéphane Affolter, Timon Kipfer, Anna Nele Meckler, and Hubert Vonhof for their collaboration on the fluid inclusion interlaboratory comparison project. Their invaluable contributions in experimental design, project development, and data discussions were key to the success of this endeavor. I also wish to thank all the laboratories involved in this project. It is through our collective effort and open collaboration that this research has progressed so smoothly, and this experience has reinforced my appreciation for the power of

scientific teamwork.

I would also like to sincerely acknowledge Prof. Dr. Ting-Yong Li, Prof. Dr. Jun-Yun Li, Chaojun Chen, and Dr. Yanxia Xue for their important support and contributions to this work. Their help in acquiring and processing domestic samples, along with their insightful academic discussions, greatly facilitated the progress of my work. Their generous support and professional guidance were instrumental in advancing this study.

I am grateful to my group members Dr. Andrea Schröder-Ritzrau, Dr. Eva Rückert, Dr. Elvira Beisel, Dr. Nils Schorndorf, Sahra Greve, Dr. Inga Kerber, Dr. Steffen Therre, Dr. Jasmin Link, Aaron Mielke, Dana Hölkermann, Amrei Grund, and Dr. Antao Xu. Beyond academic collaboration, their companionship and support have been a source of warmth throughout this journey. Their encouragement during busy experimental work, as well as the stimulating discussions we had, strengthened both our teamwork and my own confidence. I am truly fortunate to have had them by my side.

A special thank you goes to Bo Zhai and Yutong Shang, my dear companions in Germany, whose academic and personal support has made my time abroad truly meaningful. Together, we have faced challenges and shared many unforgettable moments, and their unwavering friendship has brought great joy and fulfillment to my life. I deeply value this bond and am forever grateful for their constant care and encouragement. I would also like to extend my heartfelt thanks to Ming Dai and Yangbiao Liu for their steadfast friendship and support. Whether at work or during leisure, their encouragement has been a continual source of strength and motivation, and I am truly fortunate to call them friends.

Finally, my profound gratitude goes to my family, whose unconditional love and understanding have been the driving force behind my perseverance. They have always been my greatest support, offering care and encouragement during the most challenging moments. No matter where I am, their unwavering presence has given me the strength to continue. I am truly thankful for their love, which has propelled me forward in both my personal and academic life.

I would also like to acknowledge the China Scholarship Council for their generous funding and support, which allowed me to dedicate myself fully to my research in Germany and successfully complete my studies.

NATURWISSENSCHAFTLICH-MATHEMATISCHE
GESAMTFAKULTÄT

COMBINED FACULTY OF NATURAL SCIENCES AND
MATHEMATICS

RUPRECHT-KARLS-
UNIVERSITÄT
HEIDELBERG

Eidesstattliche Versicherung gemäß § 8 der Promotionsordnung für die Naturwissenschaftlich-Mathematische Gesamtfakultät der Universität Heidelberg / Sworn Affidavit according to § 8 of the doctoral degree regulations of the Combined Faculty of Natural Sciences and Mathematics

1. Bei der eingereichten Dissertation zu dem Thema / The thesis I have submitted entitled

   Advances in Fluid Inclusion Water Isotope Analysis and Late Quaternary Hydrological Environment Reconstruction in the Asian Monsoon Region

   handelt es sich um meine eigenständig erbrachte Leistung / is my own work.

2. Ich habe nur die angegebenen Quellen und Hilfsmittel (inkl. KI-basierter Hilfsmittel) benutzt und mich keiner unzulässigen Hilfe Dritter bedient. Insbesondere habe ich wörtlich oder sinngemäß aus anderen Werken übernommene Inhalte als solche kenntlich gemacht. / I have only used the sources indicated (incl. AI-based tools) and have not made unauthorised use of services of a third party. Where the work of others has been quoted or reproduced, the source is always given.

3. Die Arbeit oder Teile davon habe ich wie folgt/bislang nicht[1] an einer Hochschule des In- oder Auslands als Bestandteil einer Prüfungs- oder Qualifikationsleistung vorgelegt. / I have not yet/have already[1] presented this thesis or parts thereof to a university as part of an examination or degree.

   Titel der Arbeit / Title of the thesis:

   Hochschule und Jahr / University and year:

   Art der Prüfungs- oder Qualifikationsleistung / Type of examination or degree:

4. Die Richtigkeit der vorstehenden Erklärungen bestätige ich. / I confirm that the declarations made above are correct.

5. Die Bedeutung der eidesstattlichen Versicherung und die strafrechtlichen Folgen einer unrichtigen oder unvollständigen eidesstattlichen Versicherung sind mir bekannt. / I am aware of the importance of a sworn affidavit and the criminal prosecution in case of a false or incomplete affidavit

Ich versichere an Eides statt, dass ich nach bestem Wissen die reine Wahrheit erklärt und nichts verschwiegen habe. / I affirm that the above is the absolute truth to the best of my knowledge and that I have not concealed anything.

………………………………………………………...……

Ort und Datum / Place and date

Unterschrift / Signature

---

[1] Nicht Zutreffendes streichen. Bei Bejahung sind anzugeben: der Titel der andernorts vorgelegten Arbeit, die Hochschule, das Jahr der Vorlage und die Art der Prüfungs- oder Qualifikationsleistung. / Please cross out what is not applicable. If applicable, please provide: the title of the thesis that was presented elsewhere, the name of the university, the year of presentation and the type of examination or degree.

The German text is legally binding.